Optimization of Higher Order Filters for Grid Connected High Frequency Power Converters

Vinod John   Parikshith B. Channegowda   Nilanjan Mukherjee

Anusyutha Krishnan   Amith Karanth

Department of Electrical Engineering

IISc Bangalore

December 2009

Abstract

Use of inverters to interconnect to the grid has become widespread for a number of power quality, regenerative motor drive and distributed generation applications. The design of passive filters for such converters has not received as much attention as that for control and operation of the semiconductor switches. Traditionally these filters have been first order inductive chokes. Design of filters used in grid-connected inverter applications involves a large number of constraints. The filter requirements are driven by tight tolerances of standards such as IEEE 519-1992–IEEE Recommended Practices and Requirements for Harmonic Control in Electrical Power Systems and IEEE 1547.2-2008–IEEE Application Guide for IEEE Std. 1547-2003, IEEE Standard for Interconnecting Distributed Resources with Electric Power Systems. Higher order LCL filters are essential to achieve these regulatory standard requirements at compact size and weight. This objective of this report is to evaluate design procedures for such higher order LCL filters and to provide insight into methodologies for improved filter design.

The initial configuration of the third order LCL filter is decided by the frequency response of the filter. The design equations are developed in per-unit basis so results can be generalized for different voltage and power levels. The frequency response is decided by IEEE specifications for high frequency current ripple at the point of common coupling. The appropriate values of L and C are then designed and constructed. Power loss in individual filter components is modelled by analytical equations and an iterative process is used to arrive at the most efficient design. Different combinations of magnetic materials (ferrite, amorphous, powder) and winding types (round wire, foil) are designed and tested to determine the most efficient design. The harmonic spectrum, power loss and temperature rise in individual filter components is predicted analytically and verified by actual tests using a 3-phase 10 kVA grid connected PWM converter setup.

Experimental results of filtering characteristics show a good match with analysis in the frequency range of interconnected inverter applications. The design process is streamlined for the above specified core and winding types. The output harmonic current spectrum is sampled and it is established that the harmonics are within the IEEE recommended limits. The analytical equations predicting the power loss and temperature rise are verified by experimental results. Based on the findings, new LCL filter combinations are formulated by varying the net L_{pu} to achieve the highest efficiency while still meeting the recommended IEEE specifications.Thus a design procedure which can enable an engineer to design the most efficient and compact filter that can also meet the recommended guidelines of harmonic filtering for grid-connected converter applications is established.

Compared to the inductive filter use of an LCL filter can lead to resonance. It has been shown that one can design effective resonance suppression by both active and passive methods. Methods to evaluate the ability for suppression of resonance has been confirmed with experimental results. Experimental results carried out in using closed loop grid interactive control confirm the design procedure for resonance damping in LCL filters. The ability to design smaller filters that meet high performance requirements leads to a cost effective filtering solution for grid connected high frequency power converters.

Acknowledgement

Preface

Background

High energy prices and environmental concerns are driving the search for alternative renewable energy sources. Simultaneously, rising cost and complexity in existing electricity distribution systems, and the inability of current systems to serve remote areas reliably has led to search for alternate distribution methods. One viable solution is use of renewable energy sources directly at point of load, which is termed as Distributed Generation(DG). Most renewable sources of energy, like wind, solar etc., are interfaced to the existing electric grid by a power converter. This eliminates the transmission and distribution losses and improves reliability of the grid power supply. But use of power converters will also introduce undesirable harmonics that can affect nearby loads at the point of common coupling to the grid. Hence, all such converters have a filter to minimize these harmonics to acceptable levels.

The present work is on design of such filters for high power (10's to 100's of kVA) pulse width modulated high power voltage source converters for grid-connected converter applications. The conventional method to interface these converters to grid is through a simple first order low-pass filter, which is bulky, inefficient and cannot meet regulatory requirements such as IEEE 512-1992 and IEEE 1547-2008. The goal of this report is the design of efficient, compact higher order filters to attenuate the switching harmonics at the point of interconnection to the grid to meet the requirement of DG standards of interconnection.

Organization of the report

The filter design analysis is logically arranged into six self contained chapters featuring filter component parameter selection, analysis and inductor design process. The concern

of grid interactive operation due to resonance in the filter is then addressed. The last chapter reports the experimental results that were used to validate the design assumptions. Filter design is normally an iterative procedure. The last chapter demonstrates that tradition design rules can lead to a bulky and inefficient filter.

Transfer Function Analysis This chapter takes a top-level system level approach to filter design. The factors which affect the initial selection of the LCL filter parameters include IEEE recommended limits on high frequency current ripple, closed loop operation requirements of a grid connected filter, EMI filtering, power system fault ride-through requirements etc.. The filter parameters obtained at the end of the chapter satisfy all the hard constraints of a high power converter interfaced to the grid. The subsequent chapters deal with the actual construction and efficiency optimization of the filter.

Filter Component Construction This chapter is focused on the design and construction of the individual components of the LCL filter. The design techniques to accurately build an inductor of required inductance are discussed in detail. The familiar area product approach for inductor design is modified and incorporated into new methods which are more accurate and material specific. The principles of construction for three different magnetic materials -Ferrite, Amorphous and Powder is discussed. Finally, capacitors and resistors suited for for high power filter applications are introduced.

Simulation Using FEA Tools Modelling and simulation of the filter inductors using Finite Element tools are described here.The tools used are FEMM and MagNet. Inductance values, plots of flux lines and flux density in the inductor core are shown in the results. Results of Finite Element Analysis of the filter inductors and measurement of air gap and core flux density in the actual inductors are available in this section.

Power Loss and Heating Effects In this chapter the filter parameters obtained from the previous chapter are examined from the point of view of efficiency and temperature rise. This efficiency and temperature optimization become highly significant as recent trends suggest that more switching power converters at higher power ratings are connected to the grid. This chapter derives the equations that describe the power loss in inductors at high frequency operation. Finally, principles of heat transfer are used to estimate the surface temperature of inductors. The entire design procedure can be validated from the expected temperature rise of the inductor.

Grid Interactive Operation and Active Damping This chapter discuss the methods that can be used for actively damping resonances in LCL filters. A state space based control design is shown to have better performance. The performance of the active damping controller is experimentally verified by operating the power converter in grid interactive manner.

Results and Optimized LCL Filter Design This chapter reports the experimental results that are used to verify the filter design model. All aspects of the design process are tested, with special emphasis placed on harmonic response and efficiency of the constructed filter components. The designed and actual measurements are compared to verify the validity of the design assumptions. The notable contribution of this report is formulation of new LCL filter combinations by varying the net L_{pu} to achieve the highest efficiency while still meeting the recommended IEEE specifications.

Contents

Chapter 1

Transfer Function Analysis

1.1 Introduction

This chapter focuses on the design procedures to implement L, LC and LCL filters for grid connected inverter applications. The design calculations are based on per-unit values, so the results obtained are generalized for any application for power levels ranging from 10's of kW upto 100's of kW. The procedure for passive damping unwanted resonance in the third order filters is also discussed in detail.

1.2 Starting assumptions

There are certain simplifying assumptions that are made to analyse the frequency characteristics of the grid connected low pass filter. The assumptions are made to keep the initial design analysis simple. These constraints are subsequently relaxed later in the course of the discussion for a more accurate analysis.

- All filter elements are considered ideal, i.e no winding resistance, inter-turn/inter-winding capacitance in case of inductor, and no equivalent series resistance, parasitic inductance in case of capacitor.

- Grid is considered as an ideal voltage source, i.e zero impedance, and supplying constant voltage/current at fundamental (50Hz) frequency. This is a reasonable assumption since any impedance at the grid can be lumped with the output impedance of the filter. We can see later that this assumption is also justifiable based on per

unitized impedance calculations of grid interconnection.

- The filter design procedure is appropriate for grid connected PWM voltage-source inverters or matrix converters. Current source inverters are not considered.

- The design procedure assumes only grid connected mode of operation. Stand alone converter applications are only briefly discussed.

1.3 Per unit system

The per unit system is used to represent the voltage, current, kVA, frequency and other electrical parameters. All the design equations are expressed in per unit basis of the converter rating. The advantage of the per unit method is that we can generalize the design procedure for a wide range of power levels and for different applications. This also makes the design procedure compatible with the grid power system ratings where most impedances are usually expressed in per unit basis.

1.3.1 Base parameters

The per unit system followed here is based on the volt ampere rating of the power converter. The line to neutral output voltage V_{LN} is the base voltage and the 3 phase KVA rating $KVA_{3\phi}$ is the base volt ampere. The fundamental frequency of 50Hz is the base frequency.

$$V_{base} = V_{LN} \tag{1.1}$$

$$KVA_{3\phi(base)} = 3\phi \, \text{Power rating} \tag{1.2}$$

$$I_{pu} = \frac{I_{actual}}{I_{base}} = \frac{KVA_{3\phi(pu)}}{V_{pu}} \tag{1.3}$$

$$Z_{base} = \frac{V_{base}}{I_{base}} \tag{1.4}$$

$$Z_{pu} = \frac{V_{pu}}{I_{pu}} \tag{1.5}$$

$$L_{base} = \frac{Z_{base}}{2\pi f_{base}} \tag{1.6}$$

$$L_{pu} = \frac{L_{actual}}{L_{base}} = Z_{pu} \tag{1.7}$$

$$C_{base} = \frac{1}{Z_{base} \times 2\pi f_{base}} \tag{1.8}$$

$$C_{pu} = \frac{C_{actual}}{C_{base}} = \frac{1}{Z_{pu}} \tag{1.9}$$

The per unit system can be easily extended to other parameters like dc bus voltage and switching frequency.

$$V_{dc(pu)} = \frac{V_{dc}}{V_{base}} \tag{1.10}$$

$$f_{sw(pu)} = \frac{f_{sw}}{f_{base}} \tag{1.11}$$

1.3.2 DC voltage per unit

A single leg of a three-phase inverter can be represented as shown in Fig 1.1. The inverter voltage and current are represented as v_i, i_i and the grid voltage and current are represented as v_g and i_g.
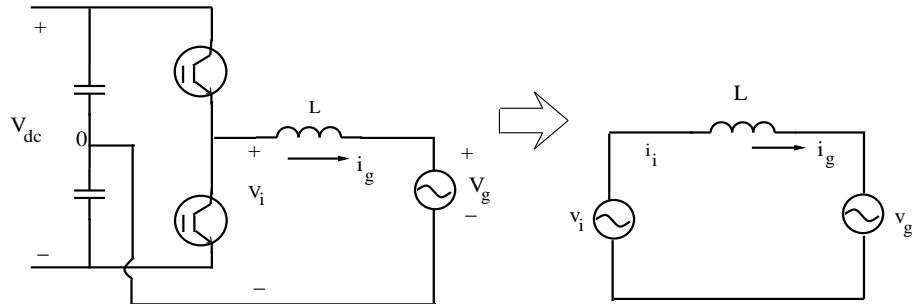
Figure 1.1: Equivalent circuit of one leg of voltage source inverter

The DC bus voltage can be expressed in per unit of grid voltage depending on the configuration of the inverter and whether reactive power compensation is required. We can define the dc bus voltage V_{dc} in terms of pole voltage V_i. The pole voltage in turn can be defined based on the base voltage $V_g = V_{base}$. The assumptions are that the grid voltage can have a maximum variation of $\pm 10\%$, and the pole voltage will be reduced by 5% because of dead band switching requirement. We are also taking into account the voltage drop due to a series filter, which usually will not exceed 10% of the inverter pole voltage.

Topology 1
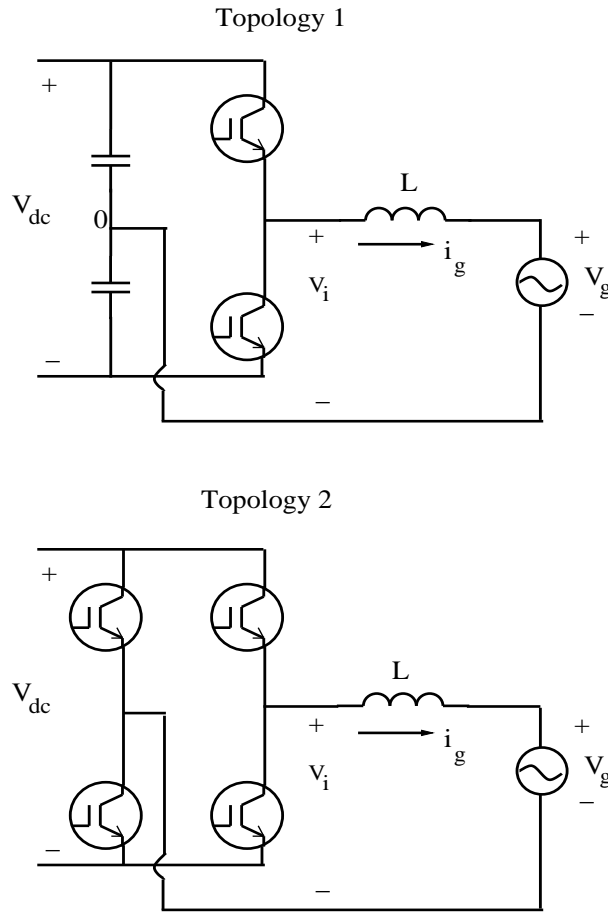
Topology 2

Figure 1.2: Different configurations of single phase inverters

For the single phase topologies shown in Fig 1.2 (Topology 1)

$$\frac{V_{dc}}{2} = V_i = V_{base} \times \sqrt{2} \times 1.1 \times 1.05 \times 1.1 \tag{1.12}$$

Similarly for Topology 2,

$$V_{dc} = V_i = V_{base} \times \sqrt{2} \times 1.1 \times 1.05 \times 1.1 \tag{1.13}$$

For the three phase topology shown in fig 1.3, the pole voltage V_i depends on the modulation method. In case of sine-triangle modulation, the peak pole voltage amplitude (in case of linear modulation) is

$$V_i = m_a \frac{V_{dc}}{2} \tag{1.14}$$

where m_a is the modulation index. So the maximum DC bus voltage will be when $m_a = 1$.

$$\frac{V_{dc}}{2} = V_i = V_{base} \times \sqrt{2} \times 1.1 \times 1.05 \times 1.1 \tag{1.15}$$

In case of space vector modulation used in 3ϕ 3 wire power converter, the maximum magnitude of the voltage space vector in α-β coordinates is,

$$V_{ref} = V_{dc} \cos 30° = V_{dc} \frac{\sqrt{3}}{2} \tag{1.16}$$

In three phase basis, the pole voltage will be

$$\frac{2}{3} V_{ref} = \frac{V_{dc}}{\sqrt{3}} = V_i = V_{base} \times \sqrt{2} \times 1.1 \times 1.05 \times 1.1 \tag{1.17}$$
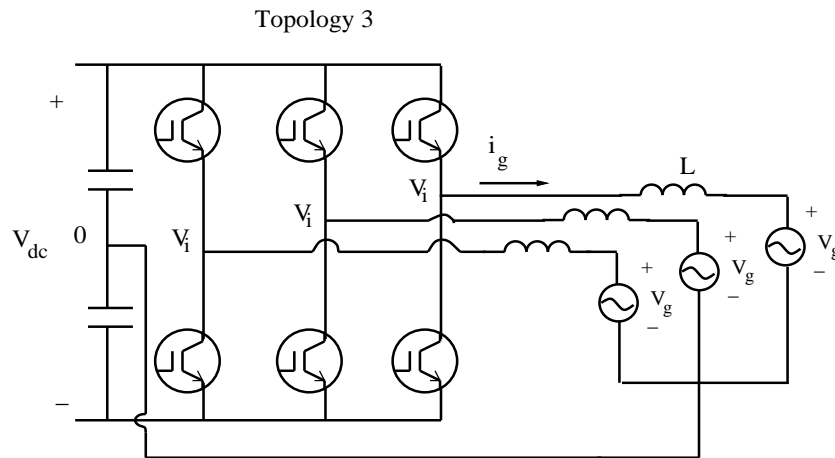
Figure 1.3: Three phase inverter configuration

1.3.3 Voltage and current ripple per unit

The per unit system is most useful to represent voltage and current ripple at switching frequency in terms of the base parameters. From Fig 1.4 if δi_{p-p} is the peak to peak ripple current in the inductor, then

$$\delta i_{rms} = \frac{\delta i_{p-p}}{2\sqrt{3}} \tag{1.18}$$

$$\delta i_{pu} = \frac{\delta i_{rms}}{I_{base}} \tag{1.19}$$
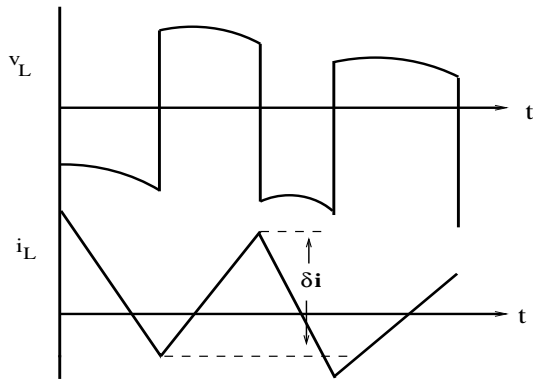
Figure 1.4: Voltage and current across filter inductor

The pole voltage is a combination of sinusoidal voltage at fundamental frequency along with harmonic voltages at various higher frequencies, including switching frequency. The rms of the harmonic voltages varies with the modulation method. We are assuming that the modulation method used is sine-triangle modulation. This assumption can be justified as this modulation method gives high harmonic voltages compared to any other advanced modulation methods, and if the designed filter can pass filtering criterion with this modulation method, it will satisfy the filtering requirements for any other advanced modulation method. But this assumption will also give a bigger filter than required if the modulation method is more sophisticated.

The grid voltage is assumed vary from -20% to +10%.

$$0.8V_g \leq V_g \leq 1.1V_g \tag{1.20}$$

where $V_g = V_{base}$=1 pu. Assuming a 10% drop in the series filter inductor, the variation in pole voltage will be

$$V_{i(pu)} = 1.1V_g \tag{1.21}$$

Since the control algorithm has to supply constant rated current at the inverter terminals even with this variation in grid voltage, the corresponding range of modulation index m_a can be calculated.

$$m_a = \frac{V_{i(pu)}\sqrt{2}}{\dfrac{V_{dc(pu)}}{2}} \tag{1.22}$$

$V_{i(pu)}$ and $V_{dc(pu)}$ can be substituted from Eqns (1.21) and (1.15). The range of modulation index to supply rated current for grid voltage variation is given in Table 1.1

As described earlier, the inverter pole voltage is a combination of fundamental voltage and harmonic voltages at various higher frequencies. By assuming that the most dominant harmonic voltage is at switching frequency, we can write the rms value of the inverter pole voltage as

$$V_{i(rms)}^2 = V_{i(50)}^2 + V_{i(fsw)}^2 \tag{1.23}$$

where $V_{i(50)}$ is the rms value of the fundamental voltage at 50Hz and $V_{i(fsw)}$ is the rms value of the switching frequency harmonic voltage. From Fig 1.5, it is clear that the total rms value of the inverter pole voltage is $V_{i(rms)} = V_{dc}/2$. The rms value of the fundamental depends on the modulation index.

$$V_{i(50)}^2 = \left(\frac{1}{\sqrt{2}} \frac{V_{dc}}{2} m_a \right)^2 \tag{1.24}$$

Hence we can find the switching frequency ripple voltage in terms of the rms pole voltage and modulation index.

$$V_{i(fsw)}^2 = V_{i(rms)}^2 - V_{i(50)}^2 \tag{1.25}$$

$$V_{i(fsw)}^2 = \frac{V_{dc}^2}{4} - \frac{1}{2} \frac{V_{dc}^2}{4} m_a^2 \tag{1.26}$$

$$V_{i(fsw)} = \frac{V_{dc}}{2} \sqrt{1 - \frac{m_a^2}{2}} \tag{1.27}$$

For the range of m_a from Table 1.1, the range of $V_{i(fsw)}$ is

$$0.739 \frac{V_{dc}}{2} \leq 0.791 \frac{V_{dc}}{2} \leq 0.872 \frac{V_{dc}}{2} \tag{1.28}$$
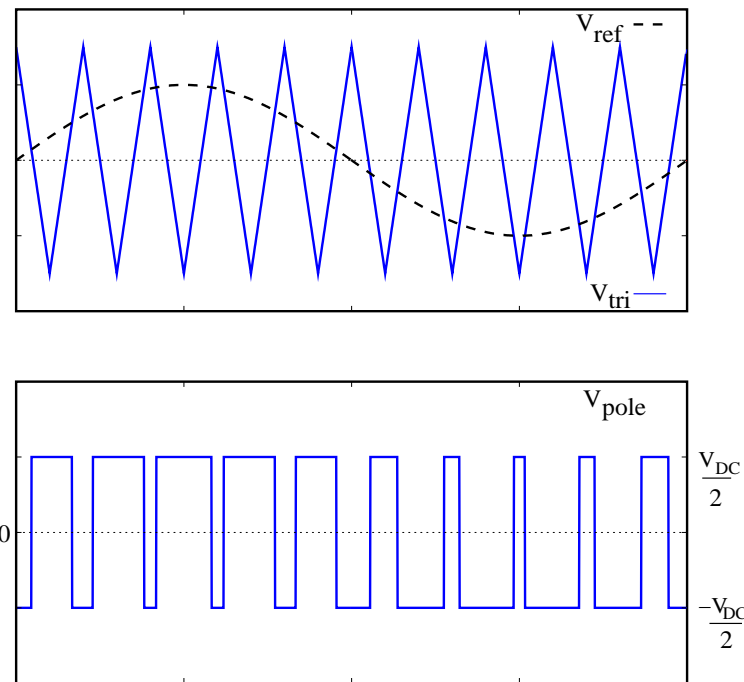
Figure 1.5: Sine triangle pulse width modulation

	Min	Nominal	Max
$V_{g(pu)}$	0.8	1	1.1
$V_{i(pu)} = 1.1V_{g(pu)}$	0.88	1.1	1.21
$m_a = \dfrac{V_{i(pu)}\sqrt{2}}{\dfrac{V_{dc(pu)}}{2}}$	0.693	0.866	0.952
$\sqrt{1 - \dfrac{m_a^2}{2}}$	0.793	0.791	0.872

Table 1.1: Effect of amplitude modulation index on switching frequency ripple

1.4   L filter
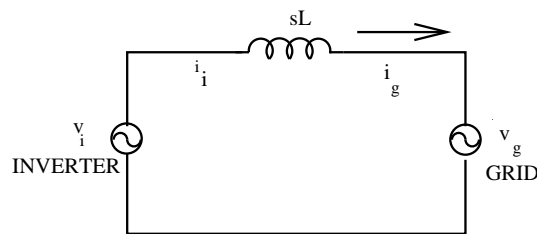
Figure 1.6: L filter inserted between active front end and grid

The design of an L filter is based on the current ripple at switching frequency that is

present in the PWM output.
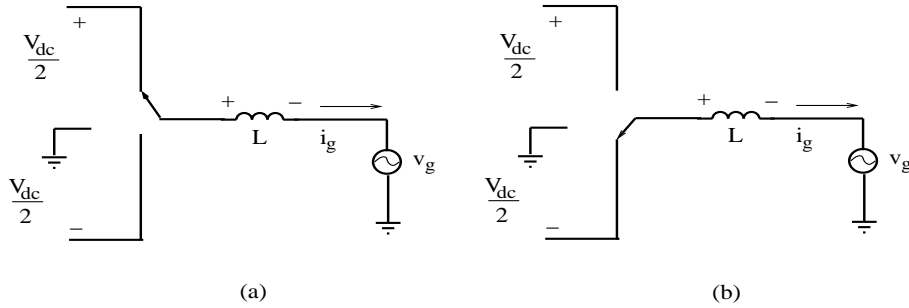
Figure 1.7: Voltage across L in T_{on} and T_{off}

If we consider one single switching cycle of the inverter, from Fig 1.7(a), during T_{on}

$$L\frac{\delta i_{p-p}}{T_{on}} = \frac{V_{dc}}{2} - v_g \qquad (1.29)$$

and during T_{off}, Fig 1.7(b)

$$L\frac{\delta i_{p-p}}{T_{off}} = -\frac{V_{dc}}{2} - v_g \qquad (1.30)$$

where $v_g = V_m \sin \omega t$, and $T_{on} + T_{off} = T_{sw}$. Since the modulation method is sine triangle modulation, the duty ratio D is

$$D = 0.5 + \frac{V_m \sin \omega t}{V_{dc}} = 0.5 + \frac{v_g}{V_{dc}} \qquad (1.31)$$

So from equations 1.29, 1.30 and 1.31, we get

$$T_{on} = L\frac{\delta i_{p-p}}{V_{dc}(1-D)} \qquad (1.32)$$

$$T_{off} = L\frac{\delta i_{p-p}}{V_{dc}D} \qquad (1.33)$$

Adding the above two equations we get

$$L_{actual} = \frac{V_{dc} \times D \times (1-D)}{f_{sw} \times \delta i_{p-p}} \qquad (1.34)$$

$$L_{actual} = \frac{V_{dc} \times D \times (1-D)}{f_{sw} \times 2\sqrt{3} \times \delta i_{rms}} \qquad (1.35)$$

$$L_{pu} = \frac{L_{actual}}{L_{base}} = \frac{V_{dc} \times D \times (1-D)}{f_{sw} \times 2\sqrt{3} \times \delta i_{rms}} \times \frac{I_{base}}{V_{base}} \times 2\pi f_{base} \qquad (1.36)$$

$$L_{pu} = \frac{V_{dc(pu)} \times D \times (1-D) \times \pi}{f_{sw(pu)} \times \sqrt{3} \times \delta i_{rms(pu)}} \tag{1.37}$$

Here D is the duty cycle of the switch such that the average voltage at fundamental frequency is sinusoidal. The worst case current ripple occurs at 50% duty cycle, so the above equation can be simplified.

$$L_{pu} = \frac{\pi}{\sqrt{3}} \times \frac{V_{dc(pu)}}{4 \times f_{sw(pu)} \times \delta i_{pu}} \tag{1.38}$$

This is the maximum current ripple for any switching cycle which will happen at every zero crossing of fundamental voltage. But IEEE standards specify the current ripple limits for multiple cycles of fundamental current, *not* for one switching cycle.

If we assume that the inverter is source of sinusoidal voltages at different harmonic frequencies, we can find the current sourced by the switching frequency harmonic. At switching frequencies, the grid is a short circuit. Hence the switching frequency current will be

$$\delta i_{rms} = \frac{v_{i(sw)}}{2\pi \times f_{sw(pu) \times L}} \tag{1.39}$$

This is the current ripple relevant for THD calculations.

1.5   LC filter
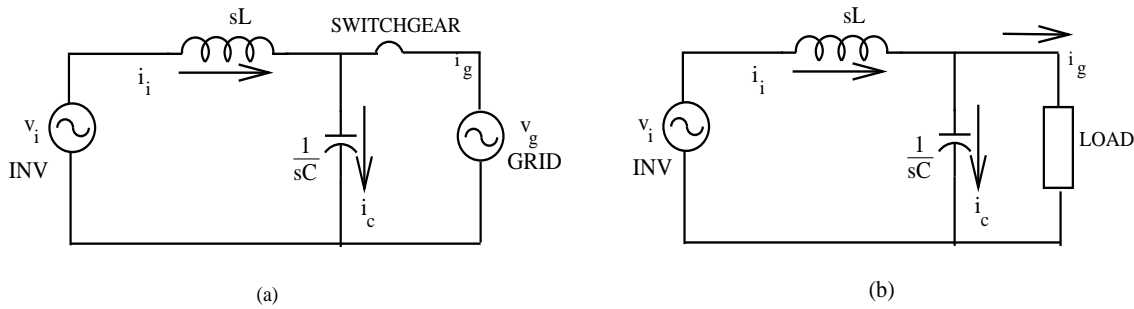
Figure 1.8: (a) LC filter inserted between active front end and grid; (b) LC filter inserted between active front end and stand-alone load

The design of LC filter is more complicated compared to L filter since the placement of the resonant frequency becomes an important factor which affects the closed loop response. The allowable current ripple is once again the criteria for designing L. The capacitor C is constrained by two factors.

- The resonant frequency of the filter elements

- The bandwidth of the closed loop system

1.5.1 Bandwidth consideration

The capacitance of the LC filter is decided by the resonant frequency. The design decision on selecting the resonant frequency depends on the bandwidth of the closed loop system. This dependency is established keeping in mind that active control methods (which are bandwidth dependent) can be used to implement loss-less resonant damping in higher order filters. Since the bandwidth of the closed loop system is decided by the filter elements and the control algorithm, it cannot be used straightaway in the design process. Here, we estimate the maximum possible system bandwidth and use it in our design procedure. The maximum possible bandwidth is certainly not achieved in practice, but this assumption is reasonable for a first pass iteration. Figure 1.9 shows the closed loop system.

The output voltage of a grid connected power converter cannot be controlled since it is decided by the grid conditions. The filter input current i_i is usually sensed and given back as feedback to close the control loop. But the grid current i_g is the control variable which is controlled by varying the inverter pole voltage. Hence, the transfer function which decides the closed loop performance of the filter is the transfer function between output current and input voltage of the filter for zero grid voltage.

Assuming the controller acts directly at the modulator without prior dynamics, there are two delays in the closed loop system which limit the bandwidth.

1. The Inverter response delay. When the voltage command to the inverter is changed, in the worst case, it takes $T_{sw}/2$ time for the voltage output of the inverter to change, where T_{sw} is the switching time period.

2. Current sampling and computational delay. If the current sampling is sampled once per pwm cycle this delay would be T_{sw}. Here we are assuming that the current is sampled twice every cycle, on the rising half and falling half of the PWM switching signal, so the delay in sensing is $T_{sw}/2$.

3. Phase delay due to the filter. This can be simplified to a constant phase delay of 90° based the assumptions listed in section 1.2.

So the total system excluding the filter is essentially modelled as a pure delay e^{-st_d}, where is $t_d = T_{sw}$. The resonant frequency is placed such that the closed loop system

including the LC filter gives a phase margin of atleast 45°. The LC filter transfer function which affects the closed loop system bandwidth is:

$$\left.\frac{i_g(s)}{v_i(s)}\right|_{v_g=0} = \frac{1}{sL} \tag{1.40}$$

Since the LC filter transfer function has a constant phase of -90° for all frequencies, the bandwidth of the system(excluding the filter) is limited at the frequency where its phase is 45°. So the frequency at which the phase margin of the total system (LC filter + delay) is 45° can be calculated.

$$\omega_{bw} = \frac{45° \frac{\pi}{180°}}{t_d} \tag{1.41}$$

Now the resonant frequency can be placed with reference to the bandwidth. If the resonant frequency is within the bandwidth of the closed loop system, active damping methods can be used to attenuate the filter resonance peaks. If the resonant frequency is outside the bandwidth of the system, passive damping methods (i.e resistors) must be used. Active damping means lower power loss at full load. Passive damping is essential in grid connected applications, in case the inverter is switched off while still being connected to the grid.

$$C_{pu} = \frac{1}{f_{res(pu)}^2 \times L_{pu}} \tag{1.42}$$

The transfer function of grid current i_g to inverter voltage v_i is same for L and LC filters when parasitic grid impedances are neglected (Fig 1.8). Therefore, the size of inductor does not change from L to LC filter. But Eq (1.40) will change if LC filter is connected to a stand-alone load. Consider an LC filter connected between an inverter and external load of R=1 pu resistance. Then the transimpedence transfer function will be

$$\frac{i_g}{v_i} = \frac{1}{s^2LCR + sL + R} \tag{1.43}$$

Additionally, a grid connected LC filter can behave as an LCL filter because of the parasitic impedances of the grid. But this arrangement is not reliable since the parasitic impedance of the grid is not under the control of the converter designer.
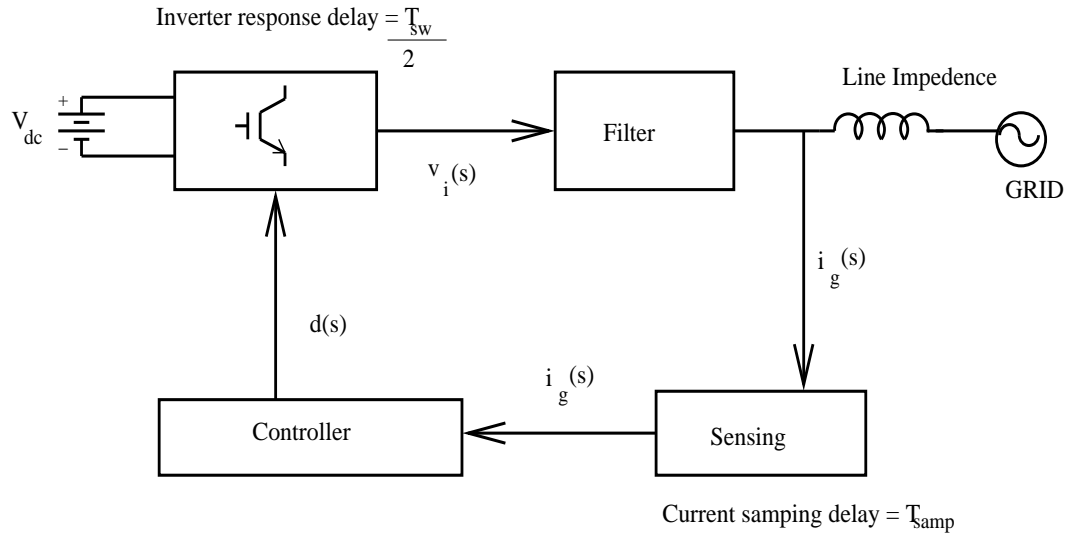
Figure 1.9: Closed loop system bandwidth assuming no delay in controller
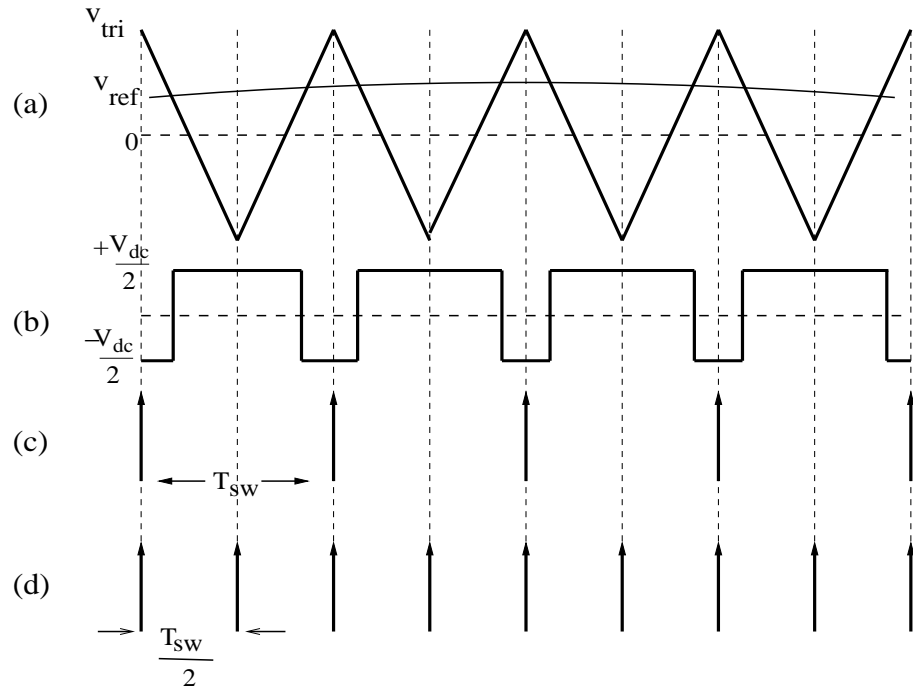
Figure 1.10: (a) PWM sine triangle modulation; (b) Output pole voltage with respect to ground; (c) Inverter output voltage update rate; (d) Current sampling rate

1.5.2 Design procedure for an LC filter

1. Selection of L_{pu} based on switching cycle ripple current consideration.

$$L_{pu} = \frac{V_{dc(pu)} \times D \times (1-D) \times \pi}{f_{sw(pu)} \times \sqrt{3} \times \delta i_{rms(pu)}} \qquad (1.44)$$

2. Selection of C_{pu} based on overall bandwidth and resonant frequency.

$$C_{actual} = \frac{1}{\omega_{res}^2 \times L_{actual}} \tag{1.45}$$

$$C_{pu} = \frac{C_{actual}}{C_{base}} = \frac{1}{\omega_{res}^2 \times L_{actual}} Z_{base} \times \omega_{base} \tag{1.46}$$

$$C_{pu} = \frac{1}{\omega_{res}^2 \times L_{pu} \times L_{base}} Z_{base} \times \omega_{base} \tag{1.47}$$

$$C_{pu} = \frac{1}{f_{res(pu)}^2 \times L_{pu}} \tag{1.48}$$

Further aspects of LC filter design is not considered as this report. Here the focus is on grid connected power converters, which requires the improved level of filtering offered by LCL filters.

1.6   LCL filter

An LCL filter is preferred to an L filter in high power and/or low switching frequency applications. This is because for the same (or lower) net inductance (i.e $L_1 + L_2$) we can get better attenuation (60dB/decade) at switching frequency.
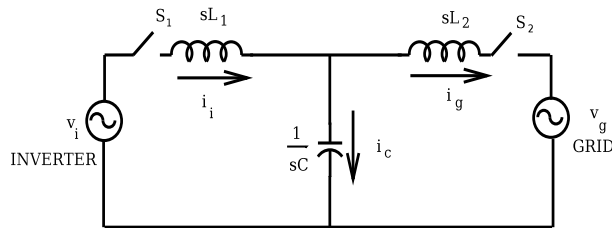
Figure 1.11: LCL filter inserted between active front end and grid

The design procedure for LCL filter cannot be treated as a progression from an LC filter, since there are more possible resonances (infact three) between the filter elements. The three possible resonant frequencies based on the open or close positions of the

switches S_1 and S_2 in Fig 1.11 are:

$$\omega_{L_1C} = \frac{1}{\sqrt{L_1C}} \tag{1.49}$$

$$\omega_{L_2C} = \frac{1}{\sqrt{L_2C}} \tag{1.50}$$

$$\omega_{L_pC} = \frac{1}{\sqrt{L_pC}} \tag{1.51}$$

The actual poles of the filter can be obtained from the characteristic equation of the system. The three poles of the system include a pair of complex conjugate poles due to ω_{L_pC} and a pole at the origin.

$$L_p = \frac{L_1 \times L_2}{L_1 + L_2} \tag{1.52}$$

The procedure for design of LCL filter as given in the current literature is as follows [3]–[7].

- L_1 is designed based on the current ripple.

- L_2 is assumed to be a fraction of L_1, maybe greater than or lesser than L_1. This is decided by the current ripple in inductor L_2.

- C is designed on the basis of the reactive power supplied by the capacitor at fundamental frequency.

This procedure has a few limitations.

- The upfront rule of thumb based selection of L and C makes it difficult to optimize the overall filter design procedure.

- It is not possible to design the LCL filter on a per unit basis, where the per unit is referenced from the VA of the power converter system.

- The resonant frequencies and their effect on system bandwidth is ignored in this method.

- Even though the aim of filter design is to attenuate the switching frequency harmonics, the basis of capacitor design is the reactive power of fundamental frequency.

- There is no simple way to compare L and LCL filters for the same application.

1.6.1   Design procedure

In the proposed method the inverter plus filter is treated as a "black box," so the only input variables for the filter design are the KVA rating of the inverter and the switching frequency output current ripple $i_g(j\omega_{sw})$. Let L be the *total* inductance of the filter,

$$L = L_1 + L_2 \tag{1.53}$$

Let L_1 and L_2 be related as

$$L_1 = a_L L_2 \tag{1.54}$$

Next, the total system bandwidth (including filter) is estimated such that there is acceptable phase margin in the system. The LCL filter transfer function which affects the closed loop system bandwidth in grid connected mode of operation is

$$\left.\frac{i_g(s)}{v_i(s)}\right|_{v_g=0} = \frac{1}{s^3 L_1 L_2 C + s(L_1 + L_2)} \tag{1.55}$$

The LCL filter transfer function has a constant phase of -90° below ω_{res} and +90° above ω_{res} as can be seen from Eq (1.55). So the bandwidth of the closed loop system will be same as that of the LC filter below ω_{res}. The resonant frequency of interest is $\omega_{L_p C}$, since this is the resonant frequency of Eq (1.55).

$$\omega_{res}^2 = \frac{1}{L_p C} \tag{1.56}$$

where

$$L_p = \frac{L_1 \times L_2}{L_1 + L_2} \tag{1.57}$$

Substituting for L_p in terms of $L = L_1 + L_2$

$$\frac{i_g(s)}{v_i(s)} = \frac{1}{sL(1 + s^2 L_p C)} \tag{1.58}$$

Converting all quantities to their per-unit equivalents, the resonant frequency is

$$\omega_{res(pu)}^2 = \frac{1}{C_{pu} \times L_{pu} \dfrac{a_L}{(a_L + 1)^2}} \tag{1.59}$$
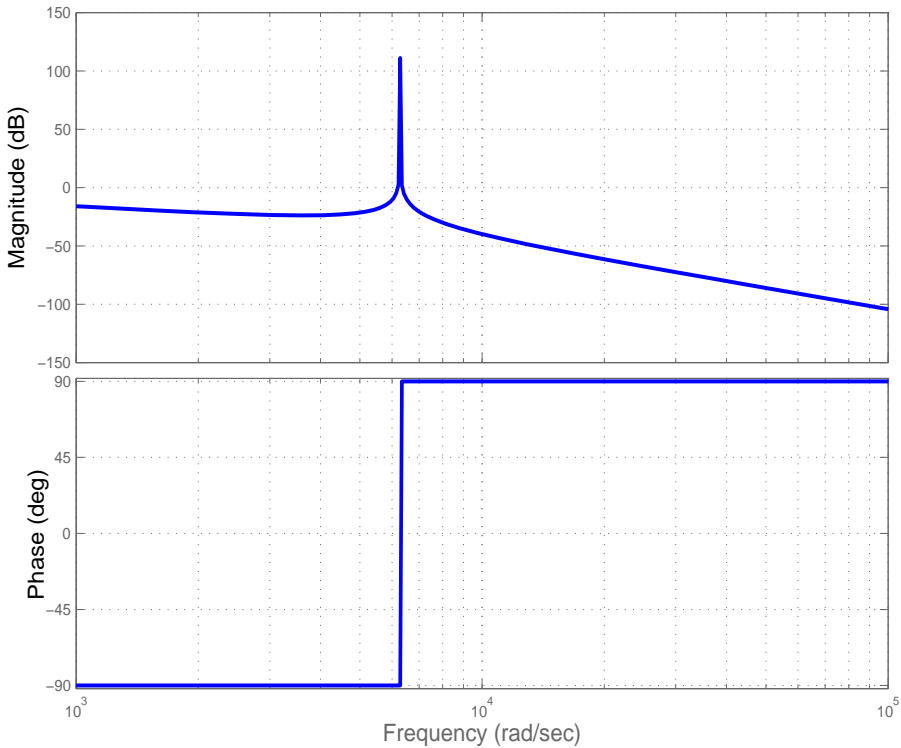
Figure 1.12: Frequency response of i_g/v_i for LCL filter

The capacitance in an LCL filter depends on the resonant frequency ω_{res} and the ratio in which we distribute the total inductance $L_1 + L_2$. Assuming we have fixed ω_{res}, the ratio of L_1 and L_2 for minimum capacitance is given by

$$\frac{\delta C_{pu}}{\delta a_L} = 0 \tag{1.60}$$

which simplifies to $a_L = 1$. So, given a fixed output harmonics attenuation, the smallest capacitance value of LCL filter is obtained when $L_1 = L_2$. Since we know the dependence of output current of filter i_g on the inverter terminal voltage v_i, we can again find the value of a_L which will give the minimum current ripple at the point of common coupling at any frequency.

$$i_g = \frac{v_i}{s^3 L_1 L_2 C + s(L_1 + L_2)} \tag{1.61}$$

$$i_g = \frac{v_i}{s^3 \dfrac{a_L}{(1+a_L)^2} L^2 C + sL} \tag{1.62}$$

$$\frac{\delta i_g}{\delta a_L} = 0 \tag{1.63}$$

$$\frac{\delta i_g}{\delta a_L} = \frac{\delta}{\delta a_L}\left(\frac{v_i(1+a_L)^2}{s^3 a_L L^2 C + sL(1+a_L)^2}\right) = 0 \tag{1.64}$$

$$[s^3 a_L L^2 C + sL(1+a_L)^2][2v_i(1+a_L)] = v_i(1+a_L)^2[s^3 L^2 C + sL2(1+a_L)] \tag{1.65}$$

$$2a_L = 1 + a_L \tag{1.66}$$

$$a_L = 1 \tag{1.67}$$

Eq (1.56) becomes

$$\omega_{res}^2 = \frac{4}{L_{pu}C_{pu}} \tag{1.68}$$

To find L_{pu} and C_{pu}, Eq (1.55) is evaluated (in per unit) at switching frequency f_{sw}.

$$\left|\frac{i_g(j\omega_{sw})}{v_i(j\omega_{sw})}\right| = \frac{1}{|-j\omega_{sw}^3 L_1 L_2 C + j\omega_{sw}(L_1+L_2)|} \tag{1.69}$$

$i_g(j\omega_{sw})$ is the switching ripple current at the point of common coupling to the grid at switching frequency. This is guided by the recommendations of IEEE 519-1992 or IEEE 1547.2-2008 standard[1]–[2]. For example, the IEEE 519 recommended maximum current distortion for a $I_{SC}/I_L < 20$ for current harmonics $\geq 35^{th}$ is 0.3%. I_{SC} refers to short circuit current and I_L is the nominal load current. This requirement of 0.3% refers to a "weak" grid. The percentage of ripple current can be higher for a "stiff" grid. Since most inverters can switch at higher frequencies exceeding 2 kHz using current IGBT technology, the standard refers to harmonics $\geq 35^{th}$. $v_i(j\omega_{sw})$ is the inverter pole voltage ripple at switching frequency, which is $V_{dc}/2$.

Eq (1.69) is solved by converting all parameters to per-unit and substituting Eq (1.68) in Eq (1.69).

$$L_{pu} = \frac{1}{\omega_{sw(pu)}\left|\dfrac{i_{g(pu)}}{v_{i(pu)}}\right|\left|1-\dfrac{\omega_{sw(pu)}^2}{\omega_{res(pu)}^2}\right|} \tag{1.70}$$

Then C_{pu} will be calculated from Eq (1.68). This is different from most current literature which focus on reactive current capability to decide value of C. The disadvantage of the previous approach was that real and/or reactive power supplied to load/grid must be known beforehand and must always have a fixed minimum. The proposed design allows for deciding the value of C without setting the reactive power requirement. The reactive power drawn by the filter can be subsequently verified to meet the system requirement.

If the reactive current drawn is seen to be excessive, then the *L* and *C* can be traded off by keeping a fixed resonant frequency or looking at the possibility of a higher power converter switching frequency.

The biggest advantage of this method is that it simultaneously satisfies four constraints of filter design for typical PWM inverter designs with f_{sw} in the 10kHz range. The voltage drop across the inductor at fundamental frequency will be less than 0.1 pu. And the reactive current sourced by the capacitor at fundamental frequency will also be less than 0.1 pu. The switching frequency attenuation requirement and bandwidth requirements are already met as discussed above.

V_{base}	KVA_{base}	I_{base}	Z_{base}
V	KVA	A	Ω
254	10	13.1	19.35

Table 1.2: Base values used for calculations

	L	LC	LCL
$L_{pu} = L_{1(pu)} + L_{2(pu)}$	2.352	2.352	0.105
C_{pu}	-	1.063e-3	0.095
$\delta i_{g(pu)}$	0.003	0.003	0.003
$f_{res(pu)}$	-	20	20
$f_{sw(pu)}$	200	200	200

Table 1.3: Comparison of pu values of filter for same grid current ripple

1.7   Resonance damping

As described earlier, the resonant frequency of the LCL filter which affects the closed loop response of the system for grid connected operation is ω_{L_pC}. The resonance effect can cause instability in the output, especially if some harmonic voltage/current is near the resonant frequency. The simplest type of damping is to put a resistance in series with the inductors. But this also increases the losses in the filter at fundamental frequency. Thus the important issue in implementing damping is to balance the trade-off between effective damping- which is measured by the Q-factor of the circuit and power dissipation due to damping elements. In this section we focus only on one passive damping method. The damping circuit is shown in Fig 1.13.
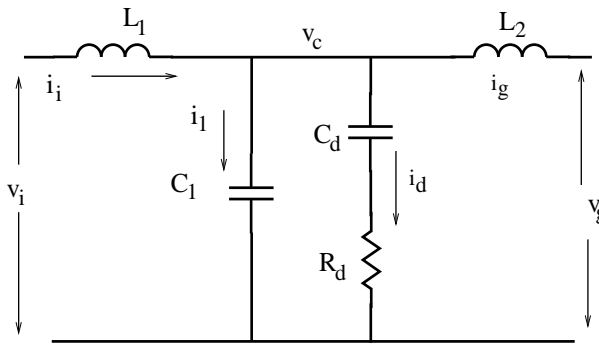
Figure 1.13: Passive damping scheme

1.7.1 Quality factor and power dissipation

The aim of damping is to reduce the Q-factor at the resonant frequency *without* affecting the frequency response at other frequencies. Simultaneously, the total power dissipation in the damping circuit is also an important parameter. Since the frequency response must not change, the resonant frequency is kept same and the *total* filter component values are unchanged ie. $L = L_1 + L_2$ and $C = C_1 + C_d$ is unchanged from an LCL filter without any damping. Let

$$L_1 = a_L L_2 \tag{1.71}$$

$$C_d = a_C C_1 \tag{1.72}$$

$$R_d = a_R \sqrt{\frac{L}{C}} \tag{1.73}$$

The transfer function which affects closed loop response is

$$\left.\frac{i_g(s)}{v_i(s)}\right|_{v_g=0} = \frac{1 + sC_dR_d}{s^4 L_1 L_2 C_1 C_d R_d + s^3 L_1 L_2 (C_1 + C_d) + s^2 C_d R_d (L_1 + L_2) + s(L_1 + L_2)} \tag{1.74}$$

Substituting

$$L_1 + L_2 = L \tag{1.75}$$

$$\frac{L_1 L_2}{L_1 + L_2} = L_p \tag{1.76}$$

$$C_1 + C_d = C \tag{1.77}$$

$$\frac{C_1 C_d}{C_1 + C_d} = C_s \tag{1.78}$$

we can simplify Eq. (1.74) as

$$\left.\frac{i_g(s)}{v_i(s)}\right|_{v_g=0} = \frac{1}{sL\left[1 + s^2 L_p C\left(\dfrac{1+sC_sR_d}{1+sC_dR_d}\right)\right]} \tag{1.79}$$

The additional passive elements increases the order of the transfer function and it is difficult to analytically estimate the resonant frequency of the fourth order system of Eq (1.74). Infact the resonant frequency now becomes a function of R_d which is difficult to derive analytically. But since the variation of resonant frequency with damping elements is not significant, the resonant frequency is assumed independent of variations in damping circuit.
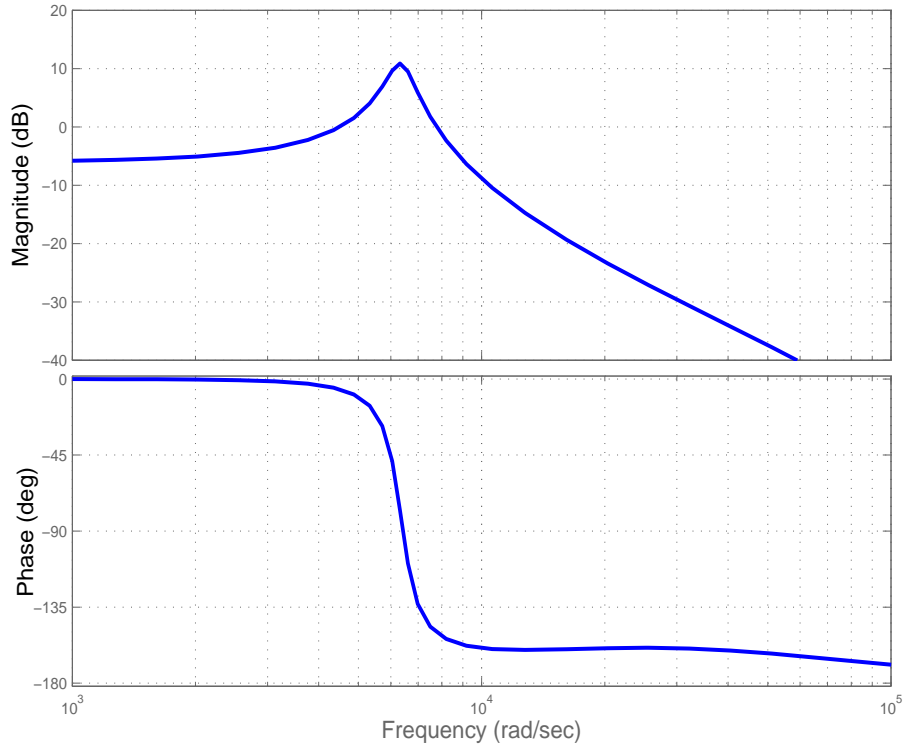

Figure 1.14: Frequency response of v_c/v_i. Here $a_R = 0.3$, $a_C = a_L = 1$

The other transfer function of significance is

$$\left.\frac{v_c(s)}{v_i(s)}\right|_{v_g=0} = \frac{sL_2 + s^2 L_2 C_d R_d}{s^4 L_1 L_2 C_1 C_d R_d + s^3 L_1 L_2 (C_1 + C_d) + s^2 C_d R_d (L_1 + L_2) + s(L_1 + L_2)} \tag{1.80}$$

The Q-factor of Eq (1.80) can be reliably determined since the frequency response of this transfer function has a constant magnitude at low frequencies. Hence this equation is used to analyze the effect of variation of damping parameters a_C and a_R on Q-factor of

the LCL filter circuit. Substituting $s = j\omega$ in Eq (1.80).

$$\frac{v_c(j\omega)}{v_i(j\omega)} = \frac{j\omega L_2 - \omega^2 L_2 C_d R_d}{\omega^4 L_1 L_2 C_1 C_d R_d - j\omega^3 L_1 L_2 (C_1 + C_d) - \omega^2 C_d R_d (L_1 + L_2) + j\omega (L_1 + L_2)} \tag{1.81}$$

Dividing numerator and denominator by $\omega(L_1 + L_2)$ and using the condition that $L_1 = L_2$

$$\frac{v_c(j\omega)}{v_i(j\omega)} = \frac{j0.5 - \omega\, 0.5 C_d R_d}{\omega^3 L_p C_1 C_d R_d - j\omega^2 L_p C - \omega C_d R_d + j1} \tag{1.82}$$

where

$$L_p = \frac{L_1 L_2}{L_1 + L_2} \tag{1.83}$$

and

$$C = C_1 + C_d \tag{1.84}$$

This can be further simplified by substituting $\omega_r = \omega_{L_p C} = 1/\sqrt{L_p C}$

$$\frac{v_c(j\omega)}{v_i(j\omega)} = \frac{-0.5\omega C_d R_d + j0.5}{\omega C_d R_d (\omega^2 L_p C_1 - 1) + j(1 - \frac{\omega^2}{\omega_r^2})} \tag{1.85}$$

By substituting

$$L_p C_1 = L_p (C_1 + C_d) \frac{C_1}{C_1 + C_d} \tag{1.86}$$

we get

$$\frac{v_c(j\omega)}{v_i(j\omega)} = \frac{0.5 + j0.5\omega C_d R_d}{\left(1 - \frac{\omega^2}{\omega_r^2}\right) + j\omega C_d R_d \left(1 - \frac{\omega^2}{\omega_r^2} \frac{C_1}{C_1 + C_d}\right)} \tag{1.87}$$

or in terms of a_C

$$\frac{v_c(j\omega)}{v_i(j\omega)} = \frac{0.5 + j0.5\omega C_d R_d}{\left(1 - \frac{\omega^2}{\omega_r^2}\right) + j\omega C_d R_d \left(1 - \frac{\omega^2}{\omega_r^2} \frac{1}{1 + a_C}\right)} \tag{1.88}$$

The frequency response of Eq (1.80) is given in Fig 1.14. To find the Q-factor of this

circuit, derive

$$\lim_{\omega \to 0} \left| \frac{v_c}{v_i} \right| = 0.5 \tag{1.89}$$

$$\left| \frac{v_c}{v_i} \right|_{\omega = \omega_r} = \left| \frac{0.5 + j0.5\omega_r C_d R_d}{j\omega_r C_d R_d \dfrac{a_C}{1 + a_C}} \right| \tag{1.90}$$

Dividing Eq (1.90) by Eq (1.89) and substituting for C_d in terms of C

$$Q(a_C) = \left| \frac{1 + j\omega_r C R_d \dfrac{a_C}{1 + a_C}}{j\omega_r C R_d \dfrac{a_C^2}{(1 + a_C)^2}} \right| \tag{1.91}$$

$Q(a_C)$ is plotted in Fig. 1.15. From the figure we can see that there is no improvement in the Q of the frequency response if a_C is increased beyond 2. Therefore, we are setting $a_C = 1$ as the best choice, since it is practically easy to configure two capacitors of same value.
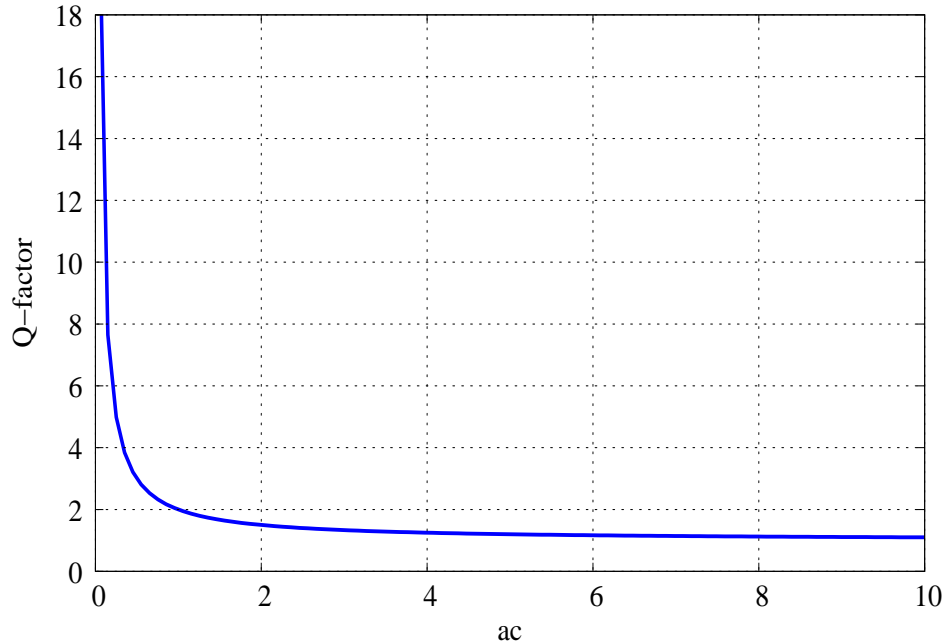

Figure 1.15: Q-factor vs a_C

The Q-factor is also affected by the choice of R_d.

$$R_d = \sqrt{\frac{L}{C}} \times a_R \tag{1.92}$$

A very small value of a_R makes R_d effectively a short circuit and does not provide any damping. Similarly, a very large value of a_R makes R_d effectively an open circuit which does not proved any damping. It is seen that selection of $a_R = 1$ is equivalent to making R_d equal to the characteristic impedance of the LCL circuit. This gives the lowest Q for the damping circuit. Since this fact is difficult to prove analytically, we can prove that by plotting the frequency response of the LCL filter with damping for different kVA ratings as shown in Fig 1.16. The system rating values for different kVA are given in Table 1.4.
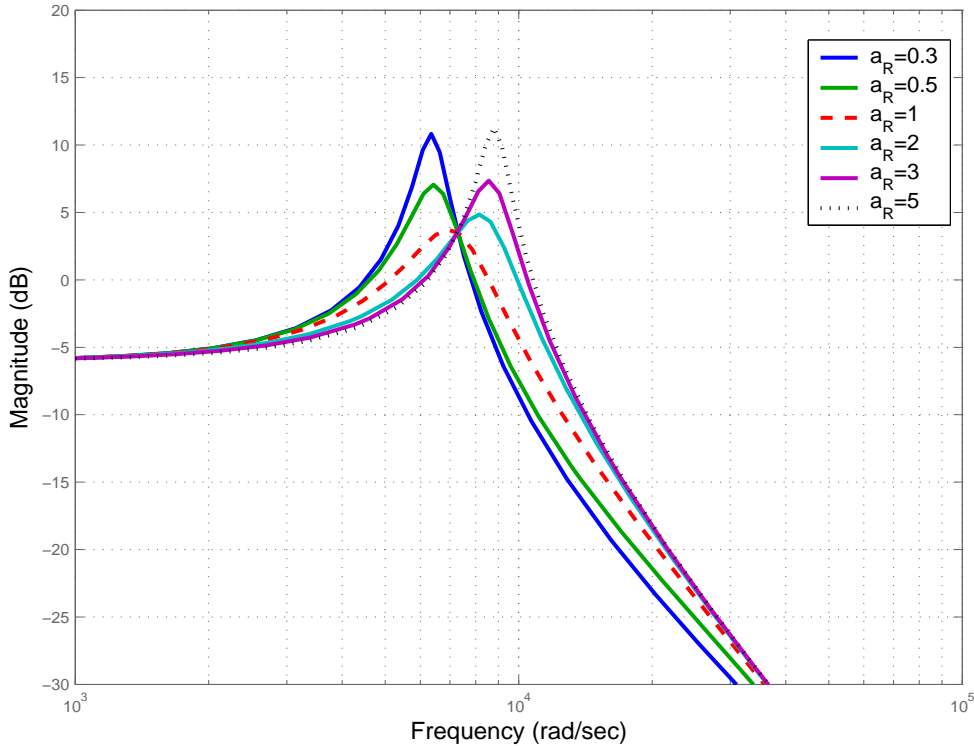

Figure 1.16: Frequency response v_c/v_i for different a_R. System rating is 1kVA.

The net power dissipation in the damping circuit is another important factor which will affect the damping parameters. The power dissipated in the damping circuit can be calculated for the fundamental and switching frequency. From the Fig 1.17, the power loss in the damping circuit for the fundamental frequency is given by

$$P_{d(50)} = \text{Real}[V_c I_d^*] \qquad (1.93)$$

where

$$V_c = V_g = 1\text{pu} \qquad (1.94)$$

$$I_d = V_c \frac{sC_d}{1 + sC_d R_d} \qquad (1.95)$$

	Unit	1kVA	10kVA	100kVA
V_b	V	254	254	254
I_b	A	1.312	13.12	131.2
Z_b	Ω	193.6	19.36	1.936
L	mH	64	6.458	0.6458
C	μF	1.569	15.69	156.9
$L_1 = L_2$	mH	32	3.229	0.3229
$C_1 = C_d$	μF	0.7846	7.846	78.46
$\sqrt{\frac{L}{C}}$	Ω	202.8	20.28	2.02

Table 1.4: Filter circuit and damping circuit designed values for different KVA grid connected inverter rating.
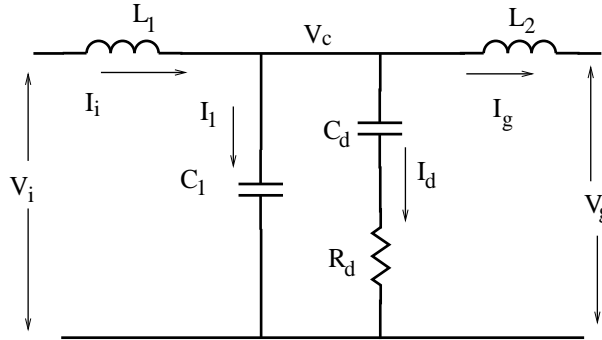
Figure 1.17: LCL circuit with C_1, C_d, R_d damping at fundamental frequency

$$I_d = V_c \frac{j\omega_{50}C_d(1 - j\omega_{50}C_dR_d)}{1 + \omega_{50}^2 C_d^2 R_d^2} \tag{1.96}$$

$$P_{d(50)} = \frac{V_c^2 \omega_{50}^2 C_d^2 R_d}{1 + \omega_{50}^2 C_d^2 R_d^2} \tag{1.97}$$

Similarly, damping circuit for switching frequency is given in Fig 1.18. From Eq. (1.88), we get

$$V_c = V_i \frac{0.5 + j0.5\omega_{sw}C_dR_d}{\left(1 - \frac{\omega_{sw}^2}{\omega_r^2}\right) + j\omega_{sw}C_dR_d \left(1 - \frac{\omega_{sw}^2}{\omega_r^2}\frac{1}{1 + a_C}\right)} \tag{1.98}$$

$$I_d = V_c \frac{\omega_{sw}C_d(\omega_{sw}C_dR_d + 1j)}{1 + \omega_{sw}^2 C_d^2 R_d^2} \tag{1.99}$$

$$P_{d(sw)} = \text{Real}[V_c I_d^*] \tag{1.100}$$
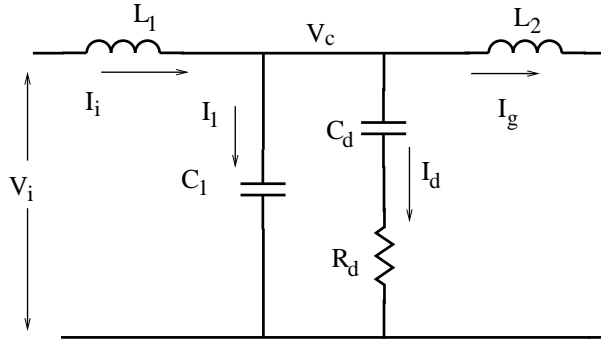
Figure 1.18: LCL circuit with C_1, C_d, R_d damping at switching frequency

Representing V_c and I_d as complex fractions,

$$V_c = V_i \frac{a + jb}{c + jd} \tag{1.101}$$

$$I_d = V_c \frac{\omega_{sw} C_d}{1 + \omega_{sw}^2 C_d^2 R_d^2} (x + jy) \tag{1.102}$$

$$V_c I_d^* = V_i \frac{a + jb}{c + jd} V_i \left(\frac{a + jb}{c + jd}\right)^* \frac{\omega_{sw} C_d}{1 + \omega_{sw}^2 C_d^2 R_d^2} (x + jy)^* \tag{1.103}$$

$$P_{d(sw)} = \text{Real}[V_c I_d^*] = V_i^2 \frac{a^2 + b^2}{c^2 + d^2} \frac{\omega_{sw} C_d}{1 + \omega_{sw}^2 C_d^2 R_d^2} x \tag{1.104}$$

From Fig 1.19, total power loss in damping branch is almost linearly proportional to a_C. For highest efficiency, a_C should be as low as possible. Hence $a_C = 1$ is a good compromise between Q-factor, shown in Fig 1.15, and Power dissipation in the damping circuit, as shown in Fig 1.16. For this selection of a_C, the power loss in the filter for damping is less than 0.2% and the damping factor is close to 2. This is a reasonable design for inverters with power levels that are in the order of 10kW.

1.7.2   Design procedure

The LCL filter design procedure is already discussed in the previous section. The extra elements of damping circuit can be derived from the above discussion.

$$a_C = 1 \tag{1.105}$$

$$C_1 = C_d = \frac{C}{2} \tag{1.106}$$
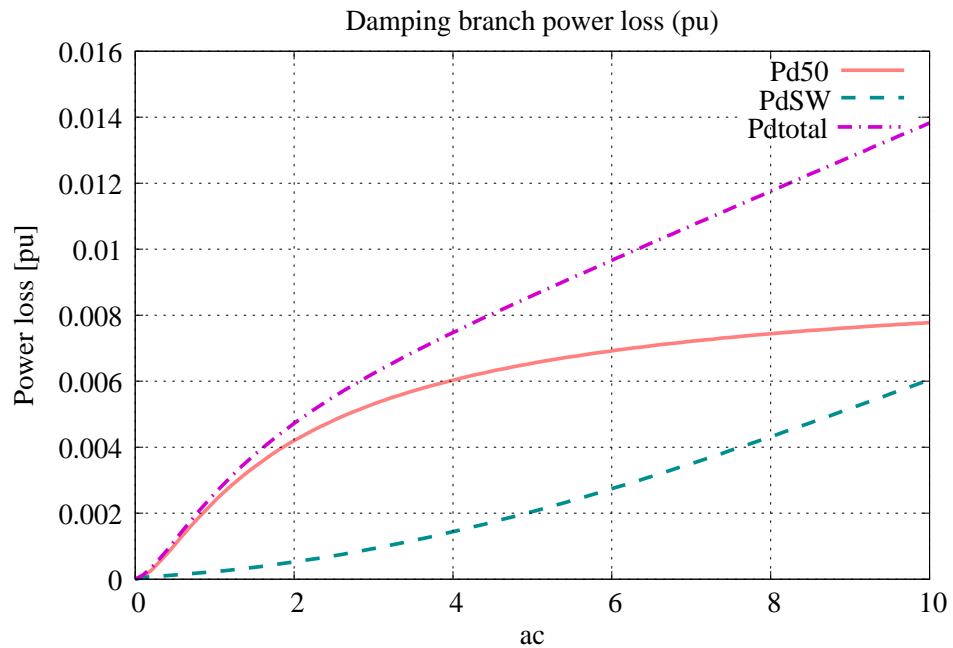
Figure 1.19: Power dissipation in per unit for damping circuit at fundamental and switching frequency. Here $a_R = 1$.

Similarly,

$$a_R = 1 \tag{1.107}$$

which means

$$R_d = \sqrt{\frac{L}{C}} \tag{1.108}$$

The comparison with and without damping is shown in Fig 1.20 and Fig 1.21.
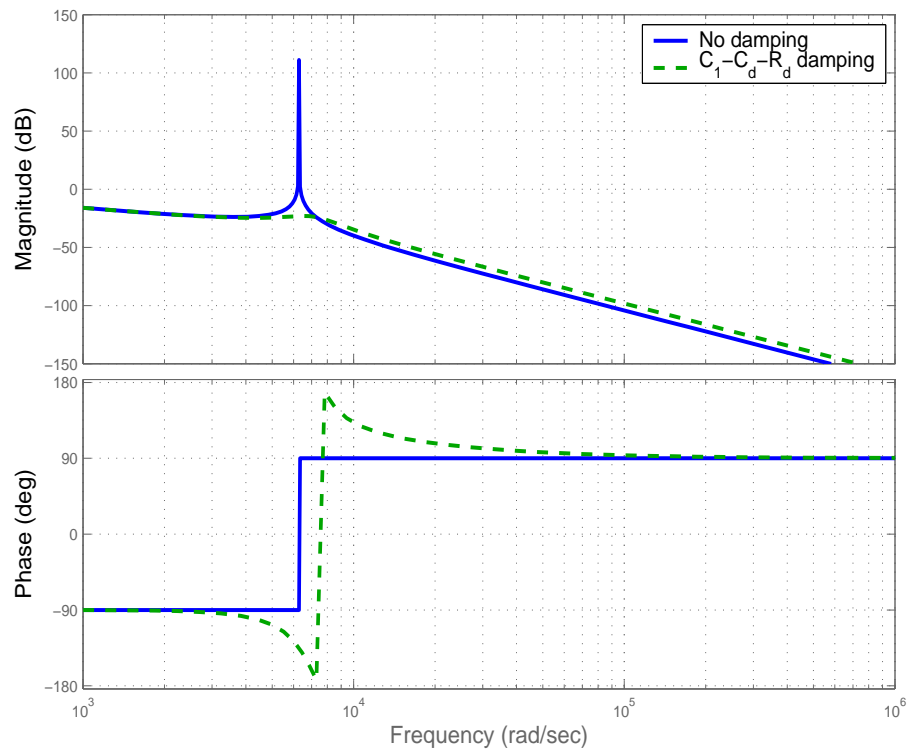
Figure 1.20: Frequency response of i_g/v_i. Here $a_R=1$, $a_C=a_L=1$, system rating 10kVA
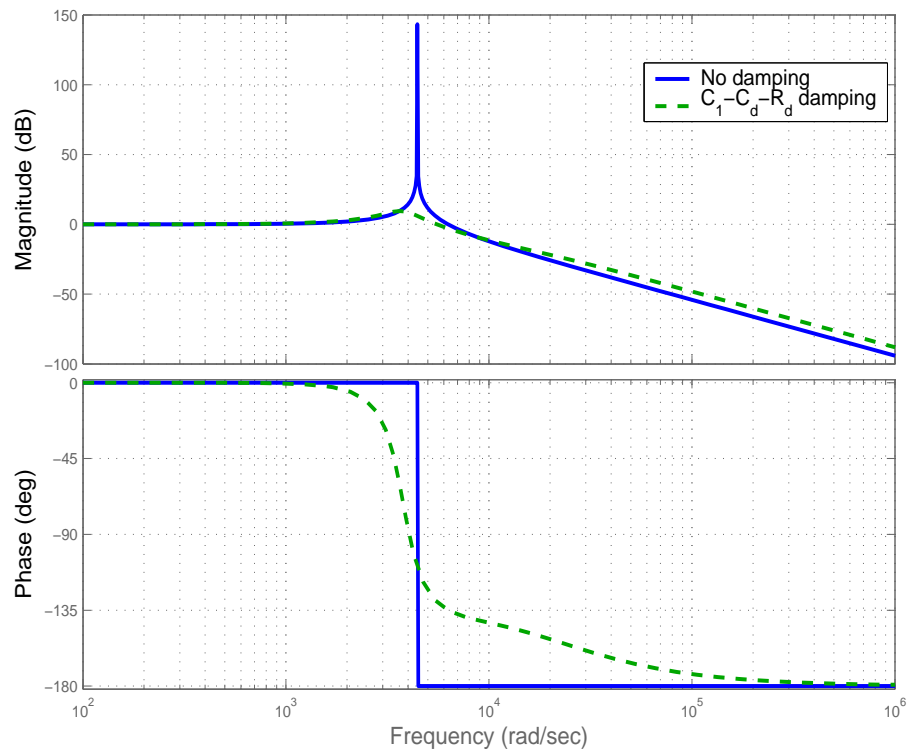
Figure 1.21: Frequency response of v_g/v_i. Here $a_R=1$, $a_C=a_L=1$, system rating 10kVA

1.8   Summary

The system level design principles for grid connected low pass filters have been thoroughly examined. The per unit method gives the flexibility to adapt the design equations for any power level. The relative merits between L, LC and LCL filter combinations are discussed. The parameters of the LCL filter are derived from bandwidth constraints and IEEE standard recommendations and are seen to be suitable for practical inverter designs. The problem of resonance damping is considered and a low loss passive damping structure is introduced.

1.9   References

IEEE Standards

1. "IEEE Application Guide for IEEE Std 1547, IEEE Standard for Interconnecting Distributed Resources with Electric Power Systems," IEEE 1547.2-2008

2. "IEEE Recommended Practices and Requirements for Harmonic Control in Electrical Power Systems," IEEE 519-1992

Transfer function analysis

3. M.Liserre, F.Blaabjerg and A. Dell'Aquila, "Step-by-step design procedure for a grid-connected three-phase PWM voltage source converter," *Int. J. Electronics*,vol. 91, no. 8, pp. 445-460, Aug 2004.

4. Y.Lang, D.Xu, et al., "A novel design method of LCL type utility interface for three-phase voltage source rectifier," *IEEE 36th Conference on Power Electronics Specialists, 2005.*

5. B.Bolsens, K. De Brabendere et al., "Model-based generation of low distortion currents in grid-coupled pwm-inverters using an LCL output filter," *Power Electronics Specialists Conference, 2004. PESC 04. 2004 IEEE 35th Annual*

6. M.Liserre, F.Blaabjerg, S.Hansen, "Design and control of an LCL-filter-based three-phase active rectifier," *Conference Record of the 2001 IEEE Industry Applications Conference, 36th IAS Annual Meeting, 2001,* v.1, pp. 299-307.

7. Dahono, P. A., Purwadi, A. e Qamaruzzaman, "An LC Filter Design Method for Single-Phase PWM Inverters," *Proceedings of 1995 International Conference on Power Electronics and Drive Systems. PEDS 95,* v. 2, pp. 571-576.

8. Parikshith B. C., V. John, "Higher Order Output Filter Design for Grid Connected Power Converters," *National Power Systems Conference 2008, IIT Bombay, Mumbai,* 16th - 18th December, 2008.

Resonance damping

9. T.Wang, Z.Ye et al., "Output filter design for a grid-interconnected three-phase inverter," *Power Electronics Specialist Conference, 2003. PESC '03. 2003 IEEE 34th Annual*, pp. 779-784

Table 1.5: Significance of transfer functions

$\dfrac{v_c(s)}{v_i(s)}$	Voltage harmonic attenuation in stand-alone mode increasing L_1/L_2 is beneficial $v_g(s) = v_c(s)$ under open circuit conditions
$\left.\dfrac{i_g(s)}{v_i(s)}\right\|_{v_g\ short}$	Inverter THD in grid connected mode
$\left.\dfrac{i_i(s)}{v_i(s)}\right\|_{v_g\ short}$	Inductor harmonic spectrum for inductor design
$\dfrac{i_g(s)}{i_i(s)}$	Current filtering in grid connected mode decreasing L_1/L_2 is beneficial
$\left.\dfrac{i_g(s)}{v_g(s)}\right\|_{v_i\ open}$	Grid admittance seen from filter when converter not switching ideally 0 meaning reject all disturbances from grid
$\left.\dfrac{i_g(s)}{v_g(s)}\right\|_{v_i\ short}$	Admittance seen from grid ignoring controller interaction

Chapter 2

Filter Component Construction

2.1 Introduction

This chapter is focused on the design and construction of the individual components of the LCL filter. The design techniques to accurately build an inductor of required inductance are discussed in detail. The familiar area product approach for inductor design is modified and incorporated into new methods which are more accurate and material specific. The principles of construction for three different magnetic materials -Ferrite, Amorphous and Powder is discussed. Finally, capacitors and resistors suited for for high power filter applications are introduced.

2.2 Area product approach

The product of core cross-section area and window area in an inductor (area product) is a measure of the energy handling capability of the inductor. The area product equation is a good starting point for design since it relates the electrical design inputs with material and geometric constraints.

The minimum cross section area of the inductor winding (a_w m^2) is limited by the rms current flowing in the winding I_{rms} A, which depends on the temperature rating of the insulation and the conductivity of the wire. The temperature limit is expressed in terms of the current carrying capacity of the conductor J_m A/m^2.

$$a_w = \frac{I_{rms}}{J_m} \tag{2.1}$$

Similarly the minimum cross section area of the inductor core (A_e m^2) is limited by the peak flux density of the core material expressed as B_m T. If N turns each carrying a peak current of I_p A create a peak flux of ϕ_m Wb, then

$$LI_p = N\phi_m \tag{2.2}$$

where

$$\phi_m = B_m A_e \tag{2.3}$$

Therefore we get

$$LI_p = NB_m A_e \tag{2.4}$$

A third constraint which affects the design is the amount of space available in the window area (A_W m^2) for the winding. In order to accommodate the winding in the available window space,

$$Na_w < A_W \tag{2.5}$$

Converting this inequality to a equation

$$A_W = \frac{Na_w}{k_u} \tag{2.6}$$

where k_w is the window utilization factor. k_w varies between 0 and 1 depending on several factors like type of conductors, number of bobbins, insulation class, winding skill etc. From Eq (2.6) and (2.4),

$$LI_p I_{rms} = k_u J B_m A_e A_W \tag{2.7}$$

The area product is defined as

$$A_p = A_e A_W = \frac{LI_p I_{rms}}{k_u B_m J_m}, \tag{2.8}$$

or

$$A_p = \frac{\text{Energy Stored}}{\text{Material Constraints}}. \tag{2.9}$$

For inductors carrying AC, the stored energy is expressed as [3]

$$\text{Energy Stored} = \frac{V_{rms} I_{rms}}{f k_f} \tag{2.10}$$

where f is the frequency of the current waveform and k_f is the form factor (k_f=4.44 for sinusoidal waves).

2.2.1 Design steps

The traditional design steps for inductor design is given below [2]. Transfer function analysis along with ripple current limits and actual power rating of the converter is used to arrive at L, I_p and I_{rms} (as already explained in Chapter 1). The flux density limit of the magnetic material B_m can be taken from vendor datasheet. The current density limit J_m is based on reasonable assumptions of current density to prevent overheating. Window utilization factor k_u depends on type of winding, number of bobbins used, type of insulation and the winding skill of the manufacturer. At the end of the design process, the temperature rise calculation is used to evaluate the effectiveness of the above assumptions. If the final operating temperature is significantly different from initial approximation, these assumptions need to be modified.

1. Compute

$$A_e A_W = \frac{L \, I_p \, I_{rms}}{k_u \, B_m \, J_m} \tag{2.11}$$

2. Select a core from core tables with area product equal to or greater than $A_e A_W$.

3. For the selected core, find A_e and A_W.

4. Compute

$$N = \frac{L \, I_p}{B_m \, A_e} \tag{2.12}$$

   Select nearest whole number of N^*.

5. Compute

$$a_w = \frac{I_{rms}}{J} \tag{2.13}$$

   Select nearest (greater) number of wire gauge and a_w^* from wire table.

6. Compute the required air gap in the core

$$l_g = \frac{\mu_o \, N^* \, I_p}{B_m} \qquad (2.14)$$

7. Check the assumptions:

   - Core reluctance $<<$ Air gap reluctance; This condition ensures that the final inductance does not vary with the tolerance of magnetic properties of the manufactured core.

$$\Re_c \ll \Re_g \; ; \frac{l}{\mu_r} \ll l_g \qquad (2.15)$$

   - No fringing:

$$l_g \ll \sqrt{A_e} \qquad (2.16)$$

8. Recalculate

$$J_m^* = \frac{I_{rms}}{a_w^*} \qquad (2.17)$$

9. Recalculate

$$k_w^* = \frac{N^* \, a_w^*}{A_w} \qquad (2.18)$$

10. Compute from the geometry of the core, mean length per turn and the length of the winding. From wire tables, find the resistance of winding at the operating temperature.

2.2.2   Limitations

1. The design procedure is simple and completes in a single iteration. But for a given core type, there is only one value of air gap and number of turns. Actually there are several combinations of these parameters which will give the same inductance but very distinct efficiency and performance characteristics.

2. This method does not take into account the fringing of the magnetic field at the air gap. The fringing effect reduces the reluctance at the air gap, which means a higher

flux density in the core. Eq. (2.16) is an *approximation* and does not ensure that the absence of fringing even if the condition is met.

3. The lack of a good reluctance model means that the core can saturate even if the area product condition is met.

It is clear that even though the area product approach is conceptually correct, certain modifications are necessary to ensure accurate modeling of the inductance. Additionally a reasonably accurate fringing model is required to prevent saturation of the core.

2.3 Graphical iterative approach

In the design process of an inductor, there are two parameters that must be accurately preserved-L and B_m and two parameters that can be adjusted-N and l_g. So L and B_m are basically functions of 2 variables.

$$L = f(N, l_g) \tag{2.19}$$

$$B_m = g(N, l_g) \tag{2.20}$$

We can define the functions $f(N, l_g)$ and $g(N, l_g)$ as

$$L = \frac{N^2}{\mathfrak{R}_t} \tag{2.21}$$

$$B_m = \frac{N I_p}{A_e \mathfrak{R}_t} \tag{2.22}$$

where $\mathfrak{R}_t$ is the total reluctance of the flux path. Both L and B_m are restricted within certain limits and the possible set of (N, l_g) which give this inductance and flux density is plotted on a graph of l_g vs N. These points are then fit using a second or third order polynomial to generate two curves, one for L and second for B_m. The intersection of both curves will give the possible (l_g, N) for which the core will not saturate as well as the required inductance is achieved. Additionally there will be also be several solutions in the neighbourhood which satisfy the inductance and peak flux density requirements.

2.3.1   Advantages

1. The number of possible solutions is larger which means there is greater flexibility in the actual construction of the inductor.

2. Since the effect of fringing at the air gap is included in terms of $\mathfrak{R}_t$, the built inductor will have the inductance very close to the initial calculation.

2.3.2   Disadvantages

1. The material properties, especially the permeability must be linear in the operating range.

2. The permeability should be independent of magnetic excitation.
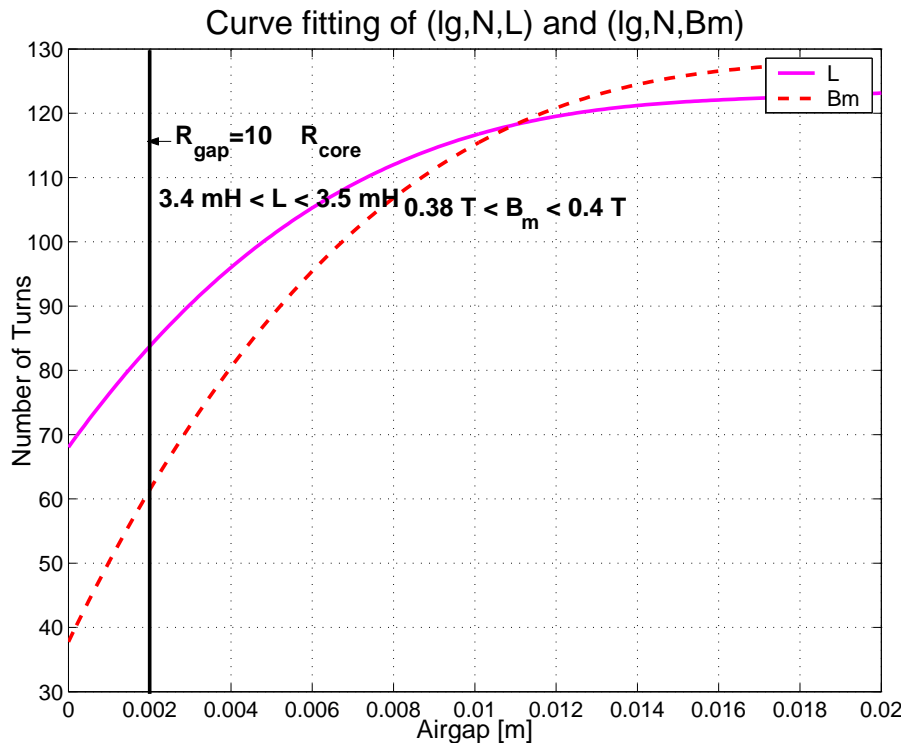
Figure 2.1: Intersection of B_m and L curves

2.4   Fringing flux

When an air gap is introduced in the magnetic flux path, the flux spreads over an area greater than the cross section of the magnetic path. The fringing of the magnetic flux at

the air gap has two effects

- It increases the cross section area of the air gap

- It increases the length of the magnetic path at the air gap

This fringing at the air gap will reduce the theoretical reluctance at the air gap, and introduce significant errors in the estimated value of the inductance. Hence there is a need for a simple yet accurate air gap reluctance model to account for the fringing effect. The fringing flux effect depends on the shape and geometry of the core at the gap, as well as shape and location of winding and other objects such as clamps, brackets etc.

Fringing effect becomes more noticeable as the air gap increases and simultaneously air gap reluctance becomes more difficult to estimate. The challenge is estimating this new reluctance analytically to get a closed-form solution using the dimensions of the core as the input.

2.4.1 Simple fringing model
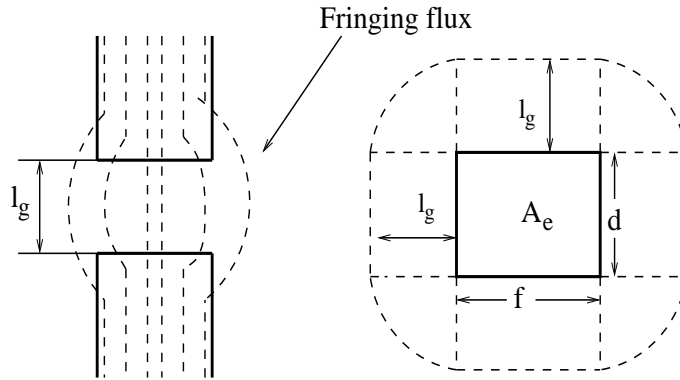
Figure 2.2: Fringing effect approximation from [2]

This model is a modification of the fringing estimate given by [2]. This model was chosen because of its simplicity and acceptable accuracy. The fringing at the air gap is modeled as increase in area of the air gap cross section, and this increase is in terms of l_g. The air gap reluctance $\mathfrak{R}_g$ for an air gap of l_g and core cross section area of $A_e = f \times d$ is given by

$$\mathfrak{R}_g = \frac{l_g}{\mu_0[A_e + (f+d)l_g + l_g^2]} \tag{2.23}$$

Eq (2.23) was giving an error of 25% between the theoretical calculated inductance and the actual measured value. The original equation was altered to reflect the actual inductance that was measured. So Eq (2.23) was modified to include fringing flux at the corners.

$$\mathfrak{R}_g = \frac{l_g}{\mu_0[A_e + 2(f+d)l_g + \pi l_g^2]} \tag{2.24}$$

In the case of EE type of core from Fig 2.3, there are three possible reluctances: reluc-
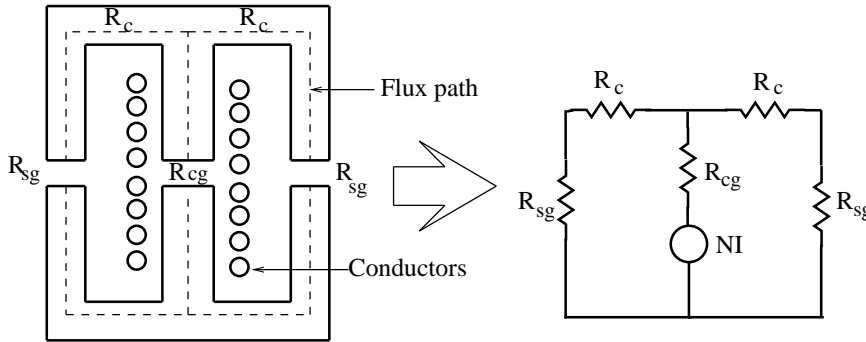
Figure 2.3: Magnetic circuit representation of EE core inductor

tance of the core $\mathfrak{R}_c$, reluctance of the center leg of E core $\mathfrak{R}_{cg}$ and reluctance of side leg of E core $\mathfrak{R}_{sg}$. The total reluctance of the magnetic path will be

$$\mathfrak{R}_t = \mathfrak{R}_{cg} + \frac{\mathfrak{R}_{sg}}{2} + \frac{\mathfrak{R}_c}{2} \tag{2.25}$$

2.4.2   Bossche and Valchev model

The authors propose basic analytical approximations for fringing coefficients for several basic cases of air gap configurations [6]-[7]. The total permeance of the air gap is a summation of the air gap permeance and product of these fringing coefficients multiplied by corresponding core dimensions.

$$\Lambda_g = \mu_0 \frac{a_e}{l_g} + \mu_0 C_g F \tag{2.26}$$

Λ_g is the permeance of the air gap; a_e is the cross section area of the core, C_g is the core dimension (in *m*) corresponding to fringing coefficient F.
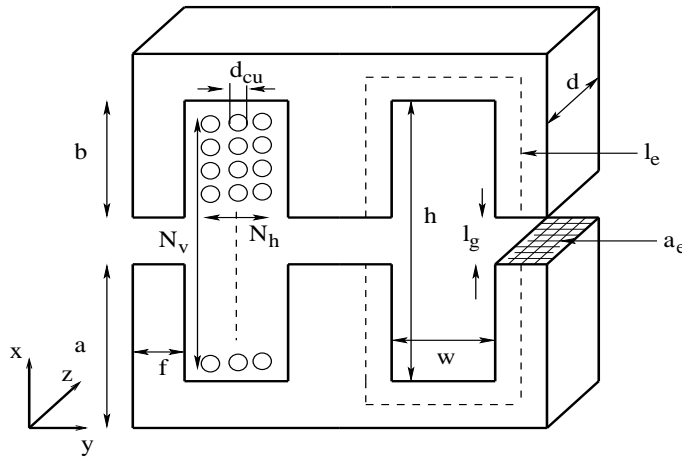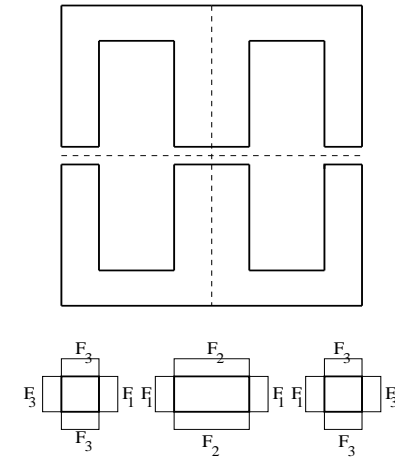
Figure 2.4: Reference EE core for indicating dimensions

Figure 2.5: Fringing coefficients F_1, F_2, and F_3 at gaped inductor

The coefficients for the basic cases possible in an EE type core are:

$$F_1(p,q,r) = \frac{2}{\pi} \ln \left(\frac{\frac{1}{q} + \frac{1}{p}}{\frac{1}{q} + \frac{1}{r}} \right) + \frac{(r-p)^2(r-0.26p-0.5q)}{3qr^2} + \frac{q}{3r} \tag{2.27}$$

$$F_2(p,q,r) = \frac{2}{\pi} \ln \left(\frac{0.44(r^2+q^2) - 0.218pr + 0.67pq + 0.33qr + 0.7825p^2}{p^2} \right)^{\frac{1}{2}} \tag{2.28}$$

$$F_3(p,s) = \frac{1}{\pi} \cosh^{-1} \left(3.4 \left(\frac{s}{p} \right)^2 + 1.3 \right) \tag{2.29}$$

With reference to Fig 2.4, the variables p, q, r and s will be

$$p = \frac{l_g}{2} \tag{2.30}$$

$$q = d_{cu} \times N_h \tag{2.31}$$

$$r = d_{cu} \times \frac{N_v}{2} \tag{2.32}$$

$$s = a + \frac{l_g}{2} \tag{2.33}$$

where d_{cu} is the diameter of bare copper conductors, N_v is number of conductor layers in vertical axis, and N_h is number of layers in horizontal axis.

The permeances of each leg of EE core are calculated separately using the fringing coefficients.

$$\Lambda_{cg} = \mu_0 \frac{2a_e}{l_g} + \mu_0 \left[2(2f)F_2 + 2dF_1 \right] \tag{2.34}$$

$$\Lambda_{sg} = \mu_0 \frac{a_e}{l_g} + \mu_0 \left[3F_3 f + F_1 d \right] \tag{2.35}$$

$$\Lambda_c = \frac{\mu_i \mu_0 a_e}{l_g} \tag{2.36}$$

where Λ_{cg} is the permeance of air gap of center leg, Λ_{sg} is permeance air gap of side leg, Λ_c is permeance of core. The corresponding reluctances are

$$\mathfrak{R}_{cg} = \frac{1}{\Lambda_{cg}} \; ; \; \mathfrak{R}_{sg} = \frac{1}{\Lambda_{sg}} \; ; \; \mathfrak{R}_c = \frac{1}{\Lambda_c} \tag{2.37}$$

The net reluctance of the flux path is

$$\mathfrak{R}_t = \mathfrak{R}_{cg} + \frac{\mathfrak{R}_{sg}}{2} + \frac{\mathfrak{R}_c}{2} \tag{2.38}$$

2.4.3   Comparison

The core measurements are given in Table 2.1. The analytical calculations from both the fringing models are compared with the actual measured values of the inductor in Table 2.2. Based on the comparison, the simple fringing model has been used in the subsequent design calculations.

a_e	840 μm^2	w	34.6 mm	Turns	120
l_e	354 mm	l_g	12 mm	N_h	4
f	28 mm	a	76 mm	N_v	36
d	30 mm	b	48 mm	d_{cu}	2.743 mm

Table 2.1: EPCOS Ferrite core UU 93/152/30 measurements used for fringing calculations

2.5 Fringing edge calculation using FEA

FEA studies were carried out to verify the accuracy of the analytical fringing effect models. The inductor was simulated for various air gap lengths to estimate how much the flux lines fringe out in the air gap of the inductor for various air gap lengths. Air gap flux density in the inductor was plotted for each case. Flux in the air gap was calculated by integrating the flux density value. Fringing edge was taken as the distance at which the flux falls to about 85% of maximum flux in the air gap (at the middle of the gap). These simulations were carried out for ferrite and amorphous core inductors.

2.5.1 Analysis

Fig. 2.6 shows the plots of flux density in the air gap of the side limb of the inductors plotted against distance across the air gap. Graphs are plotted for different air gaps varying from 1mm to 24mm. Fig. 2.10 shows the plots of fringing distance and fringing factor against air gap length. From the plot it is found that the fringing edge is almost equal to the air gap length(l_g) for large air gaps and $l_g/2$ for smaller air gap designs.

2.5.2 Results

	Unit	Measured	Simple model	B & V model
L	mH	3.439	3.064	4.145
$\Re_{cg}$	MH^{-1}		2.845	2.184
$\Re_{sg}$	MH^{-1}		3.557	2.574
Error	%		-10.9	20.5

Table 2.2: Comparison of accuracy of two fringing models
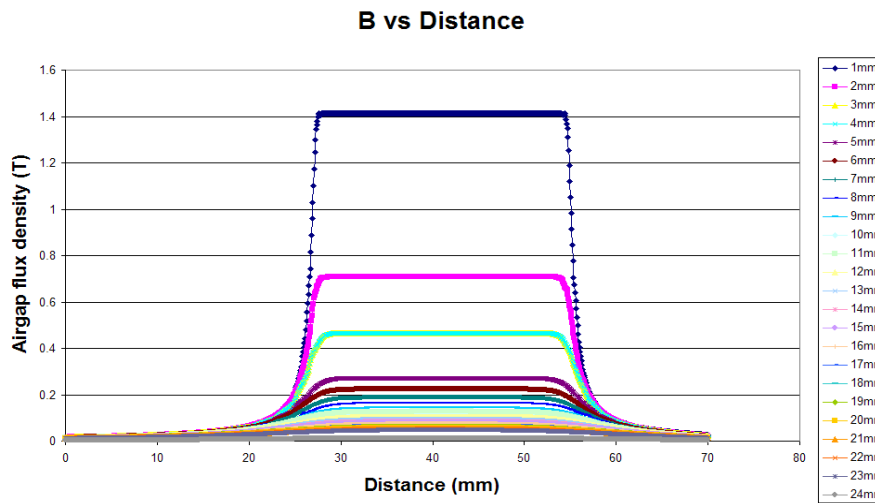
Figure 2.6: Plot of Airgap flux density vs distance
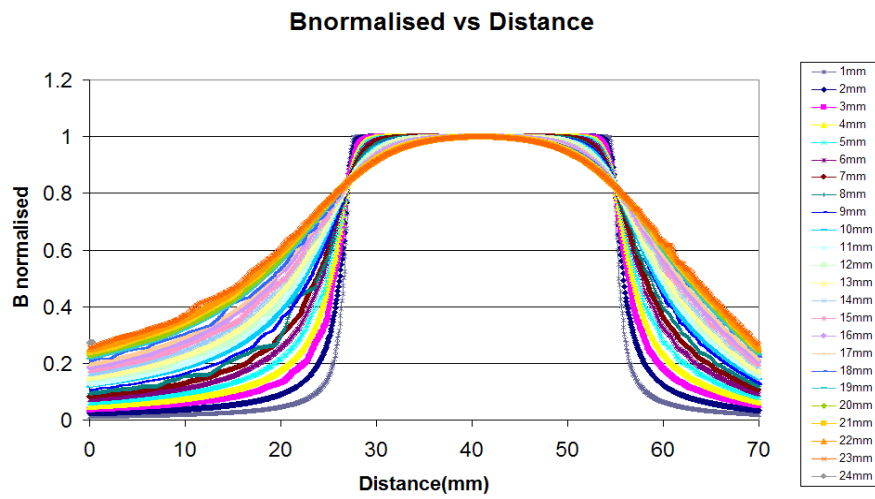
Figure 2.7: Plot of Normalised airgap flux density vs distance
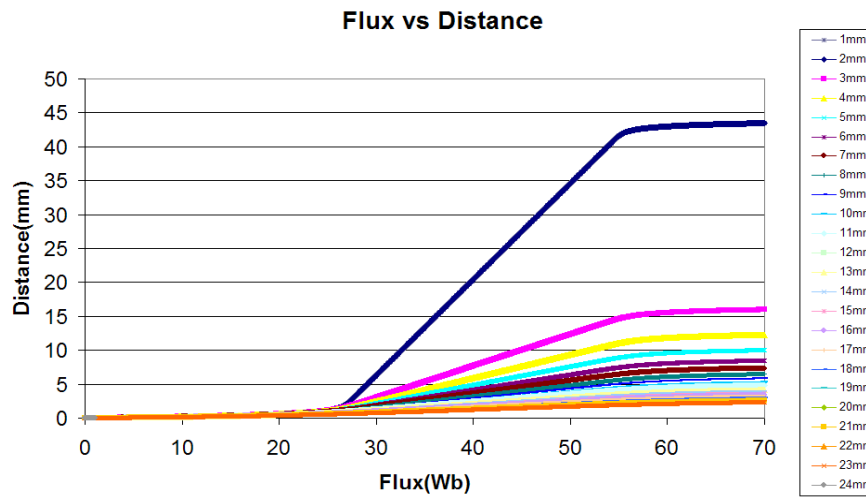
Figure 2.8: Plot of Airgap flux vs distance for one half of the sidelimb
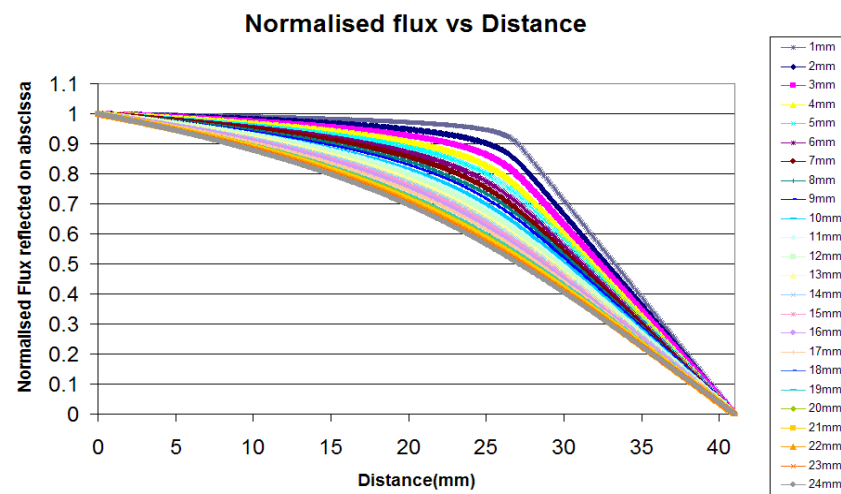
Figure 2.9: Plot of Normalised airgap flux density vs distance for one half of the sidelimb
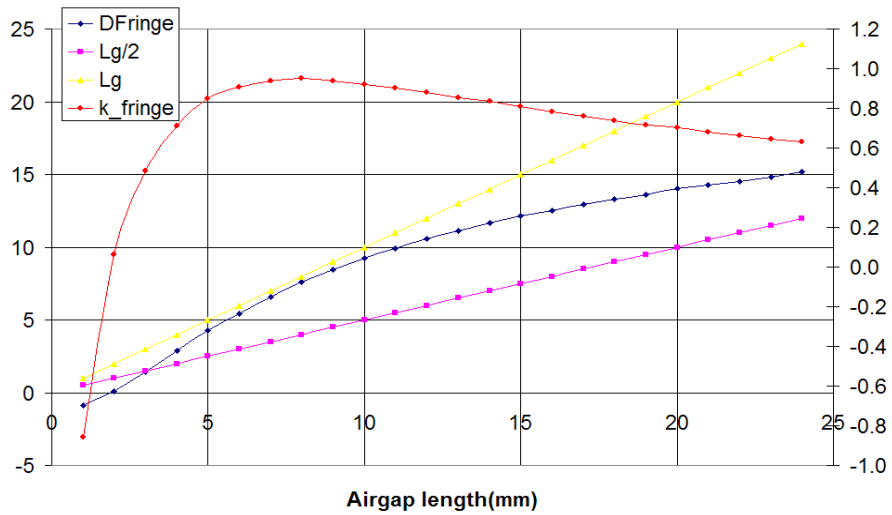
Figure 2.10: Plot of fringing edge (D_{fringe}) and fringing factor(k) vs Airgap length

2.6   Inductor design

Magnetic cores used in power electronic applications like transformers and inductors usually fall in four broad categories[9]. The first is bulk metal, like electrical steels which are processed from furnace into ingots and then hot and cold rolled. Second is powdered core materials where are manufactured from various types of iron powders mixed with special binding agents and then die-pressed into toroids, EE cores and slugs. The third is ferrite materials which are ceramics of iron oxide, alloyed with oxides or carbonate of Mn, Zn, Ni, Mg, or Co. The most recent category is of metallic glasses where the bulk metal is rapidly quenched from molten state to obtain a 'glassy' state without a regular arrangement of metallic atoms in the material.

One of the design objectives is to derive most general procedures for inductor construction. Theoretically, it should be possible to accurately design the inductor using just the property of permeability of the core material. But practically, the design procedure for Ferrite, Amorphous and Powdered material is different, mainly because vendors follow different conventions and specify the material properties in many ways. Amorphous and powder cores also have nonlinear permeability, ie the permeability varies with the applied field, temperature, air gap etc. Hence the design procedure for different materials is heavily affected by the available data from vendors, and it is not possible to define a single generalized accurate design process for all materials.

2.6.1   Ferrites

Ferrites have the most stable (with temperature, flux density and air gap) permeability of all the magnetic materials. Hence the magnetic circuit equations along with some modifications for fringing effects at large air gap are sufficient to accurately determine the inductance of ferrite cores. Ferrite materials also have very low core losses and are well suited for high frequency operation upto hundreds of kHz range. The downside is that since ferrite materials have low flux density (typically 0.3T-0.4T), the inductor will bigger than using other core materials.

1. The area product equation is the starting point. Choose a core having A_p greater than calculated.

2. Use the Graphical Iterative method described in section(2.3) to decide the number of turns and air gap, incorporating the fringing models discussed in section 3.4 in the reluctance equations.

3. Even though ferrite materials have very stable permeability, to compensate for effects of varying permeability and other manufacturing tolerance, the air gap should be selected such that the reluctance of the total air gap is at least ten times the reluctance of the core.

2.6.2   Amorphous material

Amorphous materials have a high flux density limit of upto 1.5T. The laminated structure of the amorphous cores also reduces eddy current losses. However, the layered structure of the C-cores vibrate at the switching frequency, which means in practical operation Amorphous cores can be noisy especially if the switching frequency is within the human range of hearing (upto 20 kHz). The noise is also directly proportional to the current ripple at switching frequency. The noise can be minimized with vacuum impregnation, reinforcement and by placing the cores in a damped enclosure.

Amorphous cores also have non linear permeability properties. Hence to accurately design an inductor with amorphous cores, the published A_L vs. H curves have to used.

1. Choose an amorphous core with area product greater than required for the specific application.

2. Select an air gap from the A_L curves published by the vendor (Fig 2.11). For this A_L, calculate the number of turns of copper winding

$$N = \sqrt{\frac{L}{A_L}} \qquad (2.39)$$

   where N is the number of turns of copper winding and L is the required inductance. The unit of A_L here is $\mu H/(\text{turns})^2$

3. Ensure that the core is not saturated for this range of induction.

$$B_m = \frac{A_L N I_{pk}}{A_e} \qquad (2.40)$$

   where B_m is the peak flux density in the core for the peak current of I_{pk}, A_e is the cross section area of the core. If core is saturated, increase the air gap and select new A_L. If it is not possible to choose higher air gap, go to next larger core size.

AMCC-200 Magnetization Curves

Gap (mm)	Initial A_L ($\mu H/N^2$)
0.5	1.216
1.0	0.728
1.5	0.546
2.0	0.467
2.5	0.396
3.0	0.352
4.0	0.289
5.0	0.256
6.0	0.233
8.0	N/A
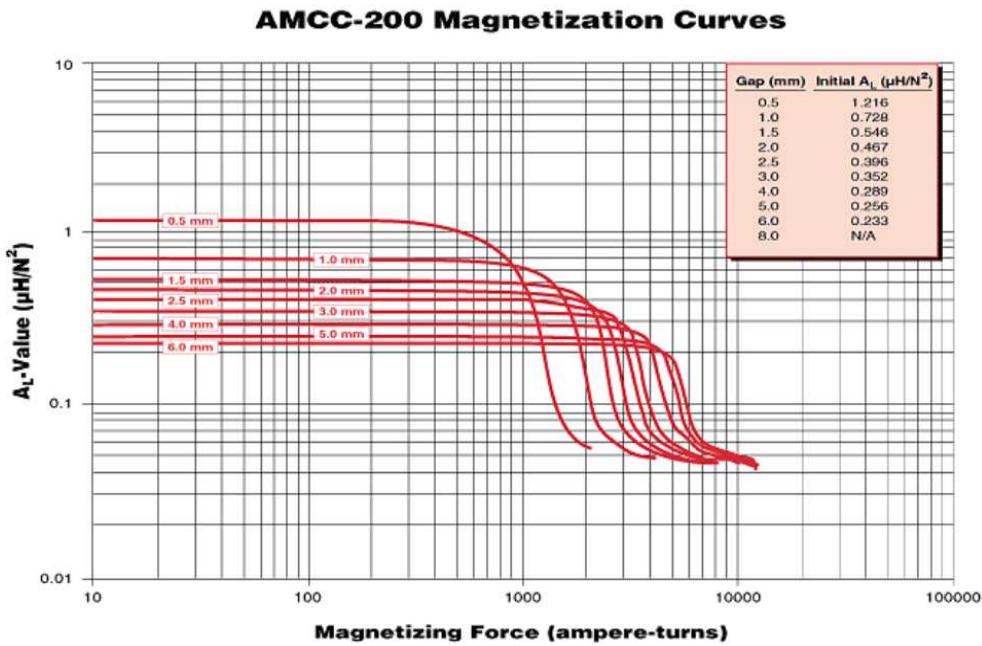
Figure 2.11: A_L vs H for AMCC 200 core. Source: Metglas Inc [12]

2.6.3 Powder material

Powder materials feature a distributed air gap and hence there is no need to include an explicit air gap. But this distributed air gap also means that these materials have the lowest permeability of all the core materials discussed. The absolute permeability ranges from $26\mu H/m$ to $300\mu H/m$ [14]. Hence a design decision should also specify the permeability of the core. Powder materials are also sensitive to temperature variations because of the binder materials used in the core, though some recent products are more resistant in this regard.

1. Choose powder core size with area product greater than required for the specific application.

2. Calculate the maximum number of turns that can be accommodated within the selected core window.

$$N_{max} = \frac{W_a k_u}{a_{cu}} \qquad (2.41)$$

where N_{max} is the maximum number of turns that can be accommodated in the core window of area W_a, a_{cu} is the bare copper conductor cross section area, k_u is the utilization factor which depends on the type of winding (round wire, foil), method of winding (square lay, hexagonal lay), number of bobbins (single, two) and finally

the winding skill.

3. Calculate the minimum permeability required for the specific application

$$\mu_{min} = \frac{Ll_e}{A_e N_{max}^2} \tag{2.42}$$

where L is the required inductance and l_e is the magnetic path length. Select a permeability higher than μ_{min} from the vendor datasheets [14]-[15].

4. A_L is usually specified by the vendor for specific core shapes and sizes. Use this information to calculate the actual required number of turns.

$$N = \sqrt{\frac{L}{A_L}} \tag{2.43}$$

2.7   Capacitor selection

Metallised Polypropylene capacitors are AC capacitors that are especially designed for high frequency operation. These capacitors are constructed from polypropylene films on which an extremely thin metal layer is vacuum deposited. The metal layer typically consists of aluminium or zinc of thickness in range of 0.02μm to 0.05μm. Several such layers are wound together in a tubular fashion to get higher capacitance.

Metallised film capacitors are characterized by small size, wide operating frequency range, low losses, low to medium pulse handling capabilities, low parasitic impedances and self-healing. In regular film-foil capacitors, if the electrode foils of opposite potential are exposed to each other because of wearing away of the dielectric, the foils will short and the capacitor will be destroyed. But in case of metallised polypropylene capacitors, because of the extremely thin metal layer, the contact points at the fault area are vaporised by the high energy density, and the insulation between foils is maintained. Due to the above reasons, these capacitors are perfectly suited for grid connected filter operation.

For the LCL filter, the capacitors are connected in star and the voltage across each capacitor will be the phase voltage. The star combination also ensures that the LCL filter provides both common mode and differential mode attenuation.

Type	AP4
Voltage rating (V)	415/440
Tolerance (%)	$\pm 5, \pm 10$
$\tan \delta$	0.001 at 1kHz
Temperature range (°C)	-40 to +85

Table 2.3: AC Capacitors specifications [19]

2.8   Power resistors

The resistors used in high power applications like grid connected inverters are termed as power resistors. There are three types of power resistors, depending on the required ohmic rating and current rating [20]-[21]. Individual power resistors are available for upto 1 kW and 100 A. Wirewound resistors are designed for high ohmic value and low current rating. Edgewound resistors which use metallic ribbon are designed for medium ohmic value and high current rating. Grid and ribbon resistors are designed for low ohmic value and high current rating. In the damping resistor for the proposed damping circuit topology, parasitic inductance is not a major concern as the resulting corner frequency is much higher than $\omega_{L_p C}$. Hence, lower cost wire wound resistors are sufficient for this application.

Voltage insulation (Vrms)	600
Tolerance (%)	+10
Temperature rating above ambient (°C)	375

Table 2.4: Power resistors specifications [20]-[21]

2.9   Design examples

The design procedure for Ferrite cores is already discussed in some detail in sections 3.3 and 3.4. This section will focus on the design examples using Amorphous and Powder cores.

Electrical		Material	
L (mH)	2.761	J_m (M A/m^2)	3
I_{rms} (A)	15.48	B_m (T)	1
I_p (A)	26.19	k_u	0.6
V_{rms} (V)	13.40	k_f	4.44
VA rating	207.25	f_b (Hz)	50

Table 2.5: Electrical and material constraints for amorphous inductor design example

2.9.1 Amorphous core example

The electrical and material constraints are detailed in Table 2.5.

1. The minimum area product is calculated.

$$A_p = \frac{V_L I_L}{k_f k_u f_b B_m J_m} \tag{2.44}$$

2. We choose amorphous core AMCC 200 from Metglas Inc. The area product of the selected core is $5.187 \times 10^{-6} \text{m}^4$.

3. The air gap for the selected C core is selected such that variations in material magnetic properties do not affect the final inductance. The air gap reluctance is taken to be 10 times the core reluctance. This gives the minimum air gap.

$$l_{g(min)} = 10 \frac{l_e}{\mu_i} \tag{2.45}$$

where $l_{g(min)}$ is the minimum selected total air gap, l_e is the magnetic path length (from datasheet) and μ_i is the initial permeability. The initial permeability of amorphous material 2605SC is specified as 1500 [3].

4. For this air gap, use the A_L curves to find number of turns and core flux density. If the core flux density exceeds B_m increase the air gap and recalculate N and B_m.

5. The final settings are

$$l_g = 4 \text{mm} \tag{2.46}$$

$$A_L = 0.467 \, \mu\text{H}/(\text{turns})^2 \tag{2.47}$$

$$N = \sqrt{\frac{2.761 \times 10^{-3}}{0.467 \times 10^{-6}}} = 77 \tag{2.48}$$

$$B_m = \frac{0.467 \times 10^{-6} \times 77 \times 26.19}{9.5 \times 10^{-4}} = 0.99\text{T} \tag{2.49}$$

2.9.2 Powder core example

Electrical		Material	
L (mH)	0.276	J_m (M A/m^2)	3
I_{rms} (A)	15.48	B_m (T)	1.4
I_p (A)	65.17	k_u	0.674
V_{rms} (V)	1.34	k_f	4.44
VA rating	20.73	f_b (Hz)	50

Table 2.6: Electrical and material constraints for powder inductor design example

The electrical and material constraints are detailed in Table 2.6.

1. The minimum area product is calculated.

$$A_p = \frac{V_L I_L}{k_f k_u f_b B_m J_m} \tag{2.50}$$

2. We choose BK 6320 (assembled unit 2) from Changsung corp. The area product of the selected core is $1.44 \times 10^{-6} \text{m}^4$.

3. The maximum number of turns for this core size will be

$$N_{max} = \frac{12 \times 10^{-4} \times 0.674}{5.48 \times 10^{-6}} = 138 \tag{2.51}$$

4. The absolute minimum permeability required for this inductor is

$$\mu_{min} = \frac{0.276 \times 10^{-3} \times 22.28 \times 10^{-2}}{12 \times 10^{-4} \times 138^2} = 2.86 \times 10^{-6} \text{H/m} \tag{2.52}$$

5. We choose MegaFlux powder core material of absolute permeability 40μ. A_L for

this core for the selected permeability is 270nH/(turns)^2.

$$N = \sqrt{\frac{0.276 \times 10^{-3}}{270 \times 10^{-9}}} = 32 \qquad (2.53)$$

6. The flux density in the core will be

$$B_m = \frac{270 \times 10^{-9} \times 32 \times 65.17}{12 \times 10^{-4}} = 0.469\text{T} \qquad (2.54)$$

Material	Cost p.u (Rs)	Weight p.u (kg)	# of units	Cost per L (Rs)	Weight per L (kg)
Ferrite (UU93/152/30)	381	0.75	4	1524	3
Amorphous (367S)	1625	1.662	1	1625	1.662
Amorphous (630)	3220	3.67	1	3220	3.67
Powder (BK7320)	340	0.2735	8	2720	2.188

Table 2.7: Core material cost

Inductor type	Core cost (Rs)	Copper cost (Rs)	Other charges (Rs)	Total cost (Rs)	Total weight (kg)
Ferrite	1524	1046	1142	3712	4.28
Amorphous (367S)	1625	3733	2435	7793	4.61
Amorphous (630)	3220	2216	1826	7263	5.23
Powder -Foil	2720	2566	1643	6930	3.66
Powder -Round wire	2720	636	1643	5000	2.966

Table 2.8: Total cost of Inductors

Capacitor rating	6 μF	8 μF	10 μF	20 μF
Cost (Rs)	72	96	95	180

Table 2.9: Cost of AC Capacitors 440V AC rating

2.10 Measurements on inductors

2.10.1 Measurement of permeability of core material

An experiment was conducted to verify the permeability of the inductor core material to see if it matched the manufacturer specified values. For this purpose a transformer was made using the same core material as that of the inductor,without adding any airgap in the fluxpath. For different values of ac current through the primary coil, the induced voltage in the secondary coil were noted. The flux density inside the core was calculated using transformer equation as below. Peak core flux density is specified in tesla (T).

$$B = \frac{E}{4.44NAf} \qquad (2.55)$$

where E = induced emf in the secondary (rms) in volts

N = number of turns in the secondary winding

f = frequency of the input voltage in hertz

A = cross-sectional area of the core in sq.m

The magnetisation (H in *Ampereturns/metre*) of the coil can be calculated as

$$H = \frac{NI}{l} \qquad (2.56)$$

where N = No. of turns in the coil

I = Current through the coil in amperes

l = Mean magnetic path length in metres

Relative permeability of the core material is obtained by using the equation

$$\mu_r = \frac{B}{H\mu_0} \qquad (2.57)$$

where μ_0 is the permeability of air.
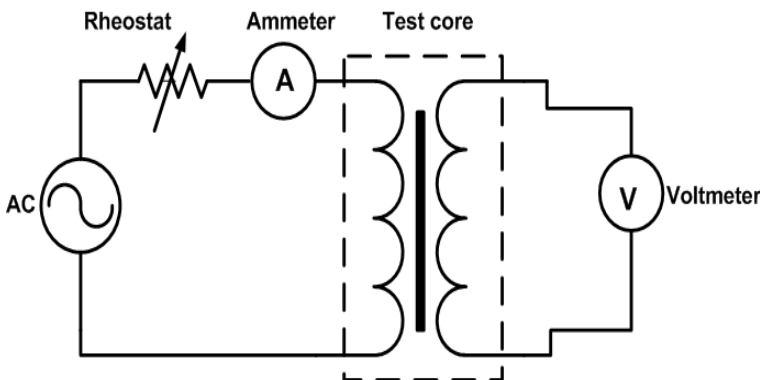
Figure 2.12: Experimental setup for measuring core fluxdensity and permeability

Core material	Relative permeability
Ferrite	3340
Amorphous (AMCC 630)	1200
Amorphous (AMCC 367S)	1800
Powdered core	45

Table 2.10: Measured relative permeability of the different core materials.

2.10.2   Measurement of airgap flux density

Flux density in the airgap of the ferrite inductor was measured using a gaussmeter to validate analytical results and FEA calculations. Plot of the airgap flux density against distance across the airgap is given in Fig. 2.13 Gaussmeter used was make: MAGNET-PHYSIK, model : FH54.

2.10.3   Measurement of core flux density

The experiment to be conducted is same as that for obtaining permeability. Flux density is calculated from the transformer equation. Refer to Table 2.11 for the results of the experiment. Better match between analytical results and measurements were observed when compared to the FEA.
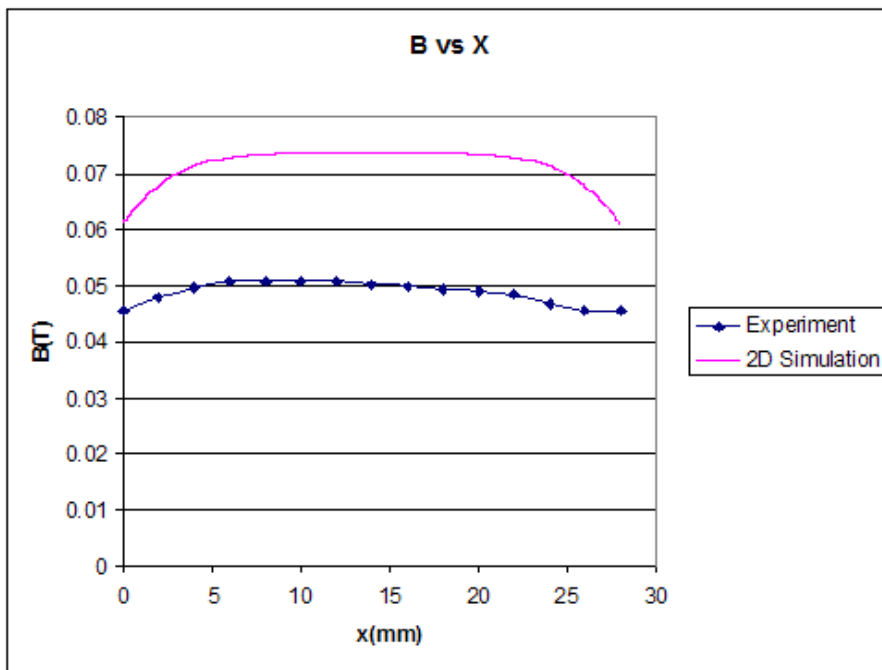
Figure 2.13: Comparison between FEA and measurements of airgap fluxdensity in ferrite core inductor.

Inductor type	Fluxdensity (T)
Ferrite	0.252
Amorphous (AMCC 630)	0.688
Powdered core	0.259

Table 2.11: Core fluxdensity in the inductors.

2.11 Summary

The familiar area product approach for inductor design has been evaluated and modifications to improve the accuracy of the final constructed inductance are suggested. A new approach for selection of air gap and number of turns in an inductor is proposed. The effect of fringing of the magnetic flux at the air gap is investigated and simple equations are suggested to model this effect. The design techniques for three magnetic materials -Amorphous, Ferrite and Powder are discussed and elaborated using actual examples. Tables 2.7 and 2.8 summarize the size and weight of the inductors. It was seen that the ferrite inductors were low cost and the powdered core had the lowest weight.

2.12   References

Area Product method

1. N.Mohan,T.M.Undeland,W.P.Robbins, *Power Electronics- Converters, Applications and Design,* 3rd ed., John Wiley and Sons, 2003, pp. 744-792.

2. G.S.Ramana Murthy, "Design of Transformers and Inductors at Power-Frequency– A modified Area-Product method," M.Sc(Engineering) Thesis, Indian Institute of Science, March 1999.

3. Col.Wm.T. McLyman, "AC Inductor Design," in *Transformer and Inductor Design Handbook*, 3rd ed., Marcel Dekker, 2004, pp. 10-1–10-13

Fringing effect

4. T.G.Wilson, A.Balakrishnan, W.T.Joines, "Air-gap reluctance and inductance calculations for magnetic circuits using a Schwarz-Christoffel transformation," IEEE Trans. on Power Electronics, vol. 12, no. 4, pp. 654-663, July 1997

5. A.F.Hoke, "An improved two-dimensional numerical modeling method for e-core transformers," A.B. Honor's Thesis, Thayer School of Engg., Dartmouth Coll., Hanover, New Hampshire, June 2001

6. A. van den Bossche, V.Valchev, T.Filchev, "Improved approximation for fringing permeances in gapped inductors," *Industry Applications Conference, 2002. 37th IAS Annual Meeting Conference Record of the*, 2002, vol.2, pp. 932- 938

7. A. van den Bossche, V.Valchev, *Inductors and Transformers for Power Electronics,* 1st ed., Taylor and Francis, 2005, pp. 333-342

Components

8. H.W. Beaty, *Electrical Engineers Materials Reference Guide*, McGrawHill Engineering Reference Series, 1990

9. Col.Wm.T. McLyman, "Magnetic cores," in *Transformer and Inductor Design Handbook*, 3rd ed., Marcel Dekker, 2004, pp. 3-1–3-48

10. H.Skarrie, "Design of Powder core inductors," Ph.D. dissertation, Dept. of Ind. Elec. Eng. and Auto., Lund Univ., Lund, Sweden, 2001

11. Ferrites and Accessories Catalog: EPCOS, (2007)
    `http://www.epcos.com`

12. Amorphous PowerLite C cores: Metglas Inc,
    `http://metglas.com/products/page5_1_6.htm`

13. MPP, SuperMSS,HiFLux : Arnold Magnetic Technologies,
    `http://www.arnoldmagnetics.com/products/powder/powder_catalogs.htm`

14. MPP, HiFlux, Kool Mu : Magnetics Inc,
    `http://www.mag-inc.com/library.asp`

15. MegaFlux power cores : Changsung Corp.
    `http://www.changsung.com`

16. *Standard Specification for Flat-Rolled, Grain-Oriented, Silicon-Iron, Electrical Steel, Fully Processed Types,* ASTM A876-03, 2003

17. *Standard Specification for Fully Processed Magnetic Lamination Steel,* ASTM A840-06, 2006

18. Silicon Steels and their applications- Key to Steel;
    `http://www.key-to-steel.com/default.aspx?ID=CheckArticle&NM=101`

19. AC Metallized Polypropylene Capacitors : Advance Capacitors Ltd,
    `http://www.advance-capacitors.com`

20. Power Resistors : Mega Resistors,
    `http://www.megaresistors.com/en/index.php`

21. Power Resistors : Powerohm Resistors,
    `http://www.powerohm.com/index.php`

Chapter 3

Simulation Using FEA Tools

3.1 Introduction

Finite Element Method is a numerical technique used to solve partial differential equations. In this method, the problem domain is discretised into different cells or regions. The field to be solved for is approximated using a polynomial in each of the cells. These polynomials are solved for using numerical methods to obtain the field values in each cell.

Simulations using Finite Element method were carried out to confirm the design of inductors for the filter. The tools employed were

1. FEMM (Finite Element Method Magnetics) : FEMM is a freeware that makes use of Finite Element Method to solve Maxwell's equations. Simulation using FEMM involves the following steps.

    (a) Draw the inductor geometry

    (b) Assign materials and boundary conditions

    (c) Make coils and apply excitation

    (d) Create Finite Element mesh

    (e) Solve using static/time-harmonic solver

    (f) View the solution results and fields

    As a first approximation, the windings of the inductor were modelled as a single sheet of copper carrying current. A refined model with different layers of copper

was chosen in the next step. Further refinement in the winding geometry was done by modelling the actual individual conductors in the winding. Flux and eddy current can be solved for. Inductance value is calculated by FEMM and is shown as a result under coil properties. Simulation using FEMM is possible only in 2D. Also it cannot take into account hysteresis in magnetic materials.

2. <u>MagNet</u> :The steps followed in simulation are same as that in FEMM. These models were simulated and solved in 2D as well as 3D. The optimum mesh size for FEM was chosen by trial and error. Models were solved using static(for dc current) and time-harmonic(for ac current)solvers. MagNet calculates the flux linkage and energy and are displayed in the post processing bar. After solving the model, the magnetic flux lines in the core can be viewed as a contour-plot. Flux density can be plotted along any required contour. Inductance can be calculated by two methods.

   (a) From flux linkage :

   $$L = \frac{\psi}{I} \tag{3.1}$$

   where ψ is the flux linkage in weber and I is the rms value of current through the inductor in amperes

   (b) From stored energy :

   $$L = \frac{2W}{I^2} \tag{3.2}$$

   where W = Energy stored in the inductor in joules

   Results of simulation using MagNet are given in the section()of appendix.

3.2   Ferrite core inductor

Table 3.2 shows the calculation done to estimate the dimensions for the winding geometry of the inductor.

Core material	Ferrite (EPCOS N87)
Core type	UU core
Inductance	3mH
Relative permeability of core	2200
Number of turns in winding	120
Copper wire gauge	12SWG
Airgap length	12mm

Table 3.1: Inductor specifications for FEA.

Core Dimension		Units
Window height (W_h)		96 mm
Window breadth (W_b)		37 mm
Air gap length (l_g)		12 mm
Dielectric thickness (D_t)		6 mm
Area of bare wire	$= W_h + lg - 2D_t$	5.48 mm^2
Available window height(H)	$= W_b - 2D_t$	96 mm
Available window breadth(B)		25 mm
Available window area	$= HB$	2400 mm^2
Diameter of copper wire including insulation (D)		2.743 mm
Turns per layer (T)	$=H/D$	35
Diameter of copper wire without insulation (D_c)		2.642 mm
Layer height	$=TD_c$	92.46 mm
Layer width	$= D_c$	2.642 mm
Insulation thickness between two layers	$= D - D_c$	0.101 mm
Number of layers (N)		4
Sweep distance for coil	$= DN$	10.972 mm

Table 3.2: Calculations for determining copper winding geometry for ferrite core inductor.
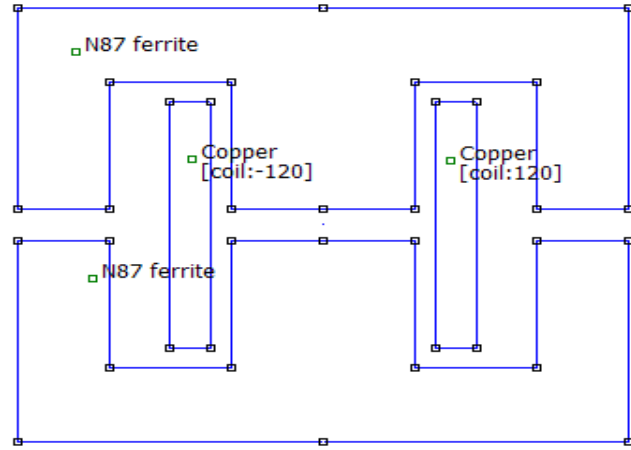
Figure 3.1: Ferrite core inductor model with single layer winding.
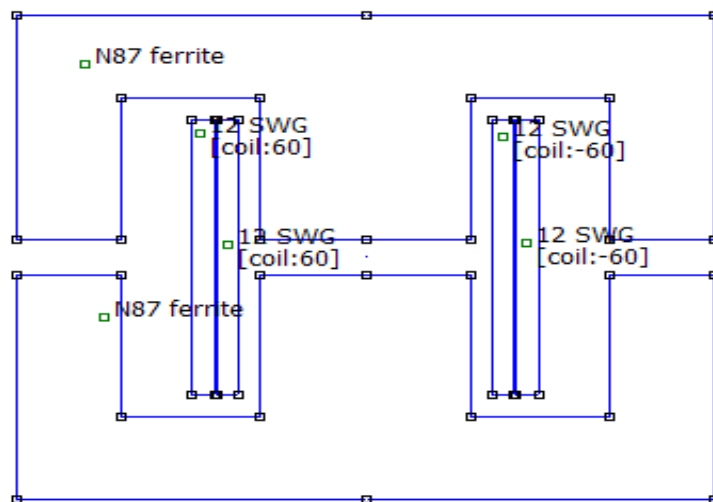
Figure 3.2: Ferrite core inductor model with two layer winding.
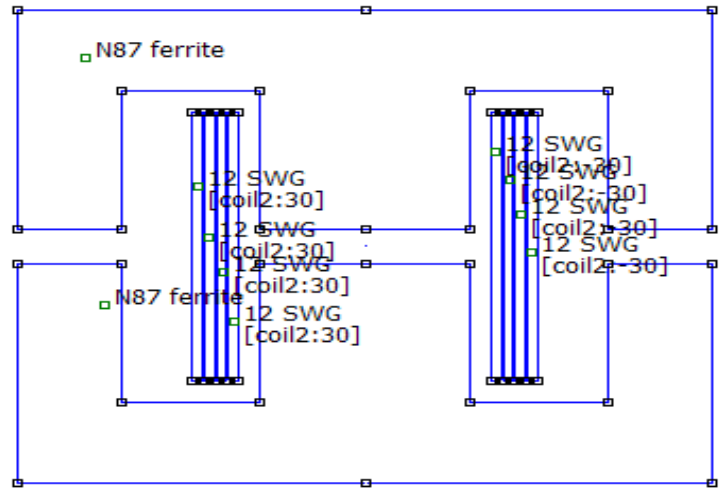
Figure 3.3: Ferrite core inductor model with four layer winding.
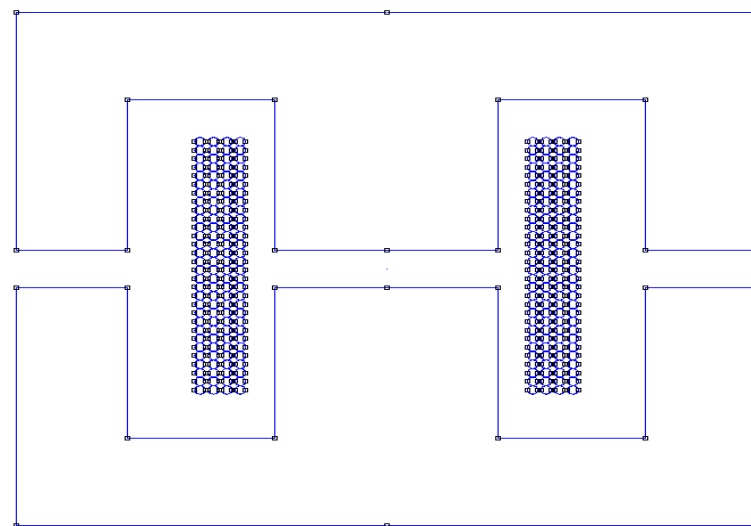
Figure 3.4: Ferrite core inductor model with individual conductors.
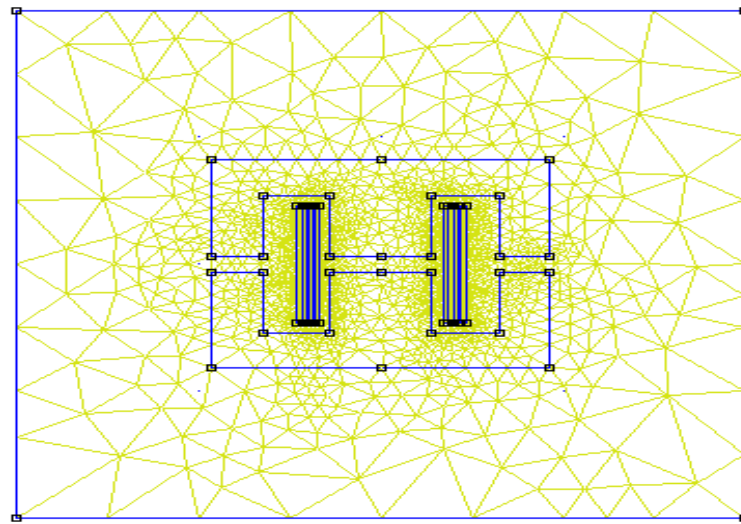
Figure 3.5: Finite element mesh created in FEMM.
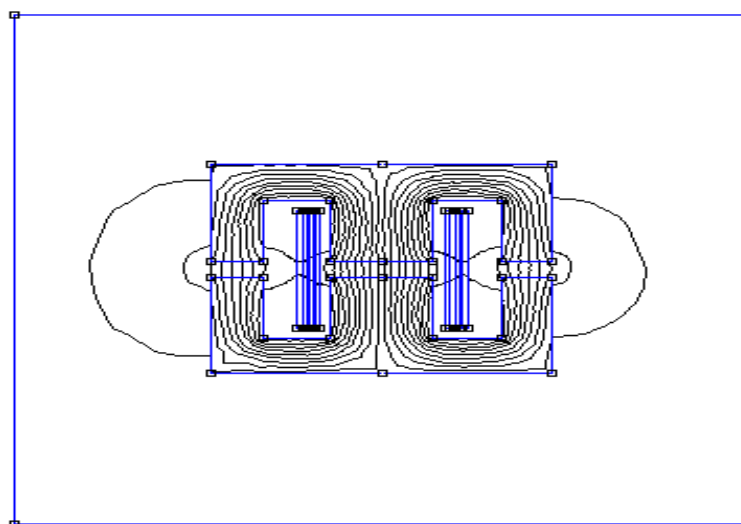
Figure 3.6: Flux plot of ferrite core inductor.
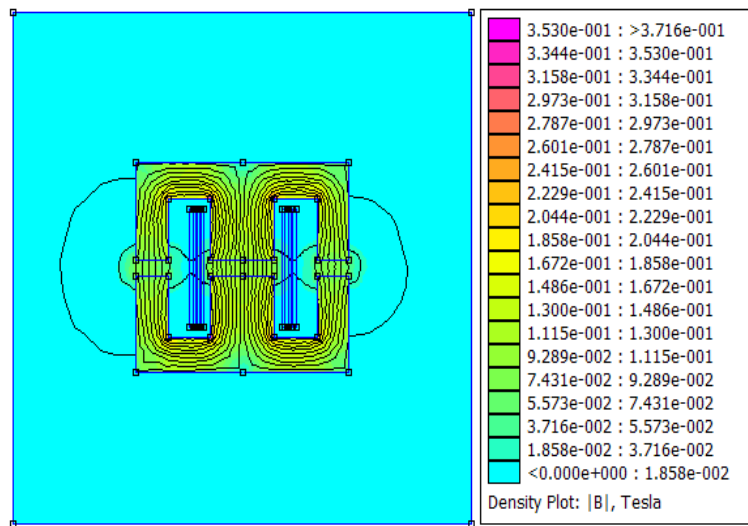
Figure 3.7: Flux density plot of ferrite core inductor.

3.3   Amorphous core inductor

Core material	Amorphous	Amorphous
Core type	C core(AMCC630)	C core(AMCC 367S)
Relative permeability of core	1500	1500
Inductance	4.975mH	4.975mH
Number of turns in winding	68	137
Conductor type	Copper foil	Copper foil
Foil thickness	5 mil	5 mil
Insulation thickness (mm)	0.127	0.2
Airgap length	1.6mm	4.6mm

Table 3.3: Amorphous core inductor specifications for FEA.
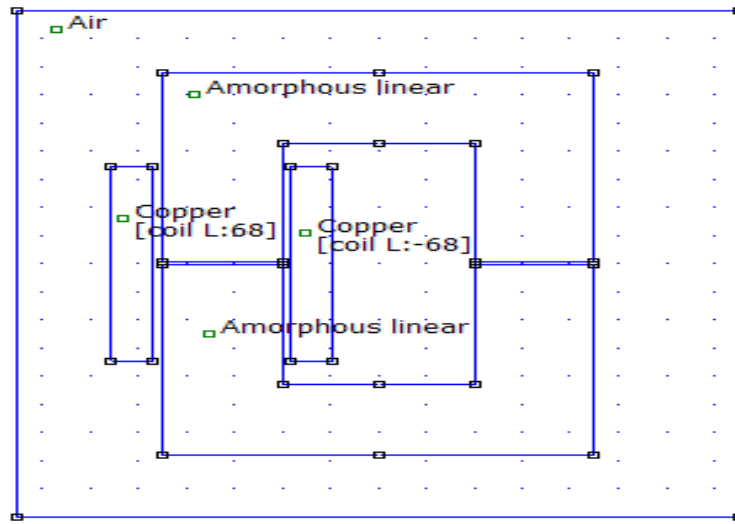
Figure 3.8: Amorphous core (core type: AMCC630)inductor model.
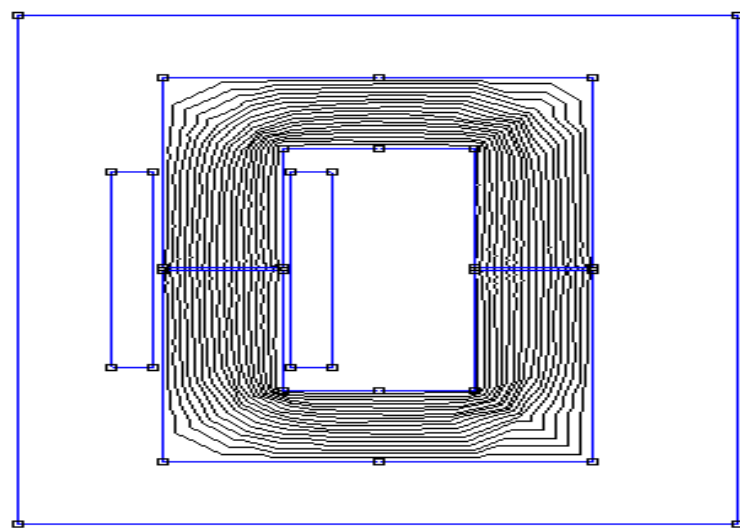
Figure 3.9: Flux in amorphous core (core type: AMCC630)inductor.

1.402e+000 : >1.476e+000	
1.328e+000 : 1.402e+000	
1.254e+000 : 1.328e+000	
1.180e+000 : 1.254e+000	
1.107e+000 : 1.180e+000	
1.033e+000 : 1.107e+000	
9.591e-001 : 1.033e+000	
8.853e-001 : 9.591e-001	
8.116e-001 : 8.853e-001	
7.378e-001 : 8.116e-001	
6.640e-001 : 7.378e-001	
5.902e-001 : 6.640e-001	
5.165e-001 : 5.902e-001	
4.427e-001 : 5.165e-001	
3.689e-001 : 4.427e-001	
2.951e-001 : 3.689e-001	
2.213e-001 : 2.951e-001	
1.476e-001 : 2.213e-001	
7.378e-002 : 1.476e-001	
<0.000e+000 : 7.378e-002	

Density Plot: |B|, Tesla

Figure 3.10: Flux density plot of amorphous core (core type: AMCC630)inductor.
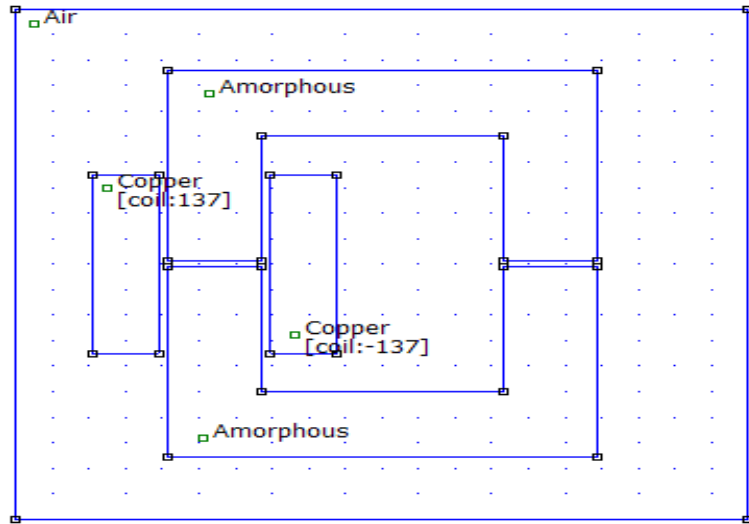
Figure 3.11: Amorphous core (core type: AMCC367S)inductor model.
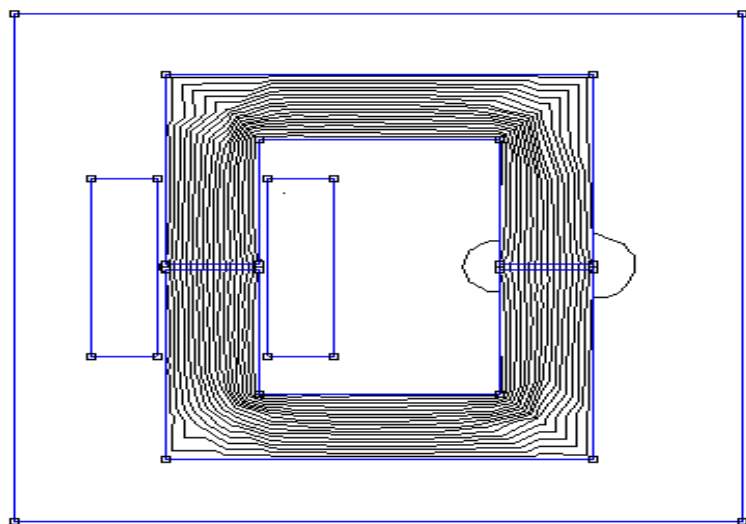
Figure 3.12: Flux in amorphous core (core type: AMCC367S)inductor.
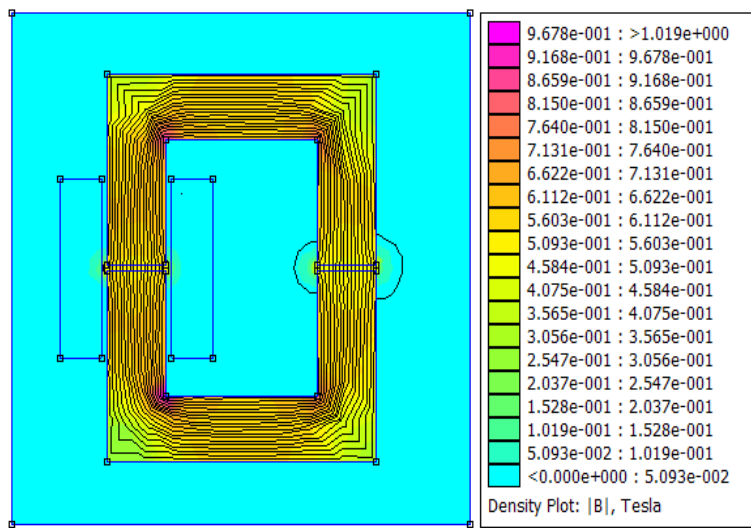
Figure 3.13: Flux density plot of amorphous core (core type: AMCC367S)inductor.

3.4 Powdered core inductor

Core material	Powdered Iron
Core type	Block core (BK 7320)
Inductance (mH)	1.7
Relative permeability of core	40
Number of turns in winding	78
Conductor type	Round conductor winding

Table 3.4: Powdered core inductor specifications for FEA.
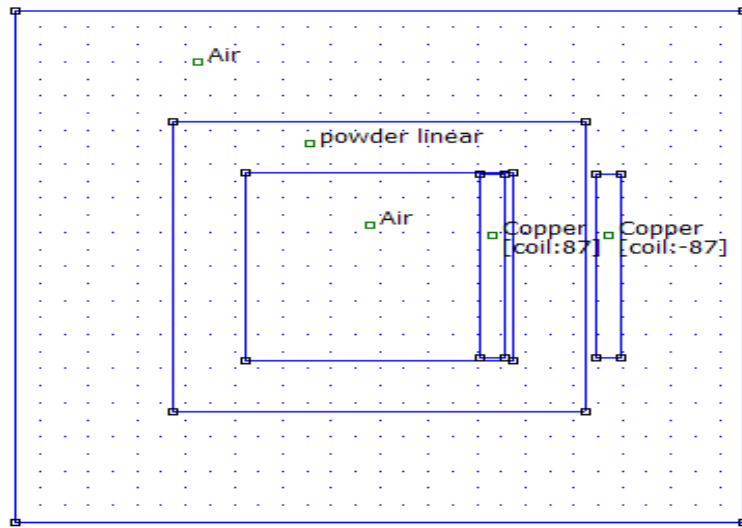
Figure 3.14: Powder core inductor model.
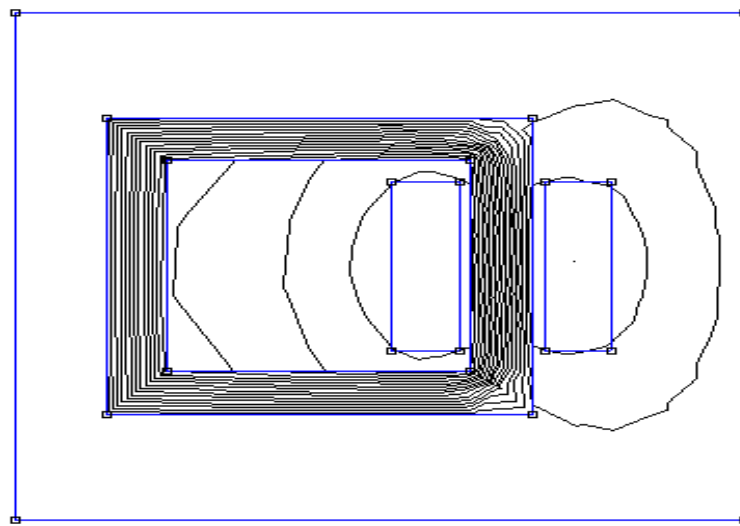
Figure 3.15: Flux in Powder core inductor.
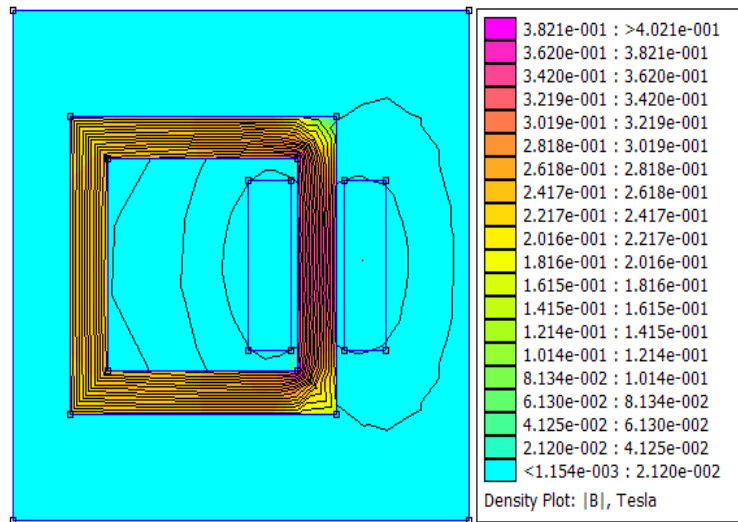
Figure 3.16: Flux density plot of powder core inductor.

3.5 Comparison of FEMM and MagNet

FEMM is a suite of programs for solving low frequency electromagnetic problems on two-dimensional planar and axisymmetric domains. It can address linear/nonlinear magnetostatic problems and linear/nonlinear time harmonic magnetic problems. FEMM is an open-source software. Three-dimensional solutions cannot be done using this tool. Also it cannot take into account hysteresis in magnetic materials. MagNet is a licensed tool. It can handle both two-dimensional and three-dimensional problems. It was seen overall that the analytical methods developed in chapter (2) is sufficient for the grid interactive inverter filter design procedure.

3.6   References

1. Ferrites and Accessories Catalog: EPCOS, (2007)
   `http://www.epcos.com`

2. Amorphous PowerLite C cores: Metglas Inc,
   `http://metglas.com/products/page5_1_6.htm`

3. MegaFlux power cores : Changsung Corp.
   `http://www.changsung.com`

4. M.V.K. Chari and S.J. Salon, *Numerical Methods in Electromagnetism*,Elsevier Inc.,2000

5. Robert Warren Erickson, Dragan Maksimovic, *Fundamentals of power electronics*, Kluwer Academic Publishers Group ,2001

6. Infolytica Corporation, MagNet User guide,
   `http://www.infolytica.com`

7. Foster Miller Inc., Finite Element Method Magnetics(FEMM) Documentation,
   `http://www.femm.info/wiki/HomePage`

Chapter 4

Power Loss and Heating Effects

4.1 Introduction

The focus of the previous chapter was on the system level design, and hence the physical characteristics of the individual filter components was understated. This chapter is focused on the power loss and efficiency of individual filter components, which has significant implication on the power converter efficiency and reliability. Losses in the inductive part of the filter are more prominent compared to capacitive losses. Hence more attention is focused on inductor core and copper losses. Analytical equations predicting the power loss in inductors are derived from the basic electromagnetic equations. The theoretical derivations in this chapter are necessarily brief and a more complete treatment can be found in the references listed for each section. The theoretical background for this chapter is covered in Appendix-A at the end of the report.

4.2 Core loss

The relationship between H and B in any magnetic material is given by the magnetization curve.The loop area of the magnetization curve represents the energy dissipated per unit volume of the material over a complete magnetization period. Let us assume that a field, slowly increasing with time, is applied by means of a magnetizing winding supplied with a current $i(t)$ to a magnetic circuit with path length l_m. At any instant of time the supplied voltage is balanced by the resistive voltage drop of the winding $R_w i(t)$ and the induced
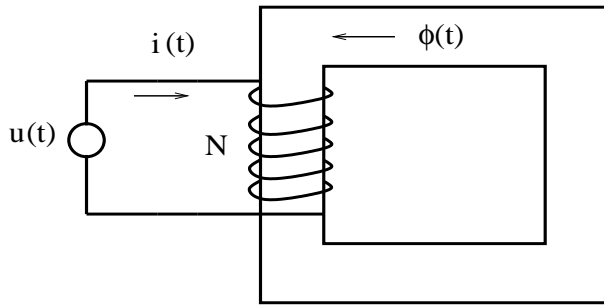
Figure 4.1: Energy balance
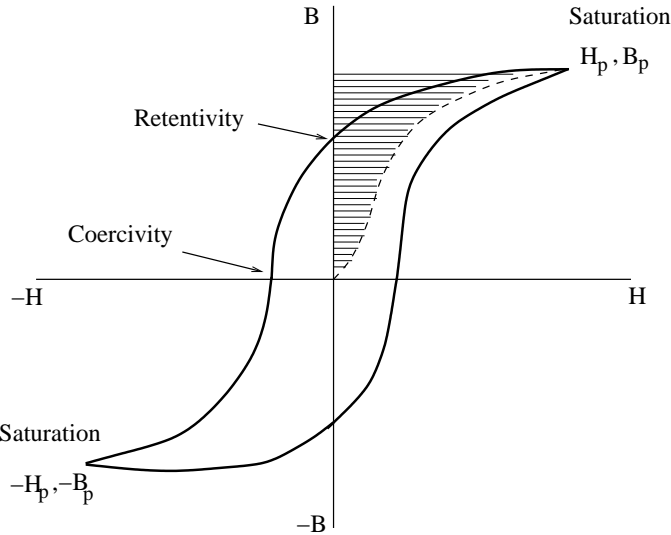
Figure 4.2: Magnetization curve of a magnetic material

emf $d\phi/dt$.

$$u(t) = R_w i(t) + N\frac{d\phi}{dt} \tag{4.1}$$

Starting from the demagnetized state, a certain final state with induction value B_p is reached after a time interval t_o. The corresponding supplied energy is E is partly dissipated by Joule heating in the conductor and partly delivered to the magnetic circuit.

$$E = \int_0^{t_o} u(t)i(t)dt \tag{4.2}$$

$$E = \int_0^{t_o} R_w i^2(t)dt + \int_0^{t_o} NAi(t)\frac{dB}{dt}dt \tag{4.3}$$

where N is the number of turns of the winding and A is the cross-sectional area of the sample. Since

$$i(t) = H(t)\frac{l_m}{N} \tag{4.4}$$

the energy delivered by the external system in order to bring the magnet of volume $v = Al_m$ to the final state is

$$U = v \int_0^{t_o} H(t)\frac{dB}{dt}dt = v \int_0^{B_p} HdB \tag{4.5}$$

The energy per unit volume to be supplied in order to reach the induction value B_p is then given by the area delimited by the BH curve and the ordinate (y) axis. If the integration in Eq. 4.5 is carried out over a full cycle, the energy dissipated per unit volume is obtained as the area of the hysteresis loop

$$W = \oint HdB = \oint \mu_o HdH + \oint \mu_o HdM \tag{4.6}$$

where Magnetization M is defined as the magnetic dipole moment per unit volume.

$$\mathbf{M} = \lim_{\Delta v \to 0} \frac{1}{\Delta v} \sum_{i=0}^{n\Delta v} m_i \tag{4.7}$$

The integral HdB over one magnetization cycle gives the energy per unit volume transformed into heat. This is termed as **loss per cycle**, whereas the term power loss is used to denote the **loss per unit time** $P = Wf$. The purely reactive term $\mu_o HdH$, integrating the energy exchanged between the supply system and the magnetic field averages out to zero. So W is decided by the second term in the equation. In general the loss per cycle W is a non-linear function of frequency, peak induction B and the harmonic content of the induction waveform. The loss per cycle increases non-linearly with f-it can be decomposed into three different components– the frequency independent term W_h(hysteresis loss), the classical loss $W_c \propto f$, and the excess loss $W_e \propto f^{1/2}$. The loss decomposition can be physically justified by the **statistical theory of losses** [11].

4.2.1 Eddy current loss

This can be directly calculated from Maxwell's equations, assuming a perfectly homogeneous conducting material. The classical loss is present under all circumstances, to which the other contributions are added when structural disorder and magnetic domains

are present [11].

$$P_c = \frac{\pi^2 \sigma d^2}{6} B_p^2 f^2 \tag{4.8}$$

where d is the lamination thickness, σ is electrical conductivity, f is magnetization frequency, B_p is peak induction (sinusoidal). For a non-sinusoidal induction where B is expressed as $B(t) = \sum_n B_n \sin(2\pi f + \phi_n)$ where ϕ_n is the phase shift with respect to the fundamental harmonic, the classical loss becomes,

$$P_c = \frac{\pi^2 \sigma d^2 f^2}{6} \sum_n n^2 B_n^2 \tag{4.9}$$

The minimum for this loss occurs for a triangular induction waveform, with dB/dt constant in each magnetization half-cycle, then the coefficient $\pi^2/6$ becomes $4/3$. Classical losses is *independent* of the magnetic property of the material and all materials behave in the same way if the geometry and electric properties are kept constant. This simplification comes since dB/dt is assumed to be uniform throughout the thickness of the material. But this condition only holds at low frequencies as the magnetic field produced by eddy currents inhibit the applied field and tend to shield the interior of the core at higher frequencies.

4.2.2   Excess loss

Excess losses occur since the eddy currents are concentrated in the vicinity of the moving domain walls, causing losses higher, or *excess* than the classical terms. In case of a lamination of thickness d with longitudinal magnetic domains of random width [11], the Maxwell's equation can be solved to find

$$P_e = \left(\frac{48}{\pi^3} \sum_{\text{odd}\,n} \frac{1}{n^3} \right) \frac{2L}{d} P_c \cong 1.63 \frac{2L}{d} P_c \tag{4.10}$$

where $2L$ is the average domain width, n is the harmonic order and P_c is the classical loss. In case of highly optimized grain-oriented Si steel, $2L/d \cong 1$. In the general case, the excess loss can be approximately computed using this expression.

$$P_e = k_e \sqrt{\sigma} (B_p f)^{3/2} \tag{4.11}$$

where the parameter k_e depends on the microscopic structure of the material.

4.2.3 Hysteresis loss

Every atom has a small magnetic moment, and in Ferromagnetic materials the inter-atomic forces tend to align these moments in the same direction over regions containing a large number of atoms. These regions are called domains; the domain moments, however vary in direction from domain to domain. When such materials are subjected to external magnetic field, the domains which have moments in the direction of the field grow at the expense of other domains. This is the process of magnetization of the material in the direction of the applied external field.

At the microscopic level, the magnetization process proceeds through sudden jumps, called *Barkhausen jumps* of the magnetic domain walls. Very intense and brief current pulses of the order of 10^{-9}s [11] are generated close to the domain wall segments. These spatially localized eddy currents induced by the domain-wall jump dissipate a finite amount of energy through the Joule effect. The sum of all the domain-wall jumps will account for the observed hysteresis loss. With a higher rate of change dH/dt the time interval will decrease, so number of Barkhausen jumps and the amount of energy dissipation per unit time is proportional to the magnetization frequency. The expression for the hysteresis loss in one magnetization cycle is

$$P_h = 4k_h B_p^\alpha f \tag{4.12}$$

The parameters k_h and α depend on the structural properties of the material at the microscopic level. No general rule exists for determining their values in different materials.

4.2.4 Total loss

A detailed evaluation of the core loss requires extensive knowledge of the microstructure of the material along with the numerical implementation of mathematical models of hysteresis. The complexity of the problem coupled with the fact that the magnetic materials chosen for filter design have very low core loss compared to copper winding loss suggests that the core loss graphs published by vendors of magnetic material are sufficient to estimate the core losses. This has been confirmed by experimental observation under steady state operating conditions where temperature rise in the core was very less compared to the winding.

4.3   Copper loss

A voltage is induced in a conductor if it is subjected to time varying magnetic flux, according to Faraday's law. The inducing field may be due to its own current, which must be time varying or due to time varying current carried by another adjacent conductor. In the first case the phenomenon is called **Skin effect** and the second case is called **Proximity effect**. The induced voltage gives rise to currents distributed throughout the body of the conductor. These currents are called **Eddy currents** and they have three major effects.

- Heat because of ohmic losses

- Opposite magnetic reaction field

- Additional forces due to interaction of induced and inducing fields

The two eddy current effects discussed above will occur simultaneously in a conductor that carries an alternating current and is positioned in an external alternating field, which is the exact situation of a conductor which is part of the winding of an inductor or transformer. The effect of these eddy currents can be calculated by formulating electromagnetic equations, either in differential form or integral form. The differential form of the Maxwell's equations describe the electromagnetic field vectors- **E**, **H**, **J**, **B** at any point in space. These differential equations can be solved by analytical or numerical methods.

Analytical solutions are limited to linear equations, with specific geometries and simple excitation. Analytical methods normally use field equations since boundary conditions are expressed in terms of magnetic and electric fields.The solutions are limited to mostly one or two dimensional problems. One dimensional problems have closed form solutions which give good insight into the problem. Numerical methods can handle complicated geometries and both linear and non-linear equations. They however, require large computation times. In most cases, numerical methods use magnetic vector potential in conjunction with electric scalar potential. The integral form of these electromagnetic equations are particularly suited for numerical methods.

4.4   Foil conductors

Foil conductors are well suited for applications which have both a high switching frequency and high rated current. By proper selection of thickness of foil, it is possible to

significantly reduce skin effect losses. Most high power inductor designs make use of foil winding to minimize high frequency copper losses. The subsequent analysis of power loss in foil winding is referred from [16], [17], [20] and [27].

4.4.1 Assumptions

1. The magnetic field distribution is solved for a winding portion. A winding portion is a part of the winding which extends in either direction along the axis of the winding height from a position of zero field intensity to the first positive or negative peak of the magnetic field intensity.

2. The conductor foils are assumed to span the entire breadth of the core window.

3. Magnetic field in the winding space is assumed to be parallel to center leg of the inductor. This is strictly accurate only in case of infinite solenoid windings. If the foil winding is assumed to span the entire window height, then this assumption is valid.

4. The winding layer is modelled as a finite portion of an infinite current sheet. This gives the solution of field equation in rectangular coordinates.

5. The curvature of the foil conductors is neglected while calculating the radial field distribution across the winding layer.

6. Almost all of the magnetic field intensity of any winding layer is assumed to exist inside the region bounded by that layer and there is negligible magnetic field outside this region.

4.4.2 One dimensional H field

Fig. 4.3 shows the typical cross section of inductor with foil windings. Ampere's law can be used to find the magnetic field intensity between conductor layers.

$$H_o = \frac{I_{pk}}{b_{win}} \tag{4.13}$$

where I_{pk} is the peak current flowing in each layer, and b_{win} is the width of the window. The field equations of **H** and **J** can be solved in rectangular coordinates. Hence the
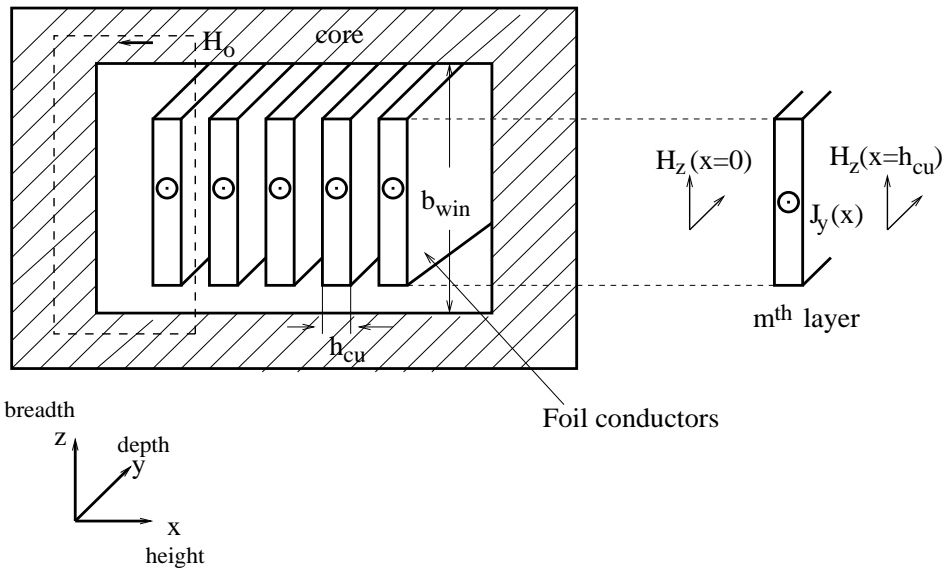
Figure 4.3: Inductor cross section with magnetic flux intensity and current density for m^{th} layer.

magnetic field intensity phasor can be represented as

$$\mathbf{H}(x,y,z) = H_x(x,y,z)\hat{a}_x + H_y(x,y,z)\hat{a}_y + H_z(x,y,z)\hat{a}_z \tag{4.14}$$

To simplify the analysis we will assume that the spatial magnetic field intensity phasor is a function of x only and directed in z direction. Then the three-dimensional diffusion equation becomes a one-dimensional equation.

$$\mathbf{H}(x,y,z) = H_z(x)\hat{a}_z \tag{4.15}$$

From the wave equation for time-harmonic fields we get,

$$\triangledown^2\mathbf{H} - \gamma^2\mathbf{H} = \frac{\partial^2 H_z(x)}{\partial x^2} - \gamma^2 H_z(x) = 0 \tag{4.16}$$

where $\gamma^2 \simeq j\omega\mu\sigma$. Here, ω if frequency of the applied current in rad/s, μ is the absolute permeability of the foil material (copper, μ same as air) and σ is the conductivity of the foil winding. The general solution has the form

$$H_z(x) = Ae^{\gamma x} + Be^{-\gamma x} \tag{4.17}$$

where A and B are determined by applying the boundary conditions of magnetic field intensity at the surface of the current sheet, $H_z(x=0)$ and $H_z(x=h_{cu})$.

Expressing in hyperbolic form using the boundary conditions,

$$H_z(x) = \frac{1}{\sinh \gamma h_{cu}} [H_z(x = h_{cu}) \sinh \gamma x + H_z(x = 0) \sinh \gamma(h_{cu} - x)] \qquad (4.18)$$

To prevent zeros from appearing in the denominator of some equations that are derived, the variable x is changed to χ, such that the new variable does not become zero for any boundary condition.

$$\chi = \begin{cases} x & \text{if} |H_z(x = h_{cu})| \geq |H_z(x = 0)| \\ h_{cu} - x & \text{if} |H_z(x = h_{cu})| < |H_z(x = 0)| \end{cases} \qquad (4.19)$$

This definition causes $\chi = 0$ to be always at the surface having the smaller of the two boundary magnetic fields, and $\chi = h_{cu}$ to be always at the surface with the larger field. If we define the boundary condition ratio as

$$p = \frac{H_z(\chi = 0)}{H_z(\chi = h_{cu})} \qquad (4.20)$$

From Fig. 4.3, the boundary condition ratio for the mth layer will be

$$p = \frac{(m-1)H_o}{mH_o} \qquad (4.21)$$

Substituting Eq. (4.20) in Eq. (4.18)

$$H_z(\chi) = \frac{H_z(\chi = h_{cu})}{\sinh \gamma h_{cu}} [\sinh \gamma \chi + p \cdot \sinh \gamma(h_{cu} - \chi)] \qquad (4.22)$$

4.4.3 Power dissipation

The current density phasor $J_y(x)$ in terms of the magnetic field intensity phasor $H_z(x)$ is derived from Maxwell's equations.

$$\bigtriangledown \times \mathbf{H} = \sigma \mathbf{E} + j\omega \varepsilon \mathbf{E} \qquad (4.23)$$

where σ is the conductivity of the material carrying the alternating current of frequency ω rad/sec, ε is the permittivity of the conducting material, which is almost same as free space. Since for a good conductor $\sigma \gg \omega \varepsilon$,

$$\bigtriangledown \times \mathbf{H} \approx \sigma \mathbf{E} = \mathbf{J} \qquad (4.24)$$

Since **J** is in *y* direction and **H** is in *x* direction and both are functions of *x*, taking the curl,

$$J_y(x) = -\frac{\partial H_z(x)}{\partial x} \tag{4.25}$$

$$J_y(\chi) = \frac{-\gamma H_z(\chi = h_{cu})}{\sinh \gamma h_{cu}} [\cosh \gamma\chi - p \cdot \cosh \gamma(h_{cu} - \chi)] \tag{4.26}$$

The power dissipated per unit volume $p_d(t)$ is

$$p_d(t) = \frac{|\mathbf{J}|^2}{\sigma} \tag{4.27}$$

The time-averaged power dissipated can be calculated from the above expression by integration. To simplify the calculation, the winding layer is assumed to be flat instead of cylindrical, extending a distance equal to length of turn in the *y* direction.
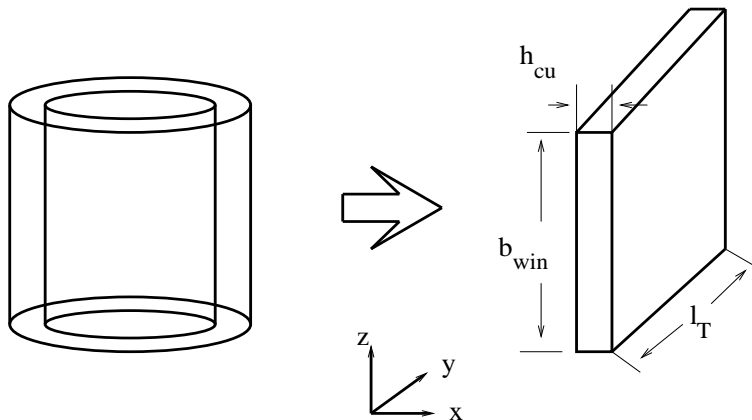
Figure 4.4: Current sheet approximation to find total power loss

$$P_d = \frac{1}{T} \int_0^T \int_0^{b_{win}} \int_0^{l_T} \int_0^{h_{cu}} p_d(t) \, d\chi \, dy \, dz \, dt \tag{4.28}$$

where *T* is the period of the waveform. For sinusoidal waveforms, we can simplify the above expression,

$$P_d = \frac{1}{2} \int_0^{b_{win}} \int_0^{l_T} \int_0^{h_{cu}} p_d(t) \, d\chi \, dy \, dz \tag{4.29}$$

l_T is the length of mean turn of coil. Since **J** does not vary with y or z, the integration with respect to those variables becomes simple multiplication.

$$P_d = \frac{b_{win}\, l_T}{2} \int_0^{h_{cu}} p_d(t)\, d\chi \tag{4.30}$$

The power dissipated per square meter in the $y-z$ plane is given by

$$[Q_J] = \frac{P_d}{b_{win}\, l_T} = \frac{1}{\sigma} \int_0^{h} J_y(\chi) \cdot J_y^*(\chi)\, d\chi \tag{4.31}$$

where $J_y^*(\chi)$ is the complex conjugate of $J_y(\chi)$ and $[Q_J]$ represents time-average. The resulting expression is

$$[Q_J] = \frac{|H_z(\chi = h_{cu})|^2}{\sigma\delta} \left[(1+p^2)\frac{\sinh 2\Delta + \sin 2\Delta}{\cosh 2\Delta - \cos 2\Delta} - 4p\frac{\sinh \Delta\, \cos \Delta + \cosh \Delta\, \sin \Delta}{\cosh 2\Delta - \cos 2\Delta} \right] \tag{4.32}$$

where skin depth $\delta = \sqrt{2/(\omega\sigma\mu)}$, $\Delta = h_{cu}/\delta$ is defined as the height of the winding layer h_{cu} normalized to skin depth δ, p is the boundary condition ratio, and $|H_z(\chi = h_{cu})|^2$ is the square of the rms value of the larger magnetic field intensity at the two surfaces of the current sheet.

Using the two following hyperbolic identities [20],

$$\frac{\sinh 2a + \sin 2a}{\cosh 2a - \cos 2a} = \frac{1}{2}\left[\frac{\sinh a + \sin a}{\cosh a - \cos a} + \frac{\sinh a - \sin a}{\cosh a + \cos a} \right] \tag{4.33}$$

and

$$\frac{\sinh 2a + \sin 2a}{\cosh 2a - \cos 2a} = \frac{\sinh a - \sin a}{\cosh a + \cos a} + 2\frac{\sinh a\, \cos a + \cosh a\, \sin a}{\cosh 2a - \cos 2a} \tag{4.34}$$

we can simplify Eq. (4.32) as

$$[Q_J] = \frac{|H_z(\chi = h_{cu})|^2}{\sigma\delta} \left[\frac{(1-p)^2}{2}\frac{\sinh \Delta + \sin \Delta}{\cosh \Delta - \cos \Delta} + \frac{(1+p)^2}{2}\frac{\sinh \Delta - \sin \Delta}{\cosh \Delta + \cos \Delta} \right] \tag{4.35}$$

Substituting for p from Eq. (4.21)

$$[Q_J] = \frac{|H_z(\chi = h_{cu})|^2}{\sigma\delta}\frac{1}{2m^2} \left[\frac{\sinh \Delta + \sin \Delta}{\cosh \Delta - \cos \Delta} + (2m-1)^2\frac{\sinh \Delta - \sin \Delta}{\cosh \Delta + \cos \Delta} \right] \tag{4.36}$$

Replacing $H_z(\chi = h_{cu})$ using Eq. (4.21) and Eq. (4.13)

$$[Q_J] = \frac{I_{pk}^2}{b_{win}^2} \frac{1}{2\sigma\delta} \left[\frac{\sinh\Delta + \sin\Delta}{\cosh\Delta - \cos\Delta} + (2m-1)^2 \frac{\sinh\Delta - \sin\Delta}{\cosh\Delta + \cos\Delta} \right] \qquad (4.37)$$

To find the average power dissipated per meter (in the y direction),

$$P_{av} = [Q_J] \cdot b_{win} \qquad (4.38)$$

4.4.4 AC resistance

In electrical terms, the average power dissipated is also given in terms of resistance as

$$P_{av} = R_{ac} I_{rms}^2 \qquad (4.39)$$

where I_{rms} is the rms current in each foil conductor. P_{av} is also expressed as,

$$P_{av} = R_{ac} \frac{R_{dc}}{R_{dc}} I_{rms}^2 \qquad (4.40)$$

where R_{dc} is the dc resistance of the foil conductor per unit length

$$R_{dc} = \frac{1}{\sigma\, b_{win} h_{cu}} \qquad (4.41)$$

Hence we get

$$P_{av} = \frac{R_{ac}}{R_{dc}} I_{rms}^2 \frac{1}{\sigma\, b_{win} h_{cu}} \qquad (4.42)$$

Equating Eq. (4.38) and Eq. (4.42),

$$R_{ac} = R_{dc} \frac{\Delta}{2} \left[\frac{\sinh\Delta + \sin\Delta}{\cosh\Delta - \cos\Delta} + (2m-1)^2 \frac{\sinh\Delta - \sin\Delta}{\cosh\Delta + \cos\Delta} \right] \qquad (4.43)$$

This is the Dowell's formula to calculate AC resistance of the mth layer of a foil winding having a dc resistance of R_{dc} per unit length.

4.5 Round conductors

Round conductors are most widely used to construct inductors because of their low cost and ease of use. But R_{ac} in case round conductors is higher than foil conductors for the same frequency, and increases much faster with number of turns and layers. The following analysis of power loss in round conductors is referred from [1], [3], [15] and [18].

4.5.1 Orthogonality

As discussed before, eddy current effects can be divided into skin effect and proximity effect losses. It is possible to separately calculate the losses due to skin effect and proximity effect since the two currents are independent of each other. The conditions in which this orthogonality is valid is detailed in [20] and [22]. A sufficient (but not necessary) condition is that the conductor must have an axis of symmetry and the current distribution due to skin effect current has odd symmetry about this axis and current distribution due to proximity effect current has even symmetry about this axis (or vice verse), as shown in Fig. 4.5 [22].
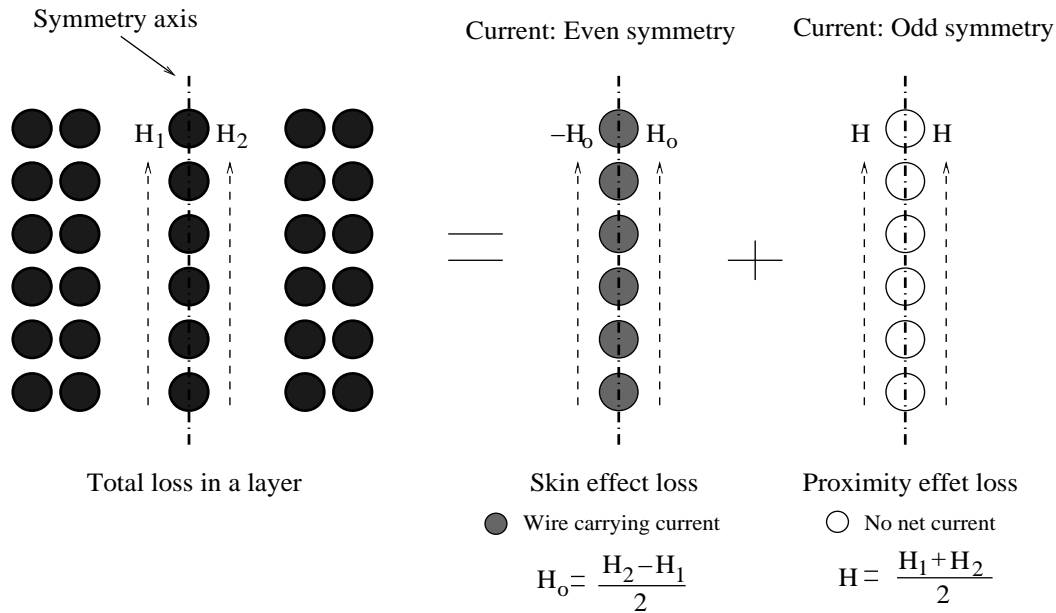
Figure 4.5: Orthogonality in Eddy current losses [22]

Let the current density vector be a function of x and z axis and directed along y axis

(Fig. 4.4),

$$\mathbf{J} = J_y(x,z) \tag{4.44}$$

The average power dissipated per unit length for sinusoidal waveforms is already mentioned as

$$P_d = \frac{1}{2\sigma} \int_A J\,J^* dA \tag{4.45}$$

where A is the cross section area of the conductor. Separating the skin effect current and proximity effect currents, J_s and J_p respectively,

$$P_d = \frac{1}{2\sigma} \int_A (J_s + J_p)(J_s^* + J_p^*)\,dA \tag{4.46}$$

Since J_s has even symmetry and J_p has odd symmetry,

$$P_d = \frac{1}{2\sigma} \int_A (J_s J_s^* + J_p J_p^*)\,dA \tag{4.47}$$

$$P_d = P_{ds} + P_{dp} \tag{4.48}$$

Hence the skin effect losses and proximity effect losses can be calculated separately. The sum will give the total eddy current losses of the conductor.

4.5.2 Skin effect loss
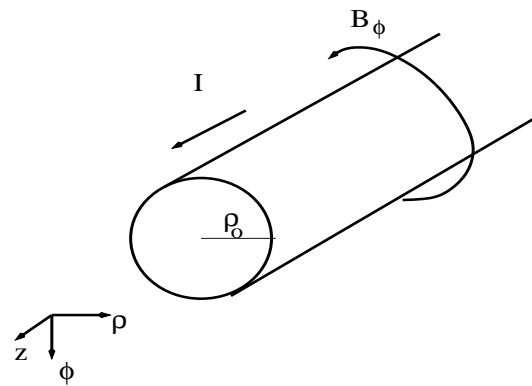
Figure 4.6: Round conductor in cylindrical coordinates

The Bessel function solution can be used to find the current distribution in round cylindrical conductors subjected to an alternating electric field **E**. All the field vectors are expressed in cylindrical coordinates (ρ, ϕ, z). Consider a round conductor of radius ρ_o

carrying a time varying current of rms value I_{rms} at a frequency ω rad/sec. For conductors, $\gamma^2 \simeq j\omega\mu\sigma$. Maxwell's equations are,

$$\nabla \times \mathbf{H} = \mathbf{J} = \sigma\mathbf{E} \tag{4.49}$$

$$\nabla \times \mathbf{E} = -j\omega\mu\mathbf{H} \tag{4.50}$$

So

$$-\frac{1}{j\sigma\omega\mu}\nabla \times \mathbf{J} = \mathbf{H} \tag{4.51}$$

Substituting Eq (4.51) in Eq (4.49)

$$-\frac{1}{j\sigma\mu\omega}\nabla \times (\nabla \times \mathbf{J}) = \mathbf{J} \tag{4.52}$$

$$\nabla^2\mathbf{J} = j\sigma\mu\omega\mathbf{J} \tag{4.53}$$

$$\nabla^2\mathbf{J} = \gamma^2\mathbf{J} \tag{4.54}$$

where

$$\gamma^2 = j\omega\mu\sigma \tag{4.55}$$

If the current density is z directed with no variation along z and ϕ, then we can expand Eq. (4.54)

$$\frac{d^2J_z}{d\rho^2} + \frac{1}{\rho}\frac{dJ_z}{d\rho} - \gamma^2 J_z = 0 \tag{4.56}$$

Multiplying throughout by ρ^2

$$\rho^2\frac{d^2J_z}{d\rho^2} + \rho\frac{dJ_z}{d\rho} - \gamma^2\rho^2 J_z = 0 \tag{4.57}$$

We can simplify the above equation as

$$\gamma^2 = j\sigma\omega\mu = jp \tag{4.58}$$

$$\gamma = \sqrt{j}\sqrt{p} \tag{4.59}$$

$$\rho^2\frac{d^2J_z}{d\rho^2} + \rho\frac{dJ_z}{d\rho} - (\sqrt{jp}\rho)^2 J_z = 0 \tag{4.60}$$

The two independent solutions are [3]

$$J_z = AI_0(\sqrt{jp}\,\rho) + BK_0(\sqrt{jp}\,\rho) \tag{4.61}$$

where $I_0(x)$ is the modified Bessel function of the first kind of order zero and $K_0(x)$ is the modified Bessel function of the second kind of order zero[1]. Since $\rho = 0$ is a solution of Eq. (4.61) but $K_0(0) = \infty$, the constant B must be zero to satisfy the solution at $\rho = 0$. So the actual solution is

$$J_z = AI_0(\sqrt{jp}\,\rho) \tag{4.62}$$

The constant A is evaluated in terms of current density at the surface($\rho = \rho_0$), assuming current density at surface to be $\sigma E_0 = J_0$. Then the above equation becomes

$$J_z = J_0 \frac{I_0(\sqrt{jp}\,\rho)}{I_0(\sqrt{jp}\,\rho_0)} \tag{4.63}$$

Or writing in terms of skin depth $\delta = \sqrt{2}/\sqrt{p}$

$$J_z = J_0 \frac{I_0(\sqrt{j}\sqrt{2}\rho/\delta)}{I_0(\sqrt{j}\sqrt{2}\rho_0/\delta)} \tag{4.64}$$

Separating the complex Bessel function into real and imaginary parts using the definition that

$$\mathrm{ber}(x) = \mathrm{Re}[I_0(x\sqrt{j})] \tag{4.65}$$

$$\mathrm{bei}(x) = \mathrm{Im}[I_0(x\sqrt{j})] \tag{4.66}$$

$$I_0(x\sqrt{j}) = \mathrm{ber}_0(x) + j\mathrm{bei}_0(x) \tag{4.67}$$

Using the above definition, Eq (4.64) becomes

$$J_z = J_0 \frac{\mathrm{ber}_0(\sqrt{2}\,\rho/\delta) + j\mathrm{bei}_0(\sqrt{2}\,\rho/\delta)}{\mathrm{ber}_0(\sqrt{2}\,\rho_0/\delta) + j\mathrm{bei}_0(\sqrt{2}\,\rho_0/\delta)} \tag{4.68}$$

Substituting $\Delta = \rho/\delta$ and $\Delta_0 = \rho_0/\delta$, we can express the current density in a solid wire of radius ρ_0 in terms of instantaneous quantities,

$$\mathbf{J} = \mathrm{Re}[\mathbf{J}e^{j\omega t}] = \mathrm{Re}[J_z e^{j\omega t}] \tag{4.69}$$

---

[1]Bessel functions are explained in some detail in Appendix A.6

$$\mathbf{J} = |J_z|\cos(\omega t + \angle J_z) \tag{4.70}$$

$$\mathbf{J} = \left[\frac{\mathrm{ber}_0^2(\sqrt{2}\,\Delta) + \mathrm{bei}_0^2(\sqrt{2}\,\Delta)}{\mathrm{ber}_0^2(\sqrt{2}\,\Delta_0) + \mathrm{bei}_0^2(\sqrt{2}\,\Delta_0)} \right]^{\frac{1}{2}} J_0 \cos(\omega t + \theta) \tag{4.71}$$

where θ is

$$\theta = \tan^{-1} \frac{\mathrm{ber}_0(\sqrt{2}\,\Delta_0)\mathrm{bei}_0(\sqrt{2}\,\Delta) - \mathrm{ber}_0(\sqrt{2}\,\Delta)\mathrm{bei}_0(\sqrt{2}\,\Delta_0)}{\mathrm{ber}_0(\sqrt{2}\,\Delta_0)\mathrm{ber}_0(\sqrt{2}\,\Delta) + \mathrm{bei}_0(\sqrt{2}\,\Delta)\mathrm{bei}_0(\sqrt{2}\,\Delta_0)} \tag{4.72}$$

Power dissipation

From Ampere's law, the relation between current flowing in a round conductor I and magnetic flux density at the surface of the conductor $\mathbf{B}$ is given by

$$\mathbf{B} = \frac{\mu I}{2\pi\rho_0}\hat{a}_\phi \tag{4.73}$$

We can find the relation between current I and current density J_z (Eq 4.63) using Maxwell's equations.

$$\nabla \times \mathbf{E} = -j\omega\mathbf{B} \tag{4.74}$$

$$\frac{1}{\sigma}\nabla \times \mathbf{J} = -j\omega\mathbf{B} \tag{4.75}$$

Using the definition of J_z from Eq (4.63), we can evaluate Eq (4.75) at $\rho = \rho_0$

$$j\omega\mathbf{B}_{\rho_0} = \frac{1}{\sigma}\left(\frac{\partial J_z}{\partial\rho}\right)_{\rho_0} \tag{4.76}$$

$$j\omega\mathbf{B}_{\rho_0} = \frac{1}{\sigma}J_0\sqrt{jp}\frac{I_0'(\sqrt{jp}\,\rho_0)}{I_0(\sqrt{jp}\rho_0)} \tag{4.77}$$

where $I_0'(j\rho)$ represents the differential of $I_0(j\rho)$. Substituting the above equation in Eq. (4.73)

$$I = \frac{2\pi\rho_0}{\mu}\frac{\sqrt{jp}}{j\omega\sigma}J_0\frac{I_0'(\gamma p_0)}{I_0(\gamma p_0)} \tag{4.78}$$

Since

$$p = \omega\mu\sigma \tag{4.79}$$

$$I = \frac{2\pi\rho_0}{\sqrt{pj}}J_0\frac{I_0'(\sqrt{jp}\,\rho_0)}{I_0(\sqrt{jp}\,\rho_0)}$$ (4.80)

The average power dissipated per unit length of the wire is

$$dP_{av} = \frac{1}{2}\frac{|J_z|^2}{\sigma}2\pi\rho\,d\rho = \frac{1}{2}\frac{J_zJ_z^*}{\sigma}2\pi\rho\,d\rho$$ (4.81)

where J_z^* is the conjugate of J_z. Conjugate of

$$\left(\sqrt{j}\right)^* = \left(\frac{1+j}{\sqrt{2}}\right)^* = \frac{1-j}{\sqrt{2}} = -j\sqrt{j}$$ (4.82)

and

$$I_0^*(\sqrt{jp}\,\rho) = I_0(\sqrt{-jp}\,\rho) = I_0(-j\sqrt{jp}\,\rho)$$ (4.83)

So the conjugate of current density J_z^* becomes

$$J_z^* = J_0\frac{I_0(-j\sqrt{jp}\,\rho)}{I_0(-j\sqrt{jp}\,\rho_0)}$$ (4.84)

$$P_{av} = \int_0^{\rho_0} dP_{av}$$ (4.85)

$$P_{av} = \frac{\pi J_0^2}{\sigma I_0(\sqrt{jp}\,\rho_0)I_0(-j\sqrt{jp}\,\rho_0)}\int_0^{\rho_0} I_0(\sqrt{jp}\,\rho)I_0(-j\sqrt{jp}\,\rho)\rho\,d\rho$$ (4.86)

The result written in terms of ber and bei functions is

$$P_{av} = \frac{J_0^2\pi\rho_0}{\sqrt{p}\sigma}\frac{\mathrm{ber}_0(\sqrt{p}\rho_0)\mathrm{bei}_0'(\sqrt{p}\rho_0) - \mathrm{ber}_0'(\sqrt{p}\rho_0)\mathrm{bei}_0(\sqrt{p}\rho_0)}{\mathrm{ber}_0^2(\sqrt{p}\rho_0) + \mathrm{bei}_0^2(\sqrt{p}\rho_0)}$$ (4.87)

From Eq (4.78) we can get the rms current I_{rms}

$$I_{rms}^2 = \frac{2\pi^2\rho_0^2}{p}J_0^2\frac{I_0'(\sqrt{jp}\,\rho_0)I_0'^*(\sqrt{jp}\,\rho_0)}{I_0(\sqrt{jp}\,\rho_0)I_0^*(\sqrt{jp}\,\rho_0)}$$ (4.88)

where $I_0'^*(x)$ is the conjugate of $I_0'(x)$, $I_0^*(x)$ is conjugate of $I_0(x)$ and $p = \omega\mu\sigma$.

$$I_{rms}^2 = \frac{2\pi^2\rho_0^2}{p}J_0^2\frac{(\mathrm{ber}_0'(\sqrt{p}\rho_0))^2 + (\mathrm{bei}_0'(\sqrt{p}\rho_0))^2}{\mathrm{ber}_0^2(\sqrt{p}\rho_0) + \mathrm{bei}_0^2(\sqrt{p}\rho_0)}$$ (4.89)

AC resistance

If R_{dc} is the dc resistance per unit length, i.e

$$R_{dc} = \frac{1}{\sigma \pi \rho_0^2} \tag{4.90}$$

then the ac resistance R_{skin} can be expressed in terms of dc resistance as

$$\frac{R_{skin}}{R_{dc}} R_{dc} \times I_{rms}^2 = P_{av} \tag{4.91}$$

$$R_{skin} = \frac{P_{av}}{I_{rms}^2 R_{dc}} R_{dc} \tag{4.92}$$

$$R_{skin} = \frac{P_{av}}{I_{rms}^2} \pi \rho_0^2 \sigma \, R_{dc} \tag{4.93}$$

From Eqs. (4.93), (4.89) and (4.87) the AC resistance representing skin effect can be calculated.

$$R_{skin} = R_{dc} \frac{\rho_0 \sqrt{p}}{2} \frac{\text{ber}(\sqrt{p}\rho_0)\text{bei}'(\sqrt{p}\rho_0) - \text{ber}'(\sqrt{p}\rho_0)\text{bei}(\sqrt{p}\rho_0)}{(\text{ber}'(\sqrt{p}\rho_0))^2 + (\text{bei}'(\sqrt{p}\rho_0))^2} \tag{4.94}$$

where ρ_0 is the radius of the cylindrical conductor.

4.5.3 Proximity effect loss

The current distribution in a round cylindrical conductor subjected to an external homogeneous magnetic field can be found from the magnetic vector potential. The magnetic vector potential in terms of current density $\mathbf{J}$ is[2]

$$\bigtriangledown^2 \mathbf{A} - \varepsilon \mu \omega^2 \mathbf{A} = -\mu \mathbf{J} \tag{4.95}$$

The net current density $\mathbf{J}$ includes conduction current density and displacement current density. The term $\omega^2 \varepsilon \mathbf{A}$ refers to the displacement current, while $\bigtriangledown^2 \mathbf{A}/\mu$ refers to the conduction current. We can ignore the displacement current since it is very insignificant in conductors. So Eq. (4.95) becomes

$$-\frac{\bigtriangledown^2 \mathbf{A}}{\mu} = \mathbf{J} \tag{4.96}$$

---

[2]This equation is derived in Appendix A.7

The conduction current can be expressed in terms of electric field

$$\mathbf{J} = \sigma \mathbf{E} \tag{4.97}$$

where $\mathbf{E}$, in terms of potentials $\mathbf{A}$ and Φ is

$$\mathbf{E} = -\nabla \Phi - j\omega \mathbf{A} \tag{4.98}$$

From Eq. (4.96), (4.97) and (4.98)

$$\frac{\nabla^2 \mathbf{A}}{\mu} = \sigma \nabla \Phi + j\omega \sigma \mathbf{A} \tag{4.99}$$

In the above case of the conductor subjected to an external magnetic field H_0, there is no applied electric field, hence no source electric potential.

$$\sigma \nabla \Phi = 0 \tag{4.100}$$

So the magnetic vector potential equation reduces to

$$\frac{\nabla^2 \mathbf{A}}{\mu} = j\omega \sigma \mathbf{A} \tag{4.101}$$

In cylindrical coordinates,

$$\frac{\partial A_z}{\partial \rho^2} + \frac{1}{\rho}\frac{\partial A_z}{\partial \rho} + \frac{1}{\rho^2}\frac{\partial^2 A_z}{\partial \phi^2} = \gamma^2 A_z \tag{4.102}$$

After simplification [7], the vector potential inside the cylinder is

$$A_z = \frac{4\mu_0 H_0 \delta}{j^{3/2}\sqrt{2}} \frac{J_1(j^{3/2}\sqrt{2}\Delta)}{F(j^{3/2}\sqrt{2}\Delta_0)} \sin\phi \tag{4.103}$$

where $J_1(x)$ is the Bessel function of the first kind of order one, and $F(x)$ is the regular Coulomb wave function. The current density in terms of magnetic vector potential is

$$J_z = -j\omega \sigma A_z \tag{4.104}$$

$$J_z = \frac{4\mu_0 H_0 j^{3/2}\sqrt{2}}{\delta} \frac{J_1(j^{3/2}\sqrt{2}\Delta)}{F(j^{3/2}\sqrt{2}\Delta_0)} \sin\phi \tag{4.105}$$

The eddy current losses per unit length of the cylinder is

$$P_p = \frac{1}{2\sigma} \int_0^{\rho_0} \int_0^{2\pi} |J_z|^2 \rho \, d\rho \, d\phi \tag{4.106}$$

Substituting Eq. (4.105) in Eq. (4.106)

$$P_p = -\frac{2\pi\gamma}{\sigma} \frac{\mathrm{ber}_2(\sqrt{p}\rho_0)\mathrm{ber}'(\sqrt{p}\rho_0) + \mathrm{bei}_2(\sqrt{p}\rho_0)\mathrm{bei}'(\sqrt{p}\rho_0)}{(\mathrm{ber}(\sqrt{p}\rho_0))^2 + (\mathrm{bei}(\sqrt{p}\rho_0))^2} H_0^2 \tag{4.107}$$

As in the case of skin effect resistance, the proximity effect ac resistance of the mth layer of a multilayer round wire winding can be derived.

$$R_{pr(m)} = R_{dc(m)} \frac{\rho_0\sqrt{p}}{2} \left[-2\pi(2m-1)^2 \frac{\mathrm{ber}_2(\sqrt{p}\rho_0)\mathrm{ber}'(\sqrt{p}\rho_0) + \mathrm{bei}_2(\sqrt{p}\rho_0)\mathrm{bei}'(\sqrt{p}\rho_0)}{(\mathrm{ber}(\sqrt{p}\rho_0))^2 + (\mathrm{bei}(\sqrt{p}\rho_0))^2} \right] \tag{4.108}$$

where $R_{dc(m)}$ is the dc resistance of the mth layer.

AC resistance

The final analytical expression for the ac resistance of the mth layer of a multilayer round wire winding is

$$\begin{aligned} R_{ac(m)} = R_{dc(m)} \frac{\rho_0\sqrt{p}}{2} \Bigg[&\frac{\mathrm{ber}(\sqrt{p}\rho_0)\mathrm{bei}'(\sqrt{p}\rho_0) - \mathrm{ber}'(\sqrt{p}\rho_0)\mathrm{bei}(\sqrt{p}\rho_0)}{(\mathrm{ber}'(\sqrt{p}\rho_0))^2 + (\mathrm{bei}'(\sqrt{p}\rho_0))^2} \\ &-2\pi(2m-1)^2 \frac{\mathrm{ber}_2(\sqrt{p}\rho_0)\mathrm{ber}'(\sqrt{p}\rho_0) + \mathrm{bei}_2(\sqrt{p}\rho_0)\mathrm{bei}'(\sqrt{p}\rho_0)}{(\mathrm{ber}(\sqrt{p}\rho_0))^2 + (\mathrm{bei}(\sqrt{p}\rho_0))^2} \Bigg] \end{aligned} \tag{4.109}$$

The R_{ac}/R_{dc} ratio is calculated for a Ferrite core inductor with round wire winding and an Amorphous core inductor with foil winding. The relevant parameters used for calculation is detailed in Table 4.1. Figures 4.7–4.8 illustrate the R_{ac}/R_{dc} curves for foil and round wire winding. We can conclude from both the figures that the proximity effect loss component is the dominant loss at frequencies close to the switching frequency. Another observation is that the proximity effect loss becomes dominant at much lower frequencies in round wire winding compared to foil winding.

	Round wire	Foil
Dia / Thickness (mm)	2.643	0.127
Skin depth 50Hz (mm)	9.348	9.348
Skin depth 10kHz (mm)	0.661	0.661
Porosity factor	0.854	*
Turns	120	137
Layers	4	137

Table 4.1: Parameter list for R_{ac}/R_{dc} calculation
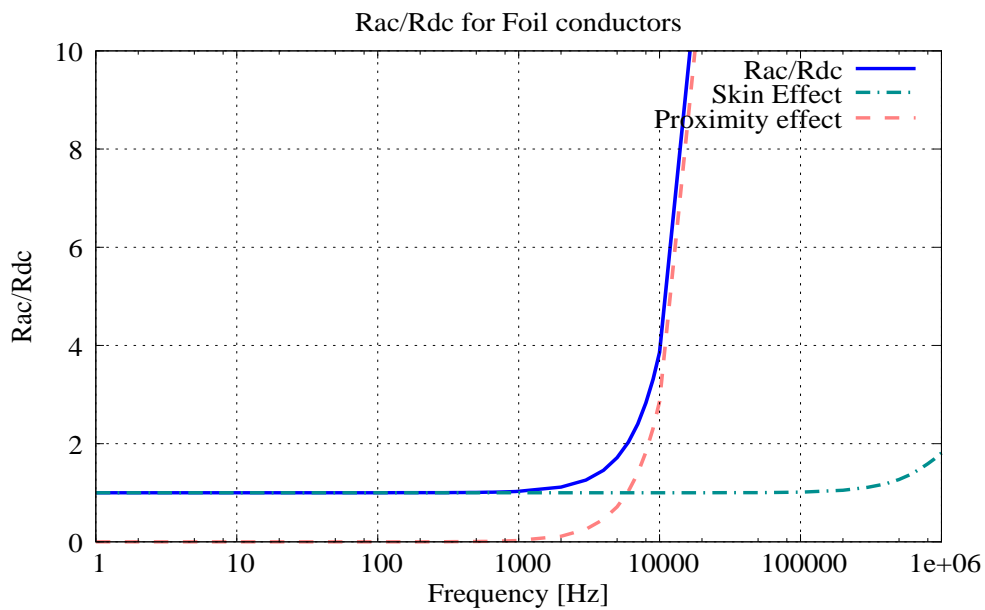
Figure 4.7: Resistance variation as a function of frequency indicating skin effect, proximity effect and overall R_{ac}/R_{dc} for foil winding.
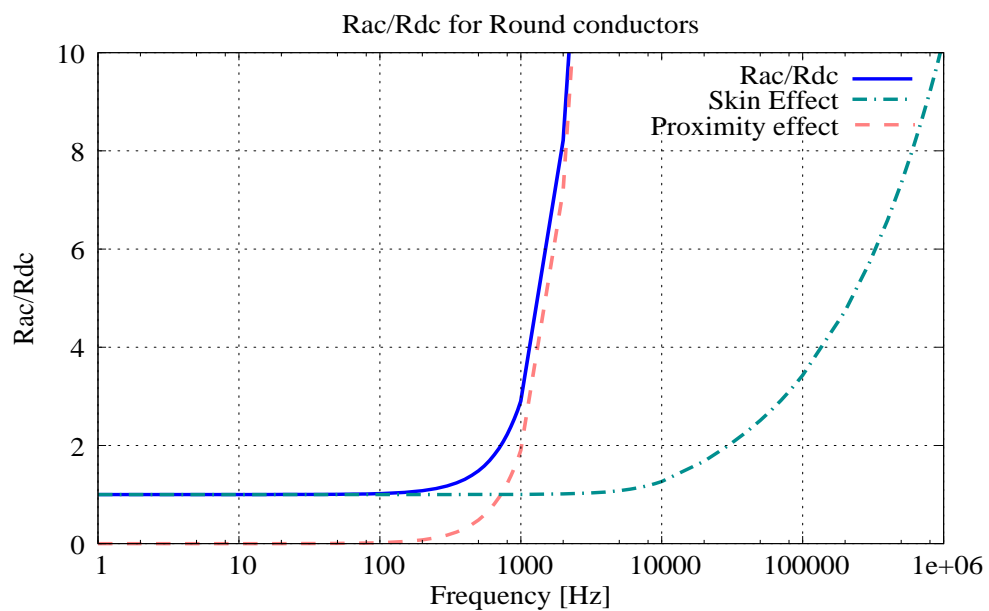
Figure 4.8: Resistance variation as a function of frequency indicating skin effect, proximity effect and overall R_{ac}/R_{dc} for round wire winding.

4.6   Thermal analysis

Heat is a form of energy that can be transferred from one system to another as a result of temperature difference. Heat transfer is the science that determines the *rate* of this energy transfer. The basic requirement for heat transfer is the presence of a temperature difference. Transfer of energy is always from a body of higher temperature to a body of lower temperature, and the transfer stops when both reach the same temperature. There are three mechanisms of heat transfer -conduction, convection and radiation. Conduction occurs in a substance when energy is transferred from more energetic particles to adjacent less energetic ones. Conduction takes place because to lattice vibrations and free flow of electrons in solids and collision and diffusion in liquids and gases. Convection is energy transfer between a solid surface and adjacent liquid or gas that is in motion, and involves conduction along with fluid motion. Radiation is energy transfer in form of electromagnetic energy. It is the fastest type of heat transfer and does not require a material medium.

The principles of heat transfer are used to estimate the surface temperature of the filter components, especially the inductor. The power loss in the inductor, including the core loss and copper loss get converted to heat. By knowing the heat transfer rate and the ambient temperature, we can find out how hot the inductor will become at rated conditions. This is the final step of the inductor design where the entire design procedure is validated on the basis of expected temperature rise. The crucial temperature constraint is the temperature rating of the insulation. The insulation used is Nomex which is rated for 200°C, but filter components are designed to operate at temperature of 100°C, at an ambient temperature of 45°C.

There are three modes of heat transfer mentioned in the previous paragraph, but in this specific case, only two are possible. Heat is transfered from the surface of the inductor by *natural* convection and/or radiation. In order to solve this heat transfer problem, certain assumptions are made to obtain the simplest model which still yields reasonable results.

1. The inductor consists of a core material (which is usually a bad conductor of heat) surrounded by copper winding (good conductor) and insulation (bad conductor). Also from the previous analysis we have concluded that copper losses far exceed the core losses. Still, from the thermal analysis point of view, the inductor is considered to be a uniform body with uniform temperature. This also rules out conduction as a mode of heat transfer from the interior to the surface, which has to be accounted for later.

2. The surface temperature of the inductor is directly proportional to the power loss and inversely proportional to the surface area available. The total surface area is the sum of the surface area of the core and the surface area of the outermost winding layer. There is some overlap between the two surfaces which will reduce the net surface area, but this is ignored.

3. The temperature of air immediately surrounding the inductor is assumed to be 45°C, while the temperature at a point far away (or room temperature) is assumed to be 25°C.

4. The inductor is designed to be cooled with natural convection currents. The convection heat transfer coefficient h_{conv} is **not** a property of the fluid. It is an experimentally determined parameter which depends on surface geometry, nature of fluid motion, properties of the fluid, bulk fluid velocity and other variables which affect convection. This means that h_{conv} cannot be accurately determined by analytical methods. Some analytical solutions exist for natural convection, but they are for specific simple geometries with further simplifying assumptions. The analytical expressions for a natural convection over a simple vertical plate is used to approximate the heat transfer in the inductor. The accuracy of this assumption is verified by experimental measurements of temperature.

4.6.1 Radiation

Thermal radiation is a form of radiation emitted by bodies because of their temperature. Unlike conduction and convection, transfer of heat through radiation does not require an intervening medium. The maximum rate of radiation that can be emitted by a surface of area A_s at a temperature of T_s K is given by the Stefan-Boltzmann's law

$$P_{rad} = \sigma A_s T_s^4 \qquad (4.110)$$

where σ=5.67×10^{-8} W/m^2 K^4 is the Stefan-Boltzmann constant.

When a surface of emissivity ε and surface area A_s at thermodynamic temperature T_s is completely enclosed by an much larger surface at a thermodynamic temperature T_{surr} separated by a gas (like air) that does not intervene with radiation, the net rate of radiation heat transfer between these two surfaces is given by

$$P_{rad} = \varepsilon \sigma A_s (T_s^4 - T_{surr}^4) \qquad (4.111)$$

4.6.2   Natural convection

Convection is a form of heat transfer from a solid surface to an adjacent liquid or gas in motion, and it involves the combined effects of conduction and fluid motion. Bulk fluid motion enhances the heat transfer between the solid surface and the fluid, but it also complicates the determination of heat transfer rates. The rate of convection heat transfer is observed to be proportional to the temperature difference, and is expressed by Newton's law of cooling as

$$P_{conv} = h_{conv}A_s(T_s - T_\infty) \tag{4.112}$$

where h_{conv} is the convection heat transfer coefficient in W/m^2 °C, A_s is the surface area through which convection heat transfer takes place, T_s is the surface temperature and T_∞ is the temperature of the fluid sufficiently far away from the surface. As mentioned before, h_{conv} is not a property of the fluid, but is an experimentally determined factor based on a variety of hard-to-estimate factors.

When the fluid motion occurs only because of the density difference between heated 'lighter' air and cooler 'heavier' air, it is termed as Natural convection. Although the mechanism of natural convection is well understood, the complexities of fluid motion make it very difficult to obtain simple analytical equations for heat transfer. However, analytical solutions exist for some simple geometries and we are using the analytical equations for natural convection over a simple vertical plate of length L and temperature T_s.

4.6.3   Temperature estimation

The quantity of interest is the final steady state surface temperature or T_s. Since the convection heat transfer coefficient h_{conv} also depends on T_s, to initiate the calculation, the surface temperature is assumed. This initial surface temperature is used to find h_{conv}. Since the net heat transfer rate is know, using the calculated h_{conv}, the surface temperature can be calculated. This process is repeated until the surface temperature converges the actual value.

1. Assume an initial surface temperature T_s'.

2. For radiation, T_{surr} is assumed to be 25°C and for natural convection, T_∞ is assumed to be 45°C. Also surface emissivity for radiation is assumed ε=0.6.

3. Calculate the film temperature

$$T_f = \frac{T_s' + T_\infty}{2}$$

(4.113)

4. For the film temperature T_f, the properties of air at 1 atm pressure are defined. k is the thermal conductivity of air (W/m K), υ is the kinematic viscosity (m^2/s) and Pr is the Prantl number.

5. The length of the vertical surface is know as the characteristic length L_c. In case of the inductor, this will be equal to the height of the inductor.

6. Calculate the Rayleigh number Ra_L and Nusselt number Nu.

$$Ra_L = \frac{g\beta(T_s' - T_\infty)L_c^3}{\upsilon^2}Pr$$

(4.114)

$$Nu = \left[0.825 + \frac{0.387Ra_L^{\frac{1}{6}}}{\left(1 + \left(\frac{0.492}{Pr}\right)^{\frac{9}{16}}\right)^{\frac{8}{27}}}\right]^2$$

(4.115)

where g is the acceleration due to gravity(9.8m/s^2) and β is the volume expansion coefficient $=1/T_s$.

7. The convection heat transfer coefficient is given by this equation.

$$h_{conv} = \frac{Nuk}{L_c}$$

(4.116)

8. The net heat transfer rate is equal to the total power dissipated.

$$P_{conv} + P_{rad} = P_{loss}$$

(4.117)

$$P_{conv} + P_{rad} = h_{conv}A_s(T_s - T_\infty) + \varepsilon\sigma A_s(T_s^4 - T_{surr}^4)$$

(4.118)

9. Solving this fourth order polynomial equation gives T_s''. Steps 3-8 are repeated till the surface temperature converges to one number, which will be the actual surface temperature of the inductor for a power loss of P_{loss}.

4.6.4   Design example

The example considered is Ferrite core inductor with a single bobbin round wire winding. The inductor shape is defined in Fig. 3.4 (Chapter 3). The power loss in this inductor for a dc current of 14 A was measured to be 37 W. The total surface area, including core and copper surface area is 0.062 m^2. The characteristic length L_c is equal to the height of the inductor. Following the steps specified in the previous section,

1. Assume surface temperature is 85°C.

2. T_f=65°C. For this T_f, the properties of air at 1 atm pressure are

    - k=0.028881 W/m K

    - υ=1.995×10^{-5}

    - Pr=0.7177

3. Ra_L=7.349×10^6, Nu=28.64, h_{conv}=5.67 W/m^2 K .

4. Substituting h_{conv} in Eq. (4.118) and solving for T_s, we get T_s=91°C.

5. Using this new T_s, we once again recalculate the convection coefficient. The new h_{conv}=5.643.

6. This time, solving Eq. (4.118) with the new h_{conv} gives the same T_s=91°C. Hence, this is the final surface temperature (the experimentally measured temperature was 88°C).

4.7   Summary

The various sources of power loss in an inductor are discussed in detail. Particular attention is given to winding copper losses in the inductor. The equations describing the copper loss at various frequencies are derived for both foil winding and round wire winding. The principles of heat transfer are used to estimate the surface temperature of the inductor. The steps involved in thermal estimation are explained using a real-world example.

4.8   References

Electromagnetics and Mathematics

1. W.R.Smythe, *Static and Dynamic Electricity* (2nd ed.), McGraw Hill Book Company, 1950

2. W.H.Hayt Jr, J.A.Buck, *Engineering Electromagnetics* (6th ed.), Tata McGraw-Hill, 2001

3. S.Ramo, J.R.Whinnery, T. van Duzer, *Fields and Waves in Communication Electronics* (3rd ed.), John Wiley and Sons, 1994

4. C.A.Balanis, *Advanced Engineering Electromagnetics* (1st ed.), John Wiley and Sons, 1989

5. A.Jeffrey, *Advanced Engineering Mathematics* (1st ed.), Academic Press Elsevier India, 2002

6. M.Abramowitz, I.E.Stegun, *Handbook of Mathematical Functions*, Dover, 1970

7. J.Lammeraner, M.Stafl, *Eddy Currents*, Iliffe Books London, 1966

Inductor total power loss

8. M.Bartoli, A.Reatti, M.K.Kazimierczuk, "Minimum copper and core losses power inductor design," in *Conference Record of the 1996 IEEE Industry Applications Conference, Thirty-First IAS Annual Meeting,*1996, vol.3, pp. 1369-76

9. M.Sippola, R.E.Sepponen, "Accurate prediction of high frequency power transformer losses and temperature rise," IEEE Trans. on Power Electronics, vol. 17, no. 5, pp. 835-847, Sept 2002

10. H.Skarrie, "Design of Powder core inductors," Ph.D. dissertation, Dept. of Ind. Elec. Eng. and Auto., Lund Univ., Lund, Sweden, 2001

Inductor Core loss

11. G.Bertotti, I.Mayergoyz, *The Science of Hysteresis*, vol. 1,3, Elesevier Inc, 2005

12. A.V.Bossche, V.C.Valchev, *Inductors and Transformers for Power Electronics*, 1st ed, CRC Press, 2005

13. W.Roshen, "Ferrite core loss for power magnetic components design," IEEE Trans. on Magnetics, vol. 27, no. 6, pp. 4407-4415, Nov 1991

14. W.Roshen, "A practical, accurate and very general core loss model for non-sinusoidal waveforms," IEEE Trans. on Power Electronics, vol. 22, no. 1, pp. 30-40, Jan 2007

Inductor Copper loss

15. W.G.Hurley, E.Gath, J.G.Breslin, "Optimizing the AC resistance of multilayer transformer windings with arbitrary current waveforms," IEEE Trans. on Power Electronics, vol. 15, no. 2, pp. 369-376, March 2000

16. N.H.Kutkut, D.W.Novotny, D.M.Divan et al, "Analysis of winding losses in high frequency foil wound inductors," in *Conference Record of the 1995 IEEE Industry Applications Conference Thirtieth IAS Annual Meeting,* 1995, vol.1, pp. 859-867

17. W.G.Odendaal, J.A.Ferreira, W.A.Cronje, "Combined numeric and analytic methods for foil winding design," in *25th Annual IEEE Power Electronics Specialists Conference,* 1994, vol.2, pp. 843-849

18. M.Bartoli, A.Reatti, M.K.Kazimierczuk. (1995, Dec). Modeling winding losses in high frequency power inductors. *J. Circuits, Systems and Computers*, vol.5, no.4, pp. 607-626

19. A.Reatti, M.K.Kazimierczuk, "Comparison of various methods for calculating the AC resistance of inductors," IEEE Trans. on Magnetics, vol. 38, no. 3, pp. 1515-1518, May 2002

20. J.A.Ferreira, "Improved analytical modeling of conductive losses in magnetic components," IEEE Trans. on Power Electronics, vol. 9, no. 1, pp. 127-131, Jan 1994

21. Xi Nan, C.R.Sullivan, "An improved calculation of proximity-effect loss in high-frequency windings of round conductors," *2003 IEEE 34th Annual Power Electronics Specialists Conference*, 2003, vol. 2, pp.853-860

22. Xi Nan, C.R.Sullivan, "Simplified high-accuracy calculation of eddy-current loss in round-wire windings," *2004 IEEE 35th Annual Power Electronics Specialists Conference*, 2004, vol. 2, pp. 873-879

23. P.Wallmeier, "Improved analytical modeling of conductive losses in gapped high-frequency inductors," IEEE Trans. on Industry Applications, vol. 37, no. 4, pp. 1045-1054, July/Aug 2001

24. V.A.Niemala, G.R.Skutt, A.M.Urling et al, "Calculating the short circuit impedances of a multiwinding transformer from its geometry," *20th Annual IEEE Power Electronics Specialists Conference - PESC*, 1989, vol.2, pp. 607-617

25. C.E.Hawkes, T.G.Wilson, R.C.Wong, "Magnetic-field intensity and current-density distributions in transformer windings," *20th Annual IEEE Power Electronics Specialists Conference - PESC*, 1989, vol. 2, pp. 1021-1030

26. M.P.Perry, "On calculating losses in current carrying conductors in an external alternating magnetic field," IEEE Trans. on Magnetics, vol. 17, no. 5, pp. 2486-2488, Sept 1981

27. J.P.Vandelac, P.D.Ziogas, "A novel approach for minimizing high-frequency transformer copper losses," IEEE Trans. on Power Electronics, vol. 3, no. 3, pp. 266-277, July 1988

28. E.E.Kriezis, T.D.Tsibourkis, S.M.Panas, J.A.Tegopoulos, "Eddy Currents: Theory and Applications," *Proc. of the IEEE,* vol. 10, no. 10, Oct 1992

Thermal analysis

29. Y.A.Cengel, *Heat and Mass Transfer - A practical approach* (3rd ed.) , Tata McGraw Hill, 2007

30. A.V.Bossche, V.Valchev, J.Melkebeek, "Thermal modeling of E-type magnetic components," *Proceedings of the 2002 28th Annual Conference of the IEEE Industrial Electronics Society*, 2002, vol. 2, pp. 1312-1317

Chapter 5

Grid Interactive Operation and Active Damping

5.1 Introduction

The previous chapters looked at the design of the LCL filter and its components. In this chapter we will study the grid interactive operation of converters with LCL filters. The basic operation of such converters have been widely studied [1,2]. The focus here is on aspects of damping that arise during grid interactive operation of the power converter. Active rectifiers and active front end converters(AFEC) have been used in drives as well as distributed generation system and are now becoming more and more popular because of their ability to control the line side power factor and load voltage at the same time. These type of converters are connected between load and the grid or utility in order to supply fine quality of power to the load.

5.2 Active front end converter

The converter consists of a three-phase bridge, a high capacitance on the dc side and a three-phase filter in the line side. The voltage at the midpoint of a leg or the pole voltage Vi is pulse width modulated (PWM) in nature. The pole voltage consists of a fundamental component (at line frequency) besides harmonic components around the switching frequency of the converter. Being at high frequencies, these harmonic components are well filtered by the high inductances (L) or some higher order line filter (LCL). Hence the
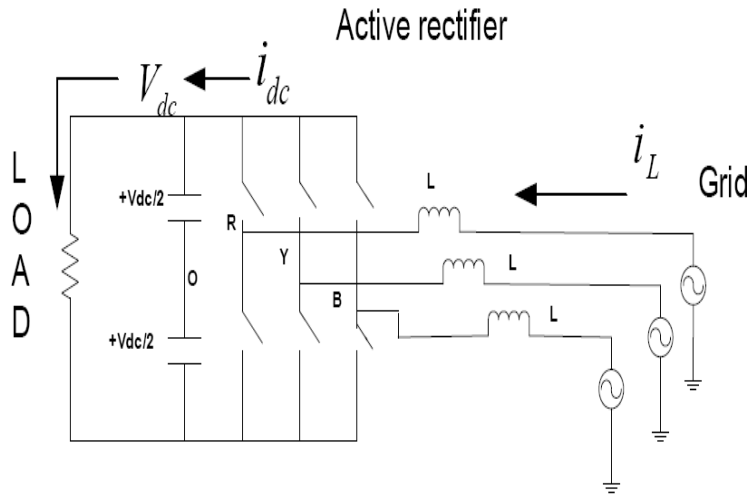
Figure 5.1: Grid connected operation with the simple L filter

current is near sinusoidal. The fundamental component of Vi controls the flow of real and reactive power.

It is well known that the active power flows from the leading voltage to the lagging voltage and the reactive power flows from the higher voltage to the lower voltage. Therefore, controlling the phase and magnitude of the converter voltage fundamental component with respect to the grid voltage can control both active and reactive power. As the grid voltage leads the converter pole voltage, real power flows from the ac side to the dc side, while the reactive power flows from the converter to the grid based on the difference in magnitude of the grid and inverter fundamental voltages.

Apart from control of real and reactive power flow, an FEC should also have a fast dynamic response. Operation of FEC with the first order L filter is well reported in the literature but operation of this type active rectifier with LCL filter has now started drawing attention [2,12].
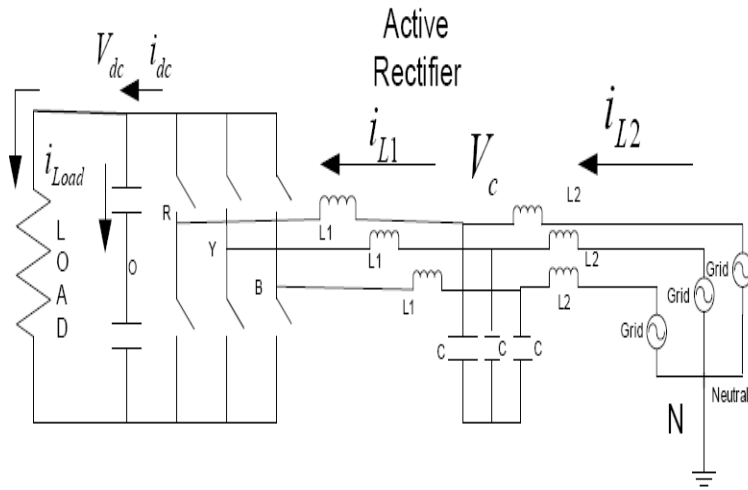
Figure 5.2: Grid connected operation with third order LCL filter
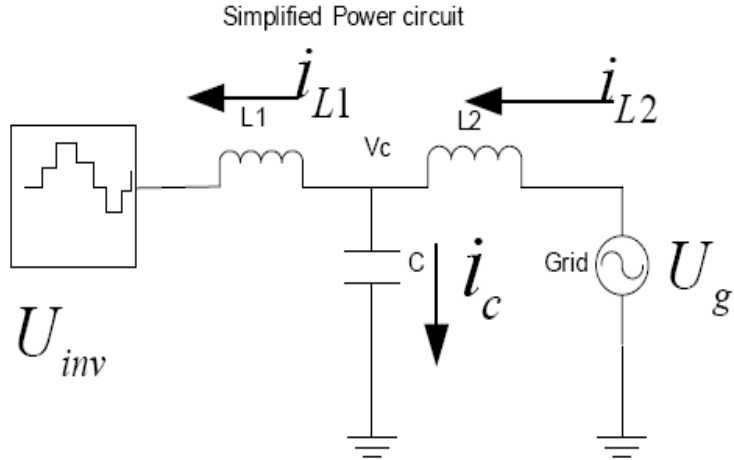
Figure 5.3: PWM waveform applied to the filter

5.3 Problem of LCL resonance

Normally grid impedance reflected back to the converter side is low and in particular, the resistive component is very less so, if the resonance is excited, the oscillation of that can continue for a long time, which can make the entire system vulnerable. Actually when the PWM converter is switched on, the filter (LCL) encounter a sudden pulse at the input as a result filter starts to oscillate in its cutoff frequency. Here is an attempt to show how the resonance is excited by PWM converter (AFEC) itself. For that LCL filter is modeled inside the FPGA based controller and fed from a very narrow single pulse from the same controller. After exciting from the pulse, filter starts to oscillate at resonant frequency.
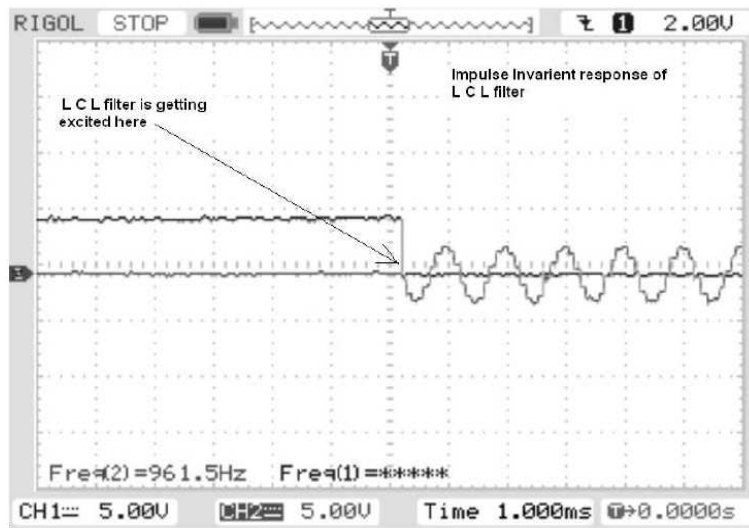
Figure 5.4: Unit impulse excitation applied to filter

Pulse is being generated in FPGA by means of switch de-bouncing logic.

In the grid-connected operation with LCL filter damping is a significant part of design if we want to utilize the full advantages of higher order filter and modern high performance digital controllers. There are two ways to damp the resonance, passive damping and active damping. The passive approach can damp resonance in all condition but it has a loss penalty that needs to be traded off with the amount of damping as seen in chapter (1). The active damping approach can act only when the power converter is switching. It is seen to be desirable to combine both active and passive approaches in a hybrid manner so that some minimum level of damping is always present which can be enhanced when the power converter is switching in a lossless manner.

5.4   Active damping

In passive damping, damping is provided by physical elements like resistors. But this process is associated with losses. To reduce losses and improve the performance inductors, capacitors are provided along with resistors in passive damping networks as seen in chapter (1).

In active damping, damping is being provided by means of control algorithm, this process is not a lossy process so this process is much more attractive. But there is a limitation of active damping, such as this control technique depends on the switching of power converter, so this is effective only when power converter is switching. In addition,

the switching frequency of the power converter is limited hence the control bandwidth of the active damping is also limited. There are broadly two methods of active damping can be thought one is based on traditional PI-controller, and the other is based on generalized state-space approach. In this chapter we will focus on a method of active damping based on state-space for arbitrary pole placement.

5.4.1 Active damping based on traditional approach

The traditional approach is based on different current control strategy such as conventional PI-controller based [3] (in rotating frame) combined with lead compensator or a resonant controller as a main compensator in $\alpha - \beta$ domain. In these approaches bandwidth of the system or settling time cannot be arbitrarily fixed as these based upon main current controller bandwidth. In other words placement of the closed loop poles is determined by the current controller design.

5.4.2 Active damping by means of state space method

This approach is more generalized than traditional PI-controller based method because of flexibility. This method gives us the freedom of arbitrary pole placements or in other words bandwidth can be independently fixed without depending upon the current controller bandwidth. More over the energy required for damping can be optimized by means of state-space based method. So, state-space based method offers good stability margin and robustness to parameter uncertainty in the grid impedance at the same time implementation is simpler in case of state-space based method. For a stable under-damped system, its poles should be on left half of s-plane. In our present case providing damping is equivalent to shifting the closed loop poles in the left half of s-plane. So all we have to do is to shift the closed loop poles in the left half of s-plane by means of a suitable gain matrix. Shifting of the poles can be determined by required settling time of the closed loop system. Along with the damping, the transient response can also be improved for the different states.

5.4.3 Filter modelling in state space

There are two inputs to the system in Fig. 5.3: PWM output of the power converter and grid voltage. First one is the active input that can be controlled and second one is the

uncontrolled disturbance input. The states of the system are elected to be the two inductor currents and one capacitor voltage.

$$\begin{pmatrix} \frac{dV_c}{dt} \\ \frac{di_{L1}}{dt} \\ \frac{di_{L2}}{dt} \end{pmatrix} = \begin{pmatrix} 0 & \frac{1}{C} & \frac{-1}{C} \\ \frac{-1}{L_1} & 0 & 0 \\ \frac{1}{L_2} & 0 & 0 \end{pmatrix} \begin{pmatrix} Vc \\ i_{L1} \\ i_{L2} \end{pmatrix} + \begin{pmatrix} 0 \\ \frac{1}{L_1} \\ 0 \end{pmatrix} U_{inv} + \begin{pmatrix} 0 \\ 0 \\ \frac{-1}{L_2} \end{pmatrix} U_1 \quad (5.1)$$

In more compact form,

$$\dot{x}_{LCL} = A_{LCL}x_{LCL} + B_1 u_{inv} + B_2 U_g \tag{5.2}$$

$$y = C_{LCL}x_{LCL} \tag{5.3}$$

where

$$A_{LCL} = \begin{pmatrix} 0 & \frac{1}{C} & \frac{-1}{C} \\ \frac{-1}{L_1} & 0 & 0 \\ \frac{1}{L_2} & 0 & 0 \end{pmatrix} \tag{5.4}$$

$$B_1 = \begin{pmatrix} 0 \\ \frac{1}{L_1} \\ 0 \end{pmatrix} \tag{5.5}$$

$$B_2 = \begin{pmatrix} 0 \\ 0 \\ \frac{-1}{L_2} \end{pmatrix} \tag{5.6}$$

$$C_{LCL} = \begin{pmatrix} 1 & 0 & 0 \\ 0 & 1 & 0 \end{pmatrix} \tag{5.7}$$

Now position of the poles are on imaginary axis hence the system is oscillatory and
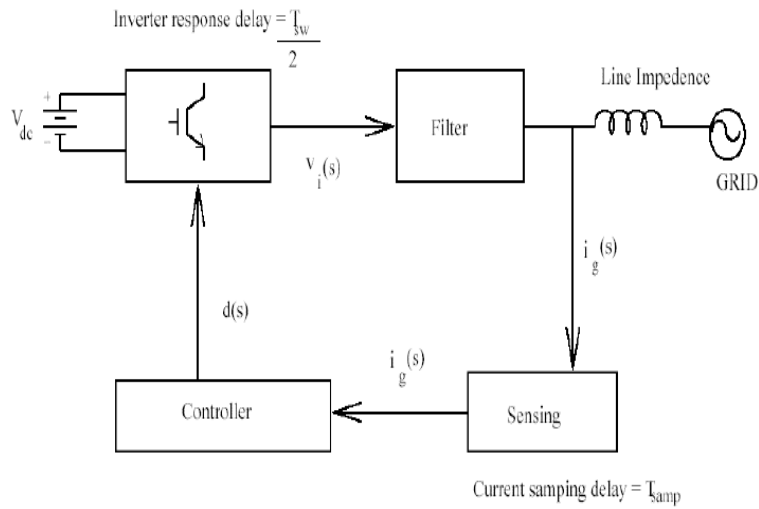
Figure 5.5: Typical scheme for active damping
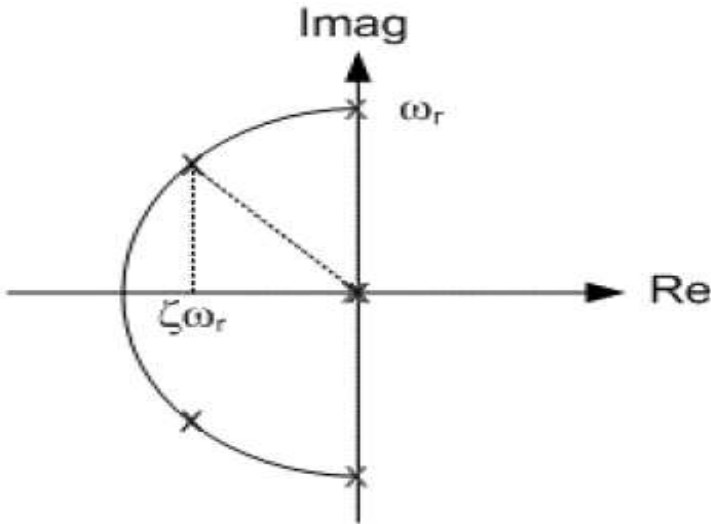
Figure 5.6: Pole placement to LHS of s-plane

highly sensitive to outside disturbances.

5.4.4 Pole placement of the system

Typical scheme (in brief) for active damping control can be visualized by Fig.5.5. PWM delay and the digital controller delays correspond to phase errors in the requirements of the active damping control.

As mentioned earlier that poles of the closed loop system is on imaginary axis for un-damped system. Now the poles can be moved to the left half of the s-plane properly

choosing the BW or settling time of the entire system.

Let the imaginary axis pole is to be shifted to $\xi\omega_r \pm j\omega_r\sqrt{1-\xi^2}$. Where ξ is the damping factor of the system. We need to select this damping factor for designing this system. ξ is taken as 0.6 in this case to provide sufficient damping. For assigning above pole in the system we use control law,

$$U_{inv} = -Kx_{LCL} \tag{5.8}$$

or in another form,

$$U_{inv} = -K_1V_c - K_2i_{L1} - K_3i_{L2} \tag{5.9}$$

The task is to find the gain matrix for the system. The system is perunitized for this purpose.

5.4.5 Per unitization

For 10kVA inverter and 440V grid voltage we can per unitize the system as below. After perunitization, $L_1 = L_2 = 3\text{mH}$ and $C = 16 \text{ mF}$ become $L_1 = L_1 = 0.05\text{pu}$ and $C = 0.09\text{pu}$ Now the required pole placement is at $-12.25 \pm j16.32$. Hence the required gain matrix is

$$K = \begin{pmatrix} -0.0005 & 1.5 & -1.5 \end{pmatrix} \tag{5.10}$$

The complete system model can be written in state-space as

$$\dot{x}_{LCL} = (A_{LCL} - B_1K)x_{LCL} + B_1r \tag{5.11}$$

Where r is reference input, which is determined by the overall control This gives the damping loop description, which is based on statespace based method.

5.4.6 Physical realization of active damping

The concepts of active damping can be realized from the equation 5.11. After splitting the state-space form we get,

$$C\frac{dV_c}{dt} = i_{L1} - i_{L2} \tag{5.12}$$
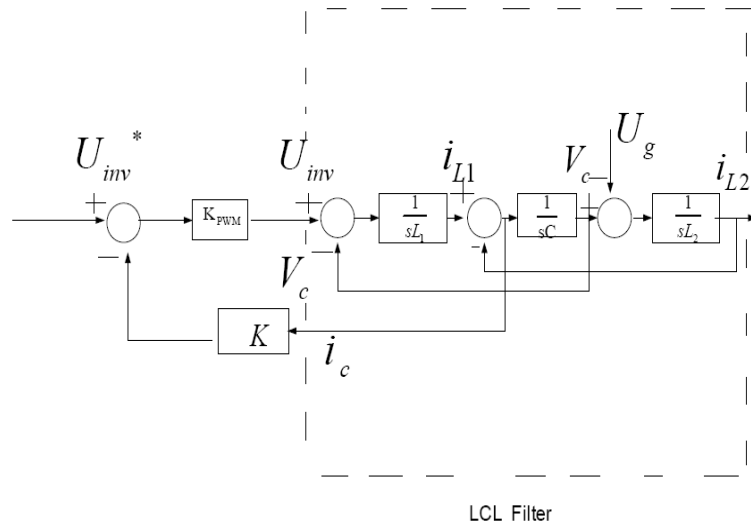
Figure 5.7: Active damping by weightage capacitive current feedback
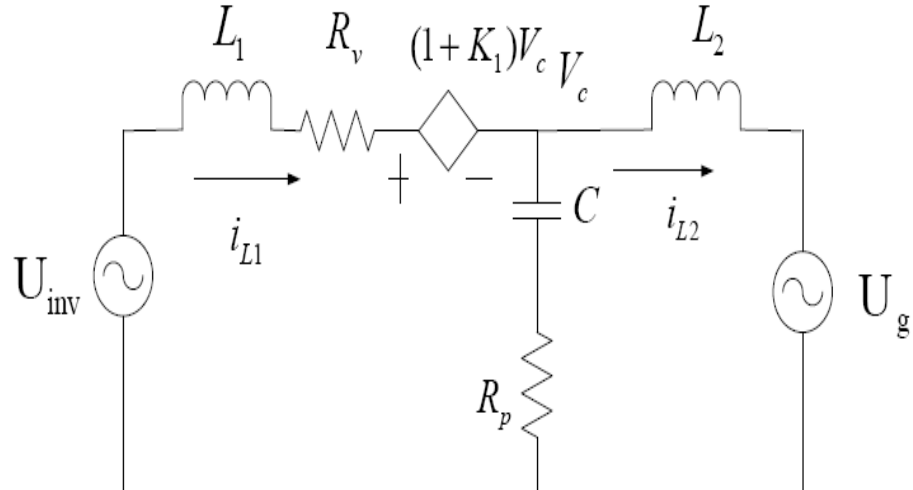
Figure 5.8: Approximate circuit representation of active damping

$$L_1 \frac{di_{L1}}{dt} = -(1+K_1)V_c - K_2 i_{L1} - K_3 i_{L2} + U_{inv} \qquad (5.13)$$

$$L_2 \frac{di_2}{dt} = V_c - U_g \qquad (5.14)$$

So if we try to synthesise the circuit form of the above equation then it can be shown to be as in Fig. 5.8. R_v is the series and R_p is the parallel virtual resistance and depends on gain matrix parameters k_2 and k_3 from equation (5.11). From circuit representation it is clear that these two resistances are providing the damping to the LCL resonance even though these resistances do not exit physically. These occur just because of control action and can be used to damp the resonance. These are treated as virtual resistances, [5]. It can be
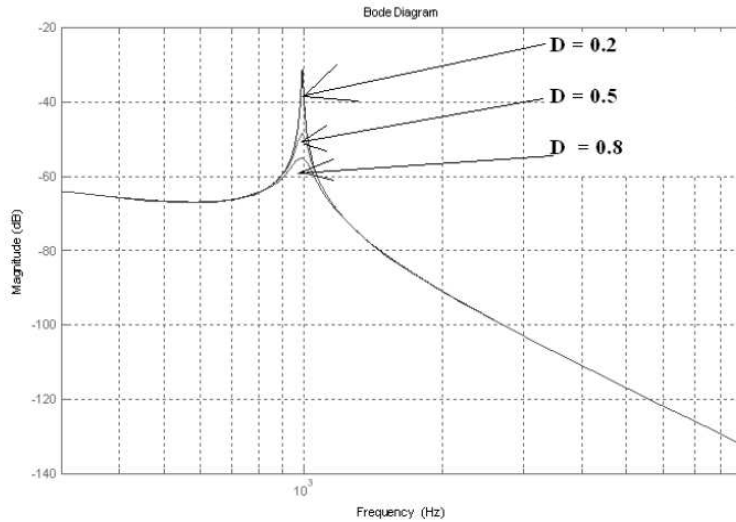
Figure 5.9: Comparison of different damping factors in active damping

seen from the following transfer functions

$$\frac{i_{L1}}{U_{inv}} = \frac{1 + s^2 L_2 C}{s L_1 L_2 C (s^2 + s\frac{K}{L_1} + w_r^2)} \tag{5.15}$$

and

$$\frac{i_{L2}}{U_{inv}} = \frac{1}{s L_1 L_2 C (s^2 + s\frac{k}{L_1} + w_r^2)} \tag{5.16}$$

that the damping factor $D = \frac{k}{2L_1 w_r}$ is proportional to k. Where $k = k_1 = -k_2$.

5.4.7   Active damping loop realization

Fig. 5.10 shows the general practical approach of active damping loop. It consists of three feedbacks with two inductor currents and one capacitor voltage. It is shown that there is no need of feeding backs the capacitor voltage for arbitrary pole placements in the previous section.
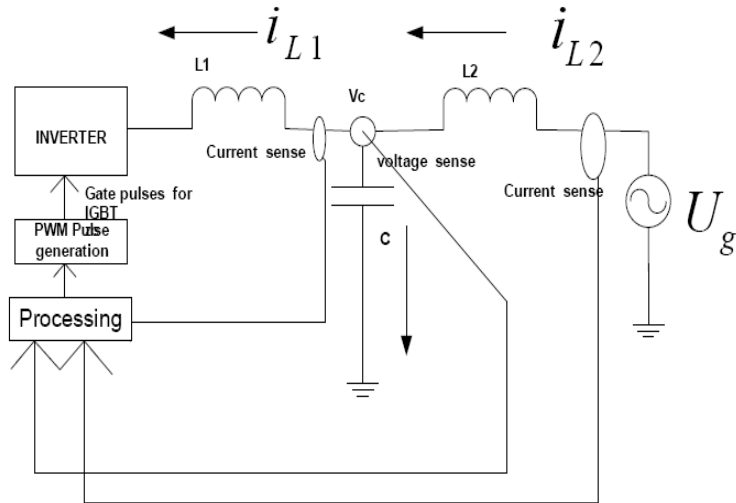
Figure 5.10: State-space based active damping loop)
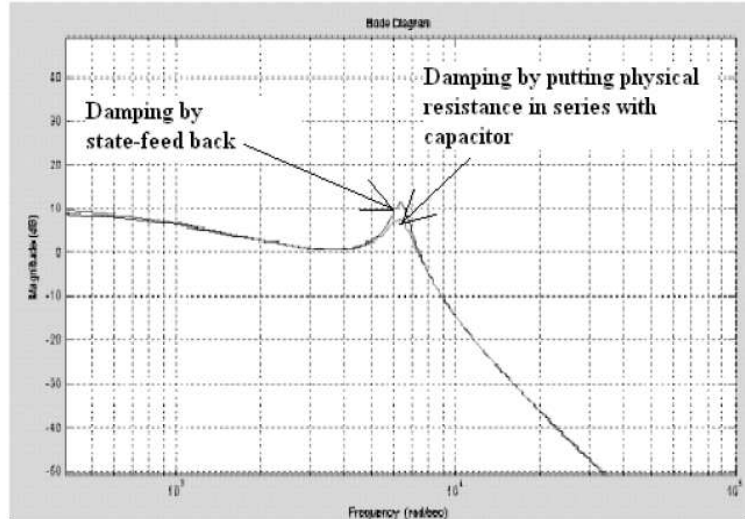
Figure 5.11: Comparison of virtual resistance based damping and actual resistance based damping

5.5 Control of the inverter in grid-interactive mode

For the control of the inverter in grid-interactive mode, dq-based control strategy [1] is adopted. The main difference between the control of LCL filter based system with that of an L filter is the addition of the active damping loop. The number of sensors are also more in case of LCL filter. The control scheme consists of inner ac current controllers, dc voltage controller and the damping controller. The at last state-space based damping loop is in between the inner ac current controller and the PWM modulator.

5.5.1   Model for control design

For control design, the grid is modelled as an ideal sinusoidal three phase voltage source without line impedances, although, in reality there are line impedances and distortions like line harmonics and unbalances. The space notation is used. Three phase values are transformed into the dq-reference frame that rotates synchronously with the line voltage space vector. From control point of view it is advantageous to control dc values since PI controller can achieve reference tracking without steady state errors.

Modeling of the LCL filter in the dq-reference frame without frequency dependence of the inductances is performed here.   The differential equations are written in space
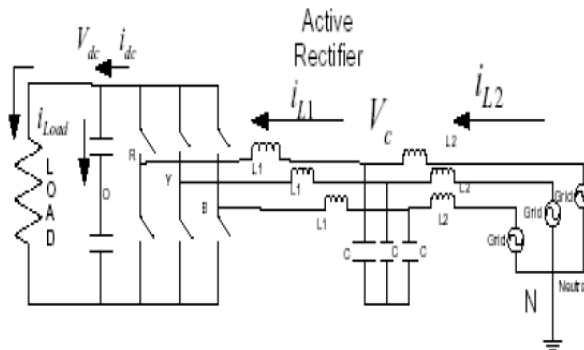
Figure 5.12: Active rectifier with LCL filter
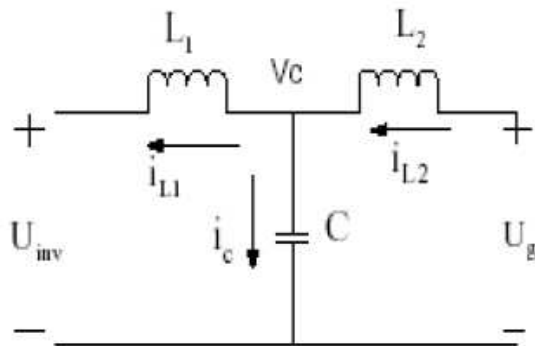
Figure 5.13: Grid connection with LCL filter

vector domain:

$$L_1 \frac{di_{L1}}{dt} = V_c - U_{inv} \tag{5.17}$$

$$L_2 \frac{di_{L2}}{dt} = U_g - V_c \tag{5.18}$$

$$C\frac{dV_c}{dt} = i_{L2} - i_{L1} \tag{5.19}$$

Here for simplicity of the analysis the parasitic resistance of the inductors is neglected and at the same time ESR of the capacitance is also being neglected. After transforming to dq-domain we get the differential equations:

$$L_1\frac{di_{L1q}}{dt} = V_{cq} - U_{invq} - wL_1 i_{L1d} \tag{5.20}$$

$$L_1\frac{di_{L1d}}{dt} = V_{cd} - U_{invd} + wL_1 i_{L1q} \tag{5.21}$$

$$L_2\frac{di_{L2q}}{dt} = U_{gq} - V_{cq} - wL_2 i_{L2d} \tag{5.22}$$

$$L_2\frac{di_{L2d}}{dt} = U_{gd} - V_{cd} + wL_2 i_{L2d} \tag{5.23}$$

$$C\frac{dV_{cq}}{dt} = i_{L2q} - i_{L1q} \tag{5.24}$$

$$C\frac{dV_{cd}}{dt} = i_{L2d} - i_{L1d} \tag{5.25}$$

If we include the dynamics of the DC-bus voltage of the power converter we get,

$$C_{dc}\frac{dV_{dc}}{dt} = i_{dc} - i_{load} = \frac{3}{2}\frac{i_{L2q}U_{gq}}{V_{dc}} - i_{load} \tag{5.26}$$

The control will contain simple decoupling terms in order to decouple the d and q axis current dynamics. No perfect dynamic decoupling can be achieved due to delays in the loop and filter resonance.

5.5.2 Overview of control loop consisting of three states of system
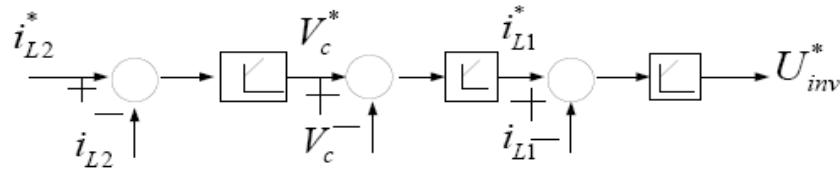
Figure 5.14: Conventional three loop control strategy for LCL filter

A traditional approach to control design is to assign a controller for each state as shown in Fig. 5.14. For this type of filter the capacitor voltage can be indirectly controlled and so there is no need of capacitor voltage controller for LCL filter. The $i_{L2} - i_{L1} = i_c$

and the $V_c = \frac{1}{C}i_C dt$, hence if we can control i_{L1} and i_{L2} separately then that itself controls the i_c followed by the V_c. The control loop may be reduced to following fashion as shown in Fig. 5.15. Here the output of the line side current controller becomes the reference of
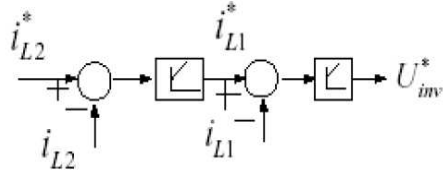
Figure 5.15: Two loop control strategy for LCL filter

converter side current. The line side current and converter side current are almost equal in magnitude and phase in fundamental, as capacitor size is limited in LCL filter because of the low reactive power burden. Hence, further more simplification is possible.

The converter side current controller can also be omitted and only line side current controller is fair enough to control the current. The output of line side current controller will become inverter input reference. Single grid current loop controller is not sufficient
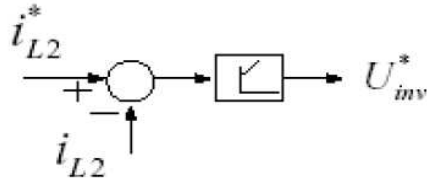
Figure 5.16: Single loop control strategy for LCL filter

for stability of the overall system. The resonance of the filter can make the system unstable as here we are only concentrating on the fundamental current where LCL filter has significant amount of resonance frequency super imposed over the fundamental. So we need to consider the resonance carefully. Higher-level control [10] loops are required to provide fast dynamic compensation for the system disturbances and improve stability.

5.5.3   Current control strategy

Conventional PI controller [7] in the innermost loops is not selected from point of view of speed and complexity. In order to control the resonance in the filter inner most current loop should be very fast, ideally instantaneous. For this type of filters inner most current loop i_{L1} can be designed by a proportional controller. This controller or this inner loop makes the system dynamic response very good by limiting the unwanted resonance in
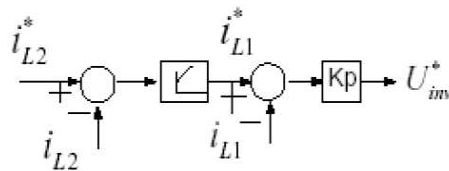
Figure 5.17: Modified two loop control strategy for LCL filter

the system or in other words it shifts the closed loop poles in LHS of s-plane. The total current control loop structure becomes as shown in Fig. 5.18 where outer loop is line side current and inner loop is the converter side current and converter current feedback is used for stability [7] for damping oscillation.
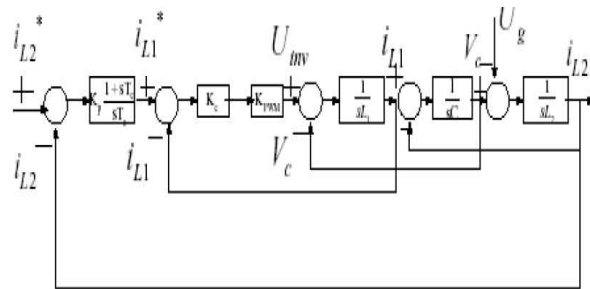
Figure 5.18: Two-loop control strategy for LCL filter

We can see the transfer function of the closed loop current controller with the inner loop, it is a 4th order system. In the outer loop PI-controller used as usual and proportional controller is used in inner loop. The closed loop transfer function is given below, is used to analyse the stability.

$$\frac{i_{L2}^*}{i_{L2}} = \frac{(K_p K_c K_{PWM})s + K_p K_c K_{PWM}/T_c}{(L_1 L_2 C)s^4 + (K_c K_{PWM} L_2 C)s^3 + (L_1 + L_2)s^2 + (K_p K_c K_{PWM} + K_c K_{PWM})s + K_p K_c K_{PWM}/T_c} \quad (5.27)$$

5.5.4   Analysis of controller performance

A Analysis of the outer loop: The outer loop is a PI-controller, where the value of K_p should be quite high value to track the reference but at the same time K_p should not be as large as wish, which can be seen from the following analysis. As it grows bigger, the poles will shift towards the right side of s-plane.

B Analysis of the inner loop: The inner loop basically improves the stability of the system and increases the robustness. In other words more important role of the
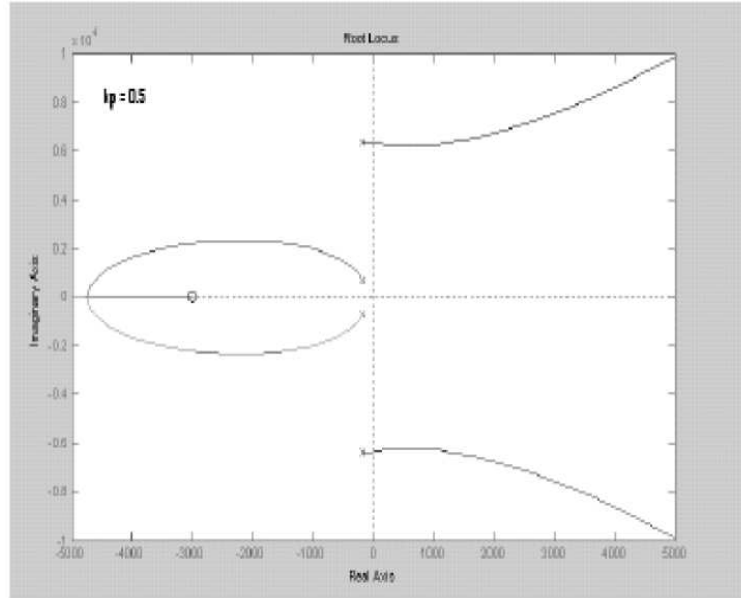
Figure 5.19: Root locus of $\frac{i_{L2}^*}{i_{L2}}$ with $K_p = 0.5$
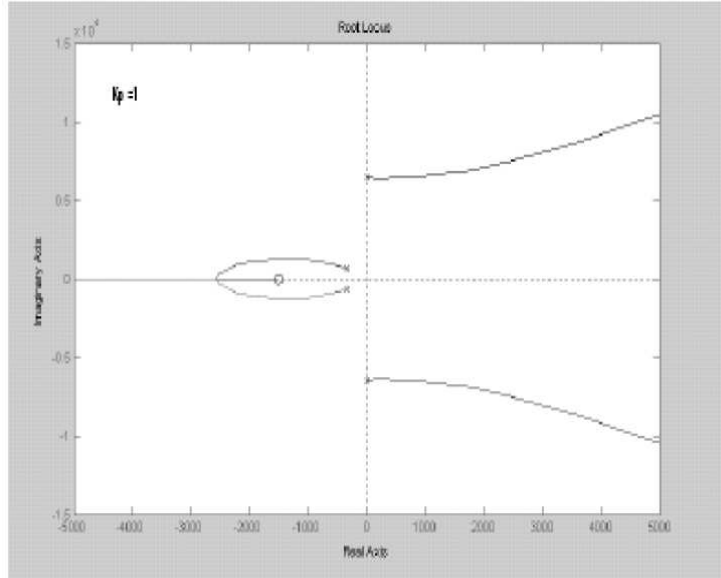
Figure 5.20: Root locus of $\frac{i_{L2}^*}{i_{L2}}$ with $K_p = 1$

inner loop is to damp the resonance peak but at the same time very high of K_c can make system unstable also. So, the value of K_c has to be limited and we cannot depend the value of K_c to damp the oscillation.
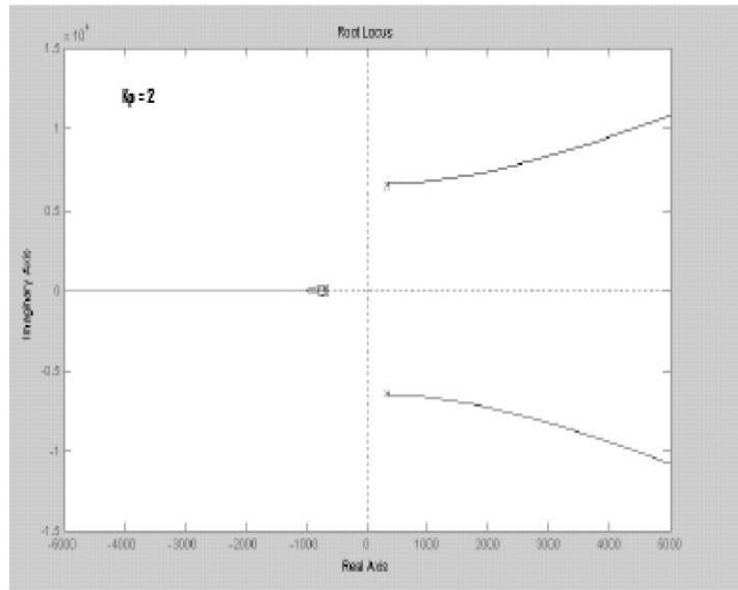
Figure 5.21: Root locus of $\frac{i_{L2}^*}{i_{L2}}$ with $K_p = 2$
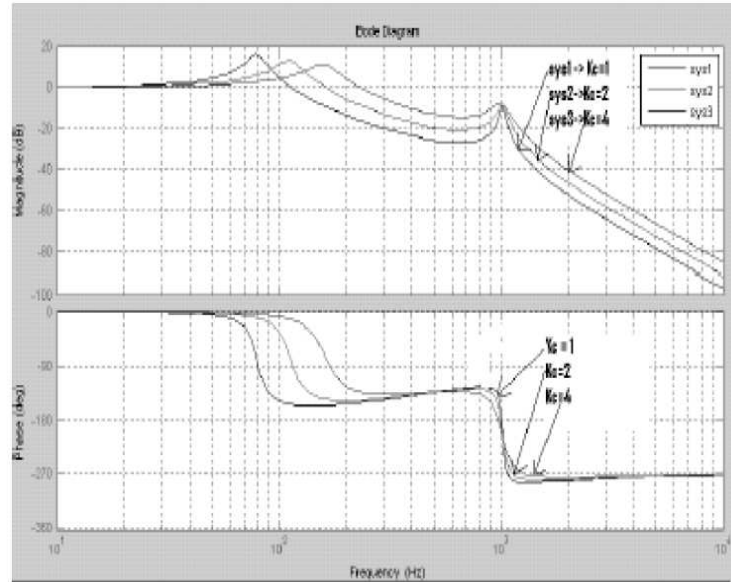
Figure 5.22: Bode-plot of $\frac{i_{L2}^*}{i_{L2}}$ with different values of K_c

5.5.5   Inclusion of innermost state-space based damping loop

As mentioned earlier that in the converter current loops the value of K_c is limited from the point of view of stability. So, when high damped system is desired this method of damping described in the previous section is not preferable.

The state-space based method offer more flexibility of choosing the controller param-

eter and at the same time robustness. The total current control loop with the damping loop is shown in Fig. 5.23. Here the value of damping can be decided as given by equation (5.16)
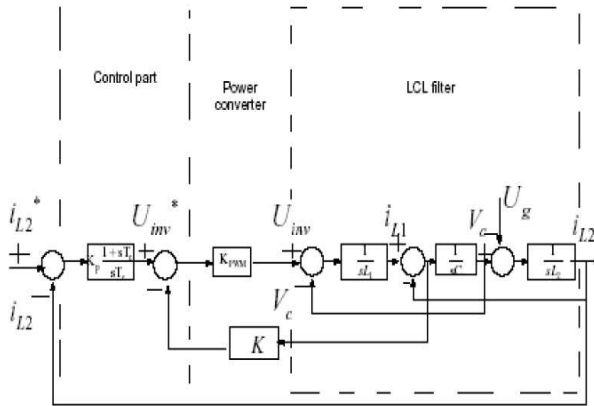
Figure 5.23: Current control with State-space based damping loop

5.5.6   Control in grid-parallel mode with LCL filter

In grid connected mode, load is connected across the DC-bus which is to be supplied from the grid with good power quality (FEC mode)[16]. So, naturally the load voltage has to be maintaining constant. Here DC-link voltage controller is must for this kind of operation.

5.5.7   Sensorless operation

For the control of LCL filter based system several loops cascaded. Naturally while implementation in practice, it needs quite a few sensors. These sensors, specially the LEM current sensors are costly. So, in the LCL filter based system minimizing the number of sensors is desirable. The way out is to estimate the corresponding quantities like voltages or currents. There are two ways to eliminate sensors, one way is to run a parallel process in the controller and then calculate quantities and use for control, the second way to design the reduced order observer to estimate the states.
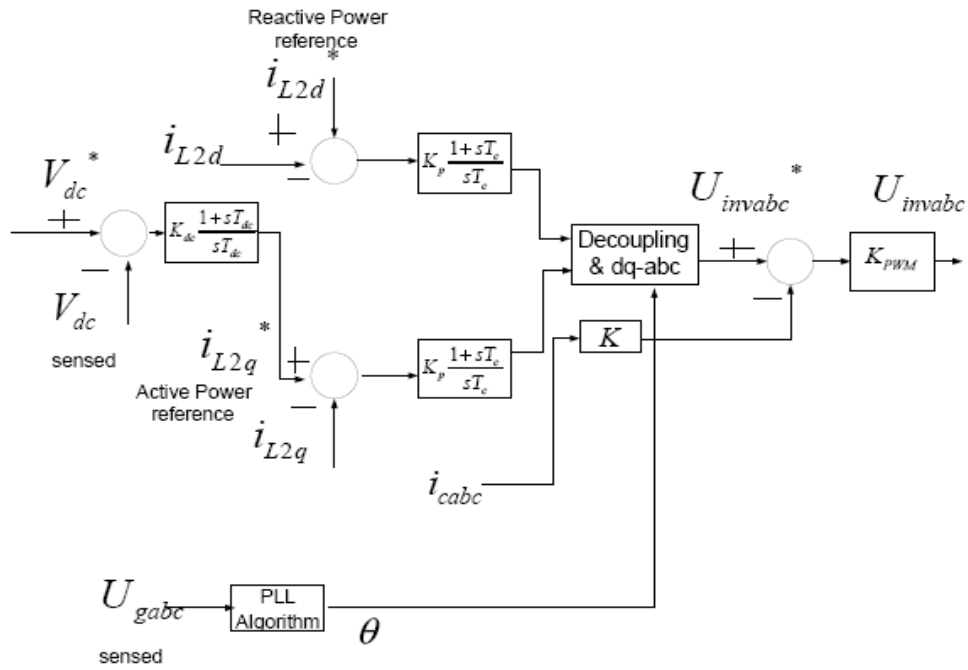
Figure 5.24: Vector control in grid parallel mode

5.6 Experimental set-up

Experimental setup consists of 10KVA power converter, LCL filter interfaced with grid, a diode-bridge rectifier, FPGA based controller and a PC programming for FPGA. Fig. 5.25 shows the main components of the experimental setup.

1. Diode Bridge Rectifier

   This is required for pre-charging the DC-bus of the power converter. This is fed from a 3-phase auto-transformer connected to grid. The autotransformer ended by a large capacitance at the output to make a pure DC. Autotransformer is adjusted to change the DC-link voltage appropriately. In the grid parallel mode of operation this precharging circuit is automatically disconnected as we boost up the DC-link voltage above the pre-charging voltage by the DC-link voltage control.

2. Pre-charging Auto-Transformer

   An auto transformer is placed before the grid and it is used to feeding the inverter DC-link voltage. This facility is used to vary the grid voltage also (we can operate the system at any grid voltage). In a practical power converter appropriately sized precharging resistor can be used.
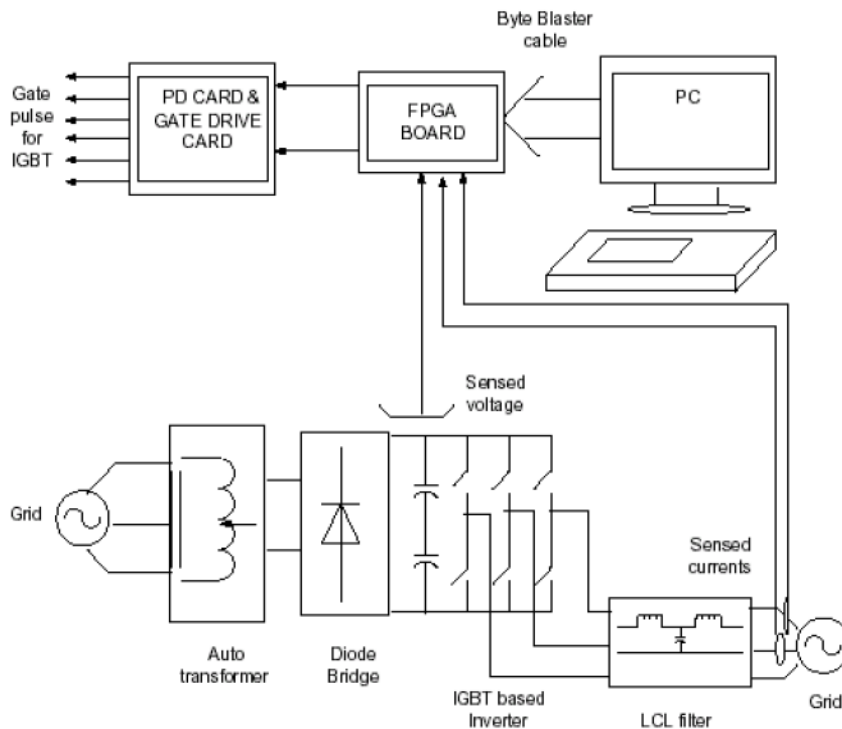
Figure 5.25: Complete Hardware Set-Up

3. IGBT based Inverter

   The power devices are used in the inverter are IGBTs . There are three legs in the inverter with two IGBTs (one module) in each leg. IGBTs are mounted on heat sink and are connected to the DC bus voltage via DC bus bar. The additional components of the IGBT inverter are protection and delay card, gate drive card, front panel annunciation card and voltage and current sensing cards.

4. FPGA Controller

   The digital platform consists of FPGA device and other devices interfaced to FPGA. The devices interfaced include configuration device (EEPROM), ADC and DAC; dedicated I/O pins are also provided. The FPGA has logic elements arranged in rows and columns. Each logic elements has certain hardware resources, which will be utilized to realize the user logic. The vertical and horizontal interconnects of varying speeds provide signal interconnects to implement the custom logic. The choice of an FPGA device for a given application is based on the size required (no. of logic elements), clock speed and number of I/O pins. ALTERA EP1CQ240C8 is found to be suitable for the given platform. The resources available in this device are listed in Table 5.1. The main components of the FPGA controller board is as follows:

- Configuration Device: The configuration device is an EEPROM (EPCS41N) which is used to a PC through a parallel port or USB using Byte blaster II or USB blaster cable. The digital design for the implementation of the proposed scheme is done using Quartus-II tool (Alteras design tool for FPGA) and the output file after compilation is downloaded to EEPROM through Byte blaster II or USB blaster cable.

- ALTERA FPGA device data
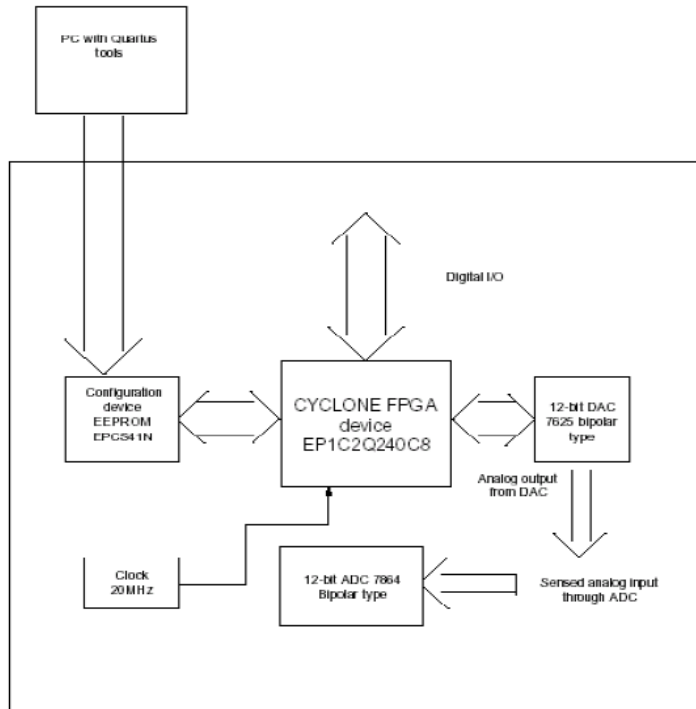
Figure 5.26: Block diagram of the FPGA Board

- Analog to Digital converter (ADC): ADC on the board, AD7864AS-1 of analog devices, is used to convert the analog input signals from the system to digital signals which are used for further processing. This MQFP packaged, 12 bit, 44-pins simultaneous ADC has 4 channels with a conversion time of 1.6 μs per channel. There are four such ADCs on the board and hence can take up to 16-analog input.

- Digital to Analog converter (DAC): DAC on the board, DAC-7625U, is used to output the digital variables in the controller in analog form. The DAC is TTL devices working with +5V and -5V power supply. This is a 12-bit, 28 pins DAC of TEXAS has 4 channels with conversion time of 10 μs.

Part Number	EP1C12Q240C8
Manufacturer	Altera
Number of pins	240
Number of I/O pins	173
Total internal memory bits	2,39,616
Package	PQFP
Number of logic elements	12,000
Number of PLLs	2
Maximum clock frequency using PLL	275MHz

Table 5.1: ALTERA FPGA device data

- Digital I/Os: Dedicated digital I/Os are necessary to interface to ADC, DAC etc which are present on the board. Apart from that 56 I/O pins are provided for the user to interface application specific hardware.

5.7   Experimental results

5.7.1   Implementation stages

The implementation can be done divided into two stages
(a) The first stage involved estimation and calculation of different quantities such as sine, cosine tables, PWM switching patterns, etc.
(b) The second stage involved controller design and realization of the overall system in the FPGA controller.

The experiments carried out focussed on the active damping performance of the inverter with LCL filter. The ac voltage was limited to less than 200V due to limitations of the voltage sensor card. The results of the experiments are given in Figs 5.27 - 5.36.
The controller was tested to check the ability of the system to function as a PWM rectifier. Figs. 5.27 and 5.28 show the transient ability of the grid connected inverter to regulate DC bus voltage in response to a change in reference command. Fig. 5.29 shown that there can be a significant current at the filter resonant frequency without any damping. The level of damping can be improved based on the state feedback gains. Appropriate

gains can be set based on the desired level of damping as shown in Figs. 5.30 and 5.31. The transient response of the power converter ac current command shows that resonate oscillations are suppressed even under transient as shown in Fig. 5.32. It can also be seen that the active damping acts rapidly in a couple of milliseconds after enabling of the damping controller in Fig. 5.34. The rapid response of the active damping loop indicates that it can be designed such that it does not interfere with the current control and voltage control loop that are used in active front end converters.

5.7.2 Summary

Its is seen that damping is an important consideration in higher order filter design. A simple state feedback gain based damping controller has been analysed. The performance of such a controller is seen to adequate for a wide range of operating conditions.
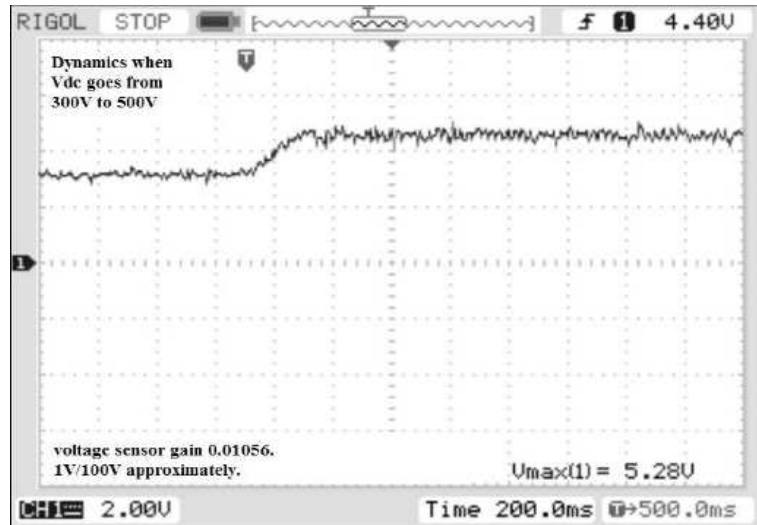
Figure 5.27: DC-Bus control test (voltage rise)
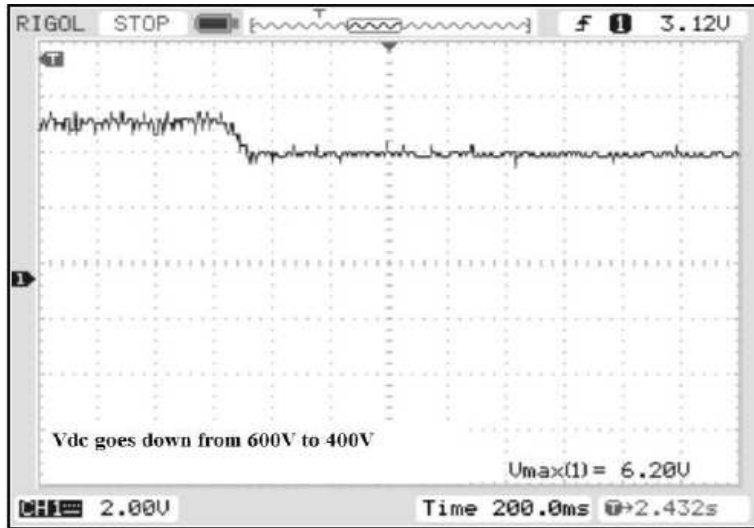
Figure 5.28: DC-Bus control test (voltage falling)
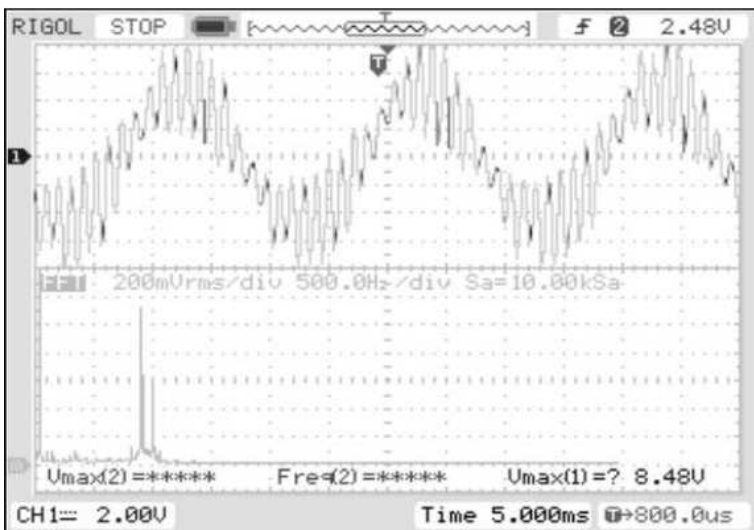
Figure 5.29: Distorted current from grid (full of resonance)
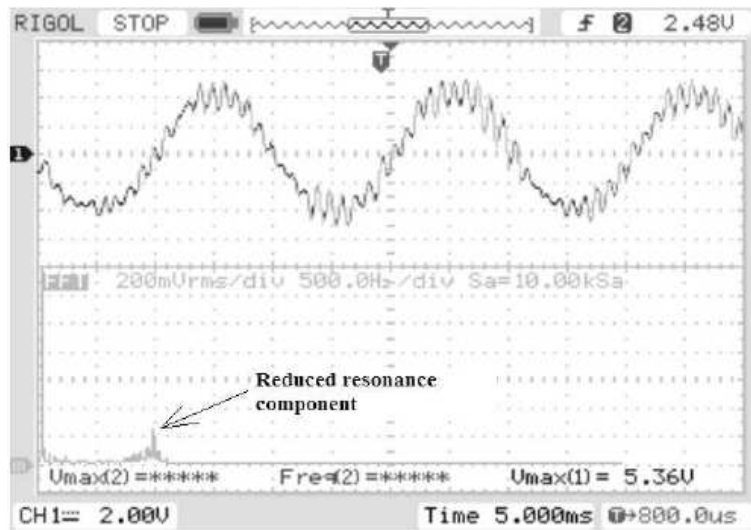
Figure 5.30: Less distorted current grid (state weightage K=10)
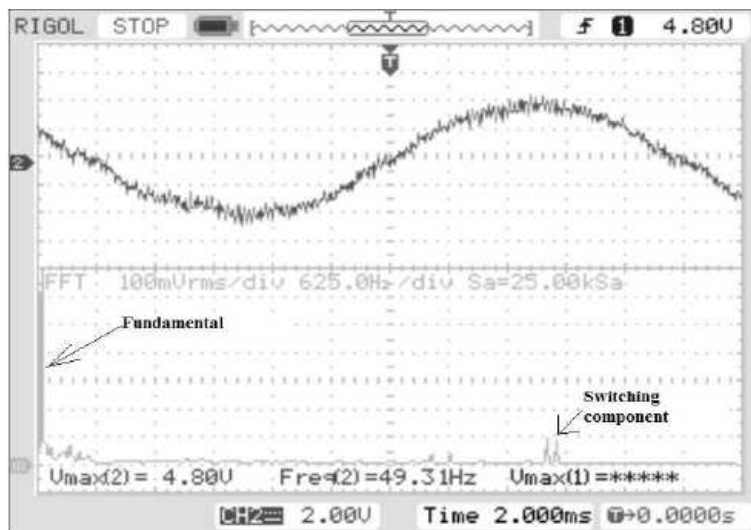
Figure 5.31: Smooth current from grid (state weightage 25) and its FFT
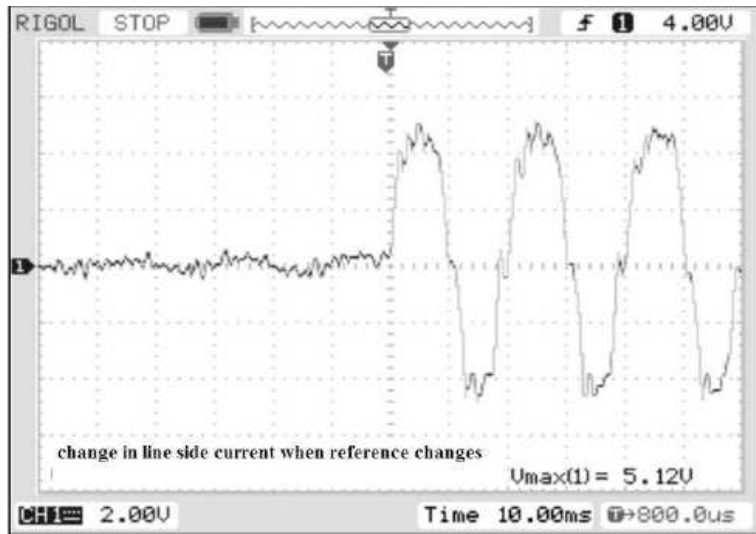
Figure 5.32: Grid side current dynamics when sudden change in load.
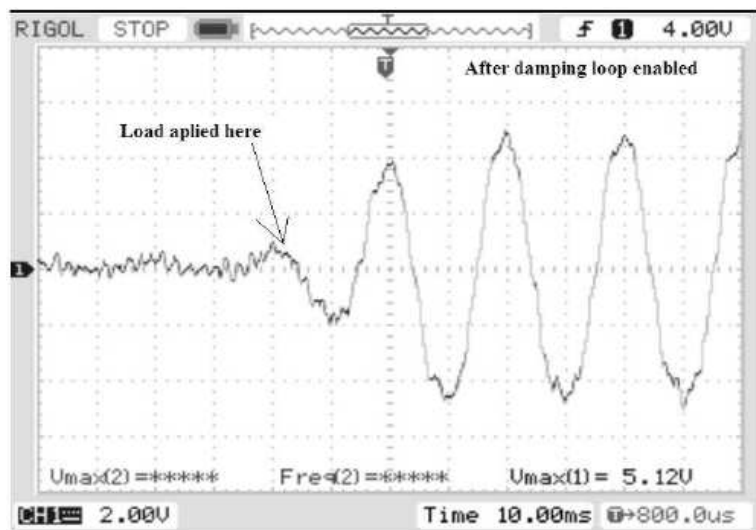
Figure 5.33: Grid side current dynamics when sudden change in load
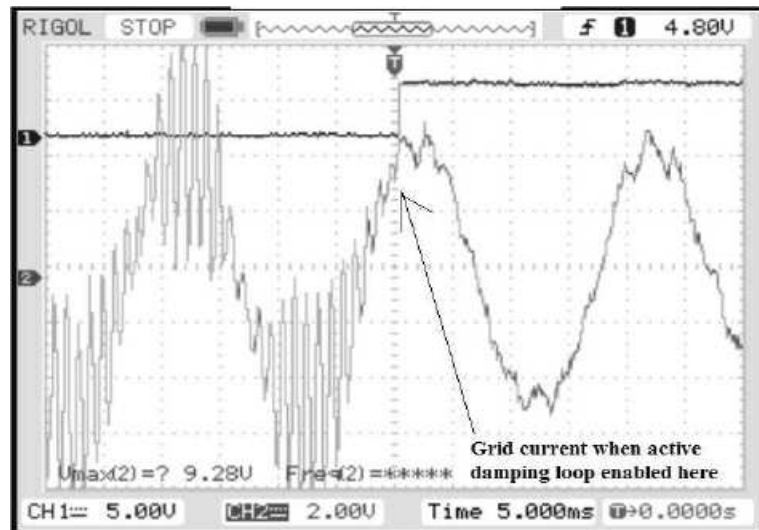
Figure 5.34: Line side current when active damping is being enabled mid-way
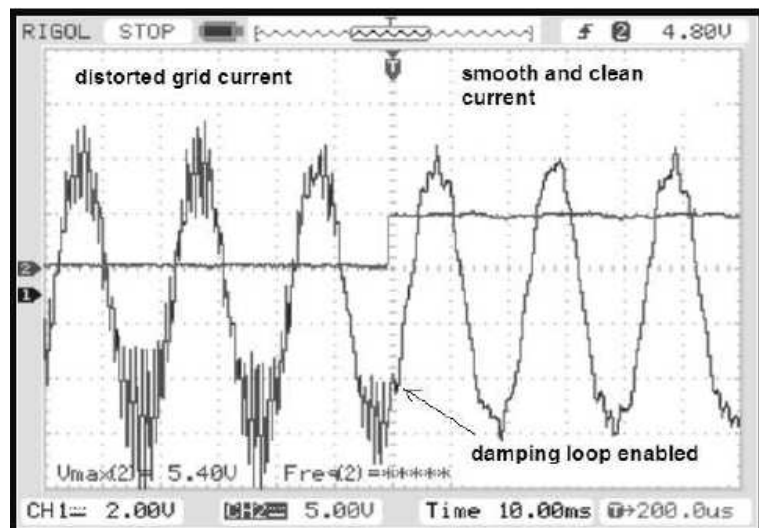
Figure 5.35: Active damping loop enabled mid-way with BW=1.2kHz
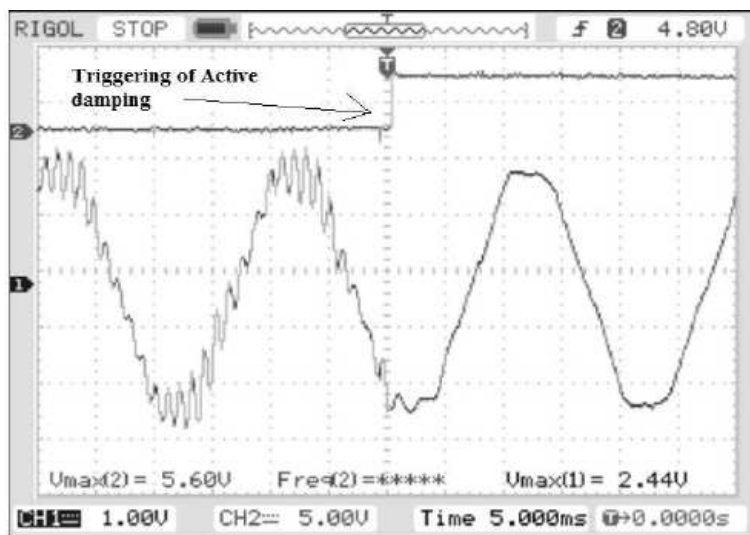
Figure 5.36: Distortion in utility voltage and smoothing out by active damping

5.8   References

1. V. Blasko and V. Kaura, A new mathematical model and control of a three-phase AC-DC voltage source converter, IEEE Trans. Power Electron., vol. 12, pp. 116123, Jan. 1997.

2. M. Liserre, F. Blaabjerg, and S. Hansen, Design and control of an LCL-filter based active rectifier, in Proc. IAS01, Sept./Oct. 2001, pp. 299307.

3. V. Blasko and V. Kaura, A novel control to actively damp resonance in input lc filter of a three-phase voltage source converter, IEEE Trans. Ind. Applicat., vol. 33, pp. 542550, Mar.Apr. 1997.

4. R. W. Erickson and D. Maksimovic, Fundamentals of Power Electronics. Boston, MA: Kluwer, 2001.

5. M. Liserre, A. DellAquila, and F. Blaabjerg, Stability improvements of an LCL-filter based three-phase active rectifier, in Proc. PESC02, June 2002, pp. 11951201.

6. P. A. Dahono, A control method to damp oscillation in the input LC filter of AC-DC PWM converters, in Proc. PESC02, June 2002, pp. 16301635.

7. E. Twining and D. G. Holmes, Grid current regulation of a three-phase voltage source inverter with an LCL input filter, in Proc. PESC02, June 2002, pp. 11891194.

8. N. Abdel-Rahim and J. E. Quaicoe, Modeling and analysis of a feedback control strategy for three-phase voltage-source utility interface systems, in Proc. 29th IAS Annu. Meeting, 1994, pp. 895902.

9. M. Lindgren and J. Svensson, Control of a voltage-source converter connected to the grid through an LCL-filter-application to active filtering, in Proc. Power Electron. Spec. Conf. (PESC98), Fukuoka, Japan, 1998.

10. Poh Chiang Loh. Analysis of Multiloop Control Strategies for LC/CL/LCL-Filtered Voltage-Source and Current-Source Inverters, IEEE Trans on Industry Applications, 2005, 2(41):644-654.

11. R. Teodorescu, F.Blaabjerg, U. Borup and M.Liserre. A New Control Structure for Grid-Connected LCL PV Inverters with Zero Steady- State Error and Selective Harmonic Compensation, APEC, 2004, vol.1: 580-586

12. Hamid R. Karshenas and Hadi Saghafi. Basic Critia in Designing LCL Filters for Grid Connected Converters, IEEE ISIE, 2006: 1996-2000

13. F.A. Magueed and J. Svensson, Control of VSC connected to the grid through LCL-filter to achieve balanced currents, in Proc. IEEE Industry Applications Society Annual Meeting 2005, vol. 1, pp. 572-8.

14. M. Liserre, A. DellAquila, and F. Blaabjerg, Genetic algorithm-based design of the active damping for an LCL-filter three-phase active rectifier, IEEE Transactions on Power Electronics, vol. 19, no. 1, pp. 76-86, 2004.

15. M. Prodanovic and T.C. Green, Control and filter design of three-phase inverters for high power quality grid connection, IEEE Transactions on Power Electronics, vol. 18, no. 1, pp. 373-80, 2003.

16. Vector control of three-phase AC/DC front-end converter - J S SIVA PRASAD, TUSHAR BHAVSAR, RAJESH GHOSH and G NARAYANAN. Sadhana Vol. 33, Part 5, October 2008, pp. 591613.

17. Operation of a three phase - Phase Locked Loop system under distorted utility conditions - Vikram Kaura, Vladimir Blasko. IEEE Transactions 1996.

Chapter 6

Experimental Results and Optimized LCL Filter Design

6.1 Introduction

This chapter discusses some of the experimental results which were used to verify the filter design model derived in the previous chapters. All aspects of the design process were tested and verified by actual experiments to confirm the design assumptions. The frequency response characteristics of the LCL filter configuration is obtained from a network analyzer. Harmonics are sampled to ensure the output current conforms to the recommended IEEE current harmonic limits. Special attention is given to verify the power loss and thermal models. Based on the percent of match between the assumed model and actual experimental data, new predictions are made to find the most efficient LCL filter combination which still gives the required harmonic filtering.

6.2 LCL filter parameter ratings

	R	Y	B
L_1 (mH)	3.385	3.374	3.349
L_2 (mH)	3.439	3.407	3.369
Damping branch	C_1=8μF	C_d=8μF	R_d=25 Ω

Table 6.1: LCL filter values for Ferrite core inductors

	R	Y	B
L_1 (mH)	5.434	5.292	5.374
L_2 (mH)	5.323	5.266	5.323
Damping branch	$C_1=6\mu F$	$C_d=6\mu F$	$R_d=25\ \Omega$

Table 6.2: LCL filter values for Amorphous core inductors

	R	Y	B
L_1 (mH)	1.737	1.784	1.737
L_2 (mH)	1.772	1.772	1.757
Damping branch	$C_1=10\mu F$	$C_d=10\mu F$	$R_d=10\ \Omega$

Table 6.3: LCL filter values for Powder core inductors

6.3   Frequency response

The impedence frequency response of the individual L and C components was measured to evaluate the differential mode parasitic impedances of each filter component. The differential mode impedence model of all inductors was found to be

$$Z_L(s) = (sL+R)||\frac{1}{sC} \tag{6.1}$$

and the differential mode impedence model of the AC capacitors was

$$Z_C(s) = \frac{1}{sC} + R + sL \tag{6.2}$$

It was observed that parasitics of the individual L and C were insignificant at the frequency range of operation of the LCL filter. All the filter components showed reasonable expected operation in the frequency range of operation (Figures 6.1-6.5).

The frequency response of the LCL filter was measured using an analog network analyzer manufactured by AP Instruments. The network analyzer has a frequency range from 0.01 Hz to 15 MHz, with a maximum output of 1.77V. Current measurements were made with Textronix TCP300 AC/DC current probe and amplifier which has a bandwidth of 120 MHz. All the transfer functions of the LCL filter as detailed in chapter 1 were measured for different combination of L and C with each measurement in the frequency range of 10 Hz to 1 MHz with atleast 1000 data points, each point averaged 40 times. Figures 6.6-6.11 show the **actual** output of the network analyzer for the transfer func-

tions of $i_g/v_i(v_g=0)$ and $v_g/v_i(i_g=0)$ compared with the **simulated** frequency response. The figures show the effect of damping with the Q-factor reducing considerably at the resonant frequency. Significant deviations in magnitude and phase can be observed in the frequency response characteristics from the expected ideal characteristics at frequencies beyond 100kHz. These deviations are caused by the parasitic impedances of the individual filter components which are dominant at such high frequencies.
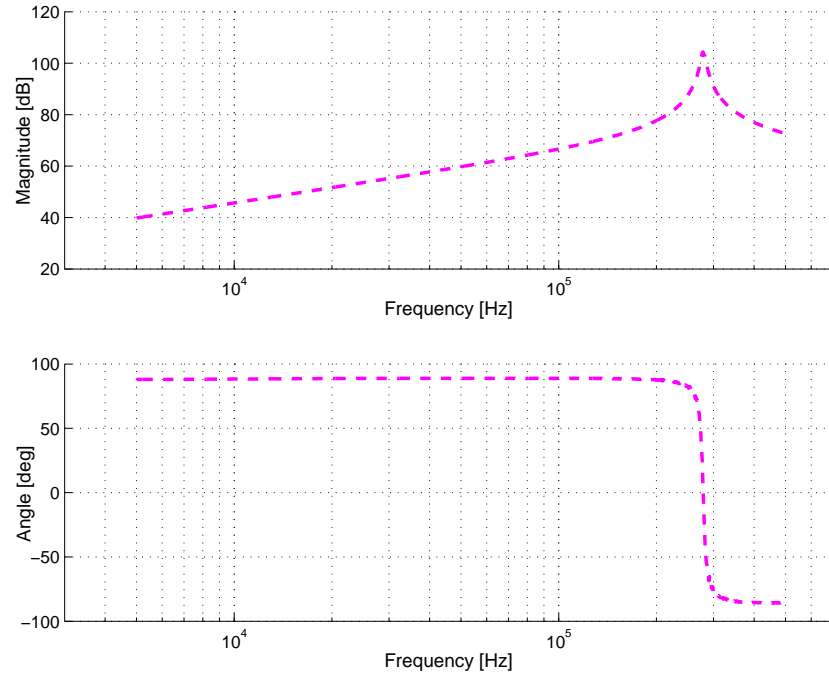
Figure 6.1: Differential mode impedence response 5 kHz to 500 kHz; Ferrite core inductor
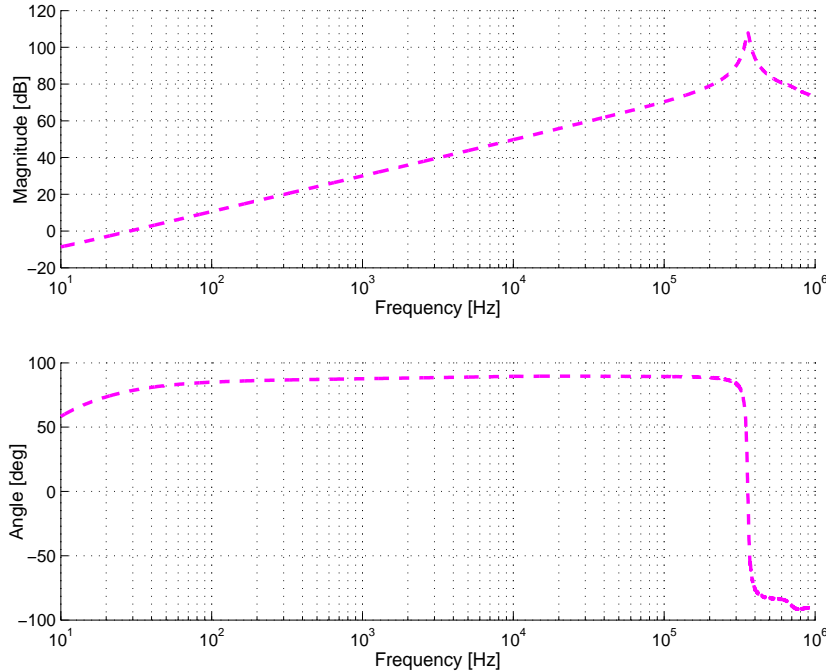
Figure 6.2: Differential mode impedence response 10 Hz to 1 MHz; Amorphous core 367S inductor
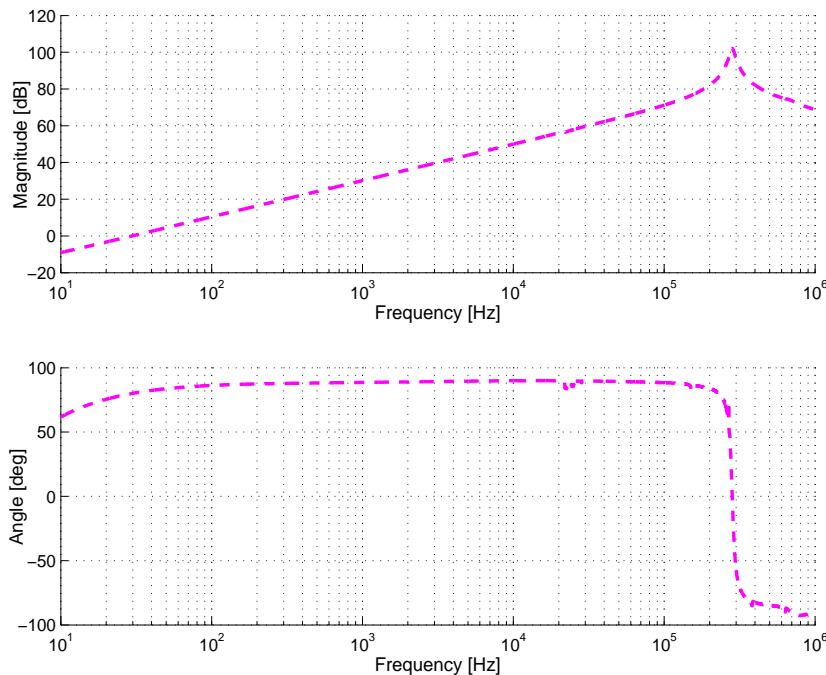
Figure 6.3: Differential mode impedence response 10 Hz to 1 MHz; Amorphous core 630 inductor
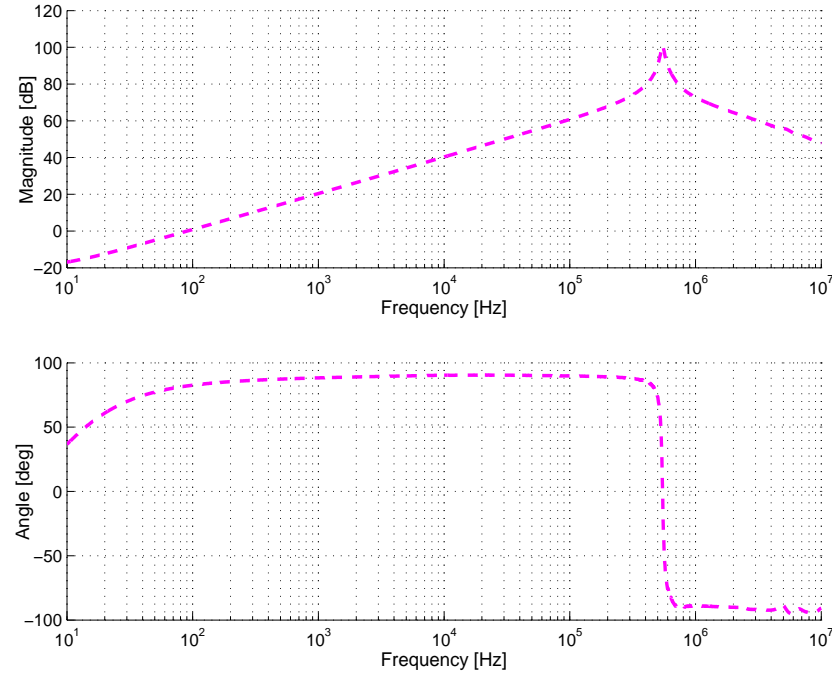
Figure 6.4: Differential mode impedence response 10 Hz to 1 MHz; Powder core inductor, foil winding
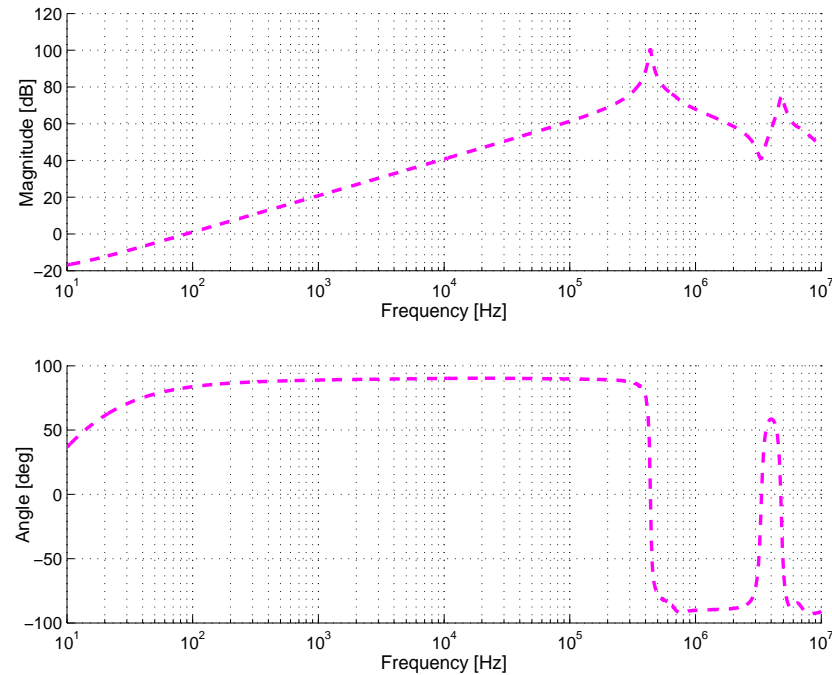
Figure 6.5: Differential mode impedence response 10 Hz to 1 MHz; Powder core inductor, round wire winding
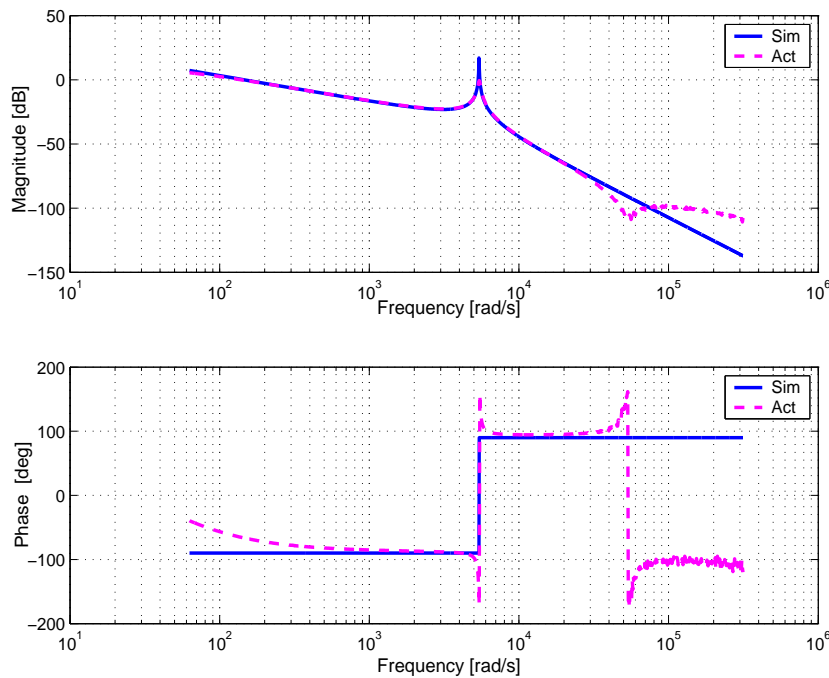
Figure 6.6: LCL filter response i_g/v_i (v_g=0); Ferrite core inductor, no damping
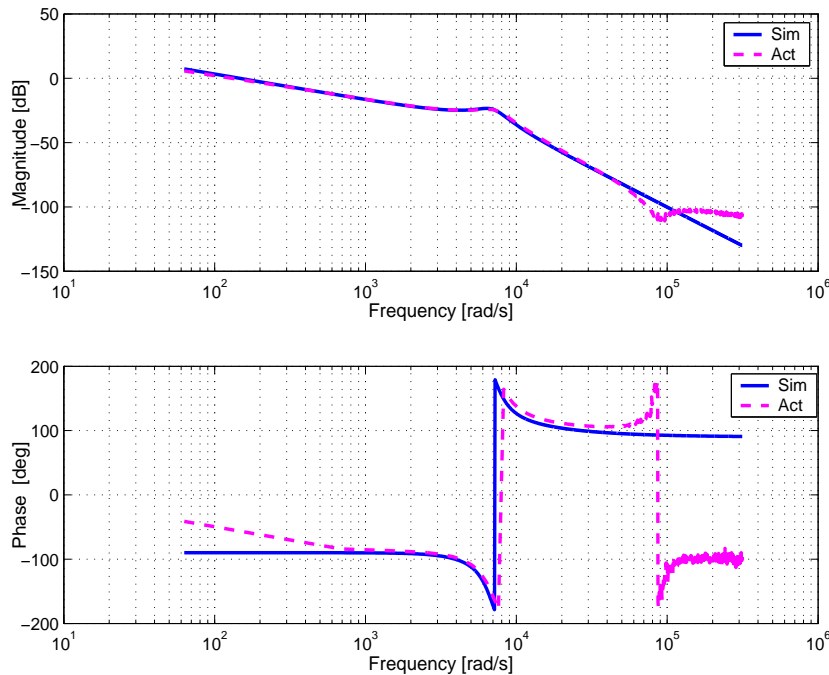
Figure 6.7: LCL filter response i_g/v_i (v_g=0); Ferrite core inductor, C_1=C_d=8μF, R_d=25Ω
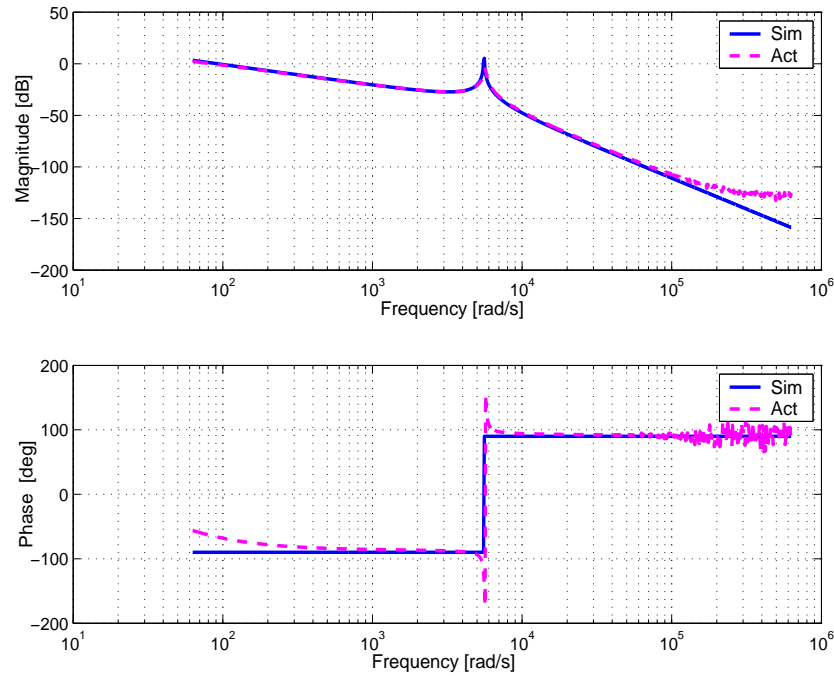
Figure 6.8: LCL filter response i_g/v_i (v_g=0); Amorphous core inductor, no damping
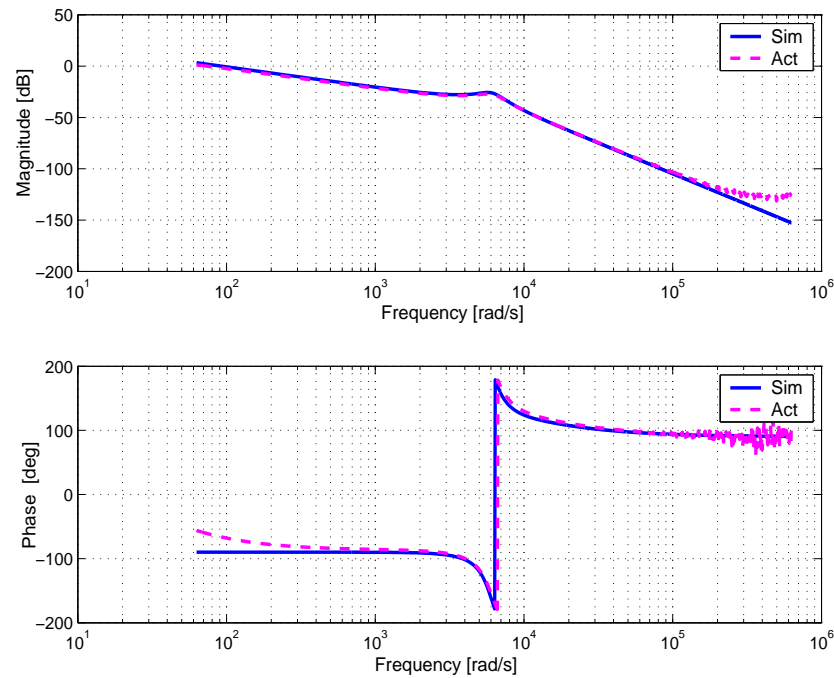
Figure 6.9: LCL filter response i_g/v_i (i_g=0); Amorphous core inductor, C_1=C_d=6μF, R_d=25Ω
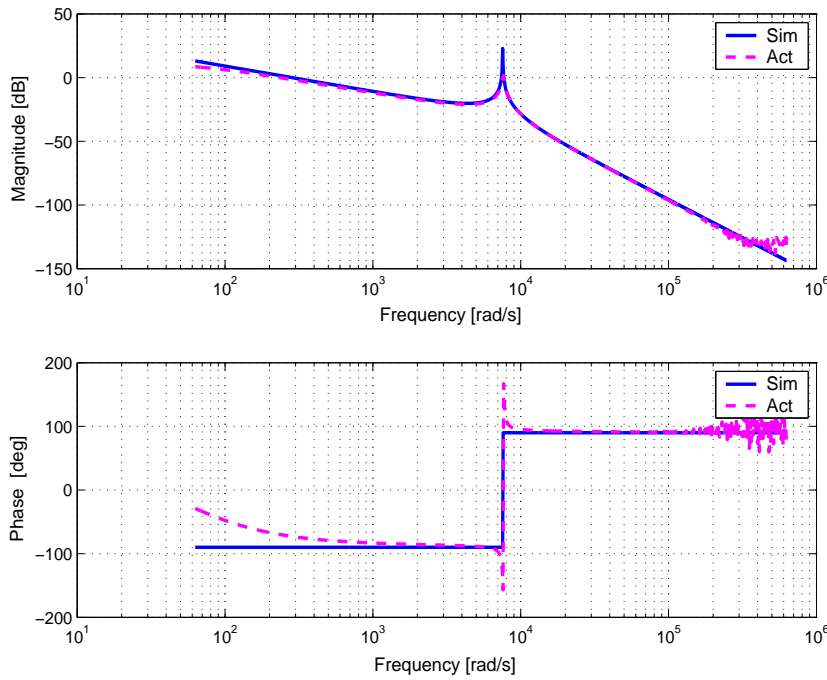
Figure 6.10: LCL filter response i_g/v_i (v_g=0); Powder core inductor, no damping
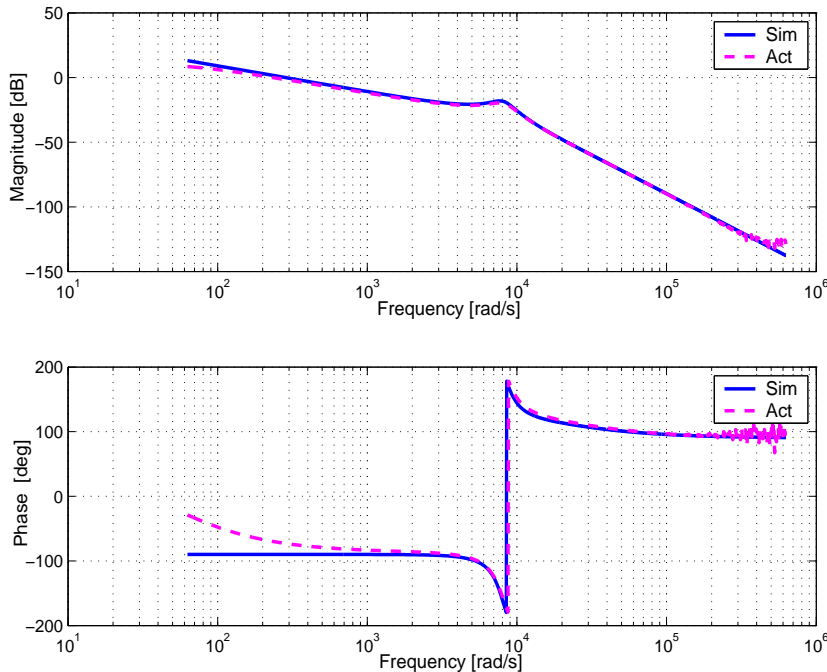
Figure 6.11: LCL filter response i_g/v_i (i_g=0); Powder core inductor, C_1=C_d=10μF, R_d=10Ω

6.4 Harmonic analysis

IEEE 519-1992 'Recommended Practices and Requirements for Harmonic Control in Electrical Power Systems' defines distortion limits for both current and voltage in order to minimize interference between electrical equipment (Table 6.5). It is a system standard applied at the point of common coupling of all linear and nonlinear loads, and assumes steady state operation. Most utilities insist that current harmonic limits should be met at the output terminals of the nonlinear equipment. Hence to measure the effectiveness of the LCL filter, it is important to measure the output current harmonics at inductor L_2 which is connected to the point of common coupling to grid.

Open loop tests were conducted with the 3 phase inverter switching at 10 kHz with the modulation index adjusted to get full rated current at full dc bus voltage of 600V. This test enabled us to test the ability of the filter to attenuate the high frequency current ripple under the worst possible ripple conditions of low modulation index and open loop sine triangle modulation.

The equation for calculating current Total Harmonic Distortion THD is

$$I_{THD} = \frac{\sqrt{I_2^2 + I_3^3 + I_4^2 + \dots}}{I_1} \times 100\% \tag{6.3}$$

The equation for calculating current Total Demand Distortion TDD is

$$I_{TDD} = \frac{\sqrt{I_2^2 + I_3^3 + I_4^2 + \dots}}{I_L} \times 100\% \tag{6.4}$$

Filter type	Modulation Index	Inverter side		Grid side	
		I_{nom} (A)	I_{sw} (A)	I_{nom} (A)	I_{sw} (A)
Ferrite	0.165	14.58	1.39	13.71	0.01
Amorphous	0.294	14.34	0.91	14.73	0.02
Powder	0.135	13.72	2.64	14.39	0.05

Table 6.4: Inverter settings for harmonic measurement; V_{dc} =600V, f_{sw}=10 kHz

Maximum Harmonic Current Distortion in Percent of I_L					
Individual Harmonic Order (Odd Harmonics)					
I_{SC}/I_L	<11	$11{\leq}h{<}17$	$17{\leq}h{<}23$	$23{\leq}h{<}35$	$35{\leq}h$	TDD
<20	4.0	2.0	1.5	0.6	**0.3**	**5.0**

Table 6.5: Current distortion limits for general distribution systems IEEE 519-1992

$L_1{=}L_2$	$C_1{=}C_d$	R_d	f_{res}	I_{nom}	I_{max}	I_{sw}/I_{max}	TDD
mH	μF	Ω	kHz	A	A	%	%
3.4	8	25	1	13.71	14.58	**0.08**	7.7
5.4	6	25	1	15.01	15.45	**0.09**	1.5
1.7	10	10	1.18	13.97	15.45	**0.32**	10

Table 6.6: Measured output current harmonics and TDD
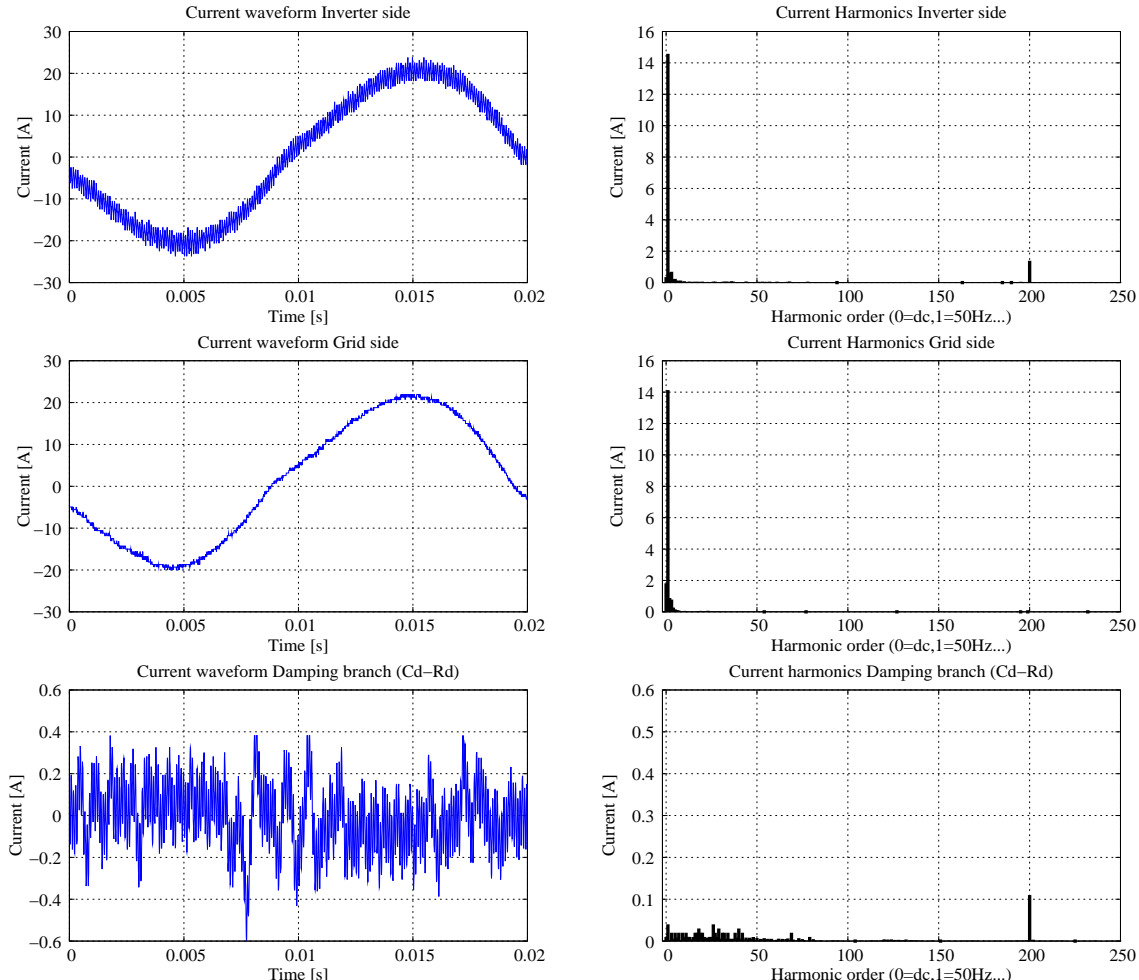
Figure 6.12: Current waveform and harmonic spectrum; Ferrite core inductor
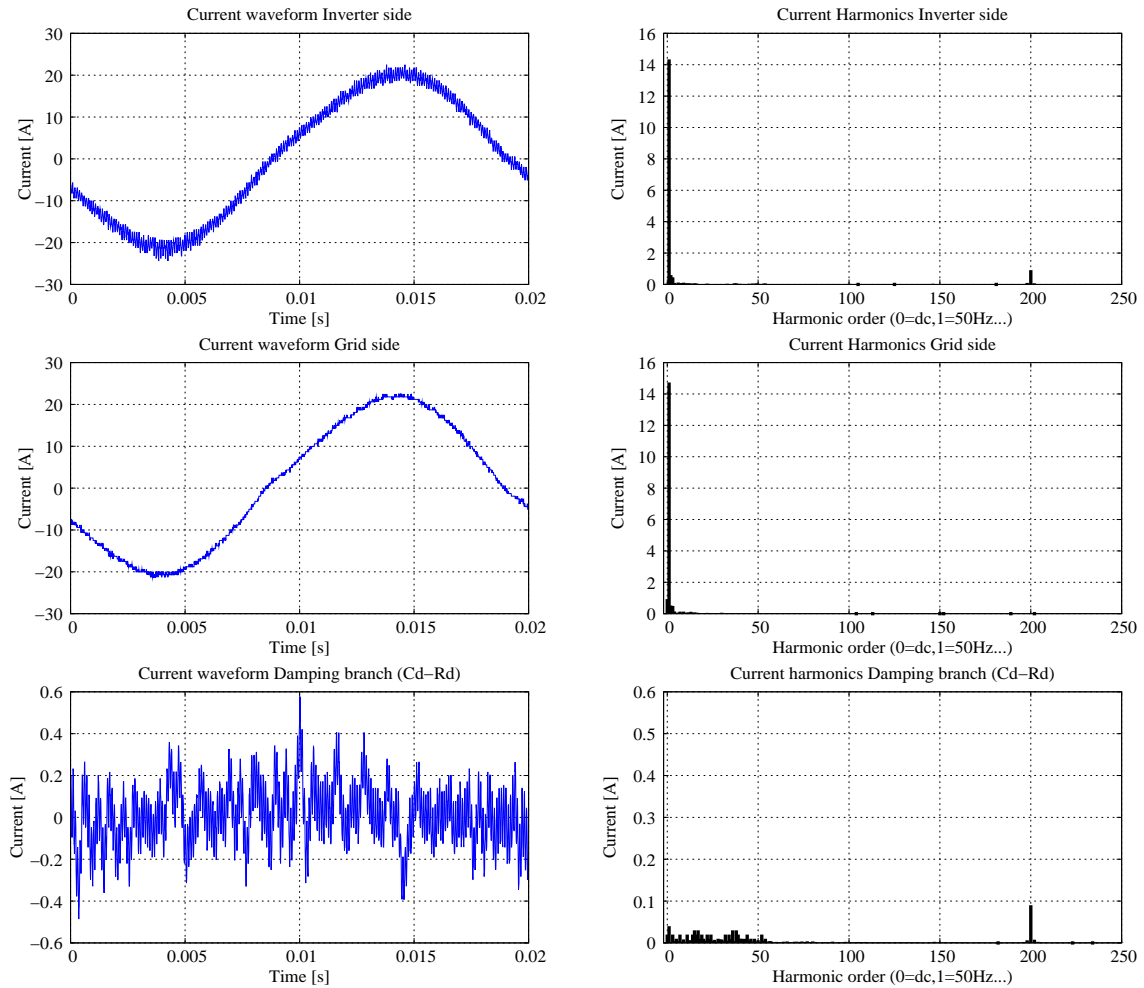
Figure 6.13: Current waveform and harmonic spectrum; Amorphous core inductor
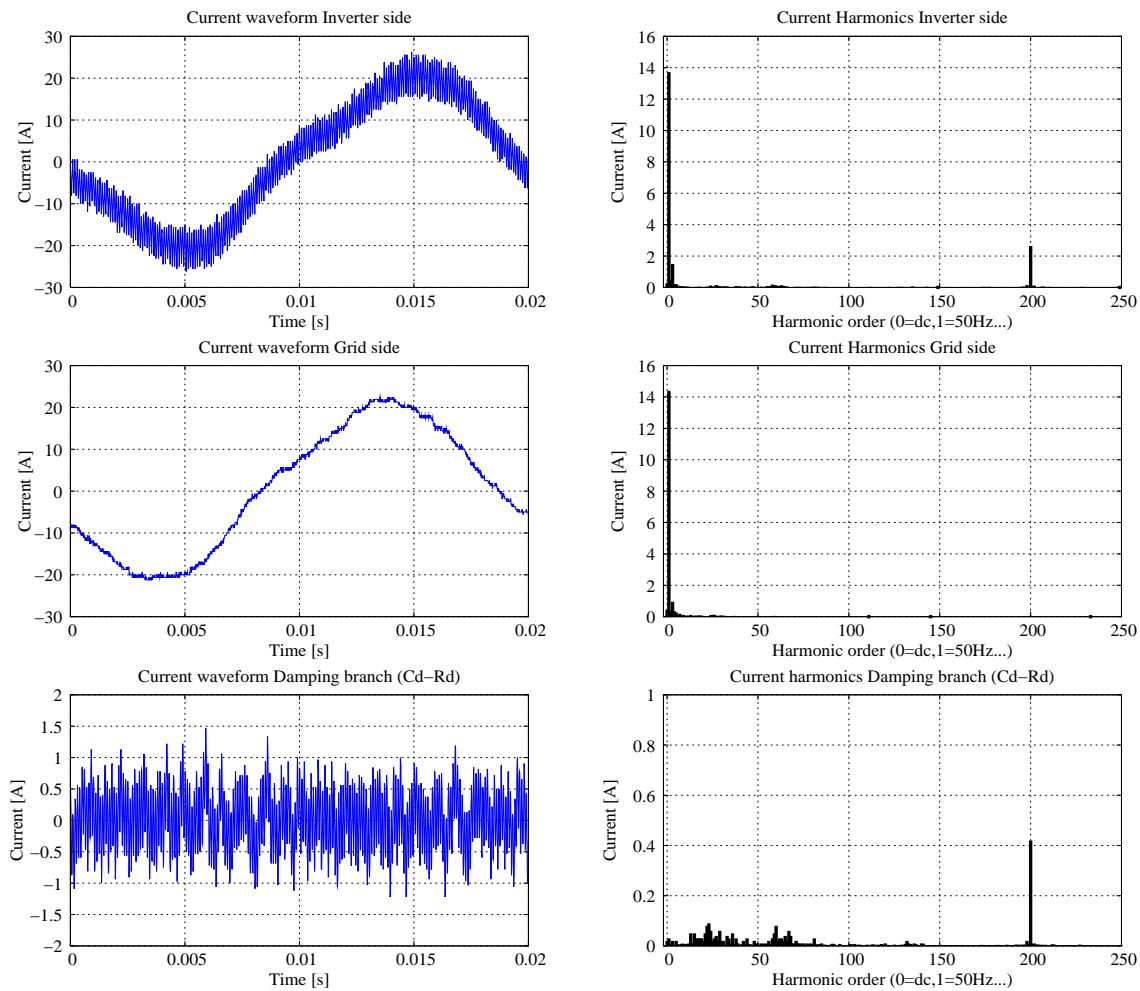
Figure 6.14: Current waveform and harmonic spectrum; Powder core inductor

6.5   Power loss

The efficiency of the LCL filter was tested under short circuit conditions (Fig. 6.15). The modulation method used was sine triangle modulation under open loop conditions. Additionally the dc bus mid-point was connected to the three phase capacitor star point. The combination of the low modulation index (to get rated current) and high dc bus voltage gave the worst case current ripple. Hence the losses in this section represent the highest possible losses for the LCL filter.

Tables 6.7-6.10 show the comparison between measured and calculated power loss. The "Designed" column shows the predicted current harmonics and power loss for the dominant harmonics of fundamental and switching frequency. The expected core loss for both fundamental and switching harmonic current is also shown as a single number. The "Actual" column shows the actual measured current harmonics and measured power loss. Harmonics were calculated from the current waveform sampled by a digital oscilloscope. Power measurements were made using a three phase six channel Yokogawa WT1600 digital power analyser. The "Expected" column shows the expected power loss -both copper and core, for the **actual** current harmonics, which were calculated by using the measured current harmonics in the power loss equations (Chapter 2). The last row shows the percent error between the measured (or actual) power loss and expected power loss.
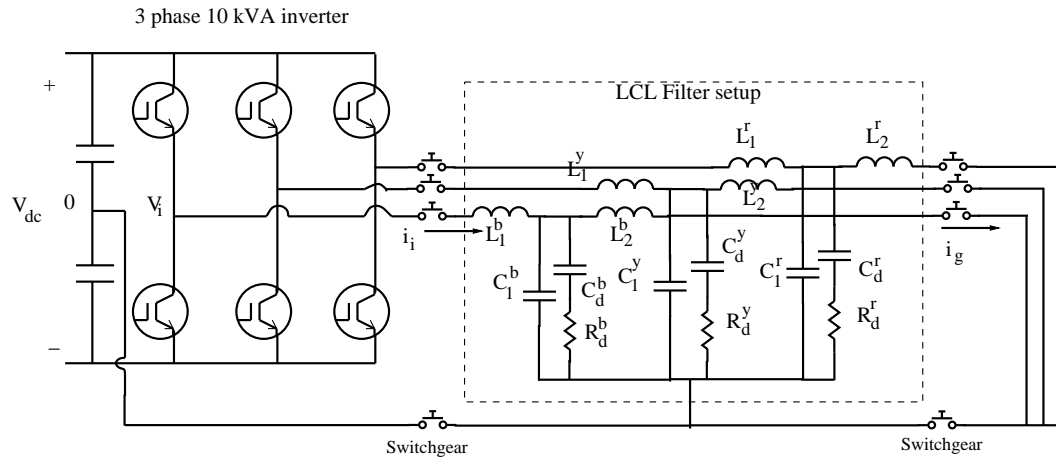
Figure 6.15: Power loss test setup

		Designed		Actual	Expected	
		A	W	A	A	W
Copper Loss	DC	0	0	5.445	5.445	2.938
	f_1	14.58	17.53	13.886	13.886	19.09
	SW	1.138	4.336	1.155	1.155	5.363
Core Loss (W)		*	0.052	*	*	*
Total Loss (W)		*	21.925	38.6	*	27.391
Error (%)		*	*	*	*	-29

Table 6.7: Comparison between designed efficiency and actual measured power loss;Ferrite core inductor-round wire winding

		Designed		Actual	Expected	
		A	W	A	A	W
Copper Loss	DC	0	0	0.264	0.264	*
	f_1	15.45	12.80	13.73	13.73	12.32
	SW	0.683	0.097	0.865	0.865	0.191
Core Loss (W)		*	3.857	*	*	6.379
Total Loss (W)		*	16.75	24	*	18.89
Error (%)		*	*	*	*	-21.3

Table 6.8: Comparison between designed efficiency and actual measured power loss; Amorphous core inductor-foil winding

		Designed		Actual	Expected	
		A	W	A	A	W
Copper Loss	DC	0	0	*	*	*
	f_1	15.45	12.18	14.29	14.29	12.71
	SW	2.115	0.494	2.741	2.741	1.012
Core Loss (W)		*	7.645	*	*	12.924
Total Loss (W)		*	20.31	35.7	*	26.64
Error (%)		*	*	*	*	-25.3

Table 6.9: Comparison between designed efficiency and actual measured power loss; Powder core inductor-foil winding

		Designed		Actual	Expected	
		A	W	A	A	W
Copper Loss	DC	0	0	*	*	*
	f_1	15.45	24.03	14.149	14.149	22.95
	SW	2.115	8.19	2.517	2.517	13.21
Core Loss (W)		*	4.766	*	*	12.924
Total Loss (W)		*	36.98	35.3	*	47.04
Error (%)		*	*	*	*	33.25

Table 6.10: Comparison between designed efficiency and actual measured power loss; Powder core inductor-round wire winding

6.6   Temperature rise

The thermal model from Chapter 2 was verified through DC temperature tests. All the inductors were connected in series with a adjustable DC current source. Initially current was set at the rated current of the inductor. The temperature of individual inductors was measured using K-type thermocouples embedded inside the winding of the inductor. In most cases, two thermocouples were used per inductor, one embedded close to the first turn ("inner") and the second at the last turn ("outer"). Concurrently, the electrical power loss in each inductor was accurately measured. When the inductor reached thermal stability the current setting was reduced to a new lower value. Again the temperature was tracked till it became constant. This ensured that precise steady state temperature reading was available for different power levels. The experiment was repeated for decreasing current levels –14 A, 10 A, 7.5 A, 5 A and 2.5 A.

Inductor type	Measured			Expected	
	Power loss W	Ambient °C	Inductor °C	Ambient °C	Inductor °C
Ferrite	38.8	30	88	25	91
Amorphous AMCC 367S	13.52	30	57	25	67
Amorphous AMCC 630	9.01	30	50	25	59
Powder foil winding	13.13	29	70	25	69
Powder round wire winding	13.32	29	70	25	72

Table 6.11: Theoretical temperature prediction and actual steady state temperature readings
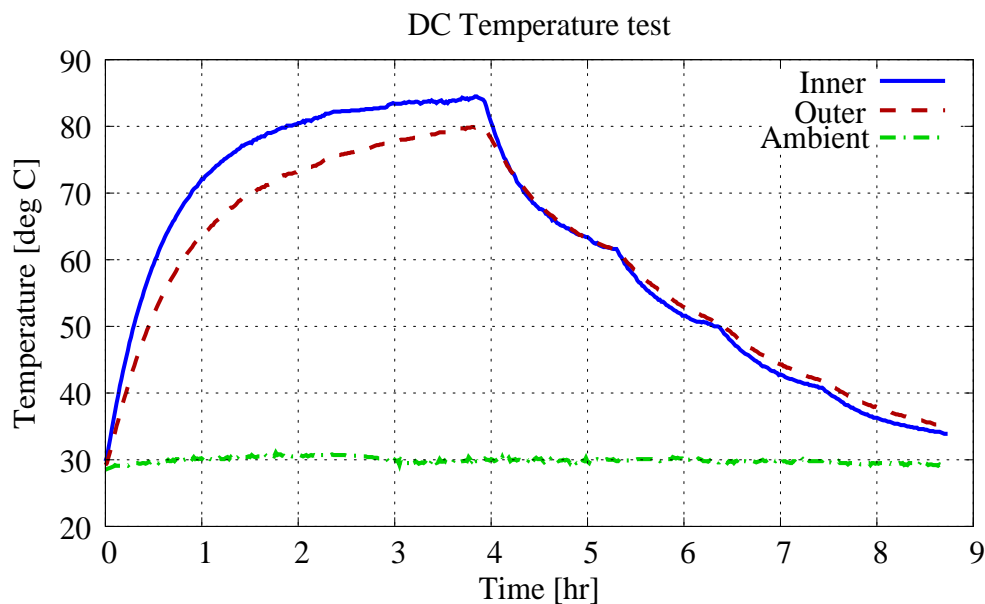
Figure 6.16: DC temperature test; Ferrite core inductor with round wire winding
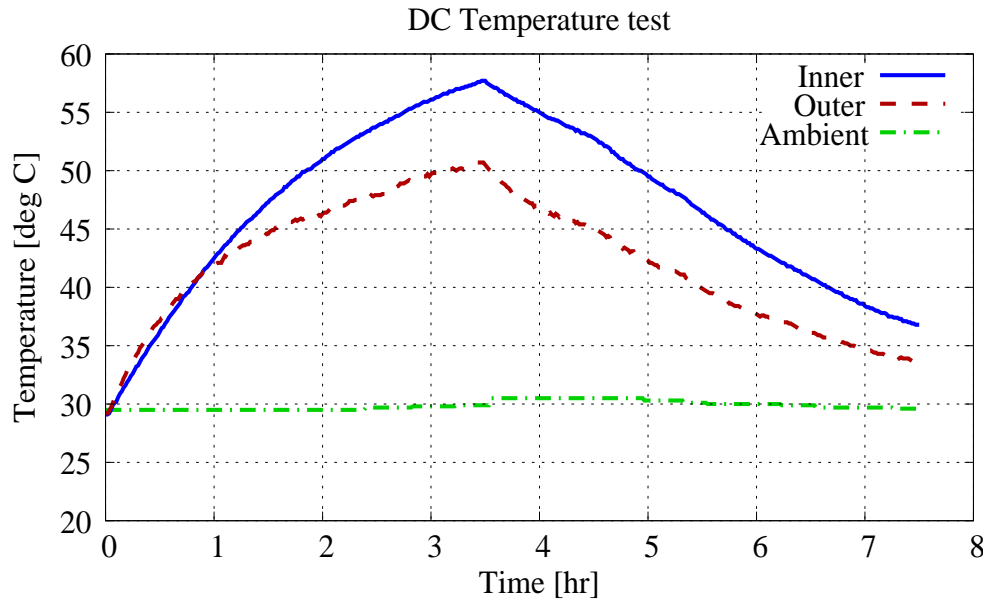
Figure 6.17: DC temperature test; Amorphous core AMCC367S inductor with foil winding
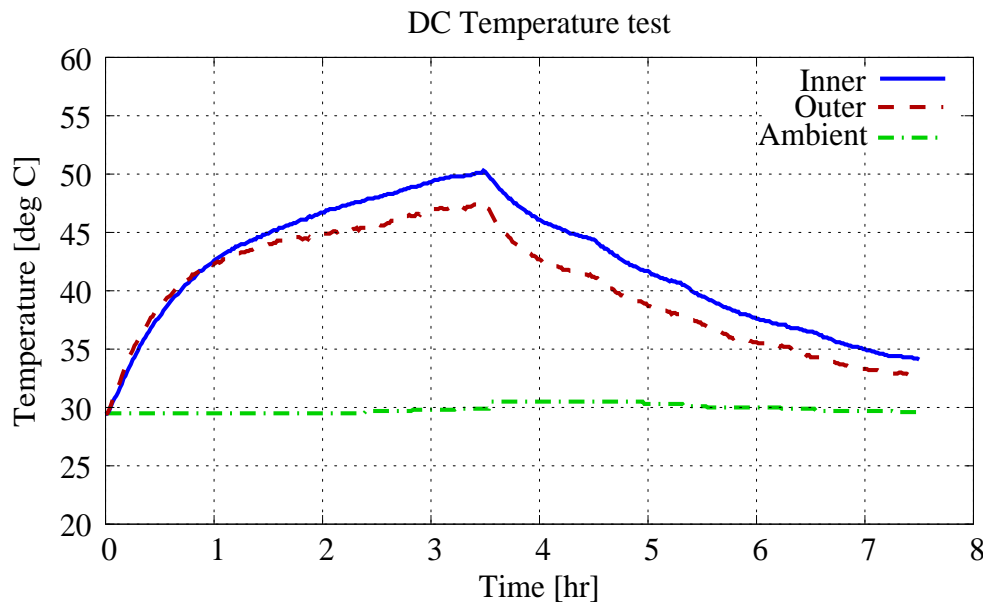
Figure 6.18: DC temperature test; Amorphous core AMCC630 inductor with foil winding
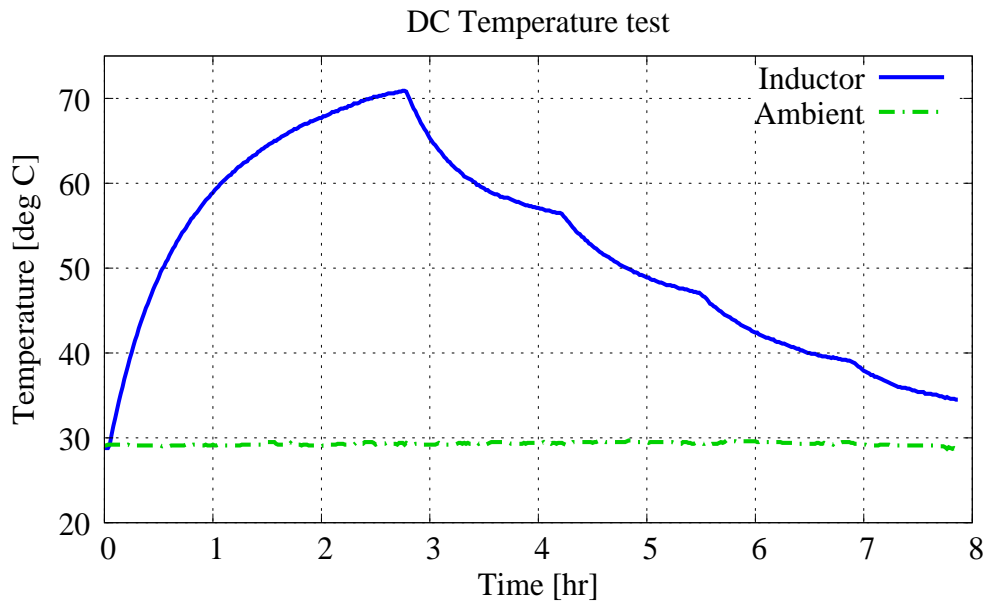
Figure 6.19: DC temperature test; Powder core inductor with foil winding
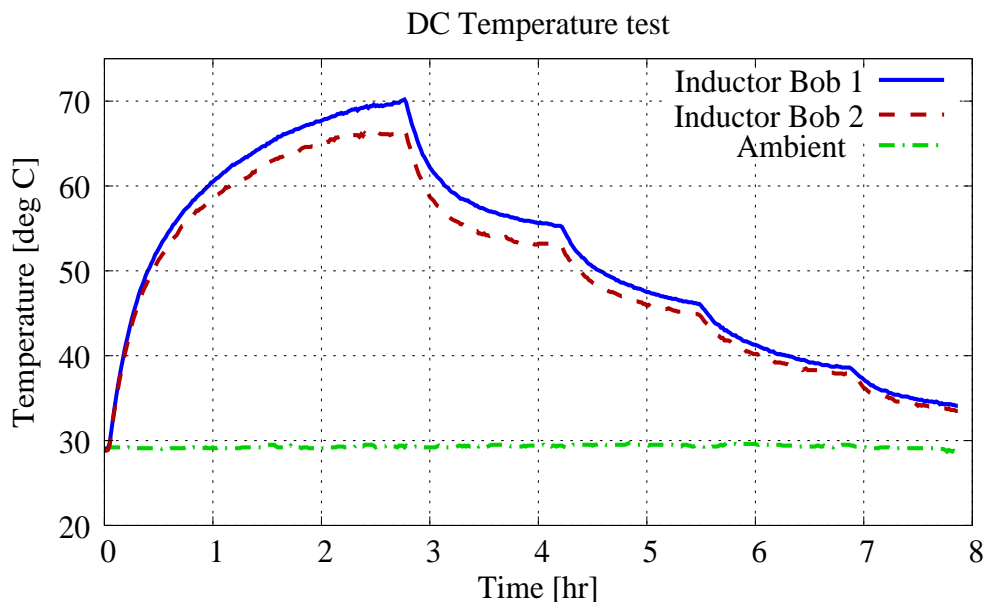
Figure 6.20: DC temperature test; Powder core inductor with round wire winding, two bobbin design

6.7   Minimum power loss design

As discussed earlier, losses in the inductor are quite significant and any efficiency and thermal optimization of the LCL filter will have to focus on the inductors L_1 and L_2 to make a noticeable difference in the efficiency of the overall filter. The cost of the passive filter components is another area where significant gains can be made by reducing the size and weight of the individual filter components. At the same time, the IEEE recommended limits for high frequency current ripple must also be met if the filter is to be used for a grid connected power converter. For a 10kVA system with a base voltage of V_{base}=239.6V operating at a switching frequency of 10kHz with the dc bus voltage at 861V, the minimum $L_{pu} = L_{1(pu)} + L_{2(pu)}$ is given by Eq. (1.70) (Chapter 1).

$$L_{pu} = \frac{1}{\omega_{sw(pu)} \left| \dfrac{i_{g(pu)}}{v_{i(pu)}} \right| \left| 1 - \dfrac{\omega^2_{sw(pu)}}{\omega^2_{res(pu)}} \right|} \tag{6.5}$$

$$L_{pu} = \frac{1}{200 \left(\dfrac{0.003}{0.898} \right) \left| 1 - \dfrac{200^2}{20^2} \right|} = 0.015 \tag{6.6}$$

The resonant frequency is set at 1kHz and voltage harmonic at switching frequency is assumed to be one-fourth of dc bus voltage.

Hence a minimum L_{pu} of 0.015pu is sufficient to meet IEEE recommendations for harmonics$\geq$35. The next step is to test if this is also the most *efficient* rating. The power loss in each individual component of the LCL filter should be examined to derive the most efficient filter configuration. The inverter-side inductor L_1 is subjected to both the fundamental load current and the switching frequency ripple current. The switching frequency ripple is attenuated sufficiently at the output of the filter, so that the power loss in the grid-side inductor will be almost exclusively because of the fundamental current. The power loss in the damping branch depends not only on the fundmental and switching frequency voltage ripple, but also the damping resistor R_d and the ratio of C_d/C_1.

The losses in an inductor depend on the type of core material and type of winding but there are certain trends that are common for all types of inductors. The copper losses at fundamental frequency directly depend on the number of turns of copper, so it will increase with higher L_{pu}. The copper losses at switching frequency is more sensitive to skin effect and proximity effect and will not change linearly with L_{pu}. In particular, losses in round wire windings are affected by the number of layers of winding. The

core loss at fundamental frequency for the magnetic materials used in high frequency operation is insignificant and can be usually ignored. But core loss at switching frequency is dependent on the flux density due to switching frequency current ripple and can be quite prominent in certain materials. High current ripple because of low L_{pu} will translate to higher core loss at switching frequency. Additionally, the total C_{pu} has to be increased to maintain the same resonant frequency while decreasing L_{pu}. The power loss in the damping circuit will increase linearly with C_{pu}.

The essence of the previous discussion is that as the L_{pu} is varied (with the minimum at 0.015 pu), the total power loss of the LCL filter will follow an approximate inverted bell shaped curve with high loss at low L_{pu} because of the higher current ripple and high loss again at high L_{pu} because of fundamental current. But there is an minimum point in this curve which will give the highest efficiency and the lowest total loss. At the same time, as this L_{pu} is greater than the minimum required, it will satisfy the IEEE requirements for filtering. The L_{pu} at which this minimum loss occurs will not be affected by the losses in the damping circuit, since this loss varies linearly. The subsequent figures investigate this optimum L_{pu} for inductors designed with different core materials and different windings. All the data points are viable designs with the least possible number of turns for each value of inductance and all designs ensure that flux density in the core is within the saturation limits. The total capacitance C_{pu} is adjusted to keep the resonant frequency at 1kHz in every case.

The minimum loss designs in Figures 6.21–6.42 are optimized considering only the LCL filter efficiency. But if we consider the entire power converter, the LCL filter is only one part of the entire converter hardware, and choice of most efficient L_{pu} can have implications for the overall efficiency of the power converter. The LCL filter is designed for high power voltage source converters switching at a minimum of 10kHz. IGBTs are the most suitable switching devices for such applications. The switching loss in IGBTs is approximately unaffected by the high frequency current ripple assuming same turn on and turn off loss. The conduction loss depends on the on-state resistance R_{DS} which actually varies with the current, which means it will be affected by the current ripple. But since R_{DS} of most common IGBT devices is less the dc resistance of the total inductance of the LCL filter, the minimum loss design is not expected to significantly increase the losses in the IGBT devices.

6.8   Loss profile for ferrite core inductors

Figures 6.21–6.28 show the power loss and temperature rise for the various components of the LCL filter for increasing L_{pu}. The inductors used are Ferrite core inductors with round wire winding. Figures 6.21–6.24 detail the various losses and estimated temperature of the inverter-side inductor L_1. From Fig. 6.21, we can observe the effect of proximity effect on the copper loss at switching frequency. As L_{pu} changes from 0.04pu to 0.05pu, the number of layers is incremented by one, hence there is a noticeable rise in the copper loss. Subsequently, as the current ripple decreases (because of higher L_{pu}) the switching frequency copper loss reduces till the number of layers is again increased at 0.11pu. But the fundamental copper loss is independent of decrease in current ripple. Core losses do not affect the total loss after inductance is increased beyond 0.04pu. Fig. 6.23 shows the total loss and the minimum loss point occurring at 0.04pu. Fig. 6.24 shows the operating temperature which mirrors the total loss in shape. It can be seen that upto a 10^oC reduction in temperature is possible at the optimum design point, corresponding to an approximate increase in component life by a factor of two.

Figures 6.25–6.26 show the losses in grid-side inductor L_2, where the switching current ripple is sufficiently attenuated and therefore does not contribute to power loss. The loss in the damping branch C_1-C_d-R_d is shown in Fig 6.27. The resonant frequency is kept constant, and hence as L_{pu} is increased, C_{pu} is simultaneously reduced, which also reduces the damping losses. The total LCL filter losses are shown in Fig 6.28. We can observe that the minimum power loss point for L_1 and the entire LCL filter are essentially same.
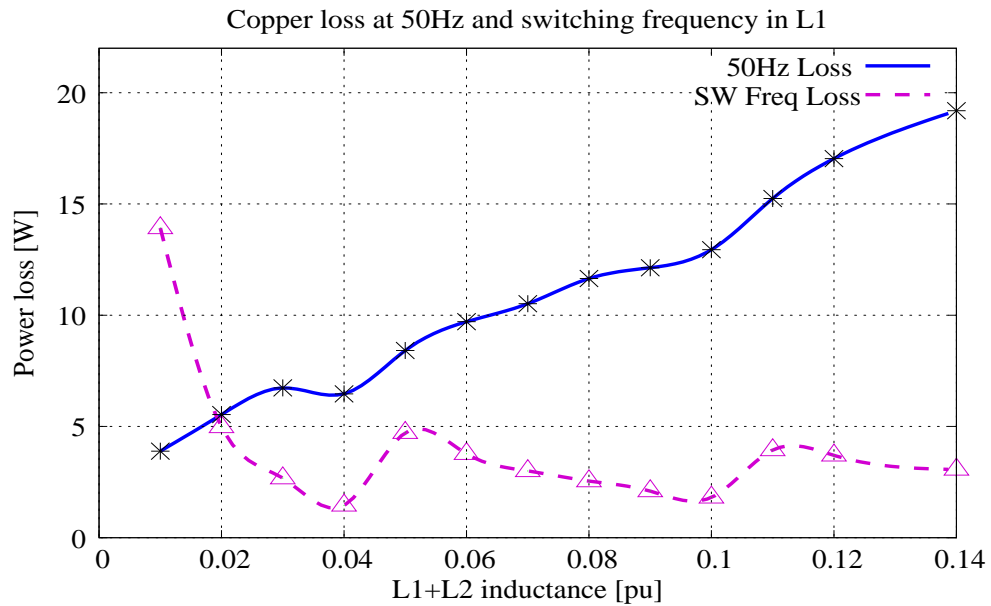
Figure 6.21: Estimated copper loss in L_1 for different pu ratings of L_1+L_2; Ferrite core inductor with round wire winding
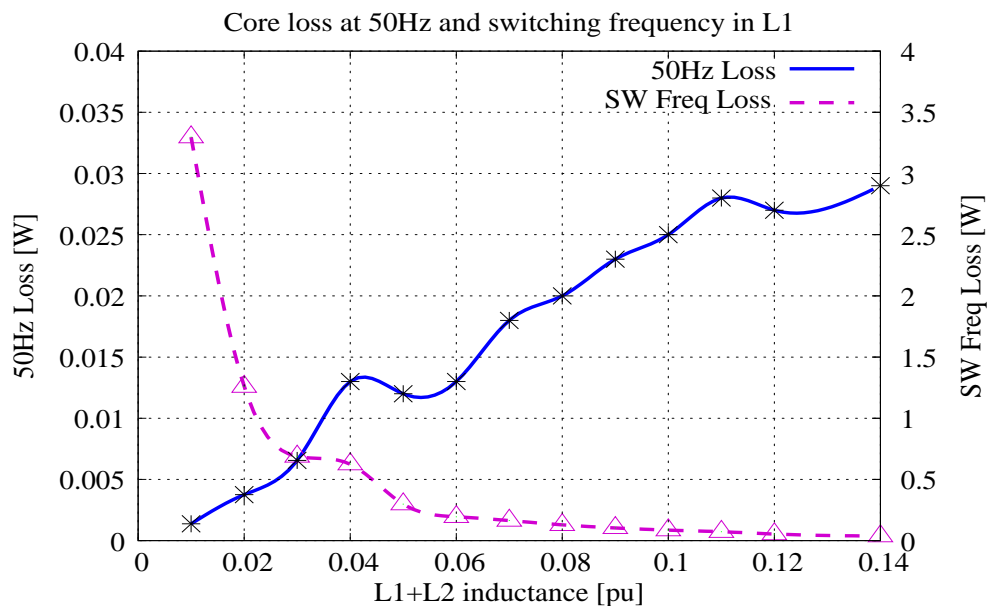
Figure 6.22: Estimated core loss in L_1 for different pu ratings of L_1+L_2; Ferrite core inductor with round wire winding
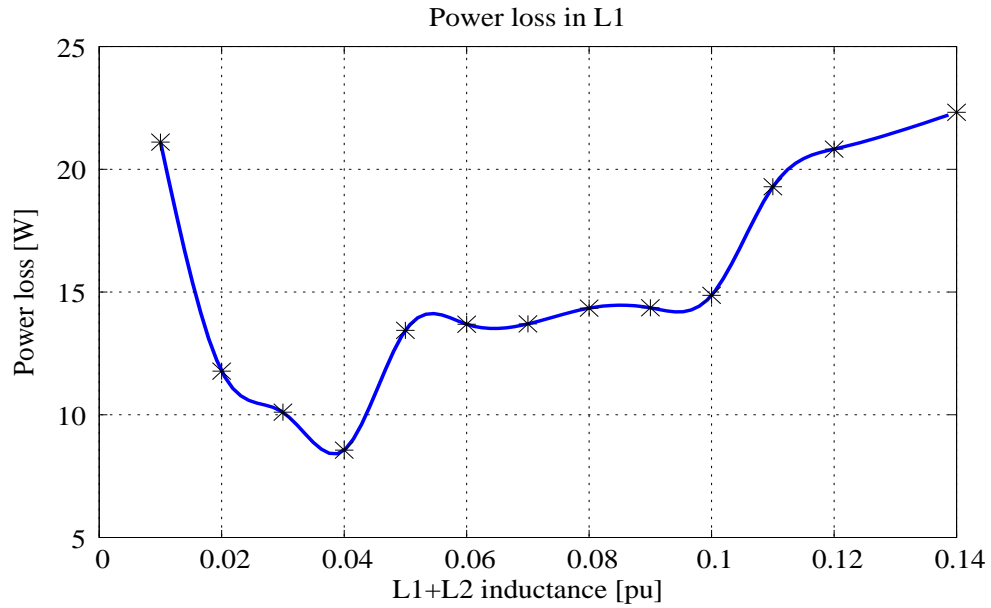
Figure 6.23: Estimated total power loss in L_1 for different pu ratings of L_1+L_2; Ferrite core inductor with round wire winding
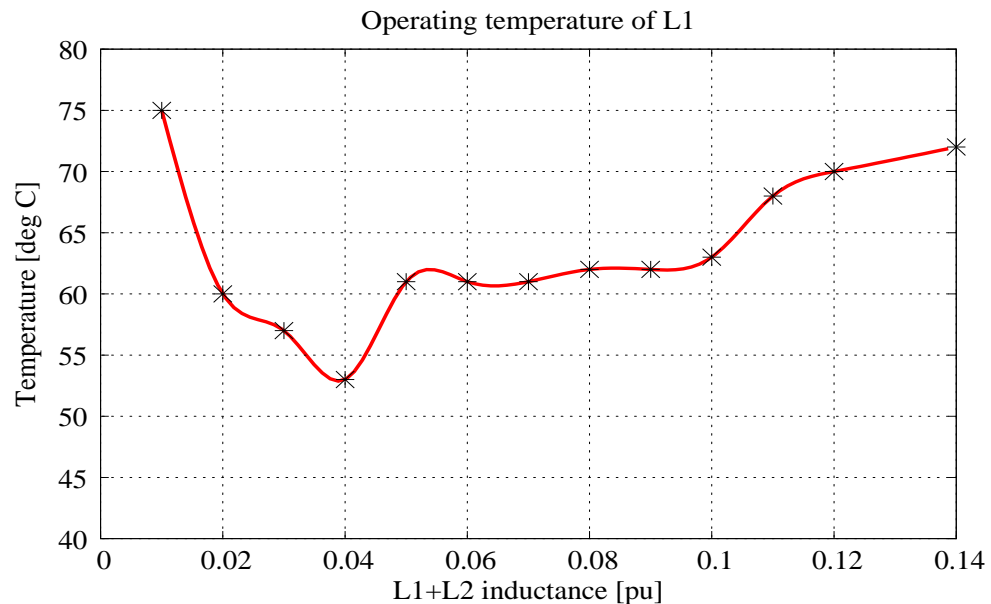
Figure 6.24: Estimated operating temperature of L_1 for different pu ratings of L_1+L_2; Ferrite core inductor with round wire winding
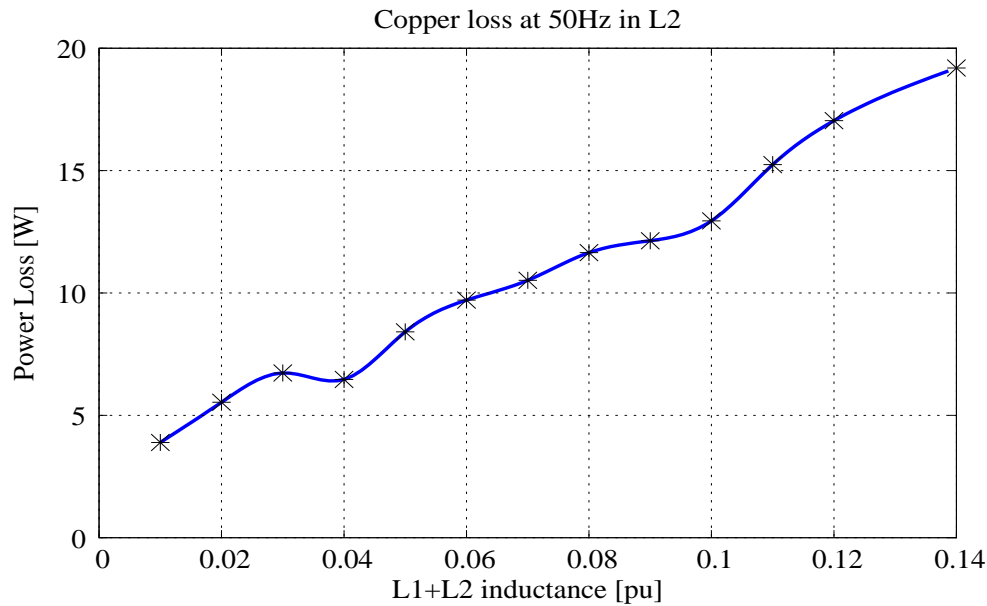
Figure 6.25: Estimated copper loss in L_2 for different pu ratings of L_1+L_2; Ferrite core inductor with round wire winding
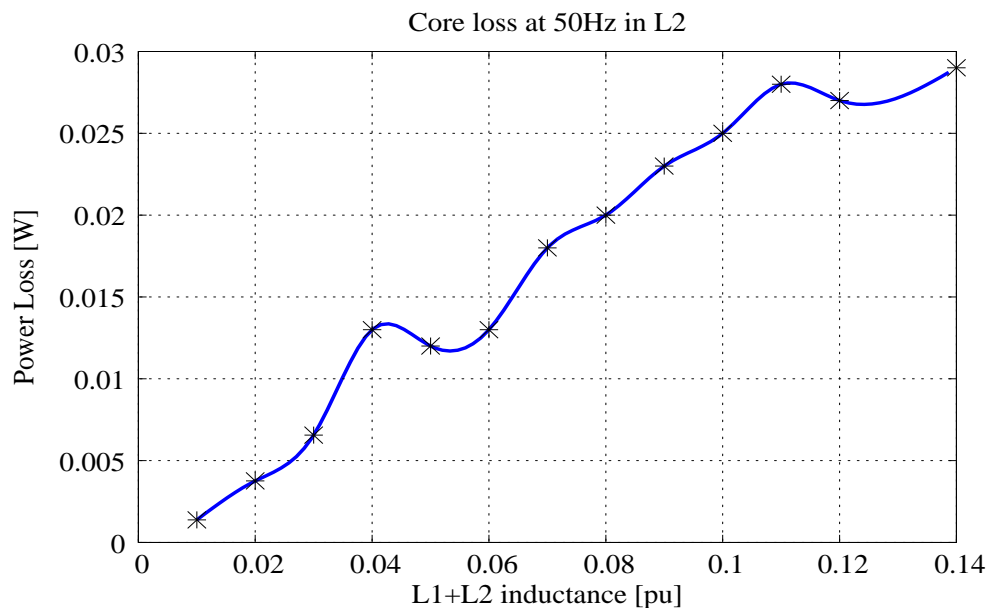
Figure 6.26: Estimated core loss in L_2 for different pu ratings of L_1+L_2; Ferrite core inductor with round wire winding
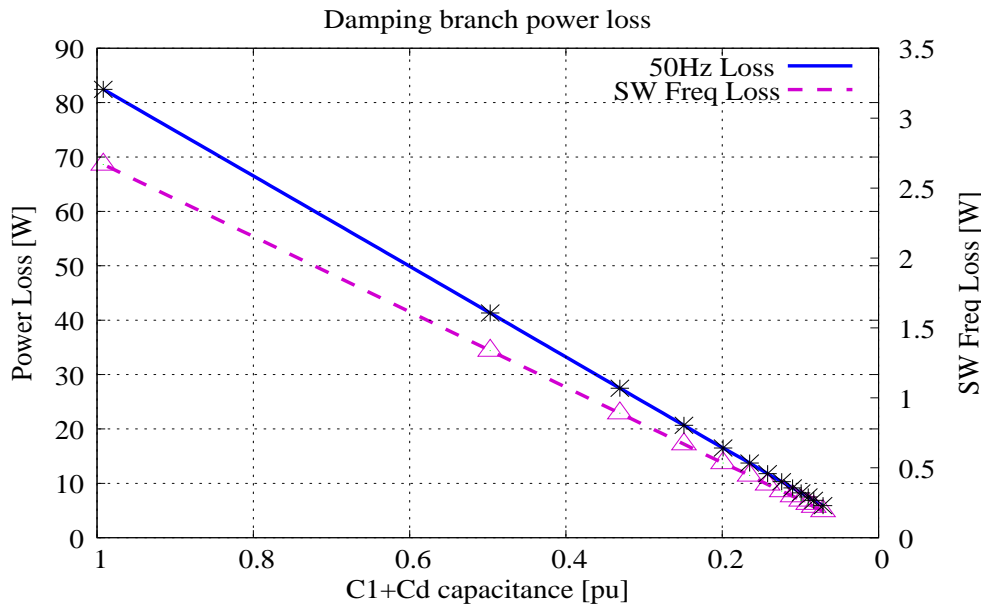
Figure 6.27: Estimated damping circuit loss for different pu ratings of $C_1 + C_d$; Ferrite core inductor with round wire winding
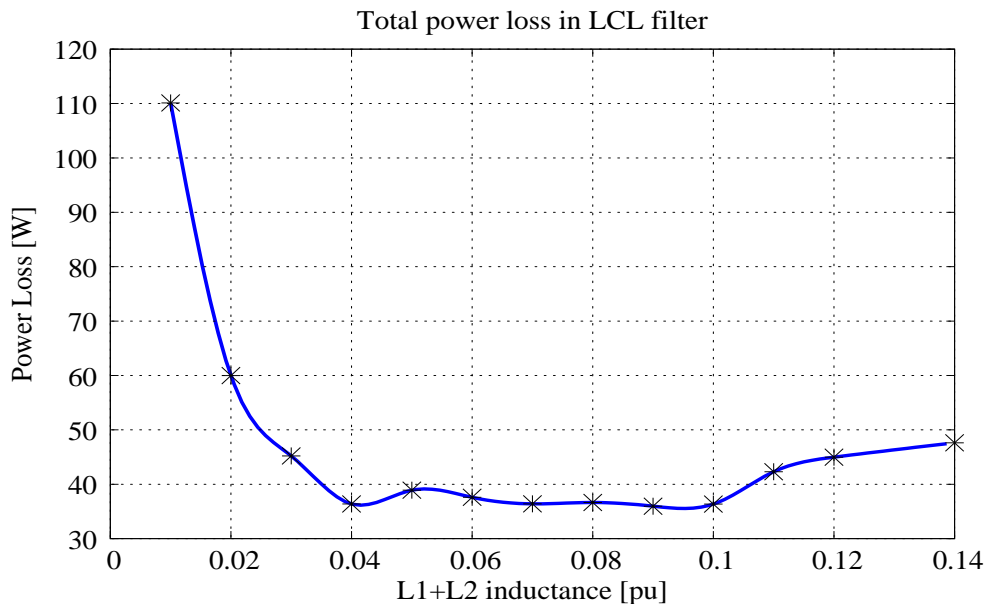
Figure 6.28: Estimated total power loss in LCL filter for different pu ratings of $L_1 + L_2$; Ferrite core inductor with round wire winding

6.9   Loss profile for amorphous core inductors

Figures 6.29–6.35 show the power loss and temperature rise for varying L_{pu} for the LCL filter made of Amorphous core inductors with foil winding. Figures 6.29–6.32 detail the power loss and temperature of inverter-side inductor L_1. Fig 6.29 indicates that copper loss at switching frequency decreases consistently with L_{pu} with no upward bumps in the curve. Amorphous core materials have higher core losses compared to Ferrite materials and it can be observed from Fig. 6.30 that at low L_{pu}, the switching frequency core loss is the dominant loss. The total power loss curve is constant from 0.04pu to 0.1pu since any decrease in switching frequency core loss is offset by increase in fundamental frequency copper loss.

The power loss in the damping circuit is not shown since it is same as Fig 6.27. The loss in the damping circuit depends on the switching frequency and base voltage rating, and is unaffected by choice of inductors. As in the case of the ferrite inductors, the minimum power loss point depends strongly on the loss curve of the inverter-side inductor L_1.
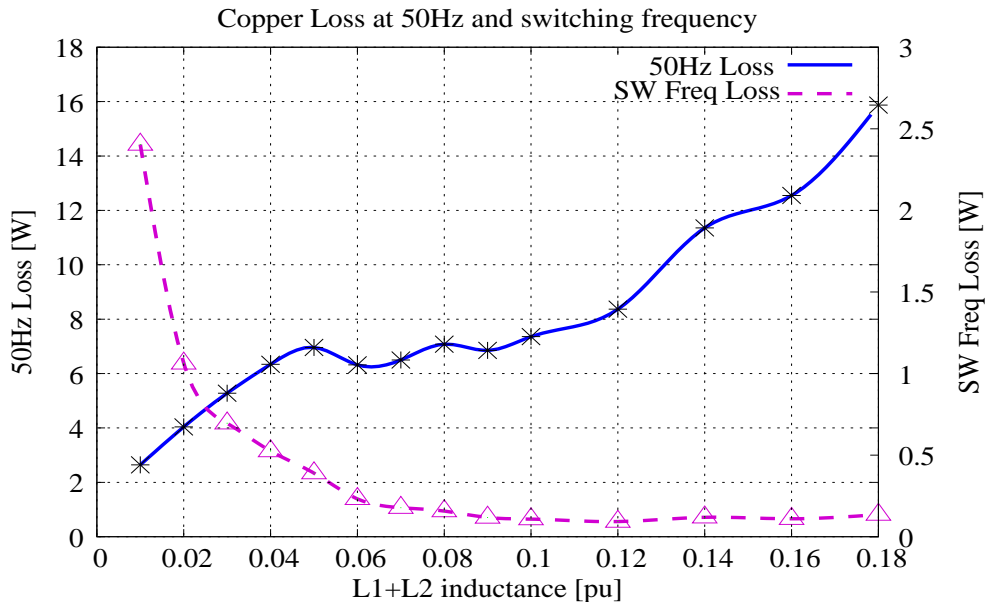
Figure 6.29: Estimated copper loss in L_1 for different pu ratings of L_1+L_2; Amorphous core inductor with foil winding
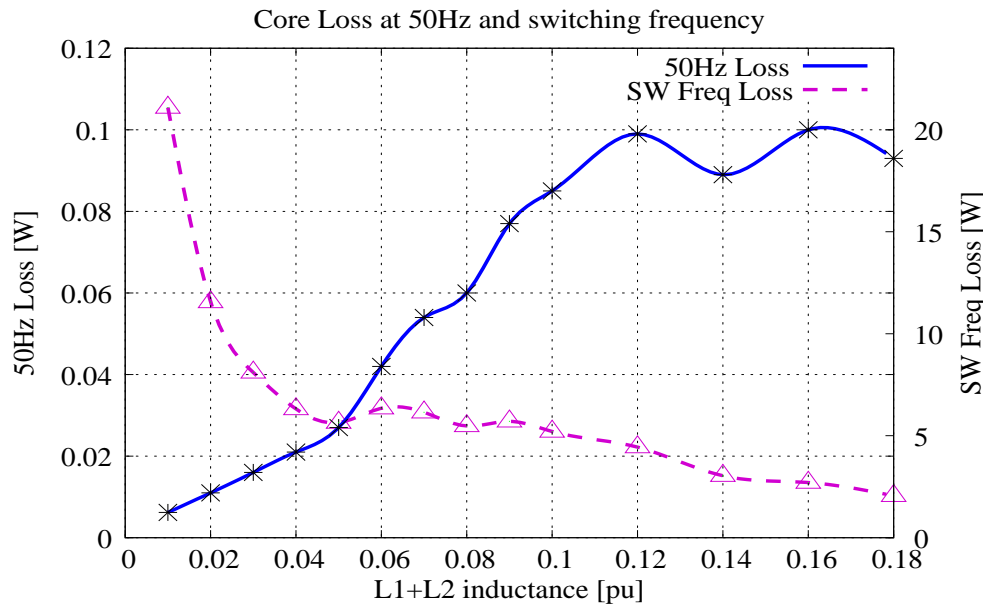
Figure 6.30: Estimated core loss in L_1 for different pu ratings of L_1+L_2; Amorphous core inductor with foil winding
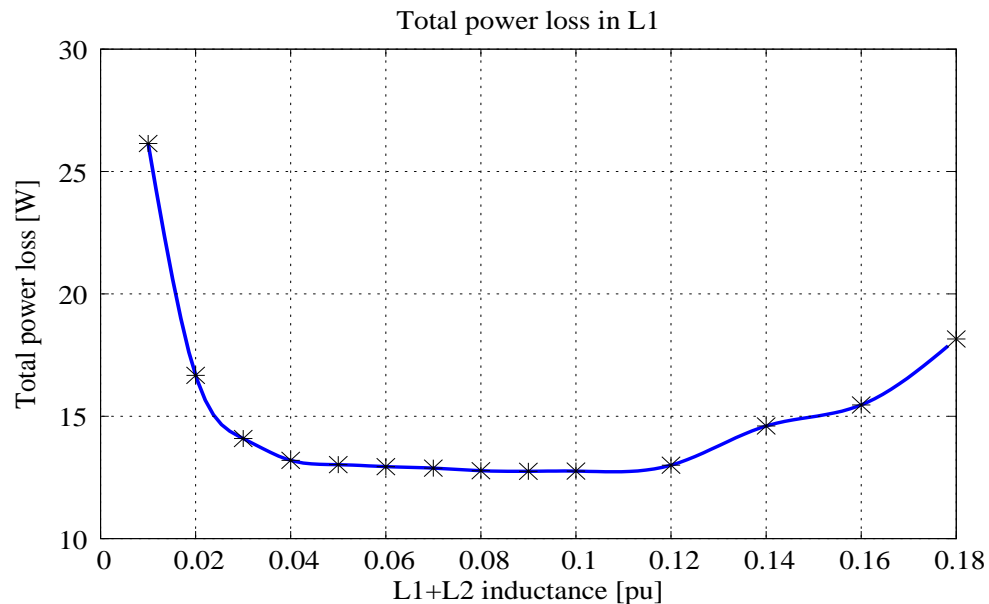
Figure 6.31: Estimated total power loss in L_1 for different pu ratings of L_1+L_2; Amorphous core inductor with foil winding
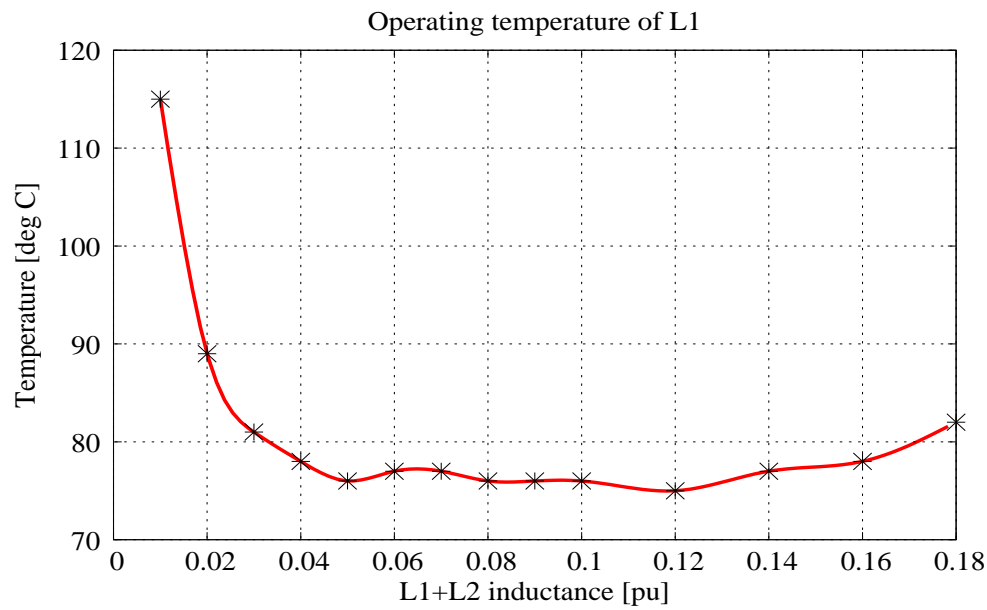
Figure 6.32: Estimated operating temperature of L_1 for different pu ratings of L_1+L_2; Amorphous core inductor with foil winding
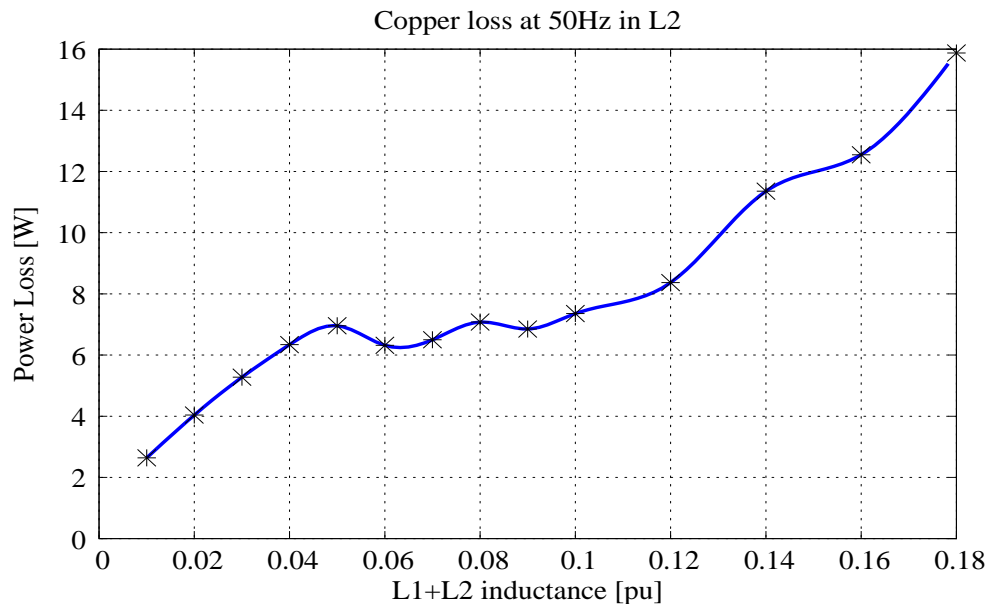
Figure 6.33: Estimated copper loss in L_2 for different pu ratings of L_1+L_2; Amorphous core inductor with foil winding
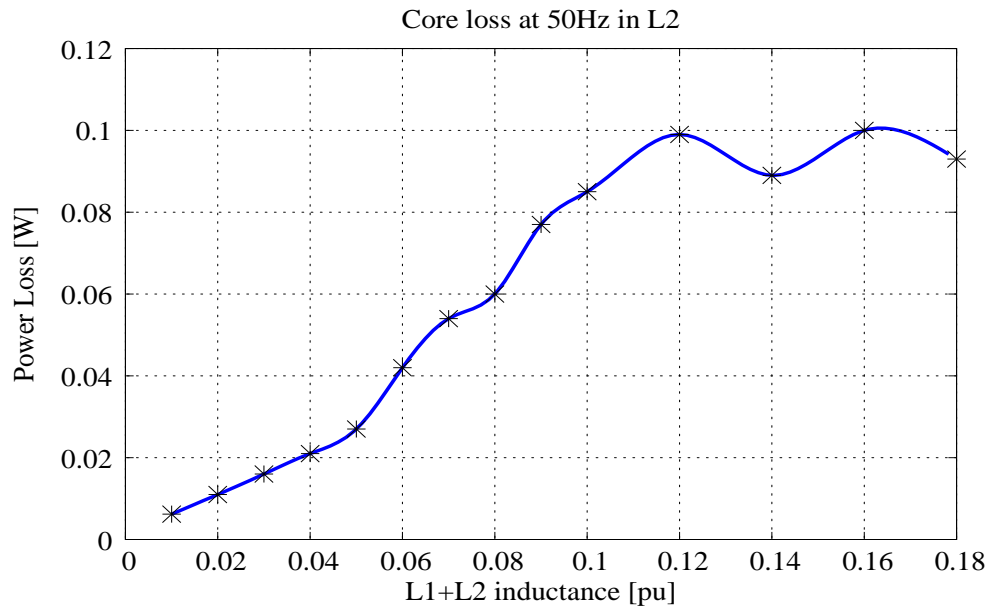
Figure 6.34: Estimated core loss in L_2 for different pu ratings of L_1+L_2; Amorphous core inductor with foil winding
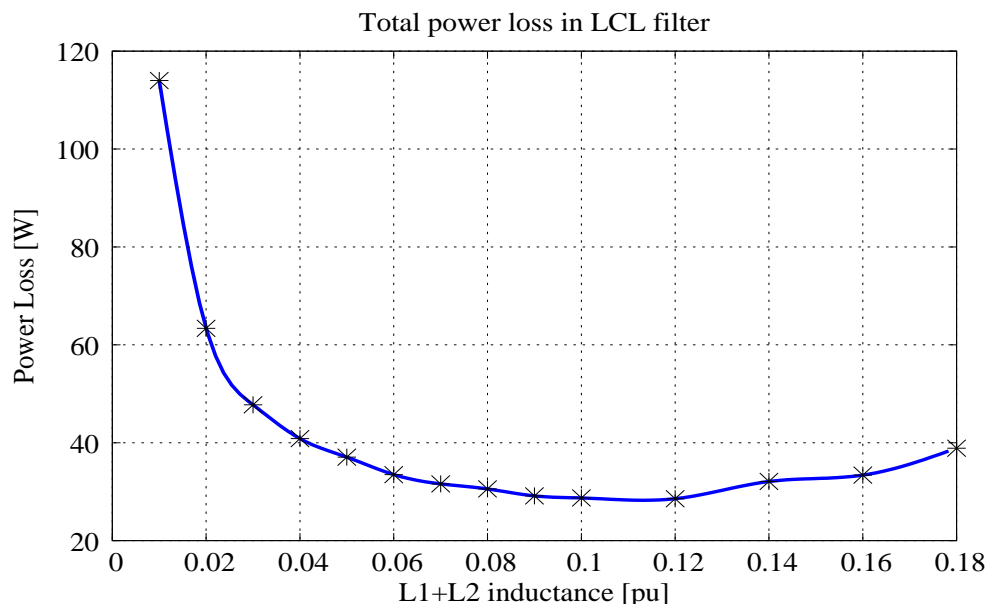
Figure 6.35: Estimated total power loss in LCL filter for different pu ratings of L_1+L_2; Amorphous core inductor with foil winding

6.10   Loss profile for powder core inductors

Figures 6.36–6.42 show the power loss and temperature rise for varying L_{pu} for the LCL filter made of Powder core inductors with round wire winding. Figures 6.36–6.39 show the power loss and operating temperature of L_1. The switching frequency copper loss curve in Fig. 6.36 is similar to Fig. 6.21, since the same proximity effect is dominant in this case. Powder core materials are temperature sensitive and maximum operating temperature is around 200°C, hence the L_{pu} designs below 0.04pu are not feasible. The minimum L_{pu} for powder core inductors is around 0.06pu which does not change even with the addition of losses in damping branch and grid-side inductor L_1.
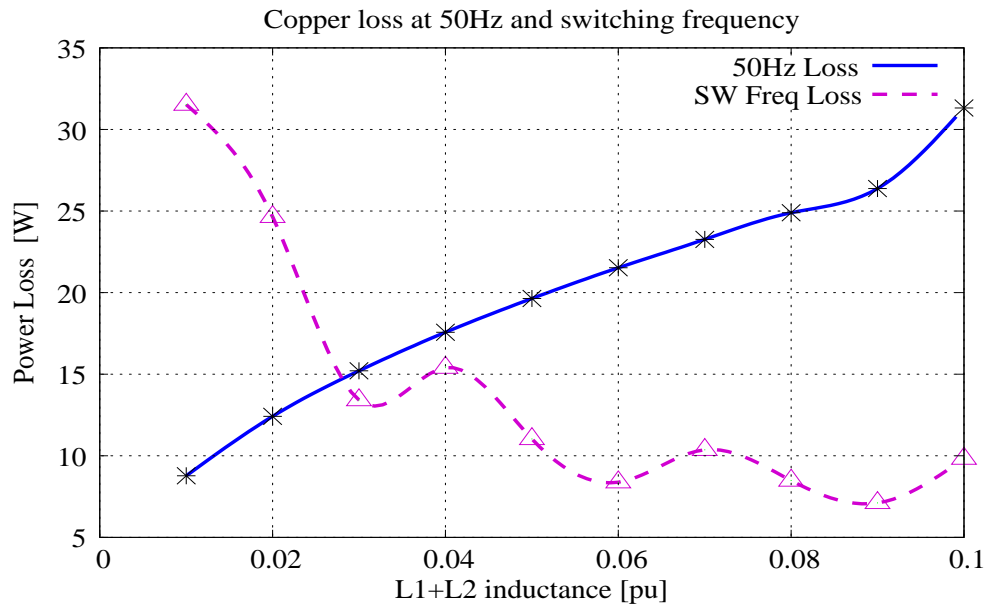
Figure 6.36: Estimated copper loss in L_1 for different pu ratings of L_1+L_2; Powder core inductor with round wire, two bobbin design
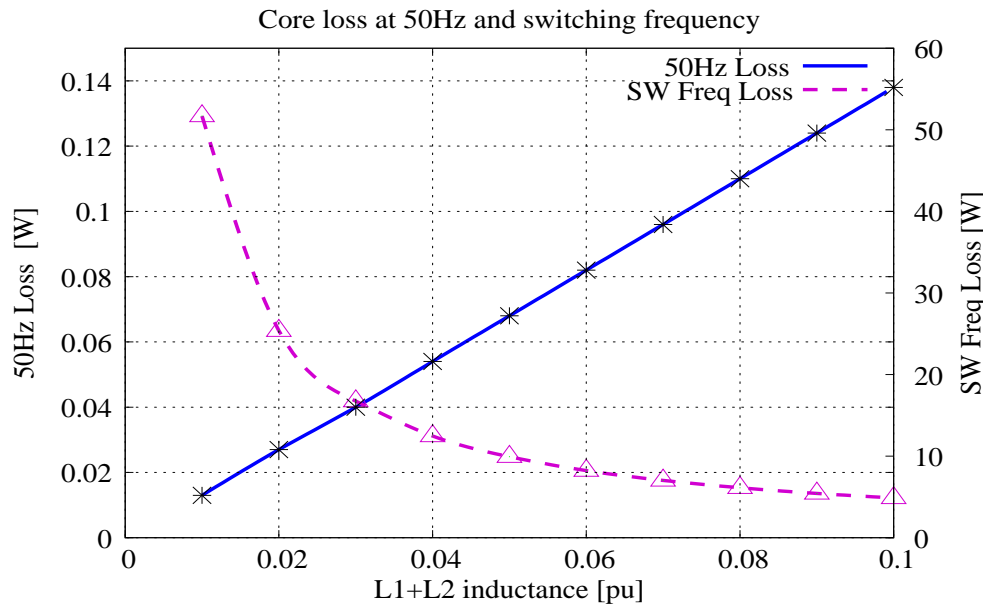
Figure 6.37: Estimated core loss in L_1 for different pu ratings of L_1+L_2; Powder core inductor with round wire, two bobbin design
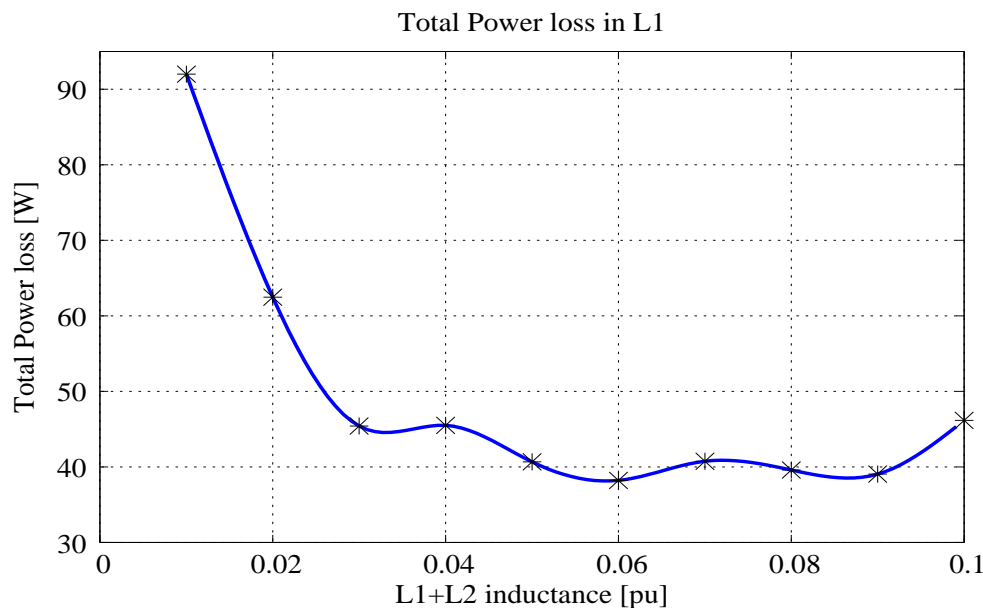
Figure 6.38: Estimated total power loss in L_1 for different pu ratings of L_1+L_2; Powder core inductor with round wire, two bobbin design
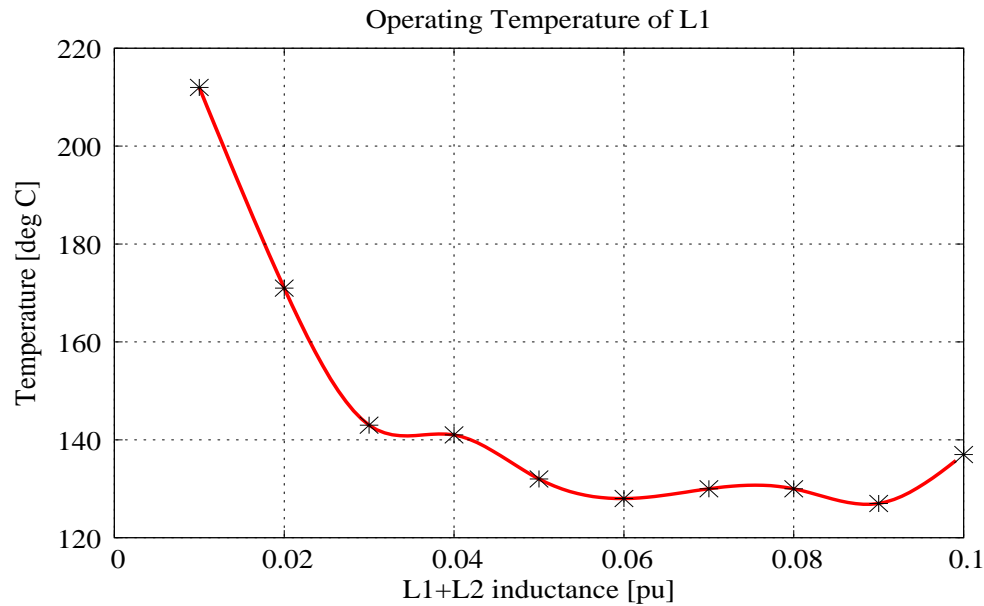
Figure 6.39: Estimated operating temperature of L_1 for different pu ratings of L_1+L_2; Powder core inductor with round wire, two bobbin design
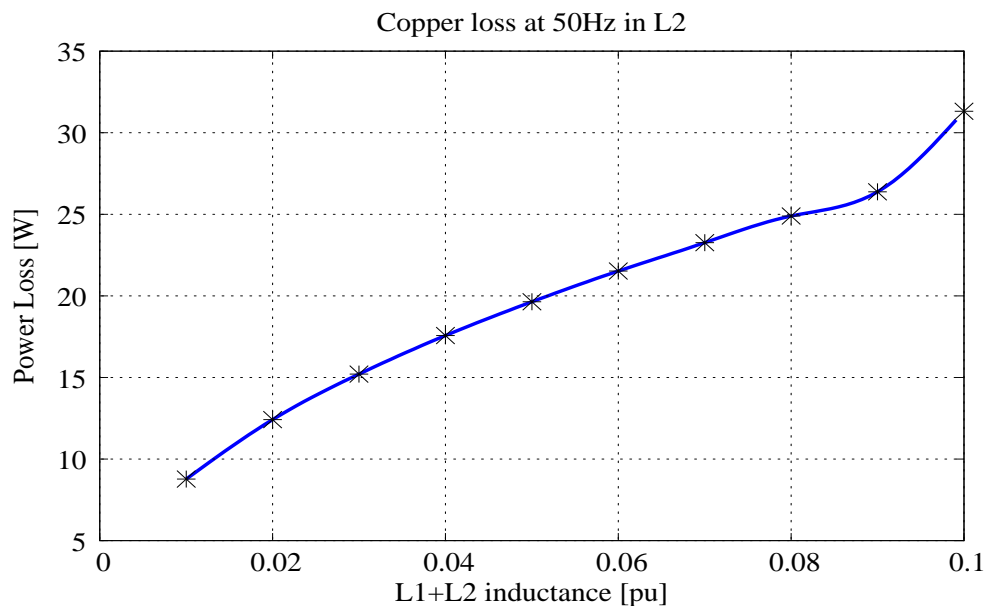
Figure 6.40: Estimated copper loss in L_2 for different pu ratings of L_1+L_2; Powder core inductor with round wire, two bobbin design
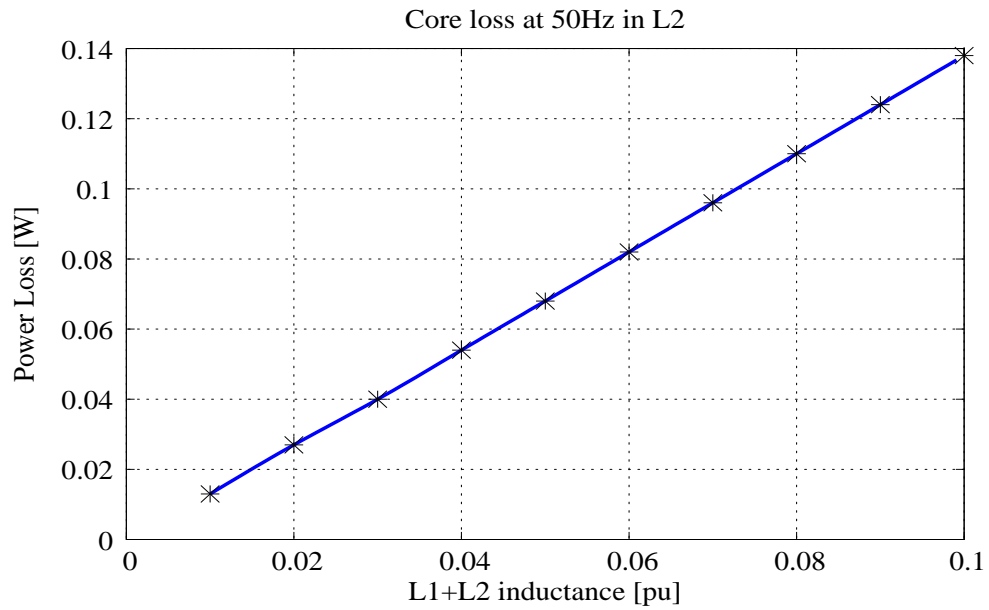
Figure 6.41: Estimated core loss in L_2 for different pu ratings of L_1+L_2; Powder core inductor with round wire, two bobbin design
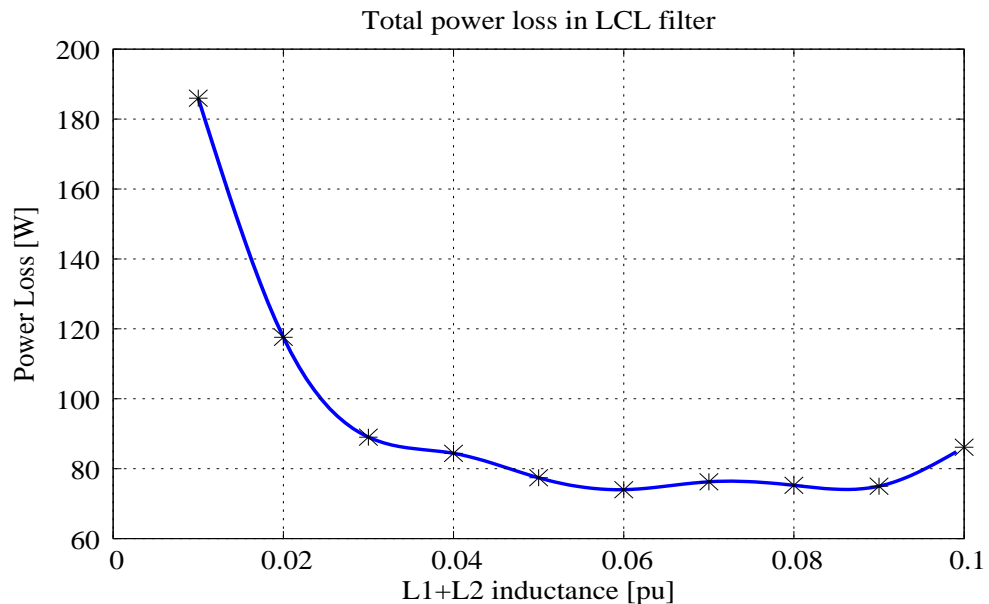
Figure 6.42: Estimated total loss in LCL filter for different pu ratings of L_1+L_2; Powder core inductor with round wire, two bobbin design

6.11　Summary

Experimental results of filtering characteristics show a good match with analysis in the frequency range of interconnected inverter applications. The high frequency harmonic spectrum of the output current was well within the IEEE specifications for the rating of the power converter. The analytical equations predicting the power loss in inductors were verified through short circuit tests using a 3ϕ 10kVA power converter. The steady state temperature rise in individual inductors was measured and compared with the expected temperature rise. Loss curves for core loss and copper loss for different per unit rating of total inductance were fomulated. Simultaneously, the total capacitance per unit was adjusted to maintain the same resonant frequency. Power loss in the damping circuit was calculated for different per unit ratings. The total LCL filter loss per phase was plotted. These loss curves were used to find the most efficient LCL filter design for three different core material -ferrite, amorphous, powder and two different winding types -round and foil.

A traditional rule of thumb approach to LCL filter design would use L_1 and L_2 in the range of 10%. Such a filter is a feasible design but would have higher losses than the proposed optimized design. It has been shown that it is possible to select lower values of L_1, L_2 and C that can lead to cost effective designs of smaller size, and that would have lower overall filter power loss.

Chapter 7

Conclusions

The present research work originated from a project to investigate the optimal size and rating of low pass filters for grid connected power converters. As part of this project, an extensive literature survey was conducted to ascertain the current state of art in the area of filter design for grid connected power converters. There were several deficiencies in the present approach that were identified -some issues include use of arbitrary "thumb-rules" for design, design procedures that resulted in over-rated designs and design assumption which would result in bulky and as well as lossy designs.

The approach followed in this report tries to overcome some of the deficiencies of the previous approaches. The third order LCL filter was found to offer a good balance between harmonic filtering as well as additional complexity in control. A system level approach is used to obtain the most relevant transfer functions for design. The IEEE standard recommendations for high frequency current ripple were used as a major constraint early in the design to ensure all subsequent optimizations were still compliant with the IEEE limits.

The inductors of the LCL filter were identified as the component with the most potential for improvement. Attention was given to the power loss in an inductor, and all the major sources of loss -copper loss, core loss were thoroughly investigated and analytical equations derived. Thermal analysis of inductors ensured that the steady state operating conditions of the entire filter was within normal bounds.

The current methods for inductor construction were tested and deficiencies in the present methods were identified. New methods to easily and accurately design inductors for three different core materials -Amorphous, Powder and Ferrite were formulated. The effectiveness of foil winding versus round wire winding was also investigated by incor-

porating both the winding types in the design.

All the design assumptions were thoroughly tested by actual construction and testing. Frequency response was measured using a network analyzer. Harmonic spectrum of output was sampled and verified to be within IEEE norms. Power loss in individual inductors was measured by short circuit testing in combination with a 3 phase 10kVA power converter. The steady state temperature rise in individual inductors was measured and compared favourably with the expected temperature rise. Using these results, the most efficient LCL filter design with least temperature rise but which still meets IEEE harmonic standards was found for ferrite, amorphous and powder core materials.

Future research possibilities

The system level transfer function analysis currently does not include several grid dependent parameters like low voltage ride-through requirements, EMI filtering, and dynamic response requirements. These additional constraints can be included to generate guidelines for the filter packaging and design process.

Presently the analytical equations used for power loss estimation have a limited range of accuracy. Similarly, thermal analysis can be enhanced by including fluid modelling methods for natural convection to accurately estimate the operating temperature of the inductors and can be extended to forced cooled designs.

The power loss of individual components in this report is tested in stand-alone converter mode under short circuit conditions. These conditions give the worst case current ripple conditions because of the low modulation index of the power converter. The efficiency of the filter can be tested in actual grid connected mode to test the variation in the losses. This test will result in lower losses and improved thermal characteristics of the filter. Additionally, advanced PWM methods with non-conventional sequences can be implemented to further reduce the high frequency ripple current losses.

The minimum loss L_{pu} designs have other implications on grid connected power converter which can be investigate to further optimize the LCL filter and the power converter including the IGBTs and the DC bus components.

List of AppendixFigures

Appendix A

Transfer Function Tests

System used for Frequency Response Analysis:

AP Instruments Inc., Frequency Response Analyzer - Model No.: 200 ISA

Frequency Response Analyzer settings (basic) under test-conditions:

Sweep Frequency Range : 10Hz - 100kHz

Averaging : 100

Points : 1000

V Level : 1.77V

DC Source : 0.0V

Bandwidth : 10Hz

A.1   Ferrite core inductor results
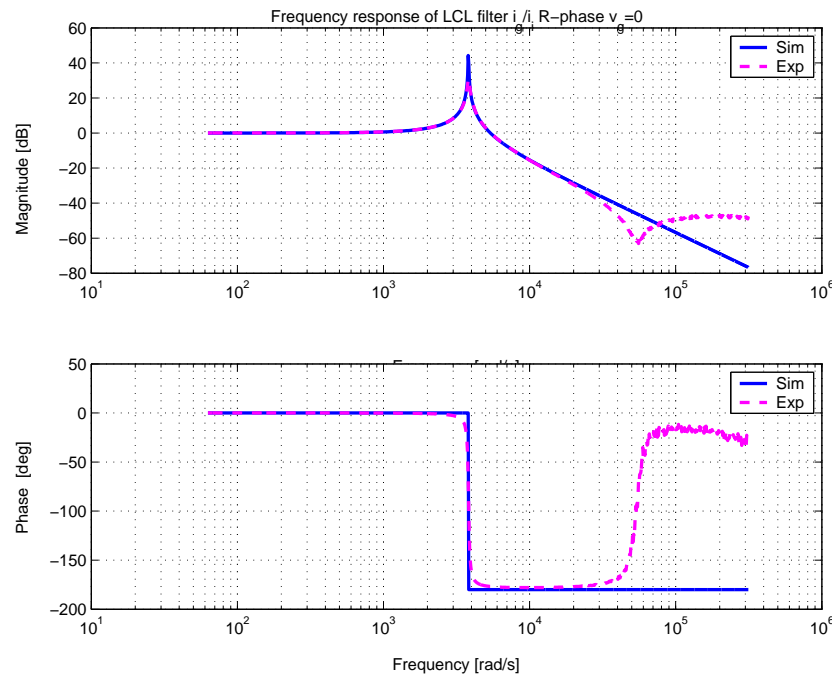
Figure A.1: LCL filter response i_g/i_i (v_g=0); ferrite core inductor, no damping
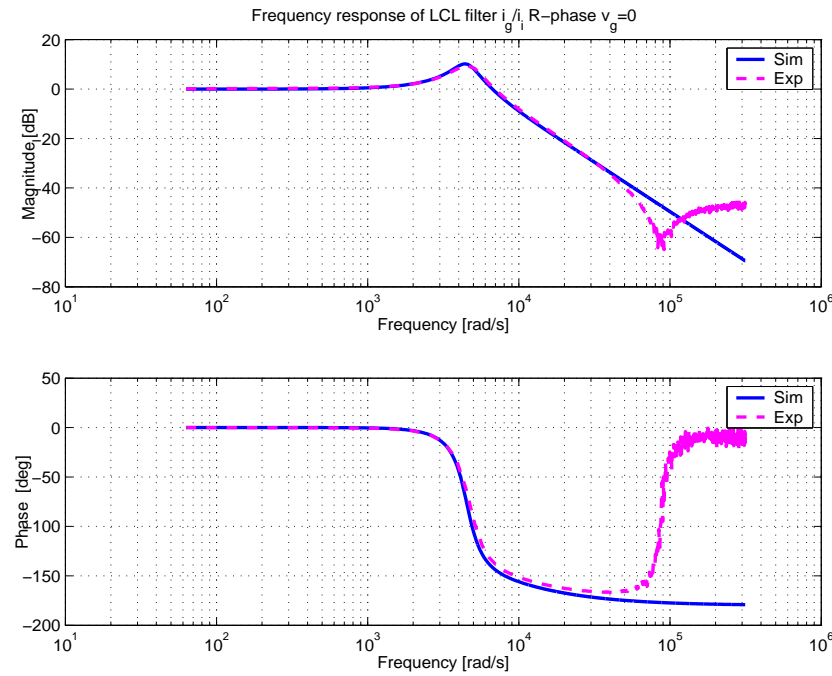
Figure A.2: LCL filter response i_g/i_i (v_g=0); ferrite core inductor, C_1=C_d=8μF, R_d=25Ω
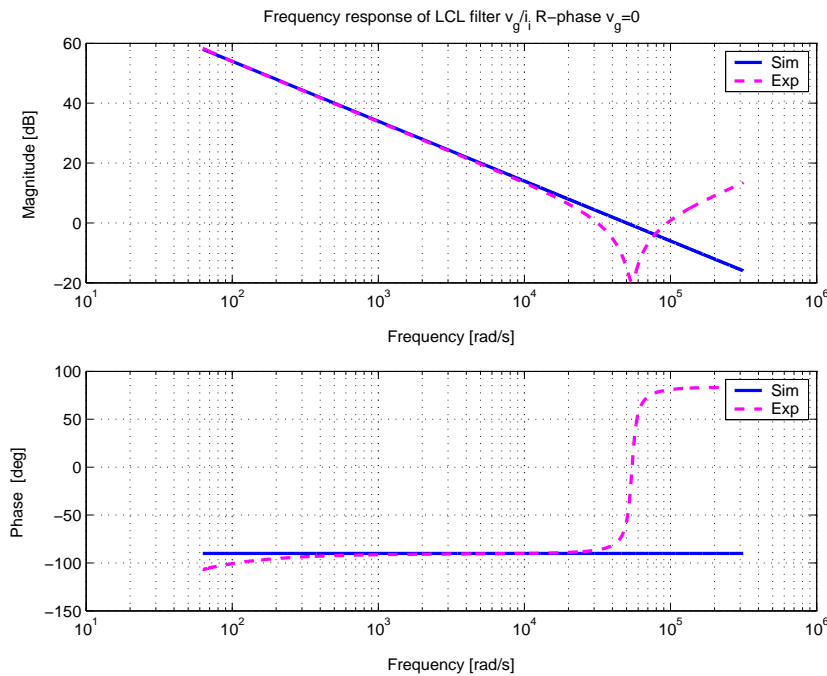
Figure A.3: LCL filter response v_g/i_i (i_g=0); ferrite core inductor, no damping
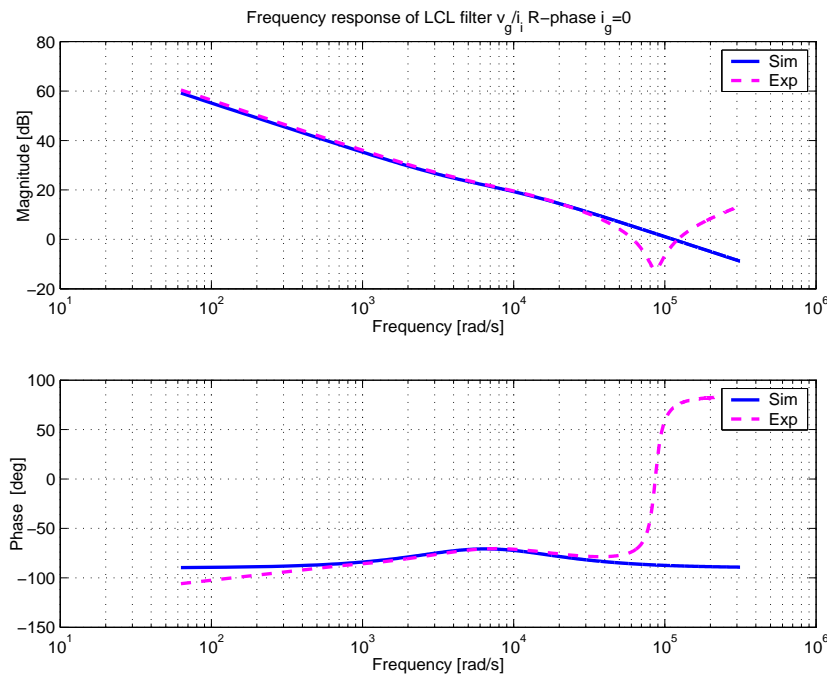
Figure A.4: LCL filter response v_g/i_i (i_g=0); ferrite core inductor, C_1=C_d=8μF, R_d=25Ω
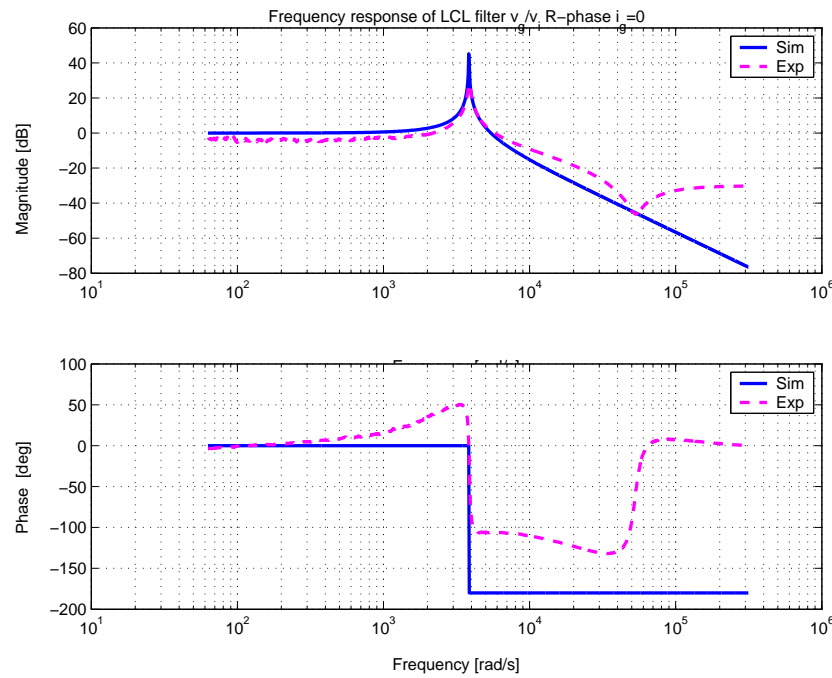
Figure A.5: LCL filter response v_g/v_i (i_g=0); ferrite core inductor, no damping
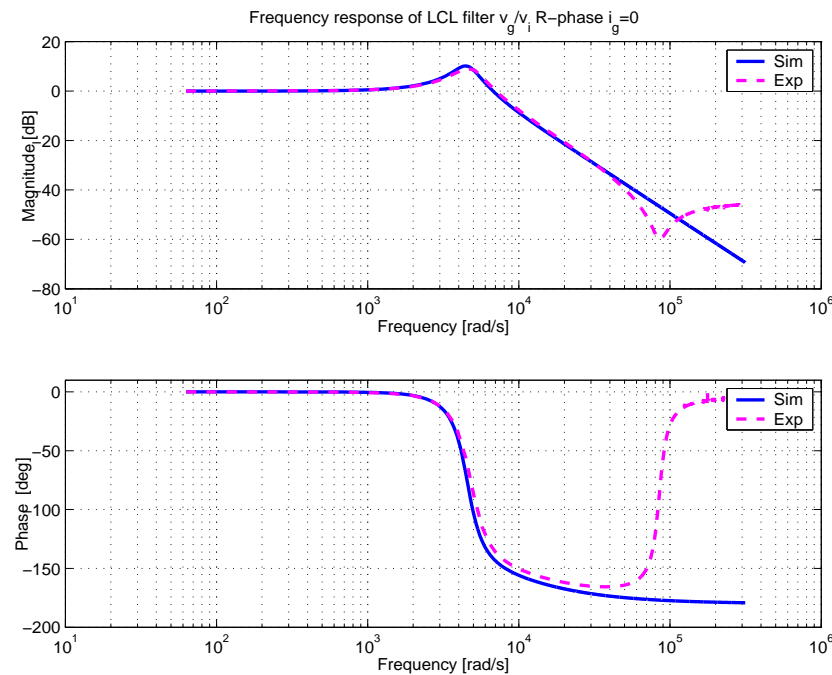
Figure A.6: LCL filter response v_g/v_i (i_g=0); ferrite core inductor, C_1=C_d=8μF, R_d=25Ω
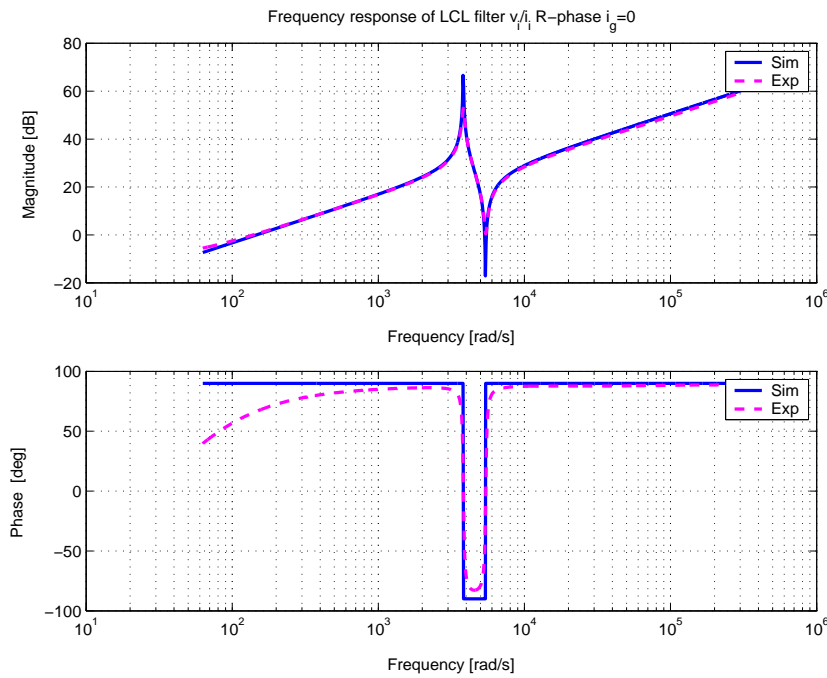
Figure A.7: LCL filter response v_i/i_i (v_g=0); ferrite core inductor, no damping
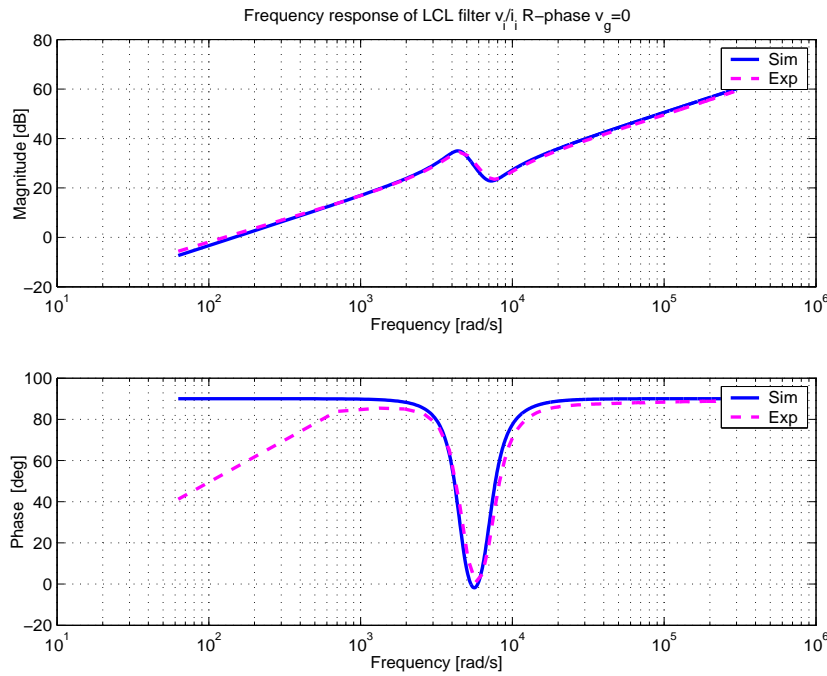
Figure A.8: LCL filter response v_i/i_i (v_g=0); ferrite core inductor, C_1=C_d=8μF, R_d=25Ω
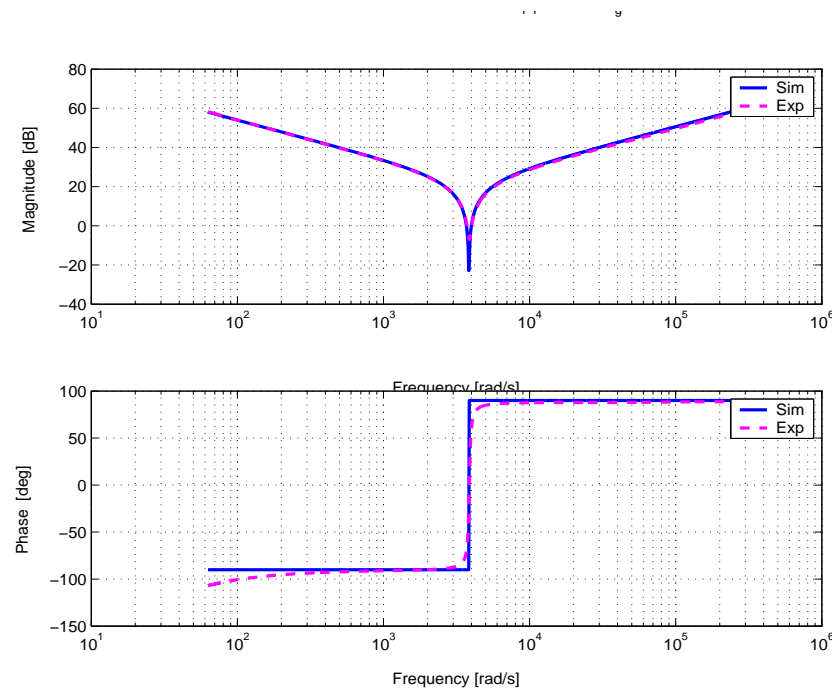
Figure A.9: LCL filter response v_i/i_i (i_g=0); ferrite core inductor, no damping
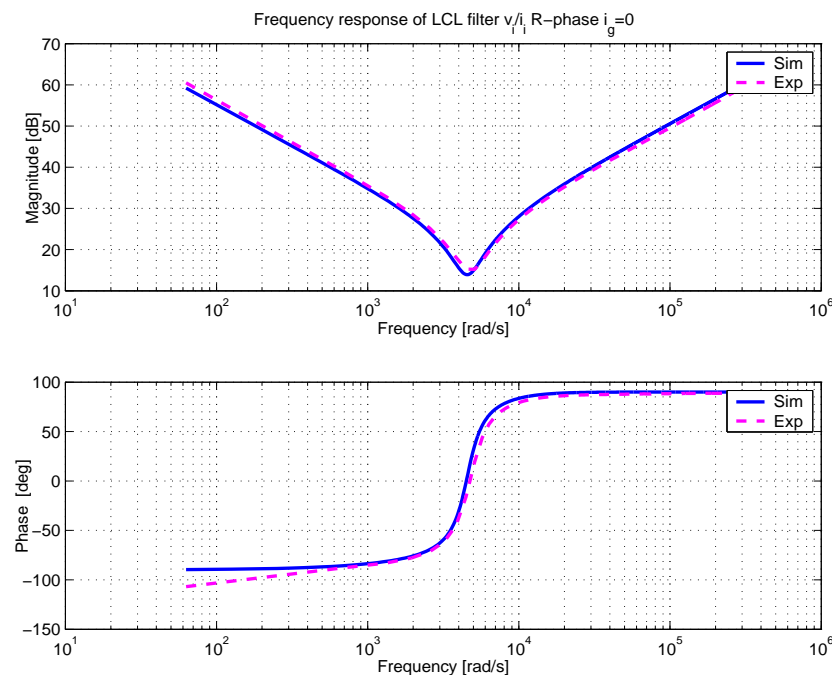
Figure A.10: LCL filter response v_i/i_i (i_g=0); ferrite core inductor, C_1=C_d=8μF, R_d=25Ω

A.2   Amorphous core inductor results
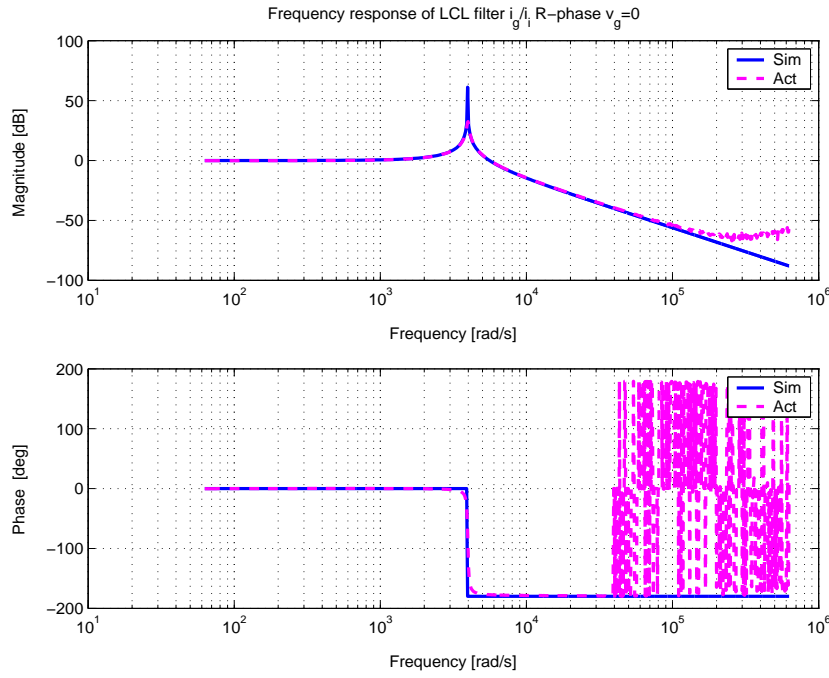
Figure A.11: LCL filter response i_g/i_i (v_g=0); amorphous core inductor, no damping
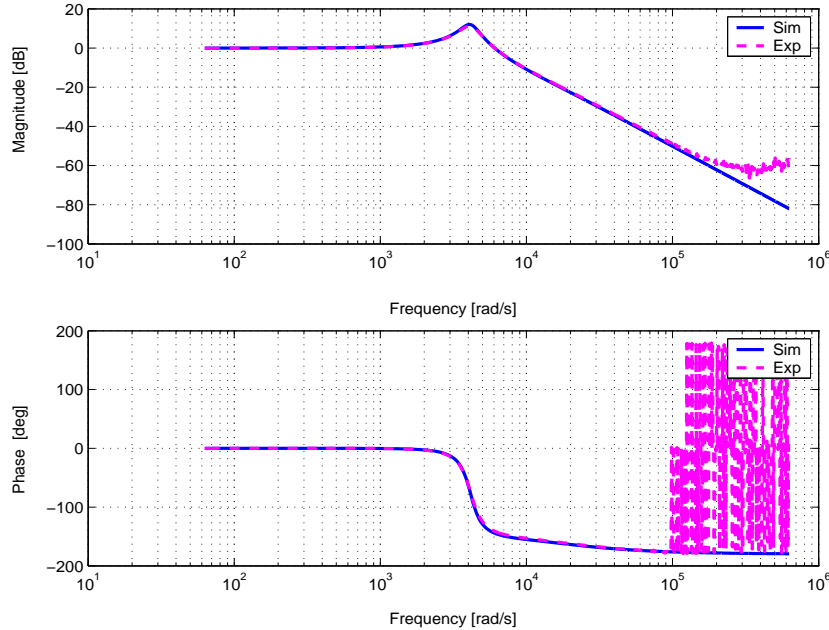
Figure A.12: LCL filter response i_g/i_i (v_g=0); amorphous core inductor, C_1=C_d=6μF, R_d=25Ω
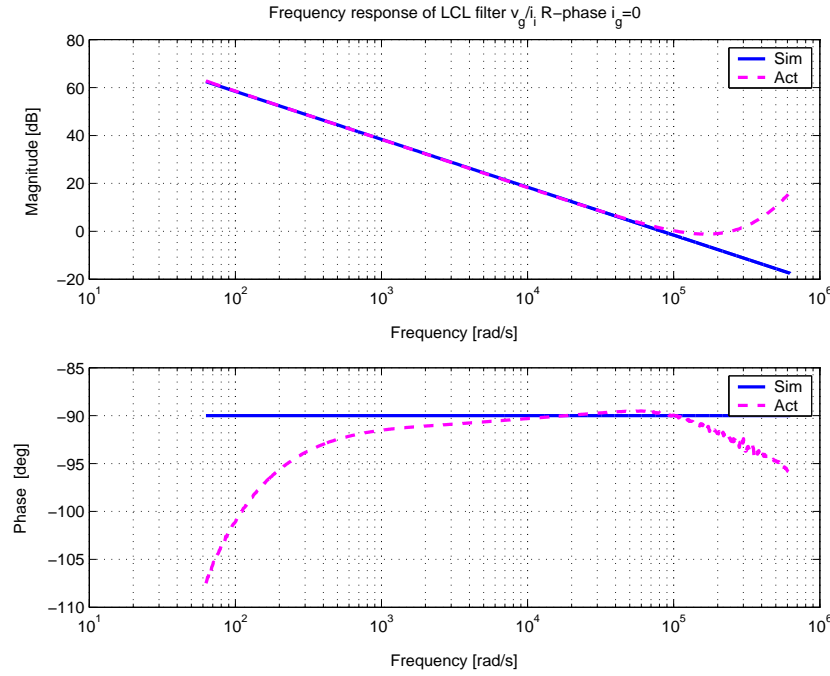
Figure A.13: LCL filter response v_g/i_i (i_g=0); amorphous core inductor, no damping
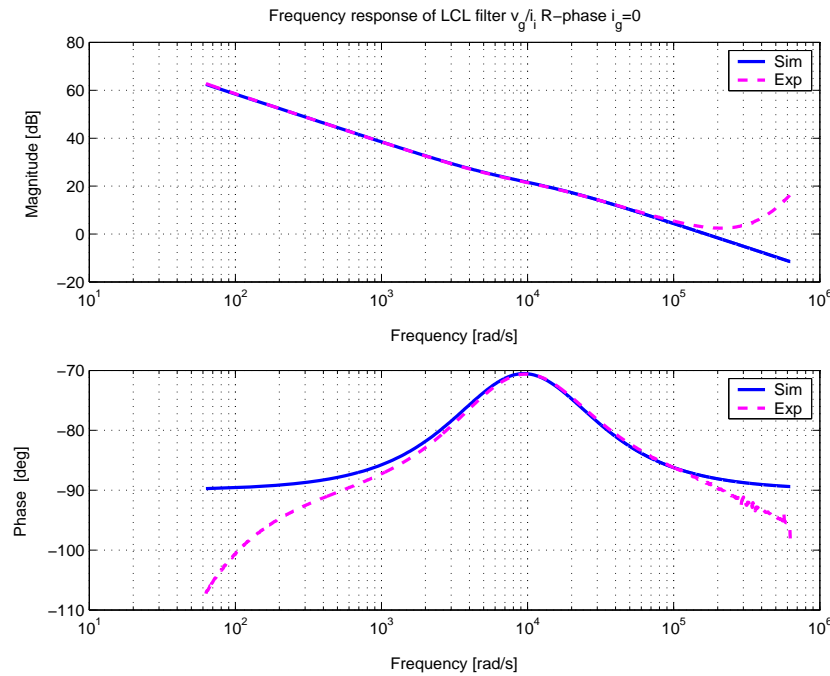
Figure A.14: LCL filter response v_g/i_i (i_g=0); amorphous core inductor, C_1=C_d=6μF, R_d=25Ω
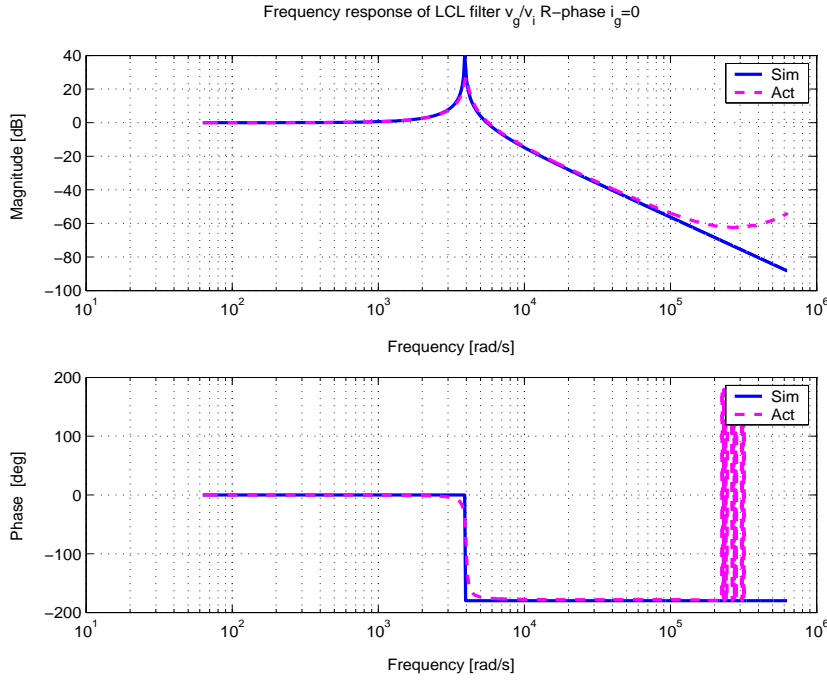
Figure A.15: LCL filter response v_g/v_i (i_g=0); amorphous core inductor, no damping
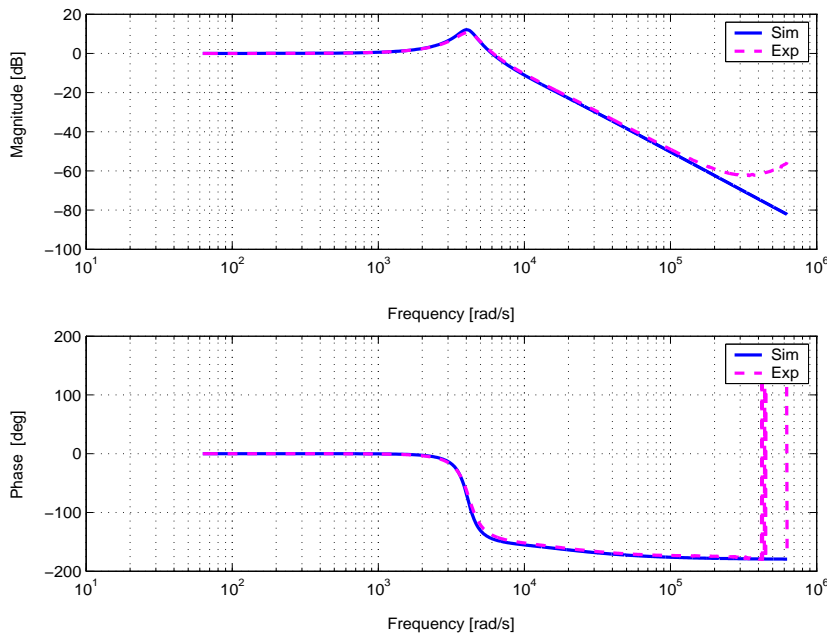
Figure A.16: LCL filter response v_g/v_i (i_g=0); amorphous core inductor, C_1=C_d=6μF, R_d=25Ω
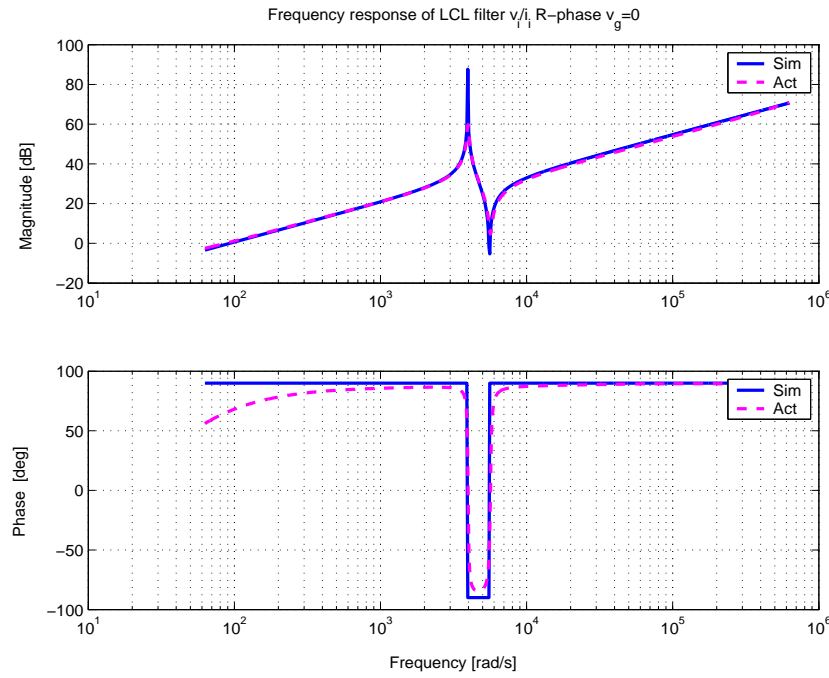
Figure A.17: LCL filter response v_i/i_i (v_g=0); amorphous core inductor, no damping
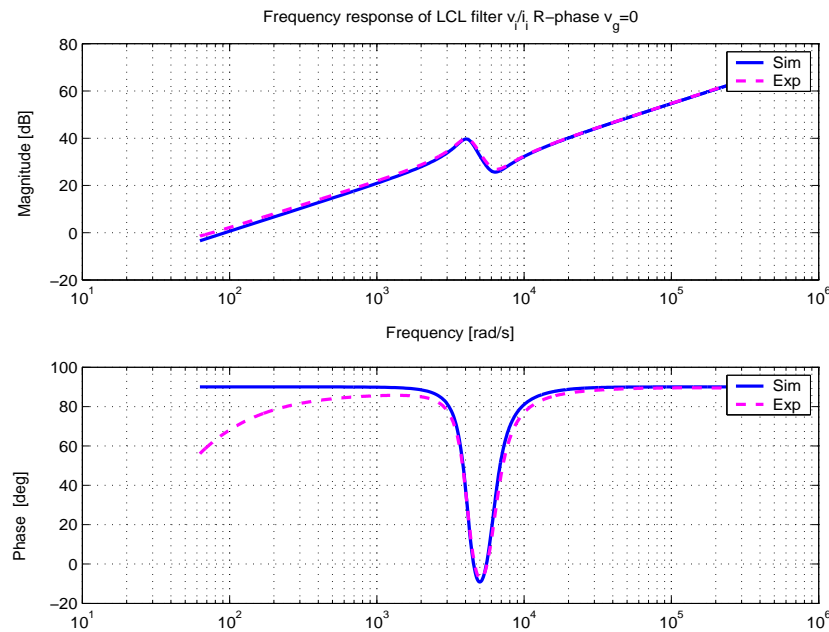
Figure A.18: LCL filter response v_i/i_i (v_g=0); amorphous core inductor, C_1=C_d=6μF, R_d=25Ω
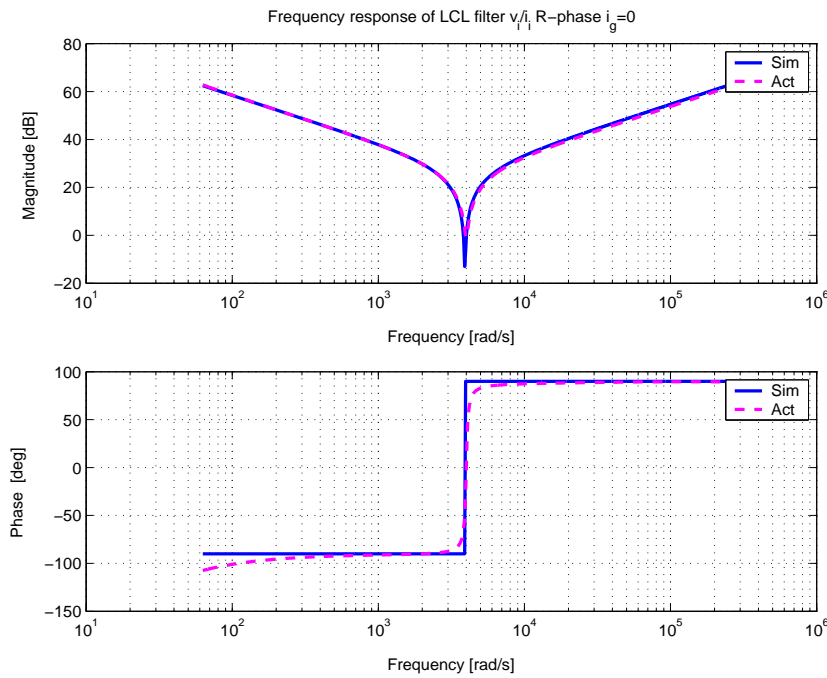
Figure A.19: LCL filter response v_i/i_i (i_g=0); amorphous core inductor, no damping
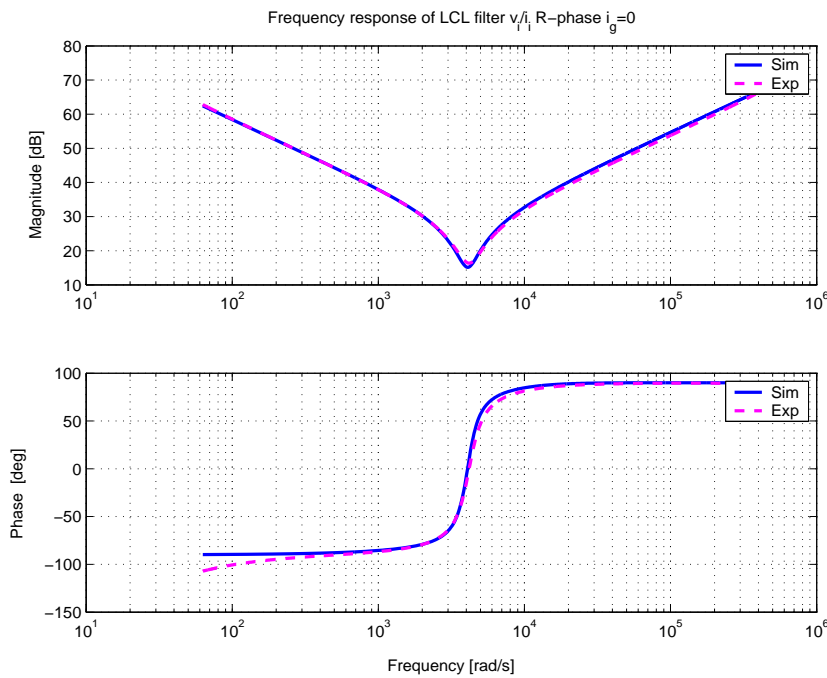
Figure A.20: LCL filter response v_i/i_i (i_g=0); amorphous core inductor, C_1=C_d=6μF, R_d=25Ω

A.3   Powder iron core inductor results
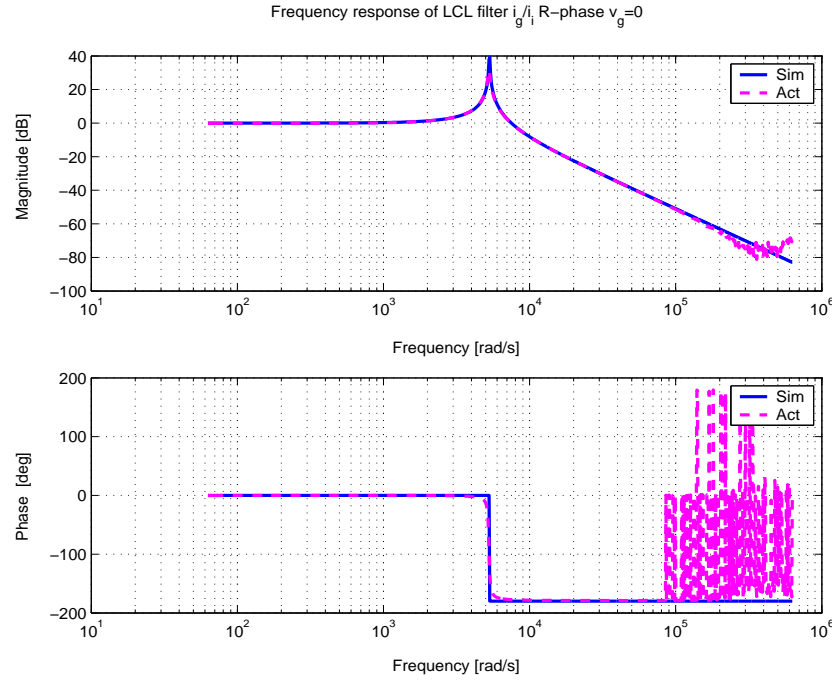
Figure A.21: LCL filter response i_g/i_i (v_g=0); powder core inductor, no damping
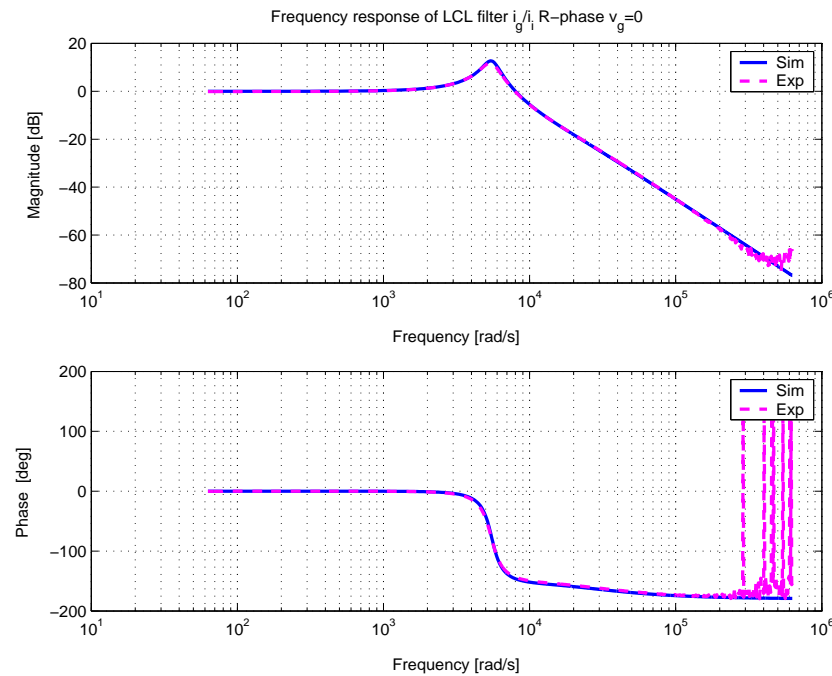
Figure A.22: LCL filter response i_g/i_i (v_g=0); powder core inductor, C_1=C_d=10μF, R_d=10Ω
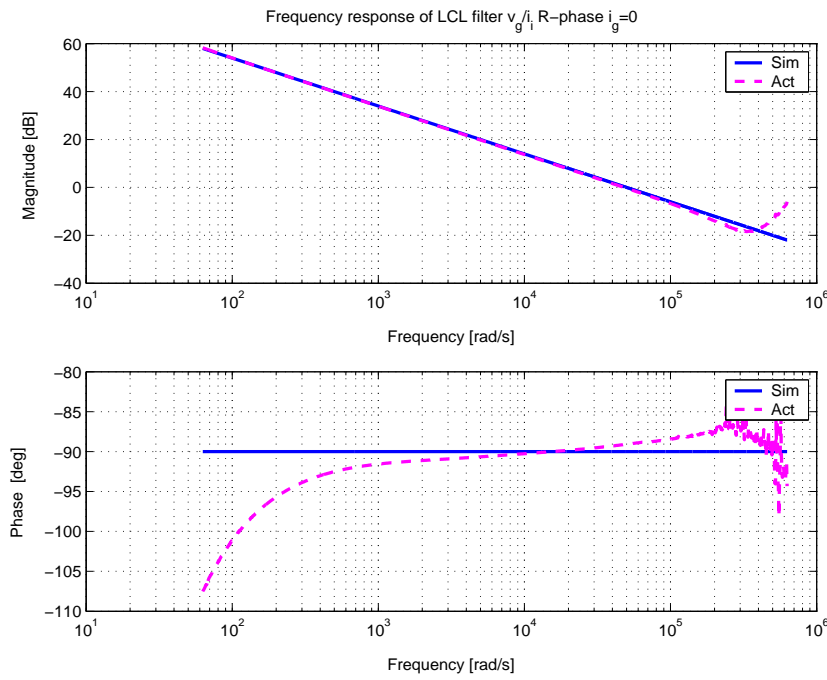
Figure A.23: LCL filter response v_g/i_i (i_g=0); powder core inductor, no damping
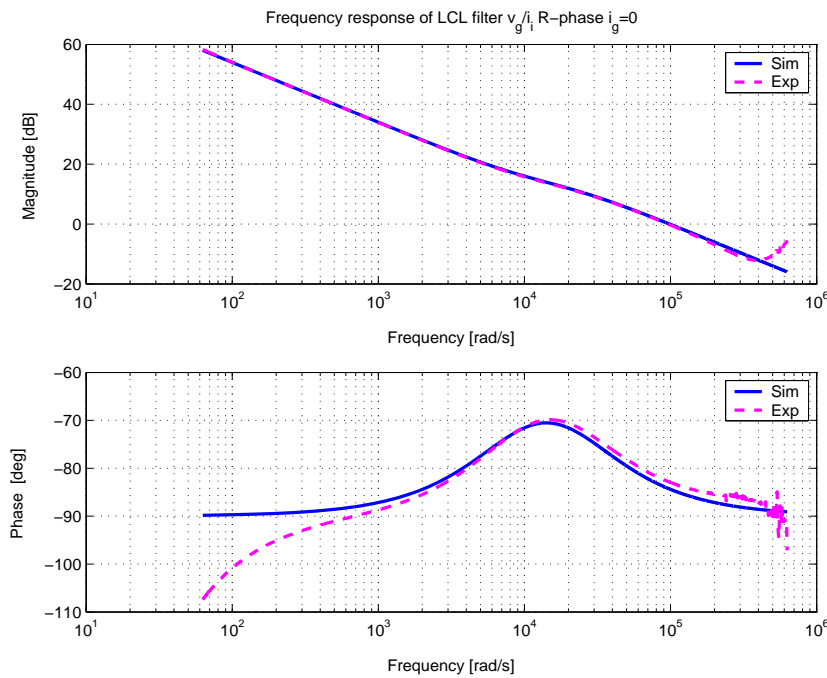
Figure A.24: LCL filter response v_g/i_i (i_g=0); powder core inductor, C_1=C_d=10μF, R_d=10Ω
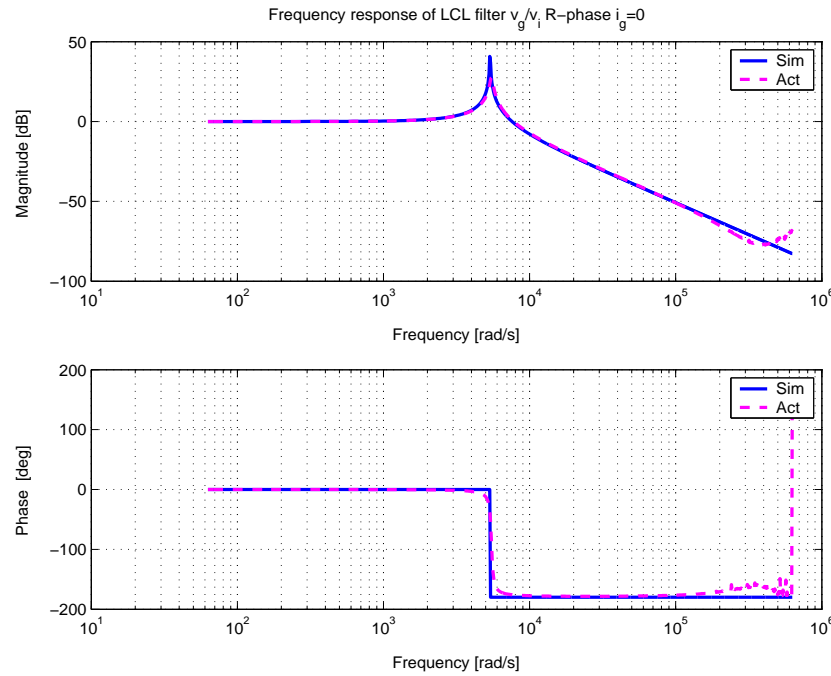
Figure A.25: LCL filter response v_g/v_i (i_g=0); powder core inductor, no damping
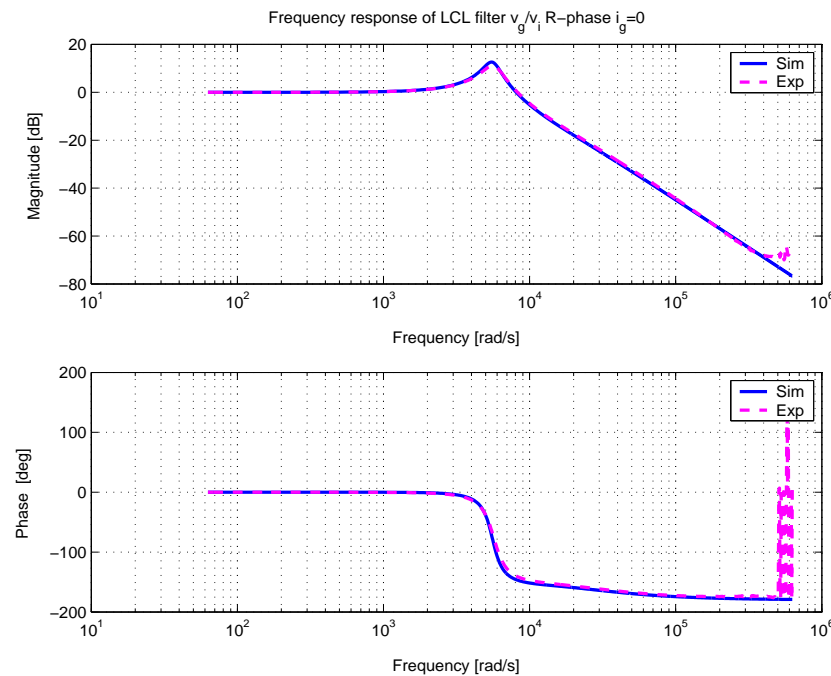
Figure A.26: LCL filter response v_g/v_i (i_g=0); powder core inductor, C_1=C_d=10μF, R_d=10Ω
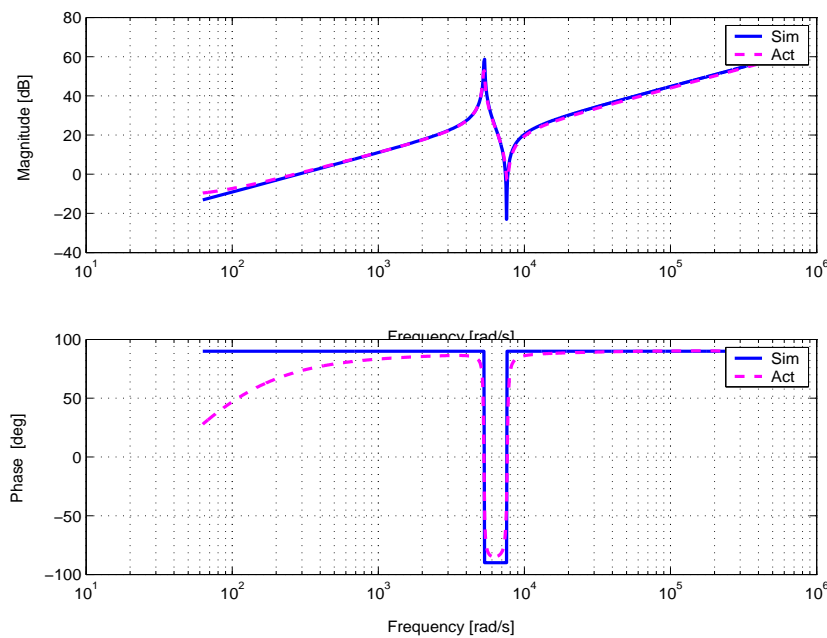
Figure A.27: LCL filter response v_i/i_i (v_g=0); powder core inductor, no damping
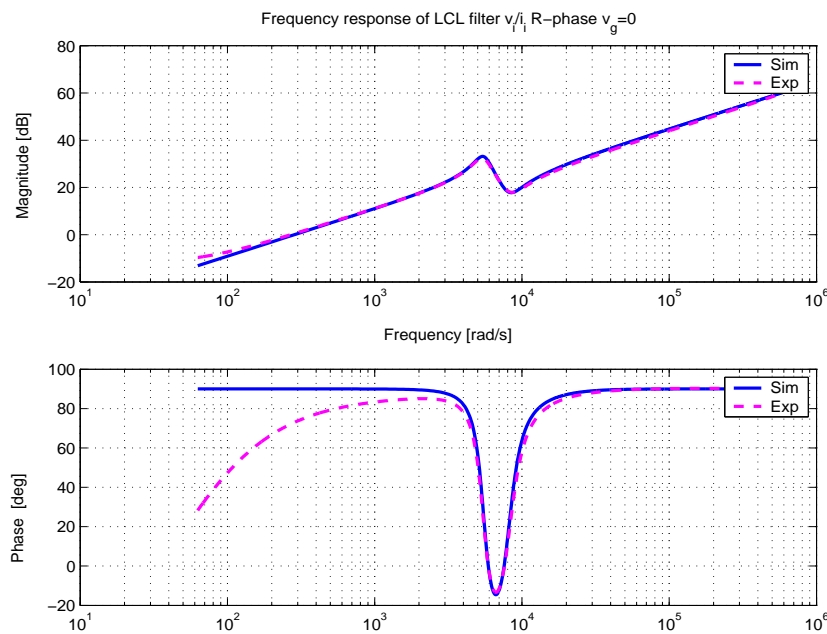
Figure A.28: LCL filter response v_i/i_i (v_g=0); powder core inductor, C_1=C_d=10μF, R_d=10Ω
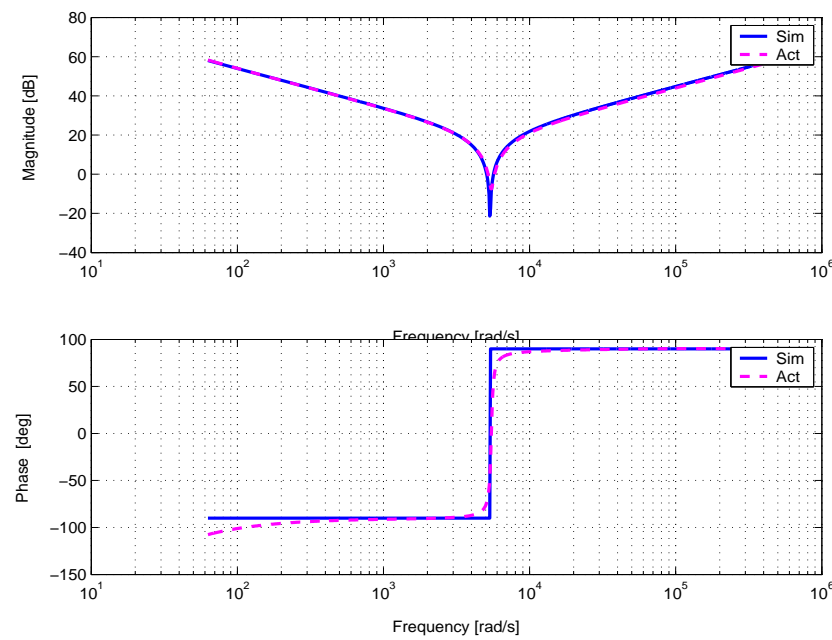
Figure A.29: LCL filter response v_i/i_i (i_g=0); powder core inductor, no damping
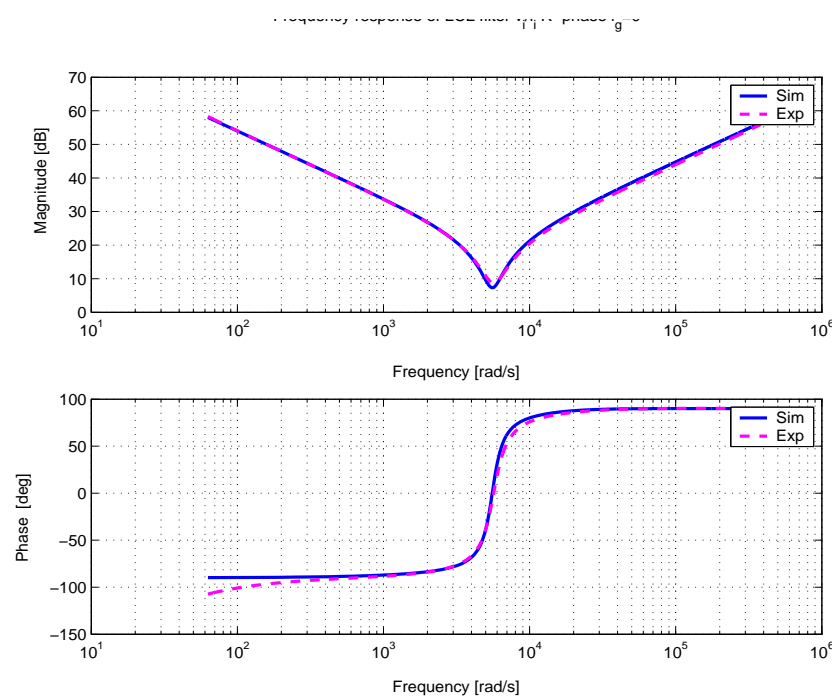
Figure A.30: LCL filter response v_i/i_i (i_g=0); powder core inductor, C_1=C_d=10μF, R_d=10Ω

Appendix B

Temperature Rise Tests

Systems used for Temperature rise tests:

DC Power Supply: Agilent Technologies - Model No.: N5768A
Specifications: 80V/19A, 1520W

Thermal Imager: Fluke Corporation - Model: Fluke-T120 INT/9
Specifications:
Temperature Range : -10^0C to $+127^0C$
Display Range : -15^0C to $+360^0C$
RTC Range : -50^0C to $+460^0C$
Detector Columns : 128
Detector Rows : 96

Data Logger: Yokogawa - Model No.: MX100
Specifications:
Logging Type : Mainly PC Measurement
Total max. no. of connect-able channels : 1200 (20 units*6 modules)
Display Monitor System : through MX100 Software or API
Operating Temp. Range : 0^0C to $+50^0C$
Power Supply Frequency : 50Hz
Standard Interface : Ethernet
Measurement Interval : 10ms to 60s
Application Software : Windows 2000/XP/Vista

Thermocouple Type : K-type (Chromel-Alumel)

Specifications:

Temperature Range : -200^0C to $+1350^0C$

Sensitivity : approximately $41\mu V/^0C$

B.1 Ferrite core inductor results
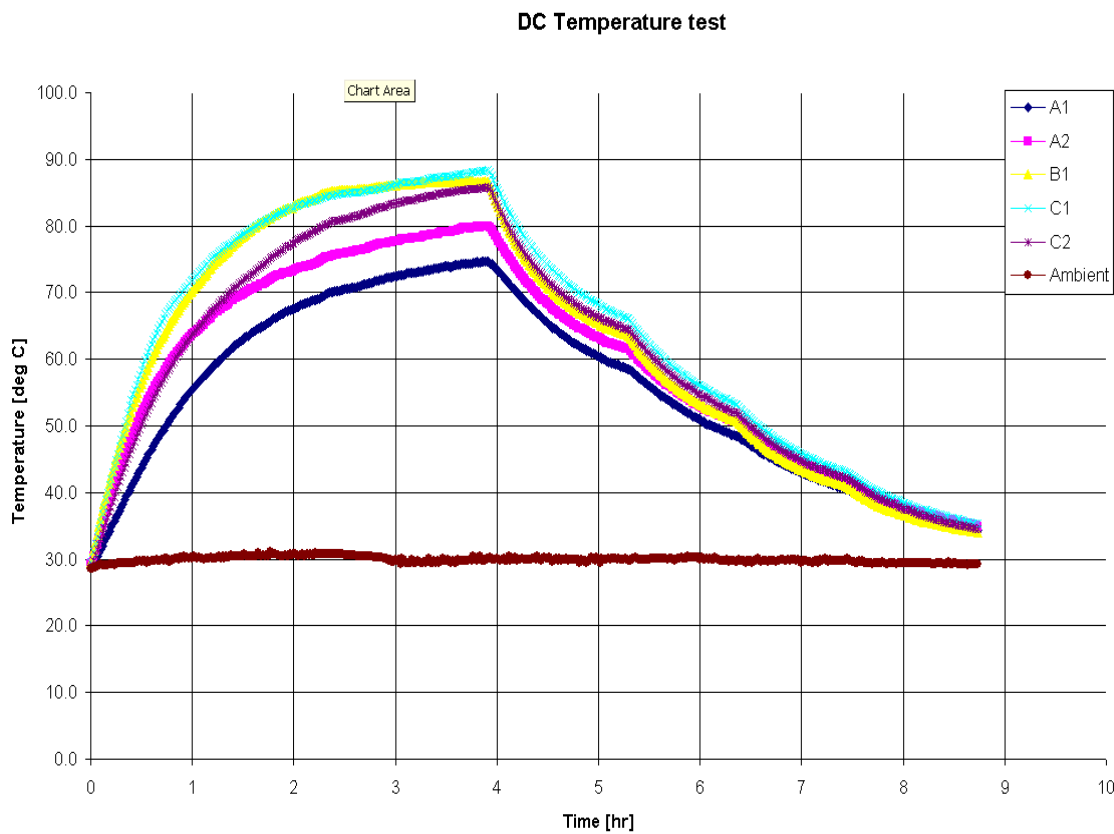
Figure B.1: DC temperature test; ferrite core inductor with round wire winding; all three phases
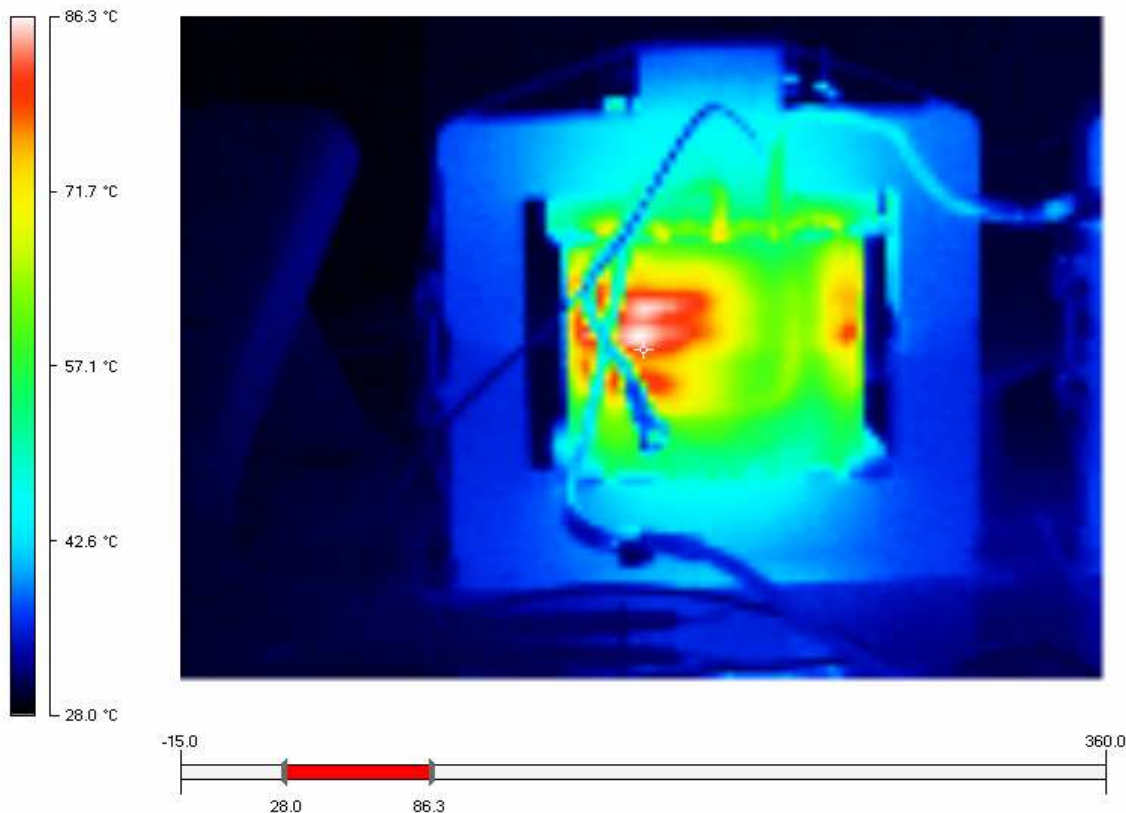
Figure B.2: DC temperature test; thermal image of ferrite core inductor - A1 with round wire winding
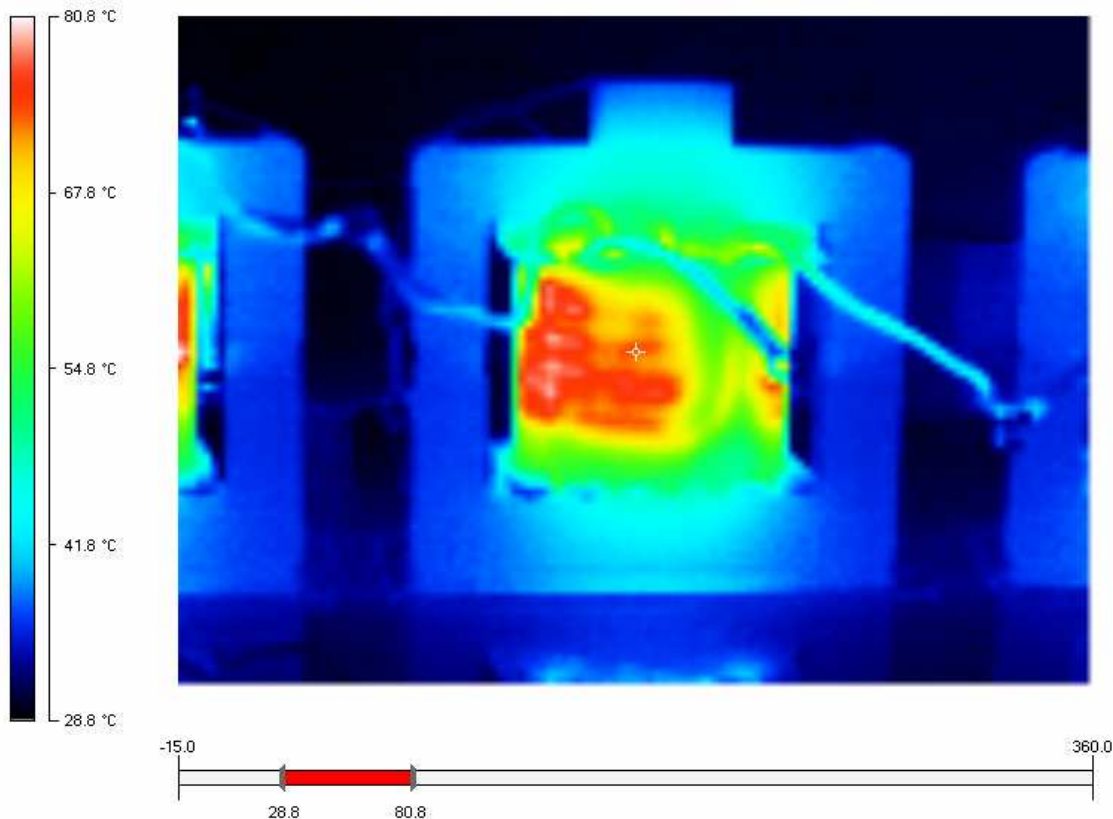
Figure B.3: DC temperature test; thermal image of ferrite core inductor - B1 with round wire winding
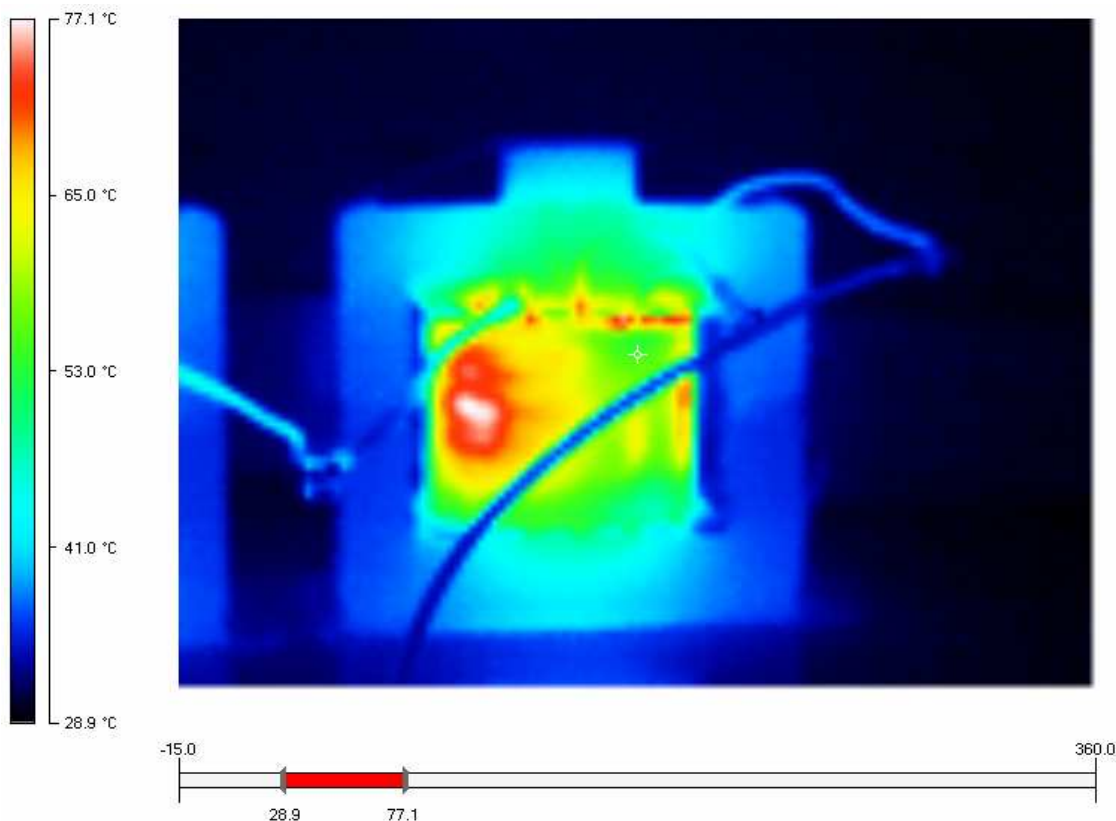
Figure B.4: DC temperature test; thermal image of ferrite core inductor - C1 with round wire winding
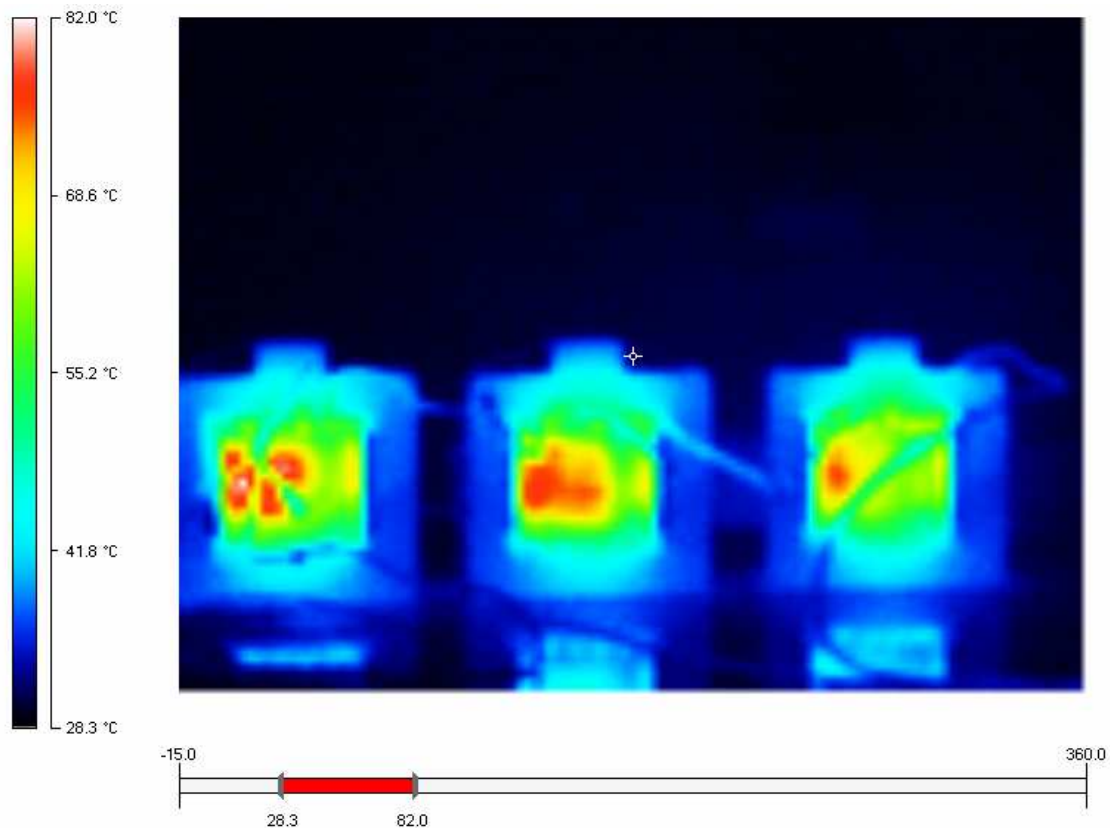
Figure B.5: DC temperature test; thermal image of ferrite core inductor - A1, B1, C1 with round wire winding

B.2   Amorphous core inductor results
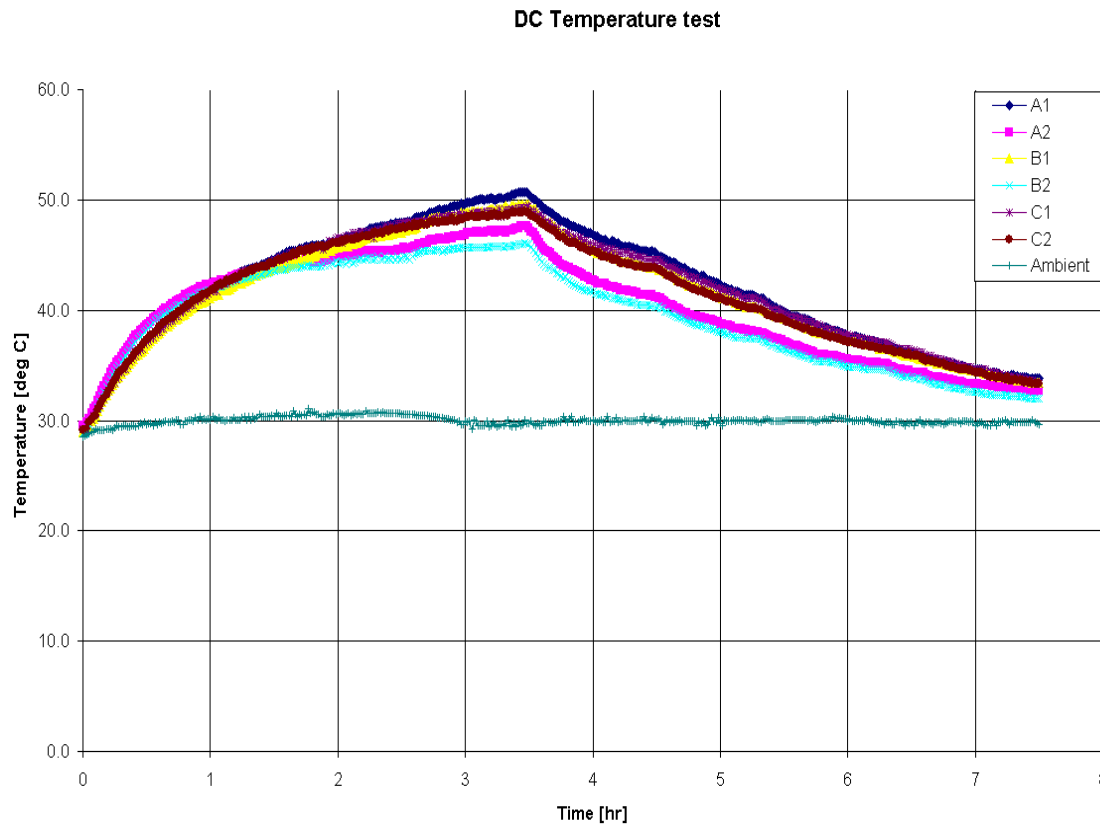
Figure B.6: DC temperature test; amorphous core AMCC367S and AMCC630 inductor with foil winding; all three phases

B.3   Powder iron core inductor results
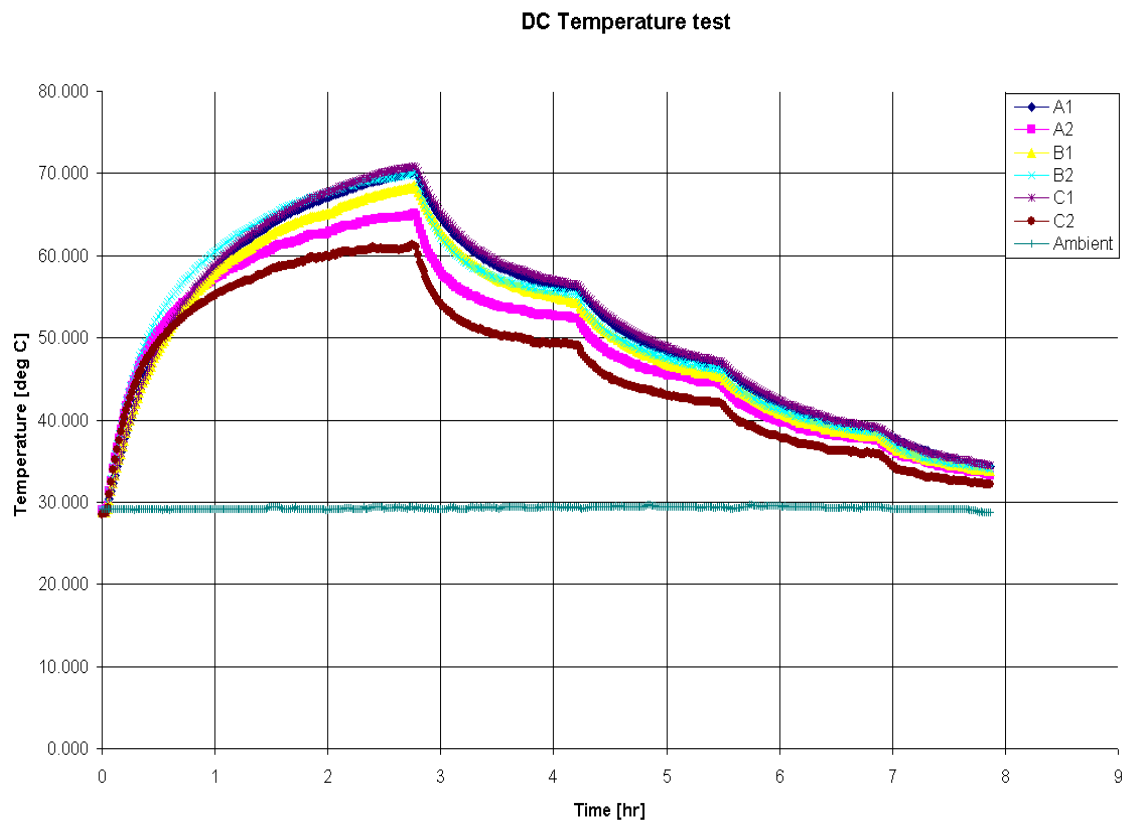
Figure B.7: DC temperature test; powder core inductor with foil winding and round wire winding - two bobbin design; all three phases

Appendix C

Test Set-up

C.1 Schematic and filter layout

The configuration of the test bed set-up is common for all three LCL filter types. The common platform facilitates appropriate physical placement of the individual filter components simultaneously satisfying the performance constraints (enables easy and immediate swapping of LCL filters connected between the Inverter and Grid for damping case and no damping case).

Key elements of the Test set-up schematic:
Variac/Auto transformer can be adjusted ranging from 0V to 230V
Rectifier is a 3-phase diode bridge rectifier ranging uptil 600V
Load is a 3-phase star connected resistive load rated for 5A per phase
Switches: S1, S2 and S3 are circuit breakers rated for 25A

Switch-S1	Switch-S2	Switch-S3	Mode
Closed	Short	Open	Standalone inverter
Closed	Open	Open	Standalone inverter
Closed	Load	Open	Standalone inverter
Closed	Grid	Open	Not connected
Open	Grid	Closed	Grid parallel

Table C.1: Test set-up schematic operating configurations
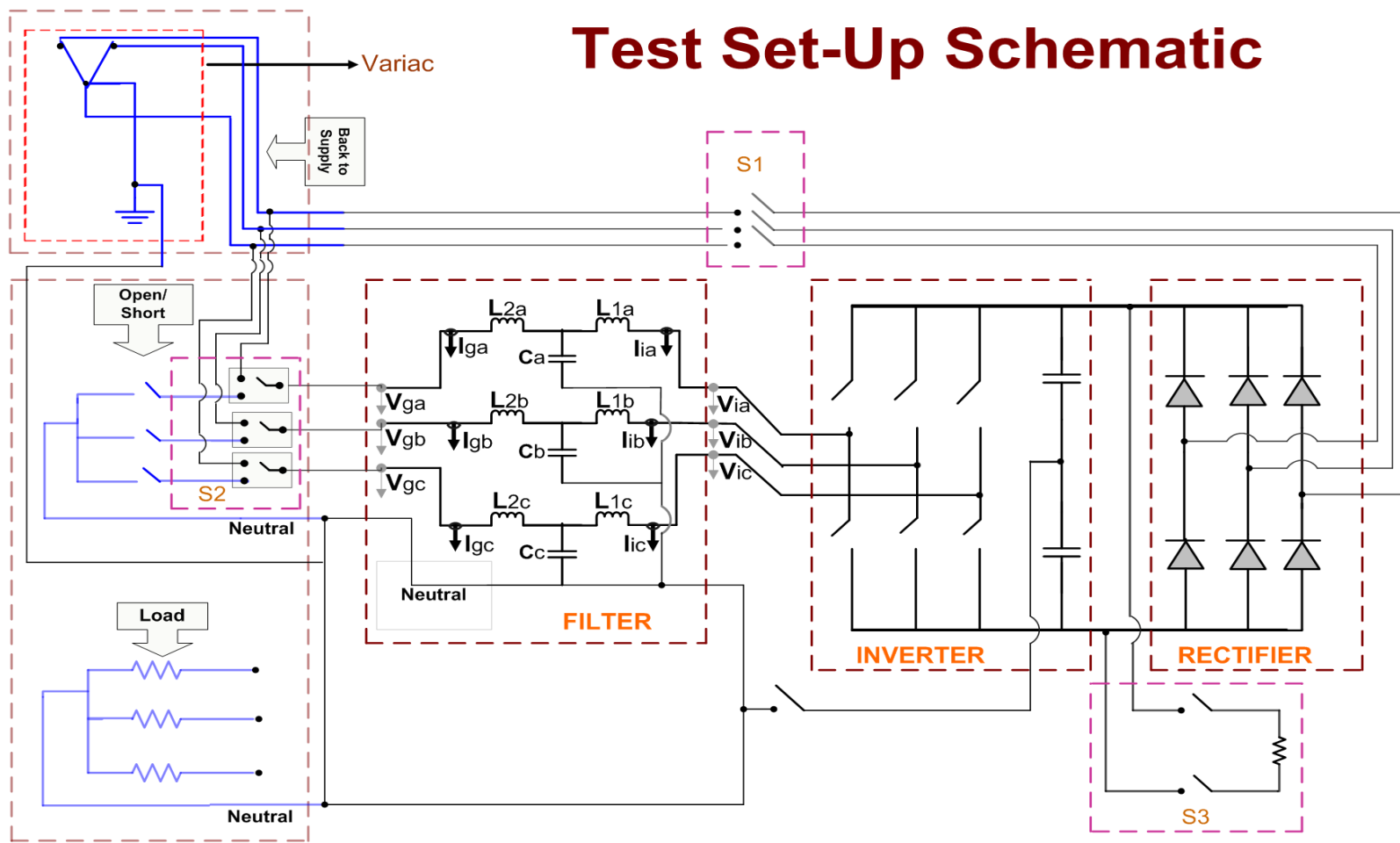
Figure C.1: Test Set-Up Schematic
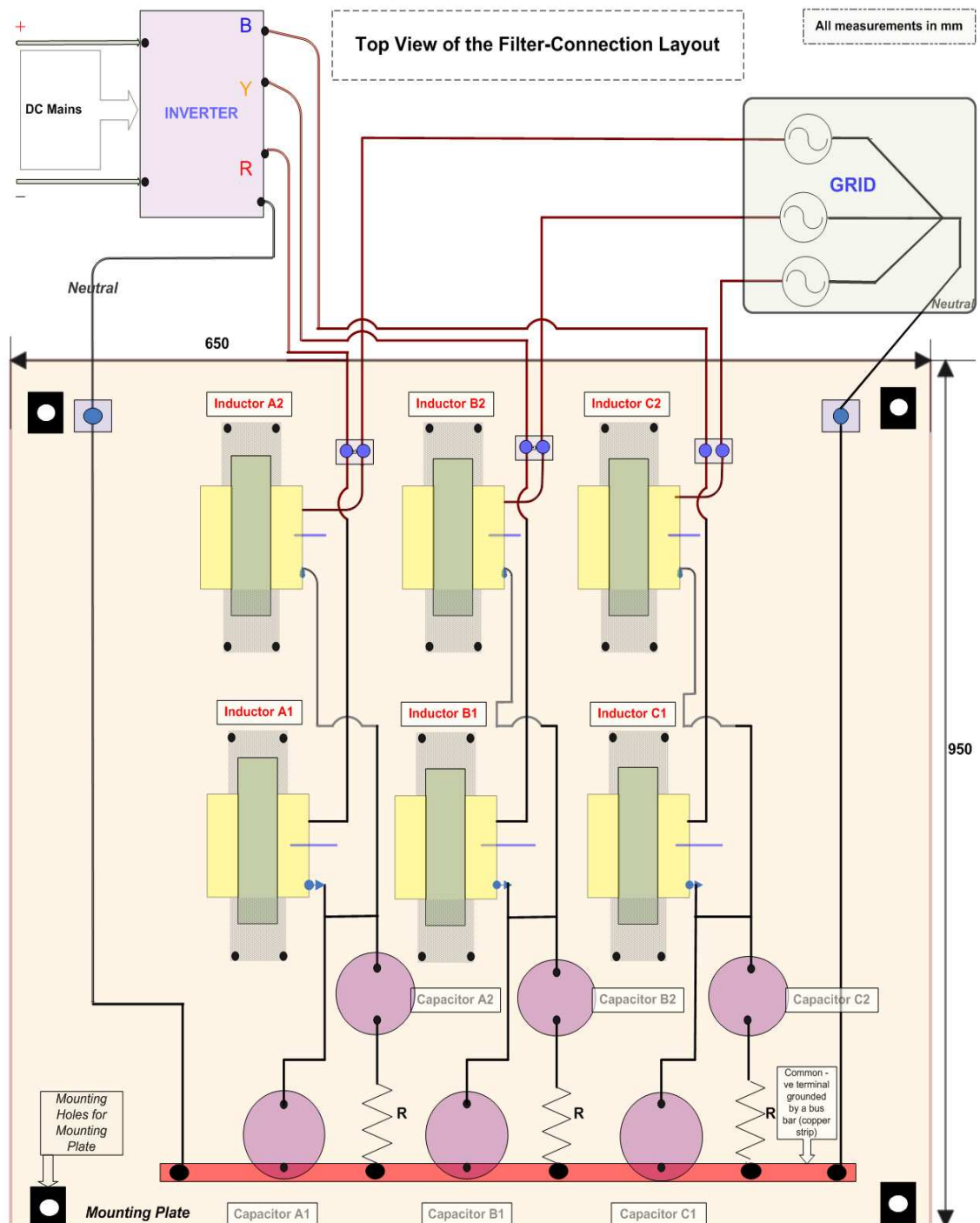
Figure C.2: Top View of Filter-Connection Layout - with damping
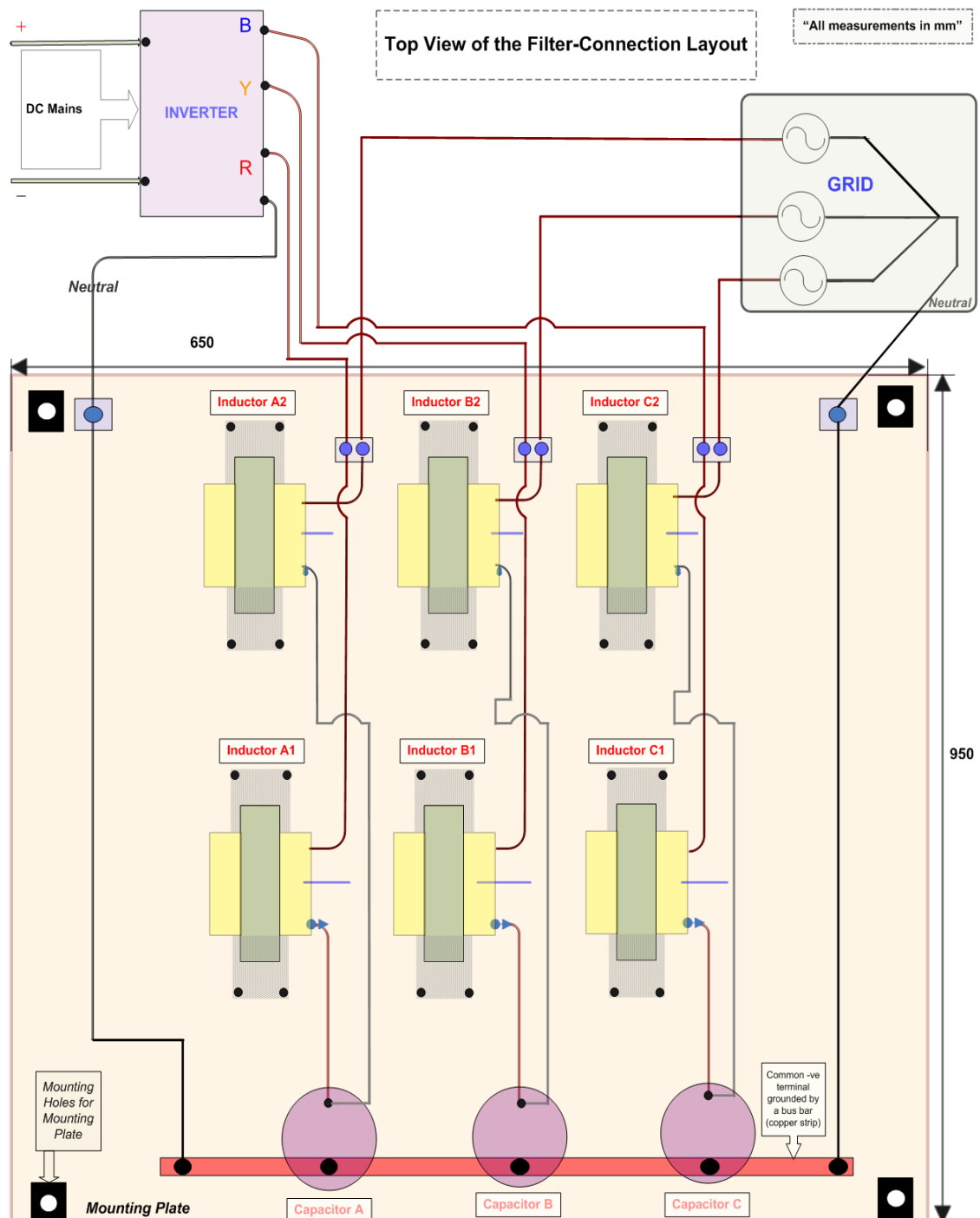
Figure C.3: Top View of Filter-Connection Layout - without damping

## C.2 Pictures of filter components and test set-up
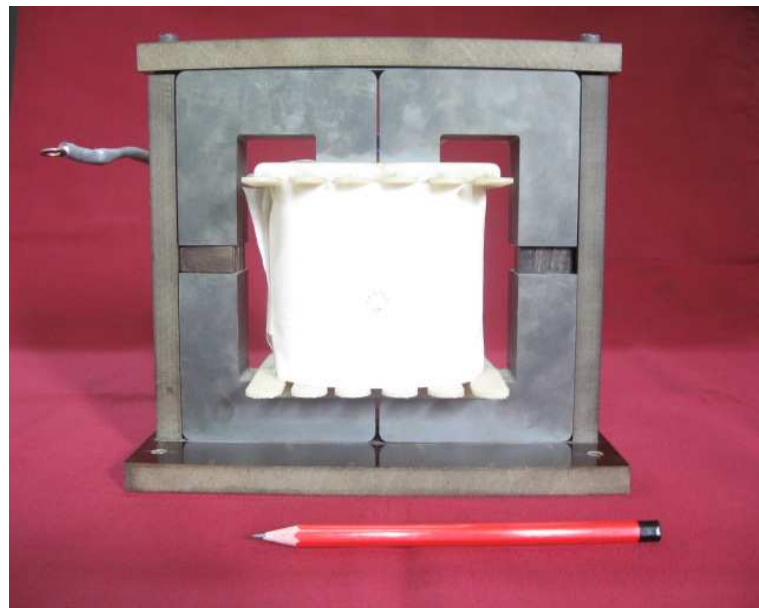
Figure C.4: Front View of the Ferrite core Inductor
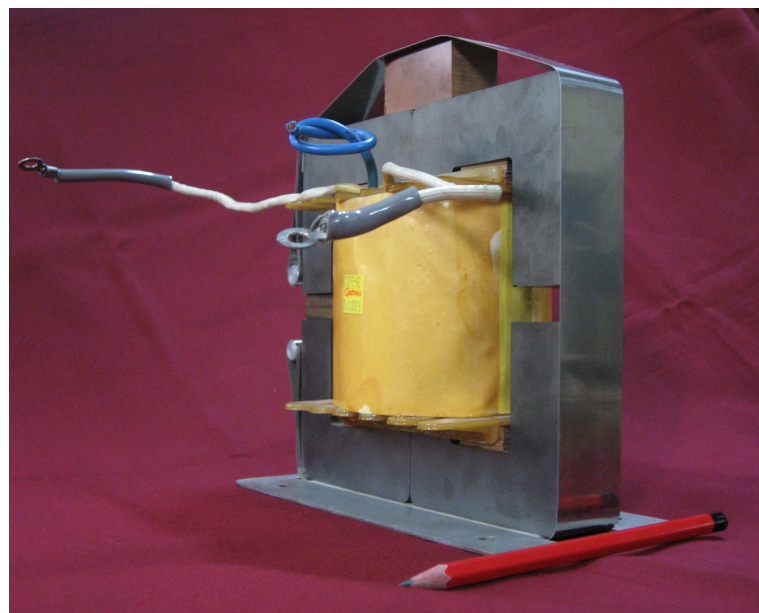
Figure C.5: Side View of the Ferrite core Inductor
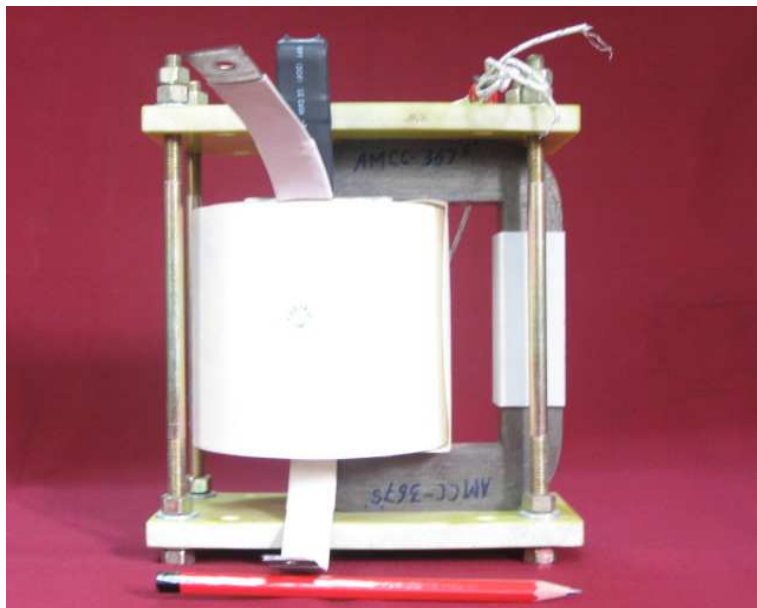
Figure C.6: Front View of the Amorphous core Inductor - AMCC367S
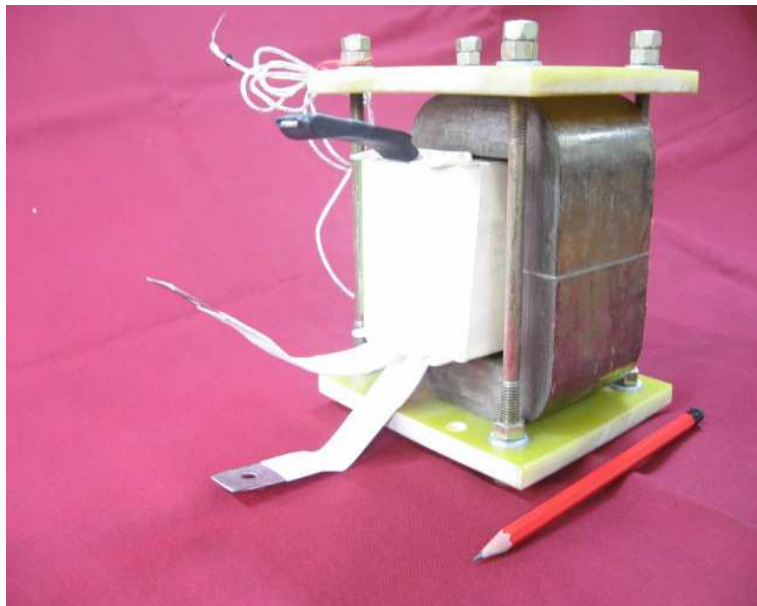
Figure C.7: Side View of the Amorphous core Inductor - AMCC630
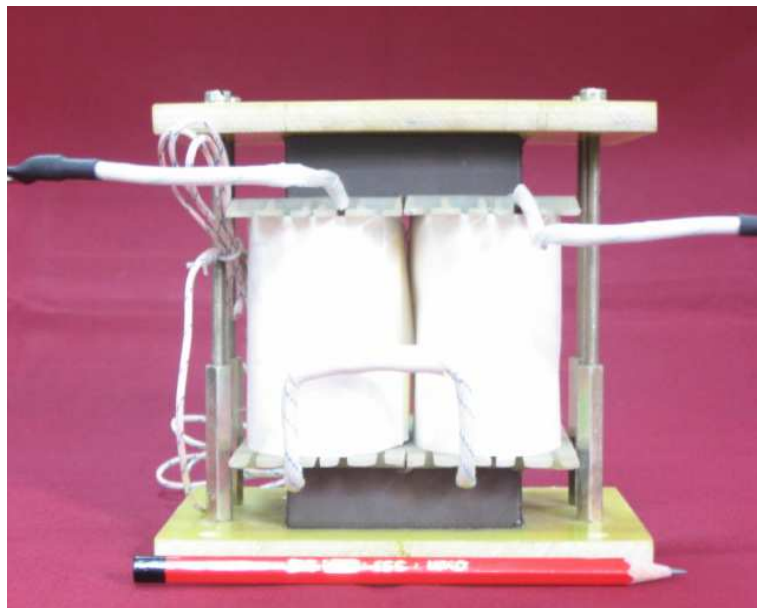
Figure C.8: Front View of the Powder core Inductor - two bobbin design
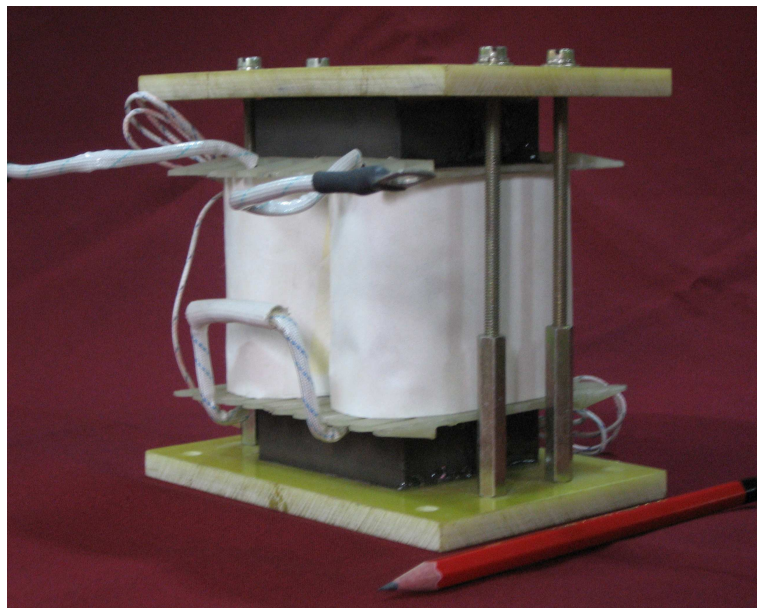
Figure C.9: Side View of the Powder core Inductor - two bobbin design
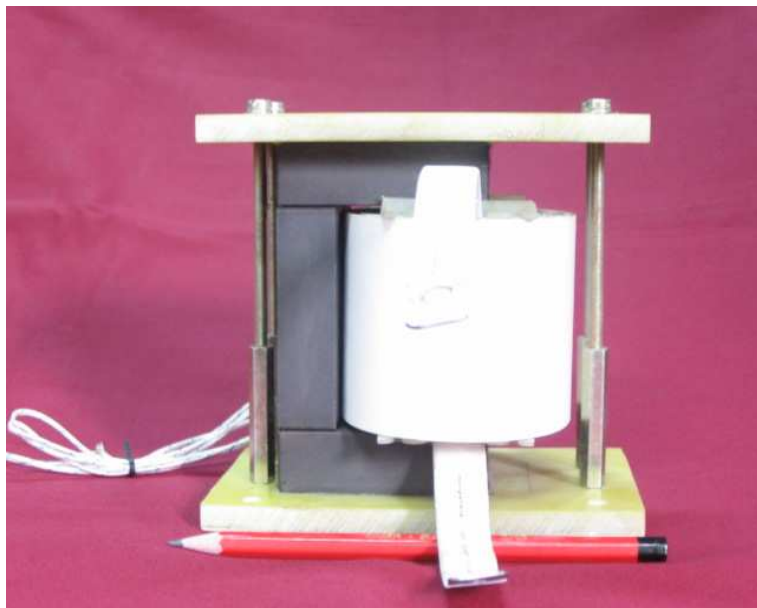
Figure C.10: Front View of the Powder core Inductor
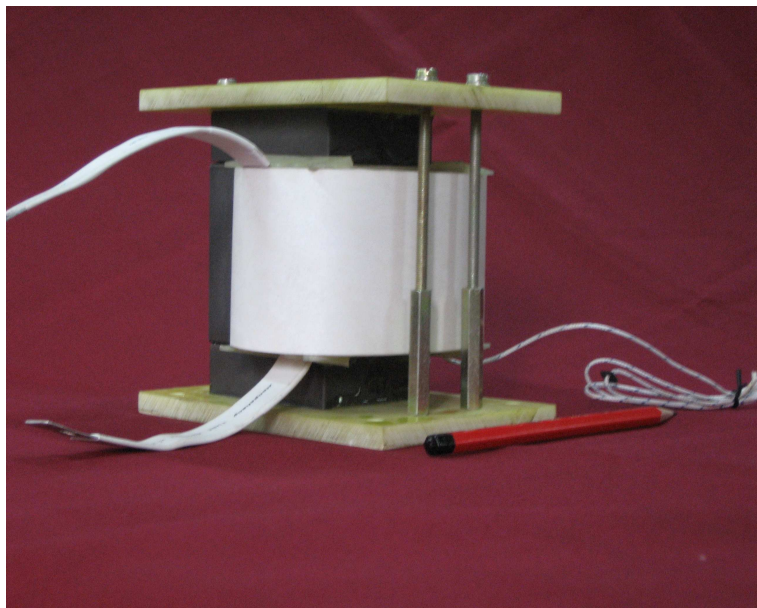

Figure C.11: Side View of the Powder core Inductor
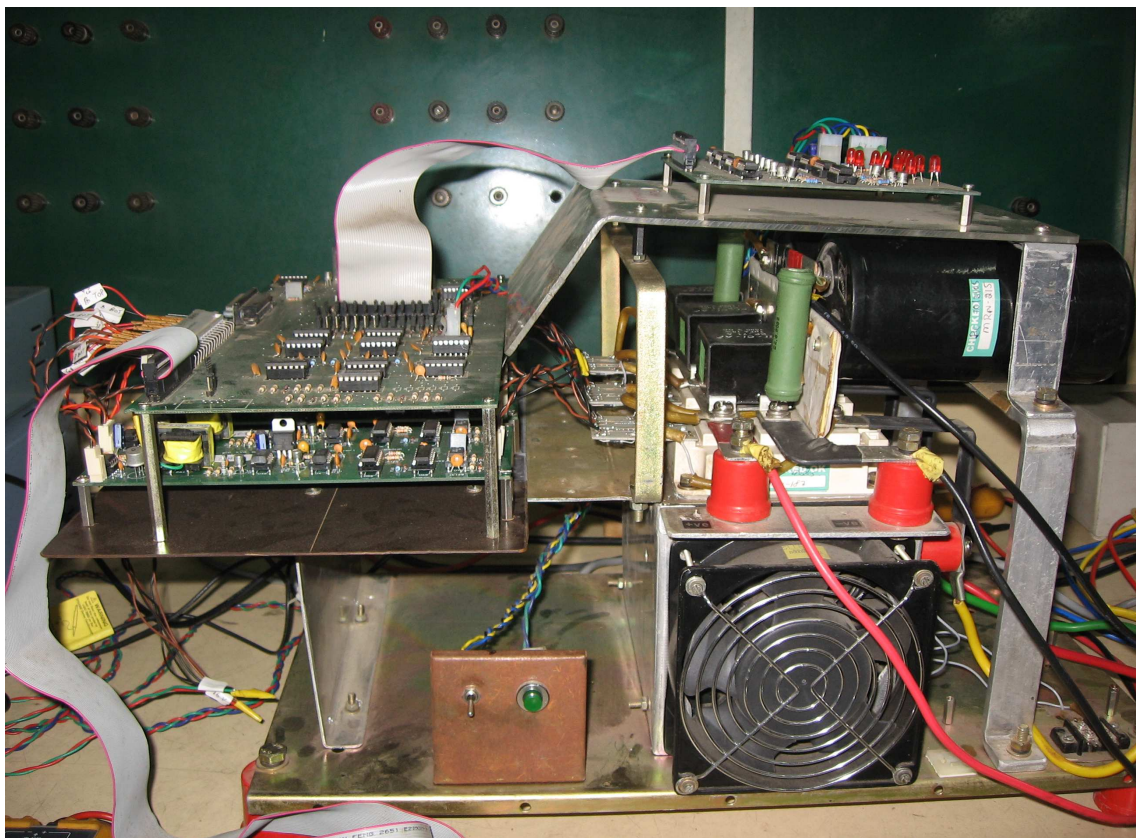
Figure C.12: Front View of the Inverter
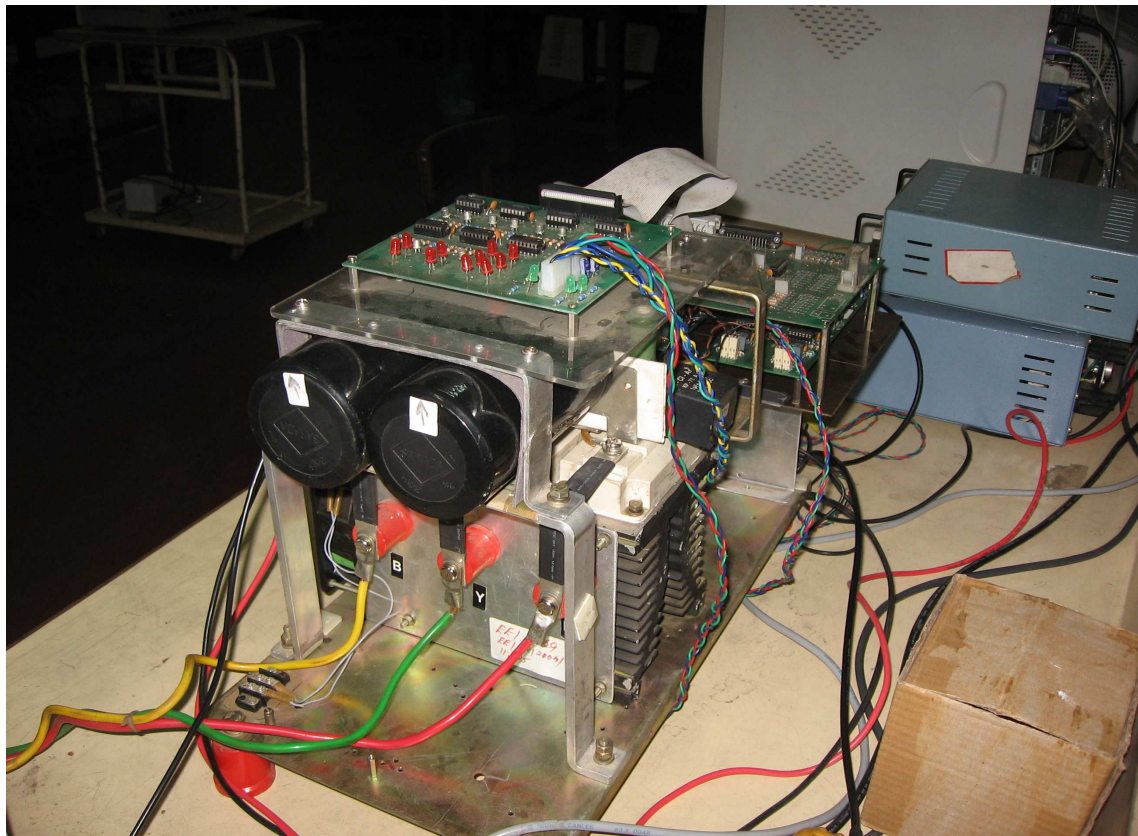
Figure C.13: Side View of the Inverter
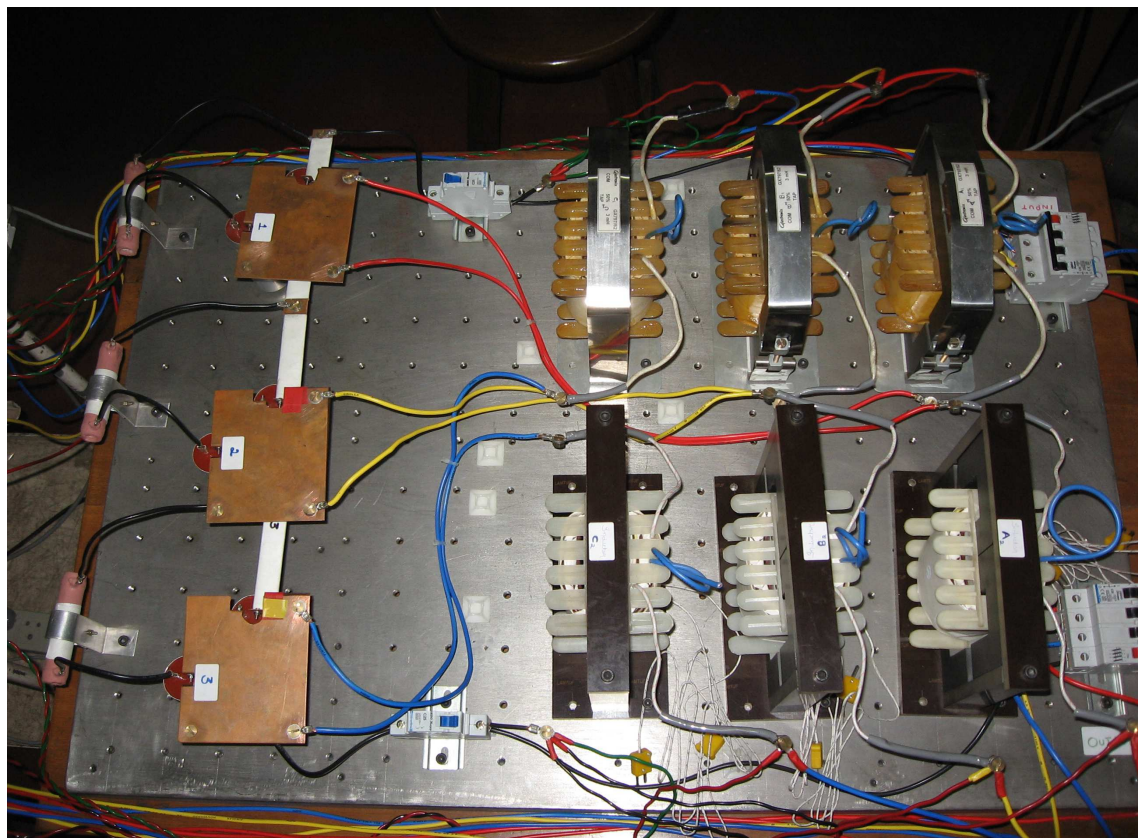
Figure C.14: Top View of the Ferrite Filter Set-Up

Figure C.15: Complete Physical Test Set-Up; for LCL Ferrite Core Inductor

Appendix D

Simulation of Inductors Using MagNet

D.1 Ferrite core inductor

This section contains the results of simulations of the filter inductor using the FEA tool called MagNet. The inductor models and plots of fluxlines and flux density are given along with the inductance values.
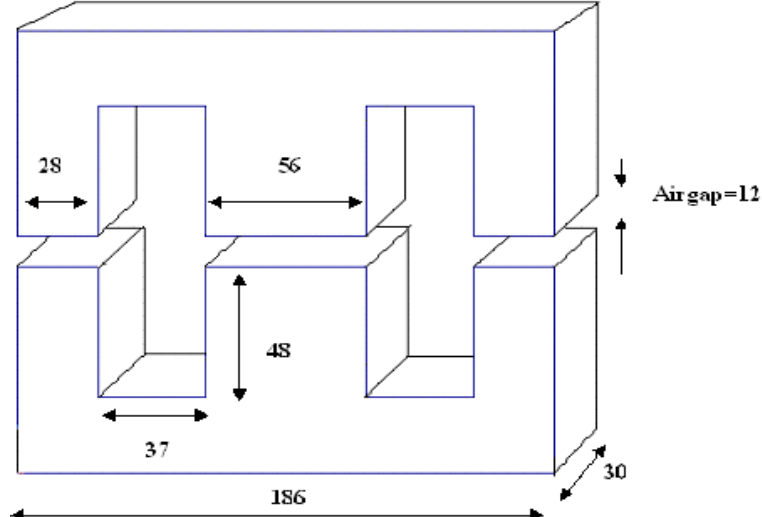

Figure D.1: Dimensions of ferrite core(in mm)
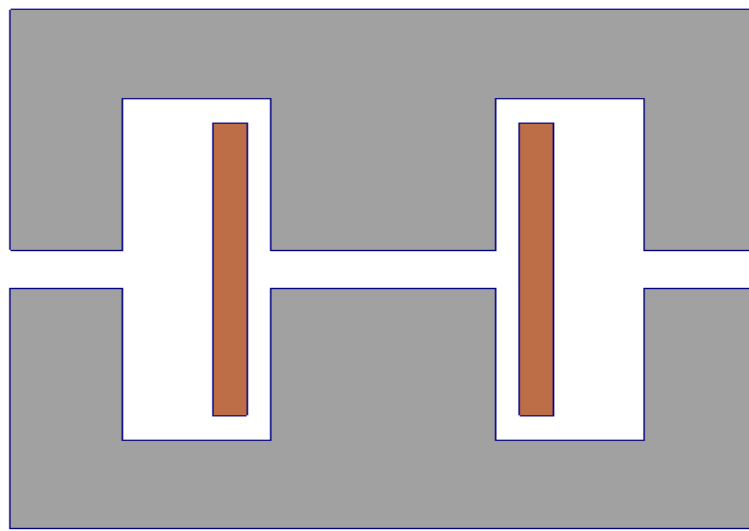
Figure D.2: Inductor model with single layer winding
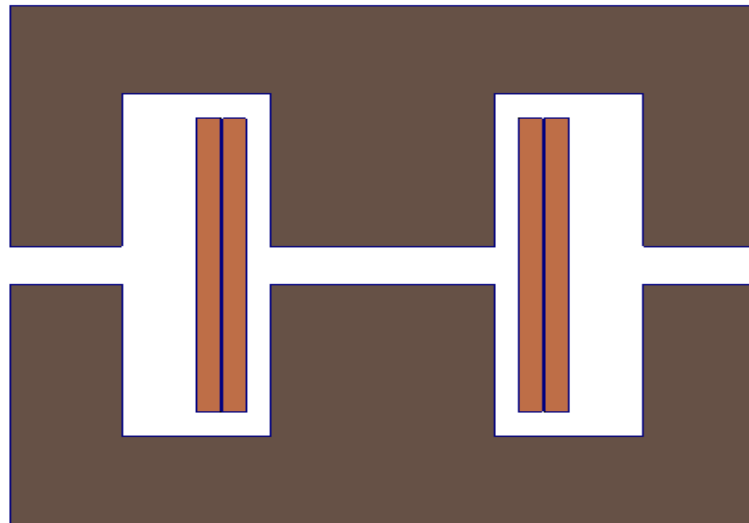
Figure D.3: Inductor model with double layer winding

Inductor model	Mesh size(mm)	Inductance (mH)
Single current sheet	1	1.911
Two layer winding	3	1.91
Four layer winding	3	1.914
Individual Conductors	0.5	1.9

Table D.1: Inductance values from simulation of Ferrite inductor (at 14.58A)
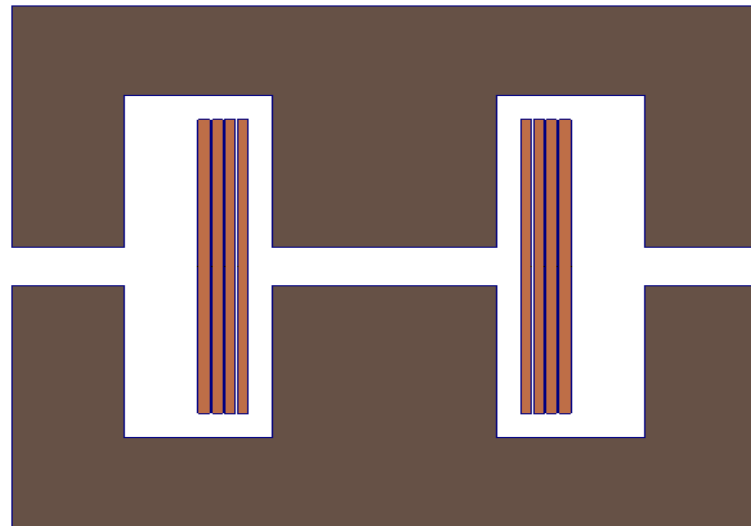
Figure D.4: Inductor model with four layer winding
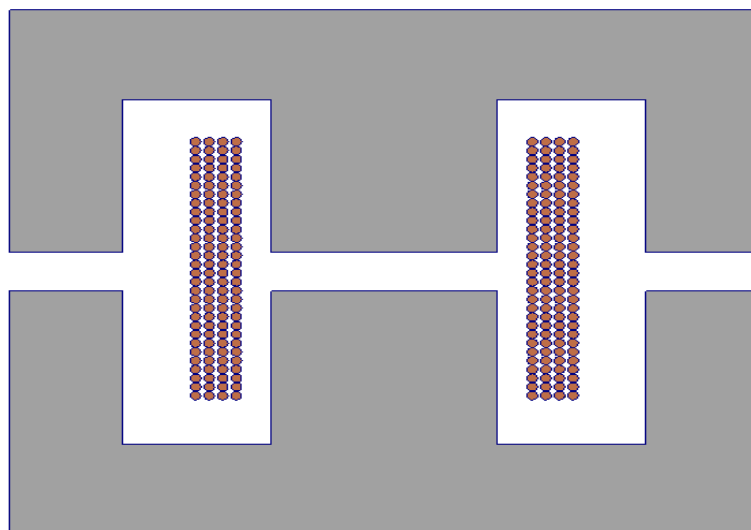
Figure D.5: Inductor model with individual conductors
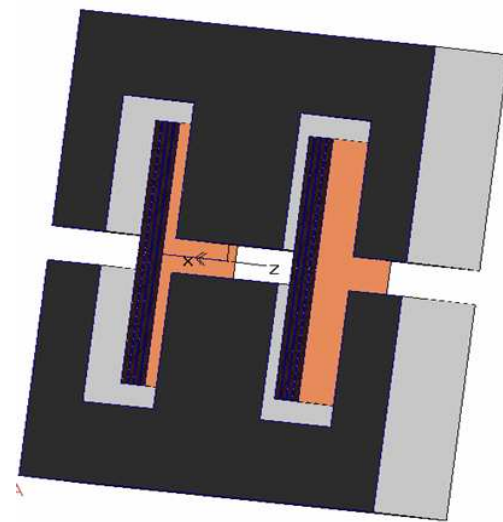
Figure D.6: 3D Inductor model
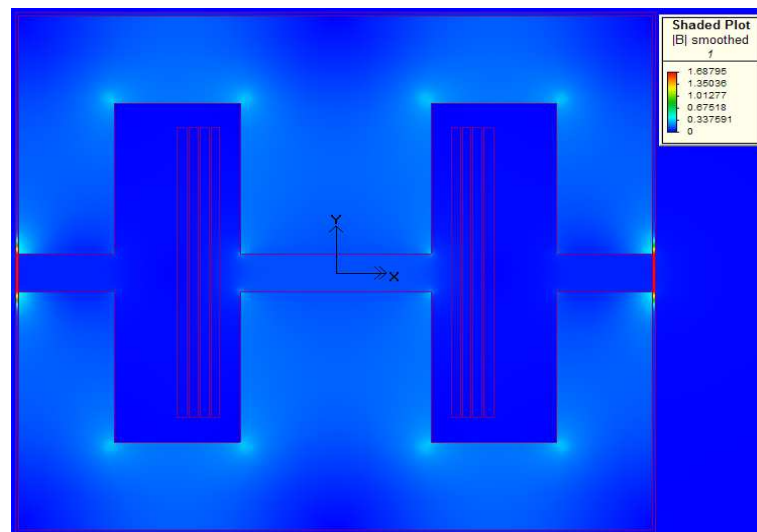
Figure D.7: Plot of Fluxdensity in the ferrite inductor with steel support
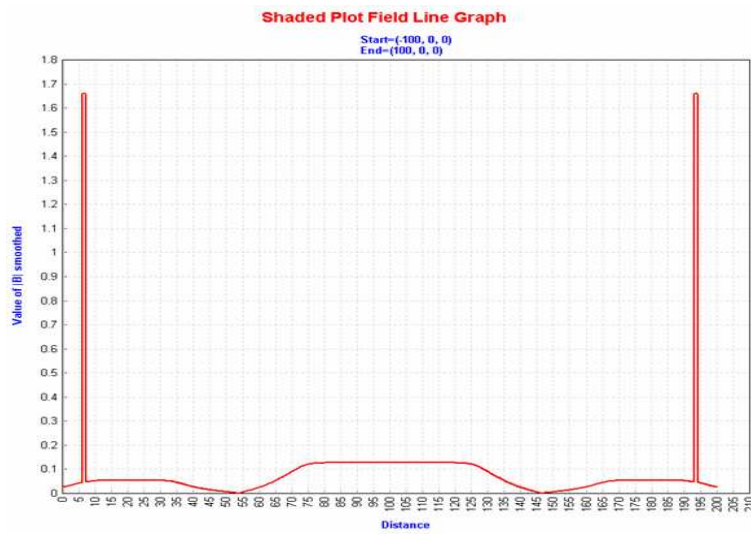
Figure D.8: Plot of flux density along the airgap of ferrite inductor with steel strap around the core

D.2   Amorphous core inductors
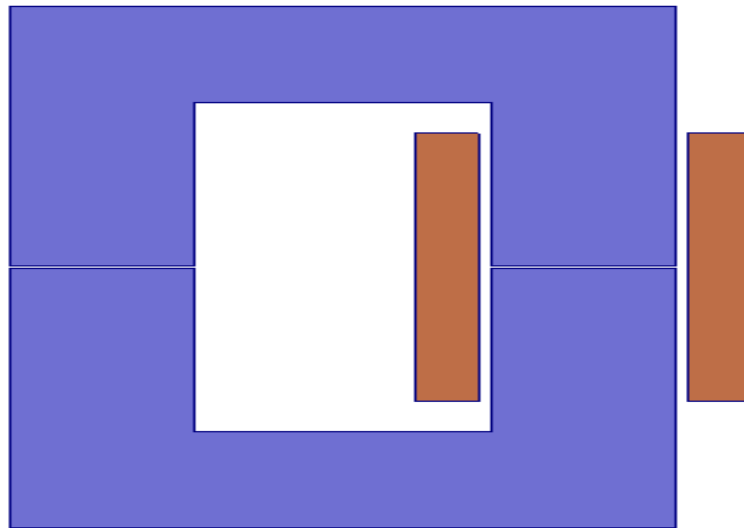
Figure D.9: Amorphous core inductor model(Core type: AMCC630)
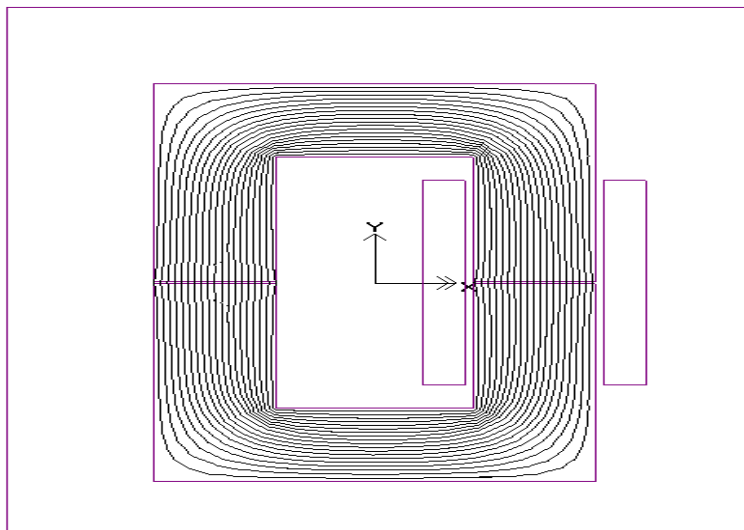
Figure D.10: Flux Plot for Amorphous inductor with AMCC630 core

Inductor model	Mesh size(mm)	Inductance (mH)
Amorphous core (AMCC 630)	5	5.73
Amorphous core (AMCC 367S)	5	3.57

Table D.2: Inductance values from simulation of Amorphous core inductor (at 14.58A)
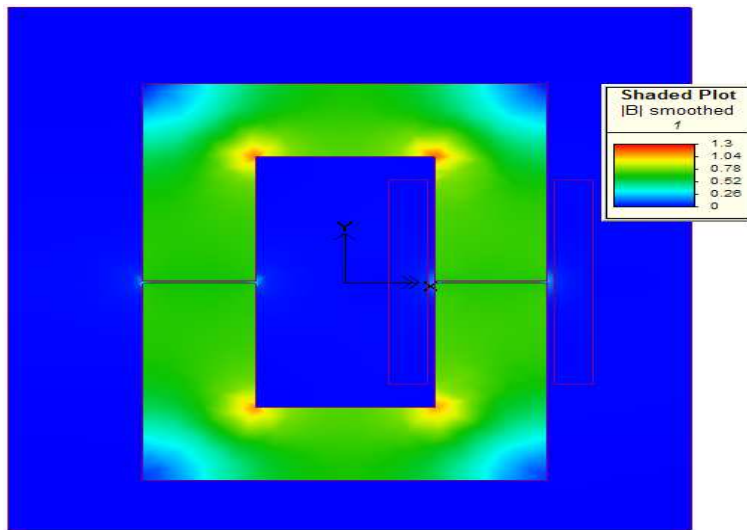
Figure D.11: Fluxdensity plot for Amorphous inductor with AMCC630 core
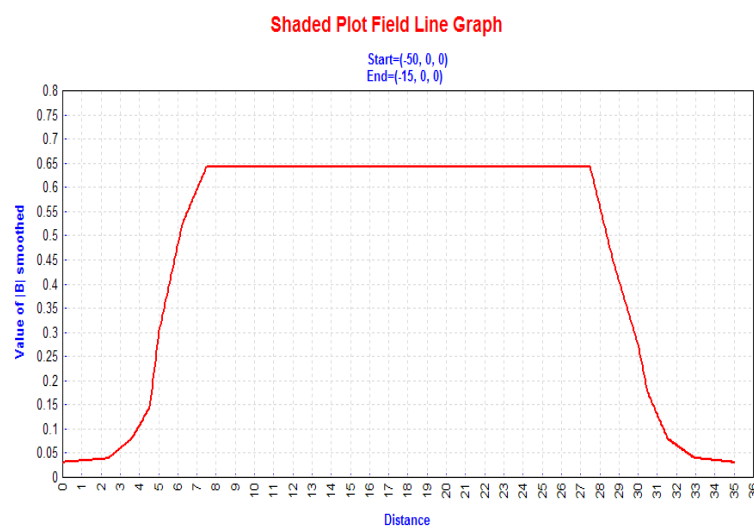
Figure D.12: Airgap flux density plot for Amorphous inductor with AMCC630 core
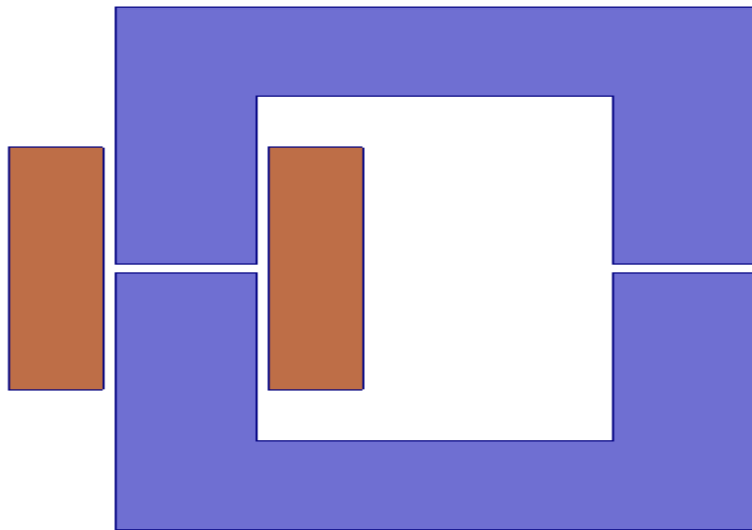
Figure D.13: Amorphous core inductor model(Core type: AMCC367S)
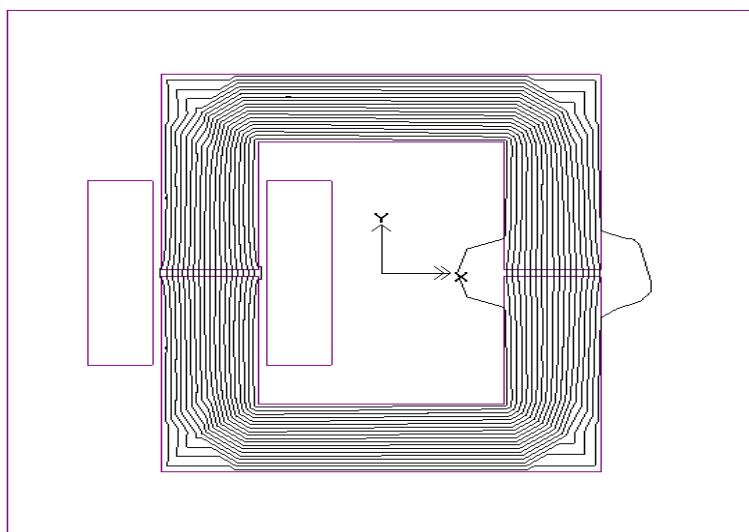
Figure D.14: Flux Plot for Amorphous inductor with AMCC367S core
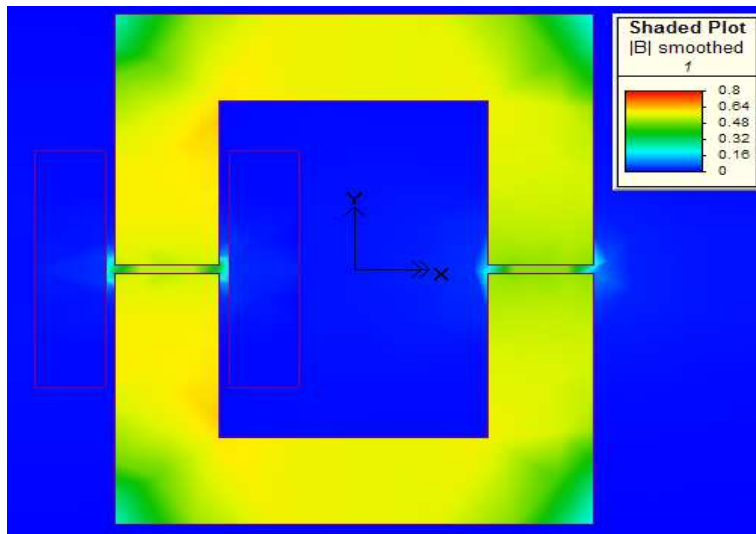
Figure D.15: Fluxdensity plot for Amorphous inductor with AMCC367S core
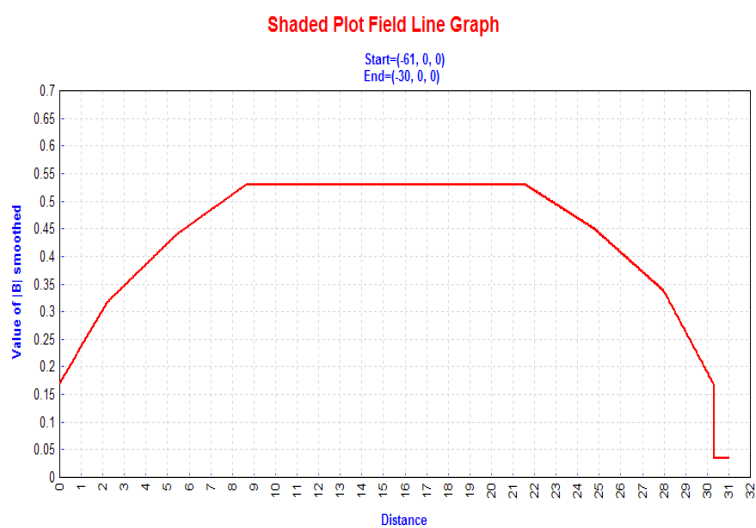
Figure D.16: Airgap flux density plot for Amorphous inductor with AMCC367S core

D.3   Powdered core inductor
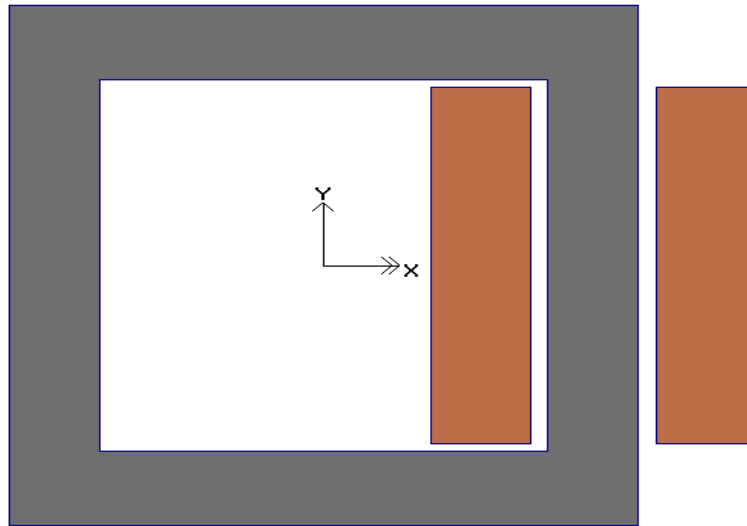
Figure D.17: Powder core inductor model

Inductor model	Mesh size(mm)	Inductance (mH)
Powdered core (BK7320)	5	1.7

Table D.3: Inductance values from simulation of Powdered core inductor (at 14.58A)
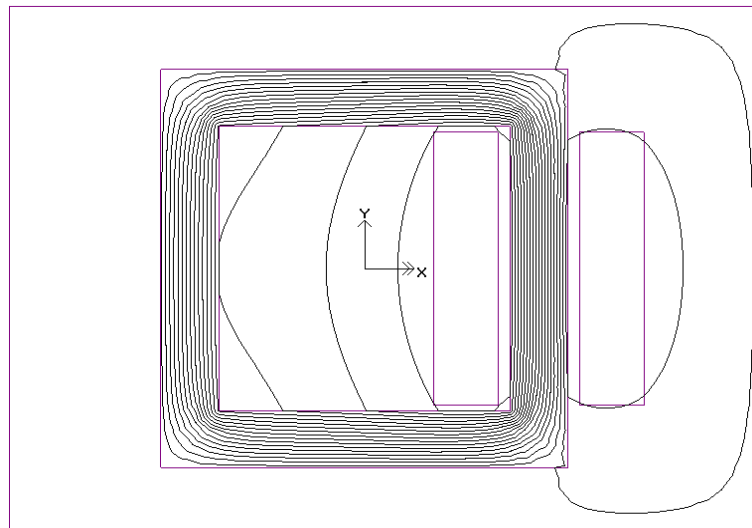
Figure D.18: Flux plot for powder core inductor
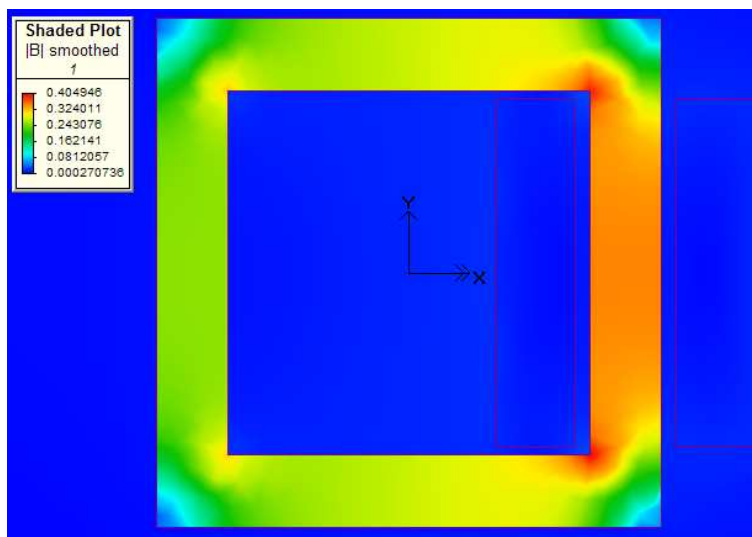
Figure D.19: Fluxdensity plot for powder core inductor

Appendix E

Electromagnetic Equations

E.1   Introduction

This appendix gives the theoretical background for the electromagnetic equations used in chapter 4. The vector equations and other derivations are referenced from established texts on electromagnetics [1]–[6].

E.2   Maxwell's Equations

The differential form of Maxwell's equations are used to describe and relate field vectors, current densities, and charge densities at any point in space at any time. These equations are valid only if field vectors are single-valued, bounded, continuous functions of position and time and exhibit continuous derivatives. But most practical field problems involve systems containing more than one kind of material. In case there exist abrupt changes in charges and current densities, the variation of the field vectors are related to the discontinuous distribution of charges and currents by boundary conditions. So a complete description of field vectors at any point requires both the Maxwell's equations and the associated boundary conditions. In differential form, Maxwell's equations are written as

$$\bigtriangledown \times \mathbf{E} = -\frac{\partial \mathbf{B}}{\partial t} \qquad (E.1)$$

$$\bigtriangledown \times \mathbf{H} = \mathbf{J} + \frac{\partial \mathbf{D}}{\partial t} \qquad (E.2)$$

$$\triangledown \cdot \mathbf{D} = q \tag{E.3}$$

$$\triangledown \cdot \mathbf{B} = 0 \tag{E.4}$$

All these field quantities - **E**, **H**, **D**, **B**, **J** are assumed to be time-varying, and each is a function of space-time coordinates, i.e $\mathbf{E} = \mathbf{E}(x, y, z; t)$. However, in many practical systems involving electromagnetic waves the time variations are of cosinusoidal form and are referred as time-harmonic. Such time variations are represented by $e^{j\omega t}$ and the instantaneous electromagnetic field vectors are related to their complex forms in a very simple manner.

$$\mathbf{E}(x, y, z; t) = \mathrm{Re}\left[\mathbf{E}(x, y, z)e^{j\omega t}\right] \tag{E.5}$$

$$\mathbf{H}(x, y, z; t) = \mathrm{Re}\left[\mathbf{H}(x, y, z)e^{j\omega t}\right] \tag{E.6}$$

$$\mathbf{D}(x, y, z; t) = \mathrm{Re}\left[\mathbf{D}(x, y, z)e^{j\omega t}\right] \tag{E.7}$$

$$\mathbf{B}(x, y, z; t) = \mathrm{Re}\left[\mathbf{B}(x, y, z)e^{j\omega t}\right] \tag{E.8}$$

$$\mathbf{J}(x, y, z; t) = \mathrm{Re}\left[\mathbf{J}(x, y, z)e^{j\omega t}\right] \tag{E.9}$$

E, **H**, **D**, **B**, **J** represent instantaneous field vectors while **E**, **H**, **B**, **D**, **J** represent the corresponding complex spatial forms which are only a function of position. Here we have chosen to represent the instantaneous quantities by the real part of the product of the corresponding complex spatial quantities with $e^{j\omega t}$. Another option would be to represent the instantaneous quantities by the imaginary product of the products. The magnitudes of the instantaneous fields represent peak values that are related to the RMS values by $\sqrt{2}$.

The Maxwell's equations in differential form can be written in terms of the complex field vectors by a simple substitution.

- Replace the instantaneous field vectors by corresponding spatial forms

- Replace $\partial/\partial t$ by $j\omega$.

$$\triangledown \times \mathbf{E} = -j\omega\mathbf{B} \tag{E.10}$$

$$\triangledown \times \mathbf{H} = \mathbf{J} + j\omega\mathbf{D} \tag{E.11}$$

$$\triangledown \cdot \mathbf{D} = q \tag{E.12}$$

$$\triangledown \cdot \mathbf{B} = 0 \tag{E.13}$$

E.3   Wave Equation

The first two Maxwell's equations (Eq (E.1) and (E.2)) are first order, coupled equations; i.e both unknown fields **E**, **H** appear in each equation. To uncouple these equations, we have to increase the order of the differential equations to second order. Taking curl on both sides of each equation,

$$\bigtriangledown \times \bigtriangledown \times \mathbf{E} = -\mu \frac{\partial}{\partial t}(\bigtriangledown \times \mathbf{H}) \tag{E.14}$$

$$\bigtriangledown \times \bigtriangledown \times \mathbf{H} = \bigtriangledown \times \mathbf{J} + \varepsilon \frac{\partial}{\partial t}(\bigtriangledown \times \mathbf{E}) \tag{E.15}$$

Substituting Eq (E.1) and Eq (E.2) and using the vector identity

$$\bigtriangledown \times \bigtriangledown \times \mathbf{F} = \bigtriangledown (\bigtriangledown \cdot \mathbf{F}) - \bigtriangledown^2 \mathbf{F} \tag{E.16}$$

we get

$$\bigtriangledown (\bigtriangledown \cdot \mathbf{E}) - \bigtriangledown^2 \mathbf{E} = -\mu \frac{\partial \mathbf{J}}{\partial t} - \mu\varepsilon \frac{\partial^2 \mathbf{E}}{\partial t^2} \tag{E.17}$$

$$\bigtriangledown (\bigtriangledown \cdot \mathbf{H}) - \bigtriangledown^2 \mathbf{H} = \bigtriangledown \times \mathbf{J} - \mu\varepsilon \frac{\partial^2 \mathbf{H}}{\partial t^2} \tag{E.18}$$

Substituting Eq (E.3) and Eq (E.4) in the above equation

$$\bigtriangledown \cdot \mathbf{D} = \varepsilon \bigtriangledown \cdot \mathbf{E} = q \Rightarrow \bigtriangledown \cdot \mathbf{E} = \frac{q}{\varepsilon} \tag{E.19}$$

$$\bigtriangledown \cdot \mathbf{B} = \mu \bigtriangledown \cdot \mathbf{H} = 0 \tag{E.20}$$

and using the constitutive parameter σ

$$\mathbf{J} = \sigma \mathbf{E} \tag{E.21}$$

we get

$$\bigtriangledown^2 \mathbf{E} = \frac{1}{\varepsilon} \bigtriangledown \cdot q + \mu\sigma \frac{\partial \mathbf{E}}{\partial t} + \mu\varepsilon \frac{\partial^2 \mathbf{E}}{\partial t^2} \tag{E.22}$$

$$\bigtriangledown^2 \mathbf{H} = \mu\sigma \frac{\partial \mathbf{H}}{\partial t} + \mu\varepsilon \frac{\partial^2 \mathbf{H}}{\partial t^2} \tag{E.23}$$

Equations (E.22) and (E.23) are referred to as vector wave equations for **E** and **H**. For source-free regions, q=0.

$$\nabla^2 \mathbf{E} = \mu\sigma \frac{\partial \mathbf{E}}{\partial t} + \mu\varepsilon \frac{\partial^2 \mathbf{E}}{\partial t^2} \tag{E.24}$$

$$\nabla^2 \mathbf{H} = \mu\sigma \frac{\partial \mathbf{H}}{\partial t} + \mu\varepsilon \frac{\partial^2 \mathbf{H}}{\partial t^2} \tag{E.25}$$

For lossless media, $\sigma = 0$,

$$\nabla^2 \mathbf{E} = \mu\varepsilon \frac{\partial^2 \mathbf{E}}{\partial t^2} \tag{E.26}$$

$$\nabla^2 \mathbf{H} = \mu\varepsilon \frac{\partial^2 \mathbf{H}}{\partial t^2} \tag{E.27}$$

For time-harmonic fields, the wave equations (for source-free media) are

$$\nabla^2 \mathbf{E} = j\omega\mu\sigma \mathbf{E} - \omega^2\mu\varepsilon \mathbf{E} = \gamma^2 \mathbf{E} \tag{E.28}$$

$$\nabla^2 \mathbf{H} = j\omega\mu\sigma \mathbf{H} - \omega^2\mu\varepsilon \mathbf{H} = \gamma^2 \mathbf{H} \tag{E.29}$$

where

$$\gamma^2 = j\omega\mu\sigma - \omega^2\mu\varepsilon \tag{E.30}$$

$$\gamma = \alpha + j\beta \tag{E.31}$$

- γ= propagation constant

- α = attenuation constant

- β= phase constant (or wave number)

If we allow positive and negative values of σ

$$\gamma = \pm\sqrt{j\omega\mu(\sigma + j\omega\varepsilon)} = \begin{cases} \pm(\alpha + j\beta) & \text{for } +\sigma \\ \pm(\alpha - j\beta) & \text{for } -\sigma \end{cases} \tag{E.32}$$

For source-free and lossless media,

$$\nabla^2 \mathbf{E} = -\omega^2\mu\varepsilon \mathbf{E} = -\beta^2 \mathbf{E} \tag{E.33}$$

$$\nabla^2 \mathbf{H} = -\omega^2\mu\varepsilon \mathbf{H} = -\beta^2 \mathbf{H} \tag{E.34}$$

Equations of the form of (E.33) and (E.34) are known as homogeneous vector Helmholtz equations.

The time variations of most practical problems are time-harmonic. Fourier series can be used to express time variations of other forms in terms of a number of time-harmonic terms. For many cases, the vector wave equations reduce to a number of scalar Helmholtz equations, and general solutions can be constructed once solutions to each of the scalar Helmholtz equations are found.

One method that can be used to solve the scalar Helmholtz equation is known as separation of variables. This leads to solutions which are products of three functions (for three-dimensional problems), each function depending upon one coordinate variable only. Such solutions can be added to form a series which represent very general functions. Also, single-product solutions of the wave equation represent modes which can propagate individually.

E.4   Rectangular coordinate system

In rectangular coordinate system, the vector wave equations are reduced to three scalar wave Helmholtz equations. Assuming source free ($q = 0$) but lossy medium ($\sigma \neq 0$), both **E** and **H** must satisfy Eqns (E.28) and (E.29). We can consider the solution to **E** and write the solution to **H** by inspection.

In rectangular coordinates, the general solution for $\mathbf{E}(x,y,z)$ can be written as

$$\mathbf{E}(x,y,z) = \hat{a}_x E_x(x,y,z) + \hat{a}_y E_y(x,y,z) + \hat{a}_z E_z(x,y,z) \tag{E.35}$$

$$\nabla^2 \mathbf{E} - \gamma^2 \mathbf{E} = \nabla^2(\hat{a}_x E_x + \hat{a}_y E_y + \hat{a}_z E_z) - \gamma^2(\hat{a}_x E_x + \hat{a}_y E_y + \hat{a}_z E_z) = 0 \tag{E.36}$$

which reduces to three scalar wave equations of

$$\nabla^2 E_x(x,y,z) - \gamma^2 E_x(x,y,z) = 0 \tag{E.37}$$

$$\nabla^2 E_y(x,y,z) - \gamma^2 E_y(x,y,z) = 0 \tag{E.38}$$

$$\nabla^2 E_z(x,y,z) - \gamma^2 E_z(x,y,z) = 0 \tag{E.39}$$

where

$$\gamma^2 = j\omega\mu(\sigma + j\omega\varepsilon) \tag{E.40}$$

Equations (E.37), (E.38) and (E.39) are of same form; once a solution of any of them is obtained, the solution to the others can be written by inspection. Choosing E_x, in expanded form

$$\nabla^2 E_x - \gamma^2 E_x = \frac{\partial^2 E_x}{\partial x^2} + \frac{\partial^2 E_x}{\partial y^2} + \frac{\partial^2 E_x}{\partial z^2} - \gamma^2 E_x = 0 \tag{E.41}$$

Using method of separation of variables, we can assume a solution for $E_x(x,y,z)$

$$E_x(x,y,z) = f(x)g(y)h(z) \tag{E.42}$$

where the x,y,z variations of E_x are separable. Substituting Eq (E.42) in Eq (E.41),

$$gh\frac{\partial^2 f}{\partial x^2} + fh\frac{\partial^2 g}{\partial y^2} + fg\frac{\partial^2 h}{\partial z^2} - \gamma^2 fgh = 0 \tag{E.43}$$

Since $f(x)$, $g(y)$ and $h(z)$ are each a function of only one variable, we can replace partial by ordinary derivatives. Also dividing by fgh we get

$$\frac{1}{f}\frac{d^2 f}{dx^2} + \frac{1}{g}\frac{d^2 g}{dy^2} + \frac{1}{h}\frac{d^2 h}{dz^2} = \gamma^2 \tag{E.44}$$

Each of the terms on the left hand side is a function of only a single independent variable; hence the sum of these terms can equal γ^2 only if each term is a constant. So Eq (E.44) separates into three equation of the form,

$$\frac{1}{f}\frac{d^2 f}{dx^2} = \gamma_x^2 \tag{E.45}$$

$$\frac{1}{g}\frac{d^2 g}{dy^2} = \gamma_y^2 \tag{E.46}$$

$$\frac{1}{h}\frac{d^2 h}{dz^2} = \gamma_z^2 \tag{E.47}$$

In addition

$$\gamma_x^2 + \gamma_y^2 + \gamma_z^2 = \gamma^2 \tag{E.48}$$

Eq (E.48) is known as the constraint equation. The solution to Eq (E.45) can take different forms. In terms of exponentials $f(x)$ has solution

$$f_1(x) = A_1 e^{-\gamma_x x} + B_1 e^{+\gamma_x x} \tag{E.49}$$

or writing in terms of hyperbolic functions

$$f_2(x) = C_1\cosh(\gamma_x x) + D_1\sinh(\gamma_x x) \tag{E.50}$$

$g(y)$ and $h(z)$ can be expressed in exactly the same form, with different constants and roots of the solution.

$$g_1(y) = A_2 e^{-\gamma_y y} + B_2 e^{+\gamma_y y} \tag{E.51}$$

$$g_2(y) = C_2\cosh(\gamma_y y) + D_2\sinh(\gamma_y y) \tag{E.52}$$

$$h_1(z) = A_3 e^{-\gamma_z z} + B_3 e^{+\gamma_z z} \tag{E.53}$$

$$h_2(z) = C_3\cosh(\gamma_z z) + D_3\sinh(\gamma_z z) \tag{E.54}$$

The appropriate form of f, g and h chosen to represent the solution of E_x is decided by the geometry of the problem. A similar procedure can be used to derive the other components of **E** i.e E_y and E_z. The instantaneous electric and magnetic field components can be obtained by multiplying the factor $e^{j\omega t}$ and taking the real part.

## E.5   Cylindrical coordinate system
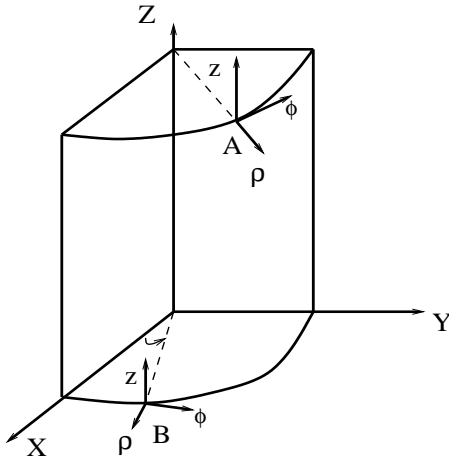
Figure E.1: Cylindrical coordinate system and unit vectors

If the geometry of the system is in cylindrical configuration then the boundary-value problem for **E** and **H** should be solved using cylindrical coordinates. As in rectangular coordinates, we can consider the solution of **E** and **H** will have the same form. In

cylindrical coordinates a general solution to the vector wave equation is given by

$$\mathbf{E}(\rho,\phi,z) = \hat{a}_\rho E_\rho(\rho,\phi,z) + \hat{a}_\phi E_\phi(\rho,\phi,z) + \hat{a}_z E_z(\rho,\phi,z) \tag{E.55}$$

where ρ(rho), ϕ(phi) and z are the cylindrical coordinates as shown in fig E.1. From Eq (E.28)

$$\nabla^2(\hat{a}_\rho E_\rho + \hat{a}_\phi E_\phi + \hat{a}_z E_z) = \gamma^2(\hat{a}_\rho E_\rho + \hat{a}_\phi E_\phi + \hat{a}_z E_z) \tag{E.56}$$

which does not reduce to three simple scalar wave equations, similar to Eqns (E.37)-(E.39) because

$$\nabla^2(\hat{a}_\rho E_\rho) \neq \hat{a}_\rho \nabla^2 E_\rho \tag{E.57}$$

$$\nabla^2(\hat{a}_\phi E_\phi) \neq \hat{a}_\phi \nabla^2 E_\phi \tag{E.58}$$

However,

$$\nabla^2(\hat{a}_z E_z) = \hat{a}_z \nabla^2 E_z \tag{E.59}$$

If we consider two different points (points A and B on fig E.1) we can see that direction of $\hat{a}_\rho$ and $\hat{a}_\phi$ are different while $\hat{a}_z$ still has same direction. This means the unit vectors $\hat{a}_\rho$ and $\hat{a}_\phi$ cannot be treated as constants but as functions of (ρ,ϕ,z). So only one of the three scalar equations reduces to

$$\nabla^2 E_z - \gamma^2 E_z = 0 \tag{E.60}$$

In the following discussion, γ is assumed to be real, to simplify calculation. Using the vector identity

$$\nabla^2 \mathbf{E} = \nabla(\nabla \cdot \mathbf{E}) - \nabla \times \nabla \times \mathbf{E} \tag{E.61}$$

Substituting for $\nabla^2 \mathbf{E}$,

$$\nabla(\nabla \cdot \mathbf{E}) - \nabla \times \nabla \times \mathbf{E} = \gamma^2 \mathbf{E} \tag{E.62}$$

Expanding the individual terms we get three scalar partial differential equations,

$$\nabla^2 E_\rho + \left(-\frac{E_\rho}{\rho^2} - \frac{2}{\rho^2} \frac{\partial E_\phi}{\partial \phi} \right) = \gamma^2 E_\rho \tag{E.63}$$

$$\bigtriangledown^2 E_\phi + \left(-\frac{E_\phi}{\rho^2} + \frac{2}{\rho^2}\frac{\partial E_\phi}{\partial \phi} \right) = \gamma^2 E_\phi \tag{E.64}$$

$$\bigtriangledown^2 E_z = \gamma^2 E_z \tag{E.65}$$

Eqns (E.63) and (E.64) are coupled (each contain more than one electric field component) second-order partial differential equations, which are the most difficult to solve. However Eq (E.65) is an uncoupled second-order partial differential equation. In each of the above equations, $\bigtriangledown^2 \psi(\rho,\phi,z)$ is the Laplacian of a scalar that in cylindrical coordinates takes the form

$$\bigtriangledown^2 \psi(\rho,\phi,z) = \frac{1}{\rho}\frac{\partial}{\partial \rho}\left(\rho \frac{\partial \psi}{\partial \rho} \right) + \frac{1}{\rho^2}\frac{\partial^2 \psi}{\partial \phi^2} + \frac{\partial^2 \psi}{\partial z^2} \tag{E.66}$$

$$\bigtriangledown^2 \psi(\rho,\phi,z) = \frac{\partial^2 \psi}{\partial \rho^2} + \frac{1}{\rho}\frac{\partial \psi}{\partial \rho} + \frac{1}{\rho^2}\frac{\partial^2 \psi}{\partial \phi^2} + \frac{\partial^2 \psi}{\partial z^2} \tag{E.67}$$

In expanded form Eq (E.65) can be written as

$$\frac{\partial^2 \psi}{\partial \rho^2} + \frac{1}{\rho}\frac{\partial \psi}{\partial \rho} + \frac{1}{\rho^2}\frac{\partial^2 \psi}{\partial \phi^2} + \frac{\partial^2 \psi}{\partial z^2} = \gamma^2 \psi \tag{E.68}$$

where $\psi(\rho,\phi,z)$ is a scalar function representing a field or a vector potential component. Using the method of separation of variables,

$$\psi(\rho,\phi,z) = f(\rho)g(\phi)h(z) \tag{E.69}$$

Substituting it in above equation,

$$gh\frac{\partial^2 f}{\partial \rho^2} + gh\frac{1}{\rho}\frac{\partial f}{\partial \rho} + fh\frac{1}{\rho^2}\frac{\partial^2 g}{\partial \phi^2} + fg\frac{\partial^2 h}{\partial z^2} = \gamma^2 fgh \tag{E.70}$$

Dividing both sides by fgh and replacing partial by ordinary derivatives,

$$\frac{1}{f}\frac{d^2 f}{d\rho^2} + \frac{1}{f}\frac{1}{\rho}\frac{df}{d\rho} + \frac{1}{g}\frac{1}{\rho^2}\frac{d^2 g}{d\phi^2} + \frac{1}{h}\frac{d^2 h}{dz^2} = \gamma^2 \tag{E.71}$$

The last term on left hand side is only a function of z, so in the same way as rectangular coordinates,

$$\frac{d^2 h}{dz^2} = \gamma_z^2 h \tag{E.72}$$

where γ_z^2 is a constant. Substituting in above equation and multiplying both sides by ρ^2,

$$\frac{\rho^2}{f}\frac{d^2 f}{d\rho^2} + \frac{\rho}{f}\frac{df}{d\rho} + \frac{1}{g}\frac{d^2 g}{d\phi^2} + (\gamma_z^2 - \gamma^2)\rho^2 = 0 \tag{E.73}$$

Now the third term on the left hand side is only a function of ϕ, so it can be set equal to a constant $-m^2$.

$$\frac{d^2 g}{d\phi^2} = -m^2 g \tag{E.74}$$

Let

$$\gamma_z^2 - \gamma^2 = \gamma_p^2 \tag{E.75}$$

Using the two substitutions, and multiplying both sides of the Eq (E.73) by f,

$$\rho^2\frac{d^2 f}{d\rho^2} + \rho\frac{df}{d\rho} + [(\gamma_p\rho)^2 - m^2]f = 0 \tag{E.76}$$

Eq (E.76) is the classic Bessel differential equation with real arguments, and Eq (E.75) is the constraint equation for the wave equation in cylindrical coordinates.

Solutions to Eq (E.72), Eq (E.74) and Eq (E.76) take the form

$$f_1(\rho) = A_1 J_m(\gamma_p\rho) + B_1 Y_m(\gamma_p\rho) \tag{E.77}$$

or

$$f_2(\rho) = C_1 H_m^{(1)}(\gamma_p\rho) + D_1 H_m^{(2)}(\gamma_p\rho) \tag{E.78}$$

and

$$g_1(\phi) = A_2 e^{-jm\phi} + B_2 e^{+jm\phi} \tag{E.79}$$

or

$$g_2(\phi) = C_2\cos(m\phi) + D_2\sin(m\phi) \tag{E.80}$$

and

$$h_1(z) = A_3 e^{-j\gamma_z z} + B_3 e^{+j\gamma_z z} \tag{E.81}$$

or

$$h_2(z) = C_3\cos(\gamma_z z) + D_3\sin(\gamma_z z) \tag{E.82}$$

$J_m(\gamma_p\rho)$ and $Y_m(\gamma_p\rho)$ represent the Bessel functions of first and second kind respectively; $H_m^{(1)}(\gamma_p\rho)$ and $H_m^{(2)}(\gamma_p\rho)$ represent Hankel functions of the first and second kind respectively. Although Eqns (E.77) to (E.82) are valid solutions for $f(\rho)$, $g(\phi)$ and $h(z)$, the most appropriate form depends upon the problem in question. Bessel functions are used to represent standing waves while Hankel functions are used to represent traveling waves. Exponentials represent travelling waves while Trigonometric functions represent periodic waves.

E.6 Bessel functions

The standard form of Bessel's equation can be written as

$$x^2\frac{d^2y}{dx^2} + x\frac{dy}{dx} + (x^2 - v^2)y = 0 \tag{E.83}$$

where $v \geq 0$ is a real number. Another useful form is obtained by changing the variable $x = u\lambda$ and replacing u by x.

$$x^2\frac{d^2y}{dx^2} + x\frac{dy}{dx} + (x^2\lambda^2 - v^2)y = 0 \tag{E.84}$$

When v is **not** an integer we can write the solution as

$$y(x) = A_1 J_v(x) + B_1 J_{-v}(x) \quad \text{for } x \neq 0 \tag{E.85}$$

or

$$y(x) = A_1 J_v(\lambda x) + B_1 J_{-v}(\lambda x) \quad \text{for } x \neq 0 \tag{E.86}$$

where

$$J_v(x) = \sum_{m=0}^{\infty} \frac{(-1)^m (x/2)^{2m+v}}{m!(m+v)!} \tag{E.87}$$

$$J_{-v}(x) = \sum_{m=0}^{\infty} \frac{(-1)^m (x/2)^{2m-v}}{m!(m-v)!} \tag{E.88}$$

$$m! = \Gamma(m+1) \tag{E.89}$$

If v is an integer, then the two functions $J_v(x)$ and $J_{-v}(x)$ become linearly dependent i.e if $v = n$ where $n = 1, 2..$

$$J_n(x) = (-1)^n J_n(x) \quad \text{for } n = 1, 2, .. \tag{E.90}$$

As the combination of two dependent solutions of a differential equation is itself a solution, the second solution of Bessel's function is

$$Y_v(x) = \frac{J_v(x)\cos(v\pi) - J_{-v}(x)}{\sin(v\pi)} \tag{E.91}$$

with

$$Y_n(x) = \lim_{v \to n} Y_v(x) \tag{E.92}$$

The function $Y_0(x)$ is also called Neumann or Weber function of order zero and denoted by $N_0(x)$. For integral values of v, $Y_v(x)$ becomes infinite at $x = 0$, so it cannot be present in any problem for which $x = 0$ is included in the region over which the solution applies. When $v = n$ is an integer,

$$y(x) = A_2 J_n(x) + B_2 Y_n(x) \quad v = n = 0 \text{ or integer} \tag{E.93}$$

So for all v, the general solution of Bessel's equation in the standard form is

$$y(x) = C_1 J_v(x) + C_2 Y_v(x) \tag{E.94}$$

or

$$y(x) = C_1 J_v(\lambda x) + C_2 Y_v(\lambda x) \tag{E.95}$$

$J_v(x)$ is the Bessel's function of the first kind of order v, $Y_v(x)$ is the Bessel's function of the second kind of order v and $\Gamma(x)$ is the gamma function.

Replacing the independent variable x in Bessel's equation by jx changes the differential equation to

$$x^2 y'' + xy' - (x^2 + v^2)y = 0 \tag{E.96}$$

which is called Bessel's modified equation of order v. This equation has two linearly

independent complex solutions $J_v(ix)$ and $Y_v(ix)$. Since they are not convenient to use, they are scaled and combined to give two real linearly independent solutions denoted by $I_v(x)$ and $K_v(x)$. These are modified Bessel functions of the first and second kinds of order v.

$$I_v(x) = \sum_{m=0}^{\infty} \frac{x^{2m+v}}{2^{2m+v} \, m! \Gamma(m+v+1)} \tag{E.97}$$

Provided v is not an integer, the general solution of Bessel's modified equation can be written as

$$y(x) = C_1 I_v(x) + C_2 I_{-v}(x) \quad v \neq 0 \text{ or integer} \tag{E.98}$$

Usually $K_v(x)$ is used in place of $I_{-v}(x)$

$$K_v(x) = \frac{\pi}{2} \left(\frac{I_{-v}(x) - I_v(x)}{\sin v\pi} \right) \tag{E.99}$$

In case v is an integer, the function K_n is defined as

$$K_n(x) = \lim_{v \to n} \frac{\pi}{2} \left(\frac{I_{-v}(x) - I_v(x)}{\sin v\pi} \right) \tag{E.100}$$

The general solution of Bessel's modified equation can be written in the form

$$y(x) = C_1 I_v(x) + C_2 K_v(x) \tag{E.101}$$

with no restriction placed on v. When the Bessel's modified equation is written in the form

$$x^2 y'' + xy' - (\lambda^2 x^2 + v^2) y = 0 \tag{E.102}$$

its general solution is given by

$$y(x) = C_1 I_v(\lambda x) + C_2 K_v(\lambda x) \tag{E.103}$$

The modified Bessel functions are related to the regular Bessel functions as

$$I_v(x) = j^{-v} J_v(jx) = j^v J_{-v}(jx) = j^v J_v(-jx) \tag{E.104}$$

$$I_{-v}(x) = j^v J_{-v}(jx) \tag{E.105}$$

Hankel functions are defined as

$$H_v^{(1)}(x) = J_v(x) + jY_v(x) \tag{E.106}$$

$$H_v^{(2)}(x) = J_v(x) - jY_v(x) \tag{E.107}$$

where $H_v^{(1)}(x)$ is the Hankel function of the first kind of order v, and $H_v^{(2)}(x)$ is the Hankel function of the second kind of order v. Since both functions contain $Y_v(x)$, both are singular at $x = 0$. The Henkel functions are related to the modified Bessel functions as

$$K_v(x) = \frac{\pi}{2} j^{v+1} H_v^{(1)}(jx) = \frac{\pi}{2}(-j)^{v+1} H_v^{(2)}(-jx) \tag{E.108}$$

If the argument is complex (i.e $xe^{3\pi i/4}$), we get Kelvin functions.

$$\text{ber}_v(x) + j\text{bei}_v(x) = J_v(xe^{3\pi i/4}) \tag{E.109}$$

The modified Bessel function of order v and argument x may be defined as the integral function given by

$$I_v(x) = \frac{1}{2\pi} \int_{-\pi}^{\pi} e^{x\cos\theta} \cos v\theta \, d\theta \tag{E.110}$$

To obtain the derivatives of $I_v(x)$, we differentiate both sides of Eq. (E.110) with respect to x to obtain

$$\frac{dI_v(x)}{dx} = \frac{1}{2\pi} \int_{-\pi}^{\pi} \cos\theta \, e^{x\cos\theta} \cos v\theta \, d\theta \tag{E.111}$$

$$\frac{dI_v(x)}{dx} = \frac{1}{2} \left[\frac{1}{2\pi} \int_{-\pi}^{\pi} e^{x\cos\theta} \cos(v+1)\theta \, d\theta + \frac{1}{2\pi} \int_{-\pi}^{\pi} e^{x\cos\theta} \cos(v-1)\theta \, d\theta \right] \tag{E.112}$$

$$\frac{dI_v(x)}{dx} = \frac{1}{2} [I_{v+1}(x) + I_{v-1}(x)] \tag{E.113}$$

Eq. (E.113) is valid for $v \geq 1$. For $v = 0$,

$$\frac{dI_0(x)}{dx} = I_1(x) \tag{E.114}$$

Similarly,

$$\frac{d}{dx} I_0(\sqrt{j}\,\omega x) = \sqrt{j}\,\omega I_1(\sqrt{j}\,\omega x) \tag{E.115}$$

E.7   Retarded potentials

The potential functions **A** and Φ for time-varying fields are called the retarded potentials. The magnetic vector potential **A** is defined in terms of the magnetic field density **B**

$$\mathbf{B} = \nabla \times \mathbf{A} \tag{E.116}$$

Substituting this in the Maxwell's equation Eq. (E.1)

$$\nabla \times \mathbf{E} = -\frac{\partial}{\partial t}(\nabla \times \mathbf{A}) \tag{E.117}$$

$$\nabla \times (\mathbf{E} + \frac{\partial \mathbf{A}}{\partial t}) = 0 \tag{E.118}$$

Eq. (E.118) says that the curl of some vector is zero, which means that the vector can be derived as the gradient of some scalar. If we assume the electric potential Φ as the scalar function

$$\mathbf{E} + \frac{\partial \mathbf{A}}{\partial t} = -\nabla \Phi \tag{E.119}$$

$$\mathbf{E} = -\nabla \Phi - \frac{\partial \mathbf{A}}{\partial t} \tag{E.120}$$

Substituting Eq. (E.120) in Eq. (E.3) we get

$$-\nabla^2 \Phi - \frac{\partial}{\partial t}(\nabla \cdot \mathbf{A}) = \frac{q}{\varepsilon} \tag{E.121}$$

Replacing **H** by **B** in Eq. (E.2) and substituting Eq. (E.116) and (E.120) we get

$$\nabla \times \nabla \times \mathbf{A} = \mu \mathbf{J} - \mu \varepsilon \left[\nabla \left(\frac{\partial \Phi}{\partial t} \right) + \frac{\partial^2 \mathbf{A}}{\partial t^2} \right] \tag{E.122}$$

or

$$\nabla(\nabla \cdot \mathbf{A}) - \nabla^2 \mathbf{A} = \mu \mathbf{J} - \mu \varepsilon \left[\nabla \left(\frac{\partial \Phi}{\partial t} \right) + \frac{\partial^2 \mathbf{A}}{\partial t^2} \right] \tag{E.123}$$

Eq. (E.121) and Eq. (E.123) can be further simplified if we define **A**. To completely define a vector, we have to specify both its curl and divergence and its value at any one point. The curl of **A** is already defined, so if we choose the divergence as

$$\nabla \cdot \mathbf{A} = -\mu \varepsilon \frac{\partial \Phi}{\partial t} \tag{E.124}$$

we can simplify Eq. (E.121) and Eq. (E.123).

$$\nabla^2 \Phi - \mu\varepsilon \frac{\partial^2 \Phi}{\partial t^2} = -\frac{q}{\varepsilon} \tag{E.125}$$

$$\nabla^2 \mathbf{A} - \mu\varepsilon \frac{\partial^2 \mathbf{A}}{\partial t^2} = -\mu\mathbf{J} \tag{E.126}$$

The potentials $\mathbf{A}$ and Φ are now defined in terms of sources $\mathbf{J}$ and q and can be used to derive the electric and magnetic fields.

For static fields the derivatives with respect to time will become zero and Eq. (E.125) and Eq. (E.126) reduce to

$$\nabla^2 \Phi = -\frac{q}{\varepsilon} \tag{E.127}$$

$$\nabla^2 \mathbf{A} = -\mu\mathbf{J} \tag{E.128}$$

For fields that are time-harmonic, Eq. (E.125) and Eq. (E.126) will become

$$\nabla^2 \Phi - \varepsilon\mu\omega^2 \Phi = -\frac{q}{\varepsilon} \tag{E.129}$$

$$\nabla^2 \mathbf{A} - \varepsilon\mu\omega^2 \mathbf{A} = -\mu\mathbf{J} \tag{E.130}$$

E.8   References

Electromagnetics and Mathematics

1. W.R.Smythe, *Static and Dynamic Electricity* (2nd ed.), McGraw Hill Book Company, 1950

2. W.H.Hayt Jr, J.A.Buck, *Engineering Electromagnetics* (6th ed.), Tata McGraw-Hill, 2001

3. S.Ramo, J.R.Whinnery, T. van Duzer, *Fields and Waves in Communication Electronics* (3rd ed.), John Wiley and Sons, 1994

4. C.A.Balanis, *Advanced Engineering Electromagnetics* (1st ed.), John Wiley and Sons, 1989

5. A.Jeffrey, *Advanced Engineering Mathematics* (1st ed.), Academic Press Elsevier India, 2002

6. M.Abramowitz, I.E.Stegun, *Handbook of Mathematical Functions*, Dover, 1970

_____